SEISMIC WAVE PROPAGATION IN IRAN AND EASTERN INDIAN SHIELD

A Dissertation Submitted to the
College of Graduate and Postdoctoral Studies
In Partial Fulfillment of the Requirements
For the Degree of Doctor of Philosophy
In Geophysics
In the Department of Geological Sciences
University of Saskatchewan
Saskatoon

By

MARYAM SAFARSHAHI

PERMISSION TO USE

In presenting this dissertation in partial fulfillment of the requirements for a Postgraduate degree from the University of Saskatchewan, I agree that the Libraries of this University may make it freely available for inspection. I further agree that permission for copying of this dissertation in any manner, in whole or in part, for scholarly purposes may be granted by the professor who supervised my dissertation work or, in his absence, by the Head of the Department or the Dean of the College in which my dissertation work was done. It is understood that any copying or publication or use of this dissertation or parts thereof for financial gain shall not be allowed without my written permission. It is also understood that due recognition shall be given to me and to the University of Saskatchewan in any scholarly use which may be made of any material in my dissertation.

Requests for permission to copy or to make other uses of materials in this dissertation in whole or part should be addressed to:

Head of the Department of Geological Sciences
Geology Building, 114 Science Place
University of Saskatchewan
Saskatoon, Saskatchewan S7N 5E2 Canada

OR

Dean
College of Graduate and Postdoctoral Studies
University of Saskatchewan
116 Thorvaldson Building, 110 Science Place
Saskatoon, Saskatchewan S7N 5C9 Canada

ABSTRACT

This dissertation addresses several important aspects of observational earthquake seismology: 1) methods for data management and processing large datasets, 2) analysis of seismic wave propagation at local to regional (up to about 700 km) source-receiver distances, 3) analysis of seismic coda, and 4) critical re-evaluation of the fundamental problem of seismic wave attenuation and measurement of the seismic "quality" factor (Q). These studies are carried out using new and previously analyzed earthquake data from Iran.

In each of the four application areas above, innovative methods are used and significant new results are obtained. First, for efficient managing and processing of large earthquake datasets, I use a flexible, exploration-style open-source seismic processing system. Custom and problem-oriented scripts using Matlab or Octave software are included as tools in this processing system, allowing interactive and non-interactive analysis of earthquake records. In the second application, I note that the existing models for body-wave amplitudes are hampered by several difficulties, such as inaccurate accounts for the contributions of source and receiver effects and insufficient accuracy at the transition between the local and regional distances. Finding a reliable model for body-wave amplitudes is critical for many studies. To achieve such a reliable model, I use a joint inversion method based on a new parameterization of seismic attenuation and additional constraints on model quality. The joint inversion provides a correct model for geometrical spreading and attenuation. The geometrical-spreading model reveals the existence of an increase of body S wave amplitudes from 90 to about 115 km from the source which might be caused by waves reflecting from the crust-mantle boundary. Outside of this distance range, amplitude decays are significantly faster than usually assumed in similar models.

Third, in two chapters of this dissertation devoted to coda studies, I consider the concept of the frequency-dependent coda Q (Q_c). Although this quantity is usually attributed to the subsurface, I argue that because of subjective selections of model assumptions and algorithms, Q_c cannot be rigorously viewed as a function of surface or subsurface points. Also, frequency dependence of the measured Q_c strongly trades off with the subjectively selected parameters of the measurement procedure. To mitigate these problems, instead of mapping a hypothetical in-situ Q_c, I obtain maps of physically justified parameters of the subsurface: exponents of geometrical

spreading (denoted γ) and effective attenuation (denoted q_e). For the areas of this study, parameter γ ranges from 0.005 s^{-1} to 0.05 s^{-1} (within Zagros area of Iran) and 0.010 s^{-1} to 0.013 s^{-1} (within the eastern Indian Shield).

Finally, from both body- and coda-wave studies, I derive estimates of seismic attenuation within the study areas. In two areas of Iran and within the Indian Shield, weak attenuation with Q-factors of 2000–6000 or higher is found. In particular, coda envelopes can be explained by wave reverberations within elastic crustal structures, and the Q-type attenuation appears undetectable.

ACKNOWLEDGMENTS

My deepest gratitude goes to my supervisor Dr. Igor Morozov. He has always been supportive and kind, and he has helped me to get to the right point. He is extremely patient with my unending questions. I am so blessed to have his supervision during my Ph.D. His tremendous support, deep vision, and knowledge have guided me to build my passion in my research. He has taught me how to approach problems and solve them in scientific research. I am gratefully indebted to his invaluable comments, suggestions which improved my communication skills to other research efficiently. This accomplishment would not have been achieved without his assistance.

I want to express my gratitude to my advisory committee: Dr. Samuel Butler, Dr. James Merriam, and Dr. Sasha Koustov, for their instructive feedback and informative suggestions on my research. They have contributed considerably to enhancing my research and presentation skills. I also thank the external examiner, Dr. Stefano Parolai, for participating in my defense.

I would like to especially thank the Iranian Seismological Center (IRSC) for providing data for my dissertation.

I thank Song Hu for his IT support and for offering quick help with all my IT queries.

I am highly grateful to the support by the Department of Geological Sciences, and particularly to Chantal Strachan-Crossman, who is our Graduate Program Administrator. I express my gratitude to my officemates. I especially thank Mohamed Haiba for his kindness in teaching me ProMAX.

Last but not least, I would like to express my huge thanks and most profound appreciation to my wonderful parents and my siblings. They constantly support me and believe in my talent. They always encourage me to follow my dreams. I am enormously grateful for having them. I am thankful to my aunt, Morvarid Rezaee. She had been on dialysis for 17 years. She passed away a year ago. We had a great phone call each week. She was one of my most incredible role models, and she taught me to embrace and appreciate life in terms of any difficulties. She always inspired me with her perseverance in her life, and her memories will always stay in my heart.

DEDICATION

This dissertation is dedicated to my wonderful family who continuously support and love me.

TABLE OF CONTENTS

LIST OF TABLES

LIST OF FIGURES

SYMBOLS AND ABBREVIATIONS

Name	**Abbreviations/ Symbols**
One-Dimensional	1D
Two-Dimensional	2D
Three-Dimensional	3D
Three-Component	3C
The Orientation-Independent Horizontal Component Amplitude	H2C
Quality Factor	Q
Coda Quality Factor	Q_c
Effective Q	Q_e
Frequency-Dependent Q at Frequency 1 Hz	Q_0
Attenuation Level $q=1/Q$	q
High Frequency Spectral Decay Parameter	κ
Power-Law Exponents of Geometrical Spreading	ν
Temporal Attenuation Coefficient	χ
Zero-Frequency Geometrical Attenuation Coefficient	γ
Exponent in the Power Law $Q\left(f\right)=Q_0 f^{\eta}$	η

CHAPTER 1

INTRODUCTION

The structure and physical properties of the Earth can be understood by the analysis of seismic waves produced by earthquakes. Quantitative measurements of the various properties of seismic wavefields and their interpretation are among the key tools for estimating and mitigating seismic hazard, understanding the physical properties and structure of the Earth, monitoring mining hazards, and nuclear weapons tests. This broad variety of goals is achieved by developing physical and mathematical models for the travel times, amplitudes, and waveforms of various types of seismic waves and quantitative correlations of these predictions with observations. Thus, accurate mathematical models capturing the essential physical phenomena, and their inversion for the Earth's properties are most important for achieving these goals.

In this dissertation, I describe new contributions to several groups of quantitative seismological research methods, including inversions for high-frequency spectral decays (the so-called "kappa" (κ)), analysis of coda (the low-amplitude long tails recorded much later after primary arrivals with exponential amplitude decay) mapping methodology, earthquake relocation, and processing of large datasets. These studies are carried out in application to seismic datasets from two areas in Iran (Rigan and Zagros), and also in a re-interpretation of a recently published study of the East Indian Shield by Singh et al. (2019). Further in this chapter, I describe the main research questions addressed in this work and its specific objectives.

1.1. Research Questions

In observational seismology, several types of waves are used for characterizing different depth ranges and types of structures within the Earth. Body waves (seismic waves moving through the interior of the Earth) recorded at distance ranges from several meters to thousands of kilometers are generally characterized by higher frequencies, and their travel times are used for constraining the seismic velocity structure. In particular, body waves are the basis of reflection seismology. Body waves are often followed by coda waves, which consist of long wave trains of scattered arrivals approximately exponentially decaying with time. The physical mechanisms of these waves are still not well understood, nevertheless, they represent a powerful and convenient tool for characterizing the Earth's crust beneath the seismic stations (Aki, 1969). Surface waves are characterized by effective propagation within a limited range of depths (meters to hundreds of kilometers), and they are broadly used for constraining layered structures. Free oscillations of the Earth represent the extreme long-wavelength type of surface waves, and they are used for constraining the structure of the Earth's core, and in particular its seismic-wave attenuation. Finally, in the recent about twenty years, seismologists started effectively using seismic noise waves (microtremor and microseisms) for producing analogues of body-wave and surface-wave imaging.

Of the different types of seismic waves described above, in this dissertation, I focus only on the higher-frequency body and coda waves at local to regional distance ranges. The term "local" refers to the separations between the earthquake source and receiver by less than the typical distance of the so-called "critical" reflection from the base of the crust, which is about 90–100 km. Larger distances beyond about 110–150 km and to about 1000 km are called "regional". These source-receiver distance ranges are represented in all datasets of this study. Beyond the regional distance range, the teleseismic range begins.

In the following subsections, I briefly pose the key research questions of this dissertation. I start with three of the more fundamental questions related to the methods of data measurement and inversion, and finish with two relatively common topics related to earthquake data analysis. Nevertheless, these topics also include significant research questions that are very important for the present project.

1.1.1. Standard models for body-wave amplitudes

For body and coda waves within the local to regional distance ranges, there are several general research questions addressed in this dissertation. First, decomposition of the spectral amplitudes of body waves into the contributions of the source, receiver, and path-related effects still presents substantial difficulties. Although a number of travel-time- (t) and frequency- (f) dependent models for seismic-wave amplitude $A(t,f)$ have been proposed, none of them achieve sufficient accuracy within both the local and regional distance ranges (Atkinson, 2012) and particularly across the transition between these ranges. In this dissertation, I identify four general reasons for this difficulty of obtaining consistent and accurate $A(t,f)$ models:

1) Usually insufficiently parameterized frequency-independent variation of amplitudes (Morozov, 2008b, 2010a). This lack of parameterization exists at both the local and regional distance ranges, but as shown in this dissertation, it is particularly strong in the transition between them.
2) The use of a frequency-dependent $Q(f)$ for modeling the travel-time (denoted t below) and frequency (f) dependent amplitudes for a seismic wave: $A(t, f) = A_0 \exp\left(-\pi Q^{-1} ft\right)$. This hypothesis of the "frequency-dependent Q-factor" is very broad in seismology, and it has been debated by Morozov (2008b, 2010a, and other papers) for some time and from multiple points of view. Despite its broad acceptance, the frequency-dependent Q has a limited physical meaning of only an apparent (measurement-specific) quantity (Morozov and Baharvand Ahmadi, 2015). Even if taken as a pure mathematical (phenomenological, or empirical) law, the above dependence with a single $Q(f)$ does not allow accurate matching of the observed $A(t,f)$ at all t. The data are usually dominated by regional distance ranges, which results in poor $A(t,f)$ fitting at local distances.
3) When modeling $A(t,f)$, all relevant physical factors such as the source and receiver coupling factors, geometrical spreading, the corresponding high-frequency source- and receiver-site parameters (often called "kappa"), and the Q need to be inverted simultaneously. This requirement (implemented in this dissertation) also represents a significant change compared to today's standard practice. In the existing approaches, the geometrical spreading is usually not analyzed, and the inversion starts with the frequency-dependent Q.
4) In the existing methods for $A(t,f)$ data fitting, it is rarely noted that the resulting amplitude errors vary systematically with travel time (t) and frequency (f). Such error trends are unacceptable in data inversion, and they need to be corrected by modification of the data-fitting methods. Contrary to what is commonly assumed, least-squares or similar fitting of data alone does not guarantee a unique or even a

correct solution. Thus, inverse methods themselves need to be carefully revised for the $A(t,f)$ fitting problem.

Solution of the above problems and finding a reliable model for body-wave amplitudes $A(t,f)$ is of key importance for many applications: measurement of seismic attenuation, inverting for physical properties of passive and active sources, determining the structure and physical state of the Earth, and for locating zones of crustal heterogeneities within the subsurface. In this dissertation, I refer to this problem as formulating a "standard model" for body-wave amplitudes and examine it on the detailed example of S waves in the study area.

1.1.2. Analysis of seismic coda

Another very general problem of time- and frequency-dependent amplitudes $A(t,f)$ considered in this dissertation is related to coda amplitudes. Since the pioneering studies of seismic codas by Aki (1969), the amplitudes $A(t,f)$ themselves are actually not analyzed, but only their logarithmic decrements $d\ln A(t,f)/dt$ are interpreted in terms of a phenomenological property of the crust called the frequency-dependent "coda Q" (denoted Q_c). The observed Q_c is further explained by similar quality-factor properties of the Earth, such as the S-wave Q, intrinsic, and scattering Q-factors. Spatial variations of these Q-factors are mapped and correlated with geological structures, zones of heterogeneity and increased temperatures, or zones containing partial melts or fluids within the Earth's crust.

However, as shown in this dissertation, all of the traditional Q-factors are still phenomenological attributes, which actually cannot be rigorously associated with spatial locations. To obtain a rigorous model of coda amplitudes and derive rigorous physical properties of the subsurface, the complete coda amplitudes $A(t,f)$ need to be inverted. The mapped properties should be carefully differentiated from the observed ones. This differentiation is somewhat complicated in the existing Q models, and it is investigated in this dissertation.

1.1.3. Physical meanings and measurement of the seismological *Q*

The analysis of body-wave and particularly coda amplitudes leads us to the question of the physical meaning and properties of the Q-factor for certain materials, structures (crust, layers, etc.), or of the whole Earth. This question is extremely broad and important but poorly understood in seismology. The notation 'Q' and the common use of the term "attenuation" in physics usually refer to amplitude decays $A(t,f)$ in some oscillatory processes, in which the relative mechanical-energy loss is proportional to the number of oscillation cycles. In seismology, this proportionality is represented by using the inverse Q-factor in the time-distance relation for a decaying harmonic wave, similar to the $A(t,f)$ relation mentioned above: $w(t,x) = A_0 \exp\left[-2\pi fi\left(t - \frac{x}{c}\right)\right]\exp\left(-\pi Q^{-1} f \frac{x}{c}\right)$, where x is the observation distance, and c is the phase velocity of the wave (Aki and Richards, 2002). Thus, Q^{-1} represents the characteristic exponential decrease of the observed wave amplitude with the travel distance x and frequency f.

However, the physical meanings and frequency dependencies of $c(f)$ and $Q(f)$ are poorly understood (Morozov and Baharvand Ahmadi, 2015). The definitions of these Q-factors and most of their measurement procedures in observational seismology rely on subjective assumptions about some "reference" geometrical spreading (Morozov, 2008b). Physical interpretations of Q_c are only supported by theoretical models of scattering on small random heterogeneities in macroscopically-homogenous media (e.g., Fehler and Sato, 2003). These models are extremely simplified and disregard even the key elastic structures of the study areas, such as the crust-mantle boundary, crustal layering, and velocity gradients. Morozov (2008b, 2010a) showed that by removing these assumptions, frequency dependencies $Q(f)$ often change from nearly proportional to frequency to frequency-independent, and the values of Q at $f = 1$ Hz typically increase by as much as 20–30 times.

1.1.4. Relocation

In addition to the "advanced" topics above, the data analysis in this dissertation addresses several research goals that are well-established and relatively common for local and/or regional seismic studies. Nevertheless, these steps of data analysis require significant efforts and provide key information for seismic characterization of the study areas.

Of such relatively standard data analysis, in this dissertation, I present results of event relocation of the Zagros area. Relocation allows obtaining more accurate locations of the earthquakes recorded in the datasets, which also helps improving any further steps of data analysis such as the travel-time tomography. Therefore, the achieved results of relocation provide significant information about how the seismicity is distributed in the Zagros area.

1.1.5. Processing of large earthquake datasets

With large and rapidly growing volumes of data collected by today's seismographic networks, efficient procedures for their analysis have become a significant issue. For example, the Zagros dataset of this study was obtained in the form of over 250,000 files recording nearly 1300 earthquakes at 62 stations. These data are arranged in multiple multi-level directories on a file system. One well-known difficulty of this dataset structure is that if it is done without proper precautions, its simple listing in Unix often returns error "Argument list too long". Each of the files contains a single-channel recording of one seismic event (usually an earthquake) from a certain station. Lists of earthquakes and stations, and files containing station responses are provided separately, and all of these data need to be tied together with the dataset. Finally, all of these files need to be looked at in various sequences and combinations, and by using various types of transformations and displays.

In seismological research, there is currently no universal and broadly available software that would allow efficient management of such amounts and complex structures of data. Thus, development of a robust data-management approach was one of the first challenges of the present project. As described in this dissertation, this task was achieved by combining a high-throughput, seismic-exploration style open-source processing system (IGeoS, Morozov, 2008a) with custom scripts using Matlab or Octave software.

1.2. Specific Objectives and Contributions

From the preceding section, the research scope of this project encompasses several significant problems in earthquake seismology ranging from the basic physics of the Earth's interior to modeling seismic wave propagation to inversion, seismological imaging and data management. In a brief summary, the specific objectives and expected contributions of this study are as follows:

1) Developing a procedure for efficiently managing large earthquake datasets and carrying out versatile data analysis;

2) Performing relocation of seismic events;
3) Proposing improvements to inversion of geophysical data using additional model-quality control and additional constraints;
4) Developing a joint inversion method for obtaining a "standard model" for seismic body wave amplitudes $A(t,f)$. This model should provide good and uniform S-wave data fitting at local and regional distances, and it should also be applicable to other types of seismic waves and other regions.
5) Together with the standard model, producing more accurate models for geometrical spreading and kappa effects, source and receiver coupling factors, and also estimates of the Q-factor inverted for the crust;
6) Performing rigorous statistical analysis of the uncertainties of the standard wave-amplitude model;
7) Study of the regionalization (mapping) methods for seismic coda properties. This study will be done for the Zagros area, with a comparison to the earlier results from the East Indian Shield (Singh et al., 2019).
8) Coda mapping by interpolation and mapping of scatterers;
9) Analysis of coda mapping methodology and interpretation of the physical meaning of coda maps.

1.3. Data and Methods

The datasets of this study will be described in chapter 2, and here, I only outline them. The main dataset is a large dataset from the area of Zagros Mountains in Iran, provided by the Iranian Seismological Center. These data were acquired in 2016-17 and consist of over 250,000 data files recorded from about 1300 earthquakes on 62 seismic three-component stations (short, medium- and broad-band).

In addition to the large Zagros dataset, I also use a small dataset from an adjacent area of southeastern Iran (Rigan). The small dataset allows detailed analysis of the inversion procedures and results, and it reveals model features which may be difficult to notice in a large and complex dataset. Rigan dataset consists of 31 records from two Rigan area earthquakes with magnitudes Mw ≈ 6.5 and Mw ≈ 6.2 (magnitudes reported by the U.S. Geological Survey) recorded in 2010 and 2011 by the Iranian Strong Motion Network. This dataset was used in my previous study (Safarshahi et al., 2013), and in the present dissertation, it is completely re-interpreted with the goal of obtaining a much more accurate standard model for body S-wave amplitudes.

Also, in the coda regionalization study (chapter 6 of this dissertation), I employ yet another single-station dataset from eastern India. However, this part of the study is purely methodological and carried out by re-interpreting the coda Q (Q_c) measurements by Singh et al. (2019). Because I have no access to the original data by Singh et al. (2019), I will not describe these data in this dissertation and only discuss the different interpretations of Q_c measurements and their implications.

The general methodology of this study can be subdivided into three parts:

1) Organization of the data and its analysis;
2) Physical and mathematical approaches to describing the seismic amplitudes and attenuation;
3) Inversion methods.

Regarding the data organization and handling in the computer (methodology 1) above), analysis of large earthquake datasets such as the Zagros dataset often presents significant challenges. Data analysis can be complex and requires combing different types of data from multiple sources, standard and customized types of data filtering, and multi-step imaging with interpretation procedures. The analysis is often elaborate and requires extraction of various subsets of the data, with numerous approaches to visualization. Combinations of “batch” processing (standalone processing of large data volumes) and interactive analysis of small subsets are needed. Use of unconventional inversion methods require creation of new software and algorithms. These requirements determine the computer methods used in this study.

In seismological research, seismic data are commonly presented by multiple single-record files and processed by specialized packages such as SAC, SEISAN, or specialized subroutine libraries used with Matlab, Python, or similar high-level interpreted computer languages. In this dissertation, I use an efficient approach to earthquake data processing, based on the software system called IGeoS (Morozov, 2008a). This package is a Unix-based, high-throughput and modular seismic processing system, so that most data-handling operations such as sorting, filtering, and maintaining any number of record headers (metadata) is performed by the system automatically. To include customizable processing of earthquake data, IGeoS includes tools allowing execution of arbitrary scripts by invoking Octave (or Matlab), Generic Mapping Tools (GMT), and other software tools.The IGeoS system natively supports multicomponent, variable-length records with unlimited headers (metadata), and its tools provide essentially unlimited options for input/output, flexible data sorting, access to databases, several types of displays, and numerous tools for single- and multichannel signal filtering and imaging. All secondary analysis of the data and inversion is performed by Octave, and the resulting databases are stored in the form of Octave workspaces. Finally, final high-quality plotting is performed by using GMT programs under Unix.

The methodology of data analysis in this project also uses many approaches standard in earthquake and exploration seismology. In particular, a large portion of the time was spent on interactive editing and quality control of the data, picking P- and S-wave travel times, examination of coda windows, and examination of ground motion in the first arrivals, and other interactive or semi-interactive data processing.

With regard to the physical and mathematical methodologies 2), this dissertation makes several significant contributions. I introduce a new model for seismic spectral amplitude $A(t,f)$, which resolves difficulties the long-standing issue of under-parameterization of geometrical spreading and over-parameterization of Q (section 1.1; Safarshahi and Morozov, 2021a) and achieves accurate data fitting at all distance ranges. The approach is general and applies to time-frequency dependencies used in many studies. Another major contribution is the first application of the new model of "geometrical attenuation" and the frequency-independent Q (Morozov, 2008b, 2010a) to new seismic data. This model applies to numerous studies of studies attenuation, and it offers a new view on the popular concept of the frequency-dependent Q.

An important general methodological observation important for many attenuation studies is made in chapters 5, 6 and 7. As argued there, the Q is only an apparent quantity, which means that this quantity can only be defined for the observed wave amplitudes, but it cannot be rigorously attributed to the Earth's subsurface. By careful differentiation between the true physical and apparent properties, physically-consistent models of the subsurface are obtained.

Regarding the inversion methodology 3) above, the dissertation also attempts reconsidering the paradigm established in the current seismological research. In the study of standard models, I show that traditional inversions based on minimizing the data misfits only is insufficient, and additional constraints are required. These constraints are imposed in the form of exact equations, which is again different from the usual ways in which, for example, smoothness constraints are used in existing methods. To evaluate model uncertainties, statistical bootstrapping of the datasets is used in several cases. In this dissertation, an original modification of inversion methods is also proposed (chapter 5).

1.4. Structure of this Dissertation

This dissertation is based on several recent publications (Morozov and Safarshahi, 2020; Safarshahi and Morozov, 2021a, 2021b, and submitted). Each of these papers is included as a chapter, and additional chapters are added for introduction. In the present chapter 1, I give a general introduction to this dissertation, pose the critical research questions, summarize the specific objectives, and outline the general approach and the significance of this research. In chapter 2, I overview the data and the relevant geology of the study areas. In the subsequent chapters, I present the different aspects of data analysis and results of this study:

1) In chapter 3, I describe the existing approaches to seismic data analysis for similar (large) earthquake datasets and present the approach used for the Zagros dataset of this study. In this chapter, I also illustrate the quality of the data and the travel time picks made in them.
2) In chapter 4, I perform relocation of seismic events and adjustment of their origin times by using picked P-wave travel times. This is a preliminary inversion procedure, which is important for subsequent analysis, such as the travel-time tomography. This procedure also gives important geological information, such as the start times of the earthquake ruptures and their improved locations.
3) In chapter 5, I invert the Rigan-area seismic data for an improved model for time- and frequency dependent amplitudes of body S waves.
4) In chapters 6, and 7, I evaluate the characters of seismic codas from two different areas. In both cases, I show that coda amplitude envelopes are nearly independent of

frequency and are likely caused by mostly elastic reverberations. In chapter 6, this is shown by re-interpreting Q_c results from a paper by Singh et al. (2019), and in chapter 7, this observation is derived from the Zagros dataset of this study.

5) Finally, in chapter 8, I recap and integrate the most significant results of this dissertation and suggest several directions for future research.

CHAPTER 2

DATA AND STUDY AREAS

This chapter gives an overview of the study areas, their geology, and the available earthquake seismic datasets. Most of the work in this dissertation is done for Iran, but in chapter 6, I also consider an adjacent area of the eastern Indian Shield. The Indian Shield dataset will be described in that chapter.

Parts of the descriptions of the seismic datasets and geology of the study areas are based on the following papers:

- Safarshahi, M., Rezapour, M., Hamzehloo, H. (2013). Stochastic finite fault modeling of ground motion for the 2010 Rigan earthquake, southeastern Iran. Bulletin of the Seismological Society of America, **103**, 223–235, DOI: 10.1785/0120120027.
- Safarshahi, M., and Morozov, I. B. (2021a). Robust empirical time-frequency relations for seismic spectral amplitudes, part 1: Application to regional S waves in southeastern Iran. Bulletin of the Seismological Society of America, **111**, 173-192, DOI: 10.1785/0120200172

The copyrights for these papers belong to the Seismological Society of America, which allows authors to use their papers in their dissertations. The texts were modified and reformatted for inclusion in this dissertation. My contributions to the papers consisted in preparing and proccessing the data, modeling, providing codes, interpretation and writing.

2.1. Introduction: Wave Types Used in this Study

An earthquake generates multiple seismic waves that propagate through the Earth and are recorded by seismic instruments. The different waves are differentiated by the mechanisms of their generation, propagation paths and styles, polarizations, and conditions (such as frequencies, distances) at which they can be recorded. According to the propagation paths, seismic waves are broadly differentiated into body waves traveling through the bulk of Earth, surface waves propagating in the vicinity of the surface, and guided waves, which may propagate within complex waveguides formed within the Earth’s crust and mantle.

Each of the seismic waves usually has a range of characteristic velocities and a pattern of ground movement by which it is recognized in the recorded seismograms. For example, the key waves used in most seismic studies are the primary (denoted P) and secondary waves (denoted S) (Figure 2.1). Body P waves are waves of volumetric (compressional) deformation, and they are characterized by relatively fast velocities and particle movement in the direction of propagation. By contrast, S waves are formed by shear deformation with particle movement perpendicular to propagation direction, and they are slower than P waves and arrive later in the seismograms (green seismogram in Figure 2.1). Surface waves represent combinations of P and S waves which exist only within the near surface (Figure 2.1). The depth of penetration for surface waves depends on their frequency, and it ranges broadly from about 1 m to 1000 km. Based on these basic wave types, numerous more complex wave types are created by their refractions, reflections and mutual transformations on various boundaries, and within the weathered near surface zone (grey in Figure 2.1). These waves are sensitive to the variations of seismic velocities, discontinuities, and other geological structures, and they are most important for seismic interpretation. In the following, I describe some of these waves used in this dissertation (Figure 2.1).

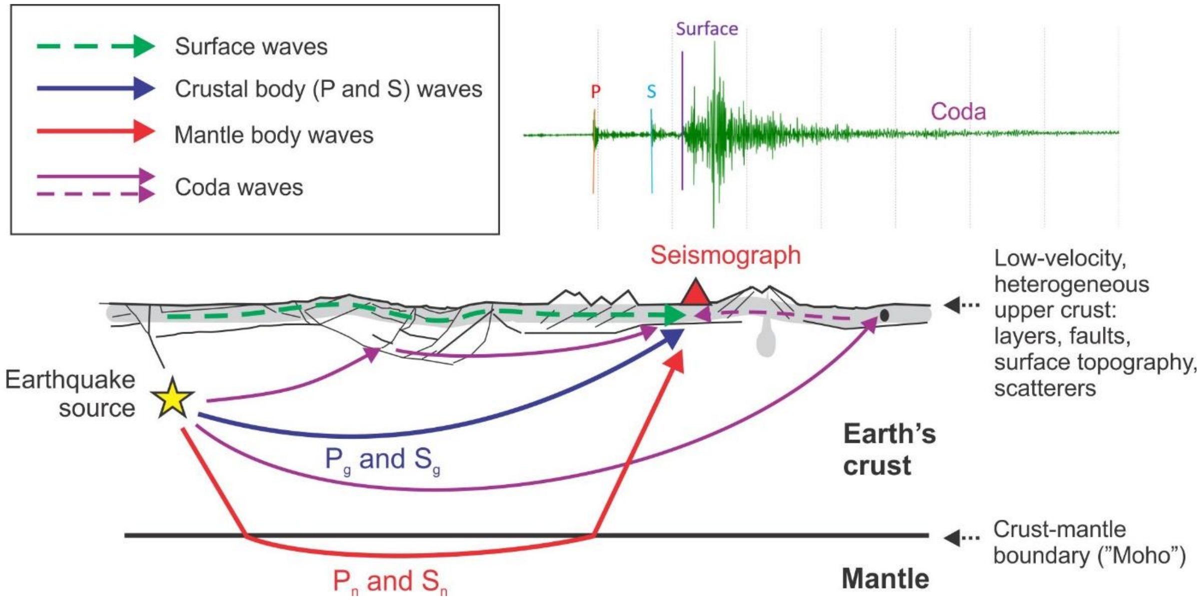

Figure 2.1. Schematic illustration of seismic waves within the Earth’s crust and uppermost mantle.

According to the IASPEI (International Association of Seismology and Physics of the Earth's Interior), a standard notation of seismic phases consisting of pairs of upper and lower-case characters. The phases considered in this dissertation are those commonly recorded in regional-distance (i.e., up to about 1000 km from the source) seismic investigations, which are denoted Pg, Sg, Pn, Sn, Lg, and "coda". Properties of these waves are briefly described in the following paragraphs.

Pg waves are the P waves propagating within the Earth's crust (with letter 'g' referring to the "granitic" crust) at average velocity around 6 km/s. This wave is observed from near zero to about 100–150 km distances. At larger distances, the Pg wave train is continued by multiple P-wave reflections within the crust. Among these reflections, the P-wave reflection from the base of the crust (called the Mohorovičić, or "Moho" discontinuity) is denoted PmP. This complex and reverberatory wave train propagates with group velocity of approximately 5.8 km/s.

Analogously to Pg, Sg waves travel within the crust, and at larger distances, Sg is extended by a superposition of multiple SmS reflections and other S-wave reverberations and conversions between P and S waves within the crustal waveguide. At larger distances, the Sg wave is conventionally designated Lg to represent its "long-range" character. The Sg/Lg wave is usually recognised as a strong and reverberatory package of transversely polarized ground motions traveling with a group velocity between 3.1 to 3.6 km/s (Figure 2.1). Due to the shearing mechanism of the earthquake source (called "double-couple"), Sg/Lg waves are often the strongest in higher-frequency seismic records at regional distances, such as used in this dissertation. In chapter 5, I use the amplitudes of S waves to measure the geometrical-spreading and attenuation properties of the crust.

Mantle velocities and structure are characterized by using the Pn and Sn waves, which are body P and S waves refracted (so-called head waves) on the Moho discontinuity (Figure 2.1). Pn waves travel with velocities near 8 km/s and are the fastest waves at these distances. Because these waves arrive before any other waves at these distances (and thus forming the "first arrivals"), these waves are generally easily detectable and most useful for source location (chapter 4) and P-wave velocity tomography. By contrast, mantle S-wave refractions (Sn) are slower than Pn and Pg. Because Sn waves arrive in the background of the preceding P waves, they are often difficult to identify. However, when picking seismic arrivals (chapter 3), I made several attempts to identify Sn in the data.

Another wave type broadly used in seismology and in this dissertation (chapters 6 and 7) is the earthquake coda (Figure 2.1). Coda waves represent the low-amplitude, exponentially decaying wavefields recorded much later than all primary arrivals. Codas are formed by superpositions of numerous waves of all types scattered from a large area surrounding the seismic station, which leads to their late arrival times (Figure 2.1). Despite its extremely complex composition, codas have relatively simple (near-exponential) shapes in which most of the detail of the source and receiver are averaged out (Aki, 1969). Therefore, codas are often viewed as a simple way for characterising the averaged properties of the crust beneath and around the seismic station (Figure 2.1). Earthquakes produce strong S waves, and therefore it is generally believed that codas also consist of predominantly S waves. Also, if the coda consists of randomly scattered waves at the state of stochastic equilibrium, each P- and S-wave mode would carry equal energy. This observation is known as the energy equipartitioning principle (Shapiro and Treitel, 1997). Therefore, because there exist two S-wave modes (polarizations) per one P-wave mode, most of the coda energy is believed to belong to S waves.

There is no universal agreement about how the coda is generated. Current coda models vary from uniformly-distributed, random, single scattering within the entire crust and parts of the uppermost mantle (Aki and Chouet, 1975) to multiple scattering (Shapiro and Treitel, 1997) and further to non-uniform scattering occurring within the shallow crust and involving surface waves (Figure 2.1; Morozov, 2011b).

Because coda represents no specific wave arrival, its start and end times are selected by convention, and in principle, these times should not affect the measurements. In practice, the coda time window is empirically estimated by the time larger than twice of the S-wave travel time after S-wave arrival time (Aki, 1969), so that both the source and receiver are located within the scattering area. However, at regional distances (more than about 100-150 km), this rule gives long times at which coda amplitudes become too low. Therefore, Lg coda time windows are empirically defined as starting at lag times corresponding to group velocity 2.6 km/s, and with fixed lengths such as 40 seconds (Lacombe et al., 2003).

As summarized above, the different seismic waves contain valuable information about the interior structure of the Earth, and they are recorded by modern seismographs (red triangle in Figure 2.1). Each seismogram recorded by a seismograph represents the time series of the three components of ground motion (horizontal and vertical movements) for a time period sufficient for capturing all seismic waves of interest and sampled at a sufficiently short time interval (Figure 2.2). The vertical component is usually directed downward, and the horizontal components oriented in the north-south and the east-west directions. The time series (waveforms) contain valuable information that can be used for a variety of seismological studies, such as finding the precise time of onset and location of the earthquake rupture, estimating the mechanism of the earthquake, analysing spectral amplitudes of different waves, and other.

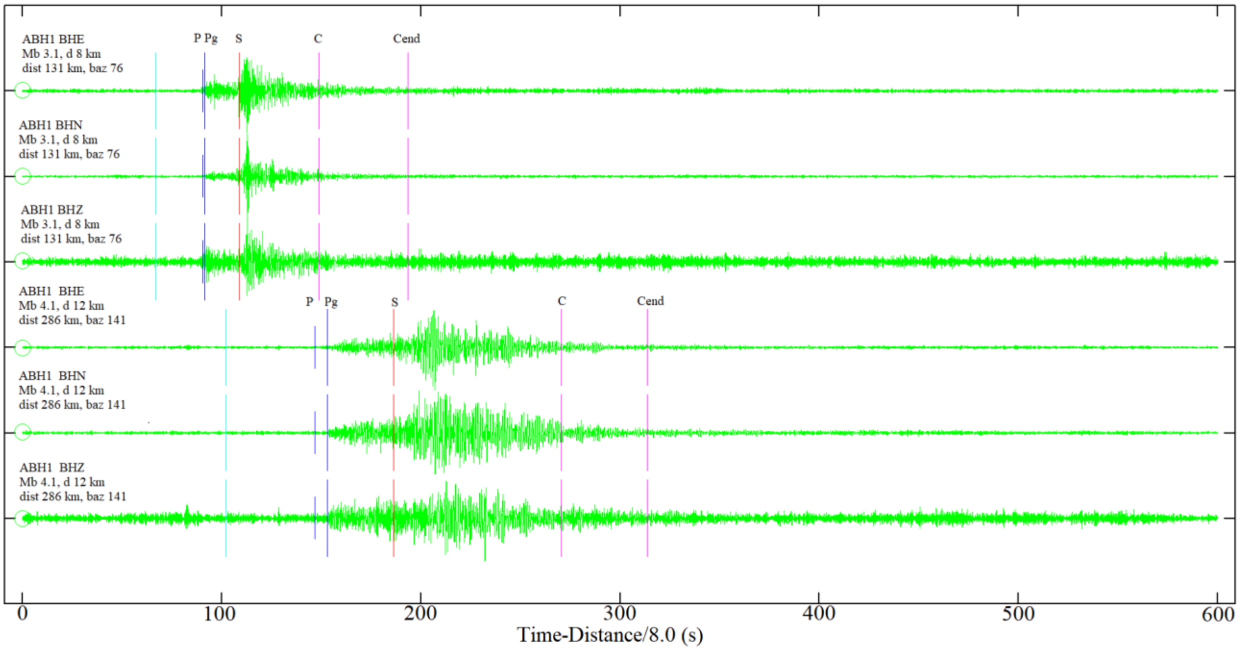

Figure 2.2. Two three-component seismograms from station ABH1. Source magnitudes (Mb), distances (dist), back-azimuths (baz), depths (d), and channel components are given in the labels. Vertical bars indicate the time picks of several types of seismic waves identified in these records such as P wave (blue), S wave (red), and the starts and ends of coda windows (magenta, labeled C and Cend). The horizontal axis is the “reduced time”, which is the time of “reference” arrival from the source with velocity of 8 km/s.

2.2. Seismic Datasets

In this dissertation, I use two earthquake seismic datasets described in the following subsections. Similar to data from many other experiments, the datasets consist of a large number of files in several formats. Here, I start by briefly summarizing the general structure of modern seismological datasets based on the information from the Incorporated Research Institutions for Seismology (IRIS) web pages (https://ds.iris.edu/ds/nodes/dmc/data/types/, last accessed April 21, 2021). IRIS is a global consortium of universities dedicated to maintaining and disseminating seismic data from the U.S. and global seismographic networks. After about 30 years of operation, this consortium is currently being merged with a similar consortium in geodesy (UNAVCO), to form an organisation dedicated to solid-Earth science research, called EarthScope.

The earthquake data from regional networks in Iran were received in the format called miniSEED. MiniSEED as a simplified subset of the format SEED (the Standard for the Exchange of Earthquake Data). SEED is the foundation for the data archiving system used for the past 30 years by the International Federation of Digital Seismograph Networks (FDSN) and IRIS Data Management System. The SEED format is fairly complex, and it is capable of storing the waveform time series as well as channel calibration information and various metadata such as names and parameters of the instruments, coordinates, sensor orientations, earthquake parameters, etc. By contrast, miniSEED contains the waveform data (time series) only and includes no geographic coordinates of stations, instrument response, or other auxiliary information.

To provide station parameters and channel calibration information (response spectra), additional files in the so-called “dataless SEED” format were provided by the seismic data centers. Dataless SEED files contain no waveform records but include the metadata including instrument responses, channel parameters, and geographic coordinates of stations. By using the *rdseed* computer program (SEED reader) from IRIS, the dataless SEED format can be converted into text formats, which can be further used by other software.

The third key component of the datasets consists of multiple lists of earthquake parameters. In this study (as well as in most traditional studies), I utilize time windows extracted from continuous recordings and corresponding to certain identified earthquakes. For each earthquake, a time window containing the arrivals of all waves of interest (from Pn to coda) was extracted and saved in a miniSEED file. A catalog of these earthquakes including the estimated epicentre coordinates, magnitude, time, depth, and other parameters was also provided in a text file.

Thus, the datasets of this study come as a large number of files (hundreds of thousand of miniSEED and dozens of other), and it requires efficient software for its handling and reformatting. In chapter 3, I will describe this processing procedure by using the IGeoS package (Morozov, 2008a).

2.2.1. Rigan area dataset

The Rigan area dataset is relatively small and consists of 31 records from two earthquakes in Rigan region of the southeastern Iran: the 20 December 2010 and 27 January 2011 earthquakes with magnitudes $M_w \approx 6.5$ (denoted 1 in Figure 2.3) and $M_w \approx 6.2$ (earthquake 2 in Figure 2.3). The magnitudes and coordinates of these earthquakes were reported by the U.S. Geological Survey. The seismic data were recorded by the Iranian Strong Motion Network, using three-component SSA-2 accelerometers at sampling frequency 200 Hz.

I performed initial data processing and analysed the Rigan-area records in a previous study (Safarshahi et al., 2013), and in this dissertation, I use these edited and pre-processed data from that study. Examples of the data and more detail about their processing are given in chapter 5.

The analysis by Safarshahi et al. (2013) was performed by using several well-established methods which led to results corroborating those found in many other areas of the world. These results are briefly described in section 2.4. However, as also shown in section 2.4, a new look at these established methods also reveals a number of fundamental questions which are still unanswered by conventional interpretations. In this dissertation (chapter 5), I revisit these data from a completely different viewpoint and by performing an unusually detailed and critical analysis of the inversion methods. The localized and relatively small Rigan dataset is ideal for achieving this analysis of the methodology, which is also applied to other parts of the present study.

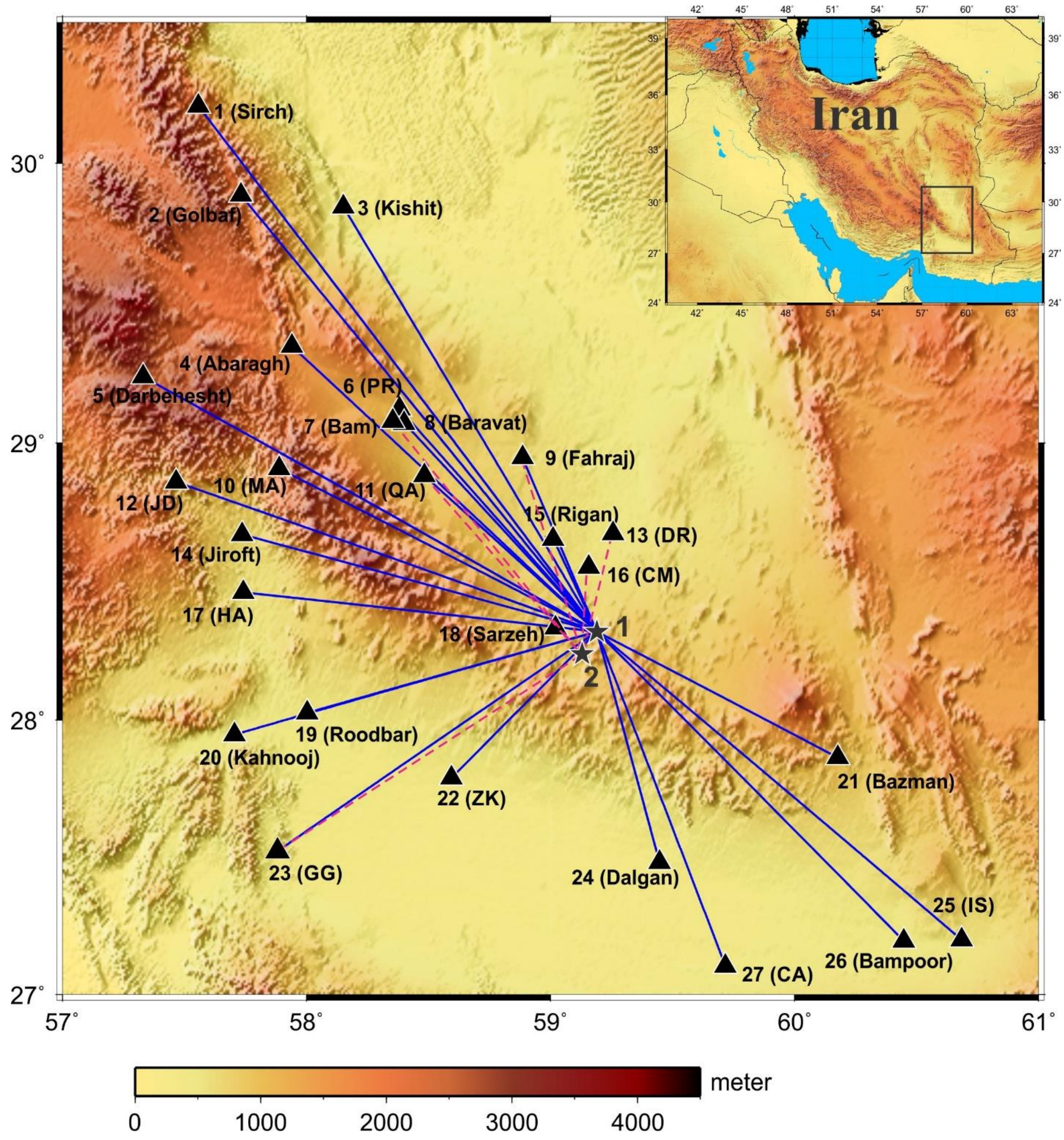

Figure 2.3. Location map of the earthquakes (stars), receiver stations (triangles), and source–receiver pairs (lines) in Rigan area (box in the insert; Safarshahi et al., 2013). Labels show site numbers and names and earthquake numbers in this study (chapter 5). Several site names are abbreviated: CA – Chah Ali; CM – Chah Malek; DR – Deh Reza; GG – Ghaleh Ganj; HA – Hossein Abad; IS – Iran Shahr; JD – Jiroft Dam; MA – Mohamad Abad; PR – Posht Rood; QA – Qotb Abad; ZK – Zeh Kelot.

2.2.2. Zagros area dataset

In most of the dissertation (chapters 3, 4, and 7), I use a large and raw dataset provided by the Iranian Seismological Center (IRSC, http://irsc.ut.ac.ir/, last accessed December 2017). The dataset contains over 250,000 miniSEED files extracted for 1300 earthquakes from continuous recordings on 62 seismic three-component stations in the Zagros region of Iran. Figure 2.4 shows the locations of these stations and earthquakes.

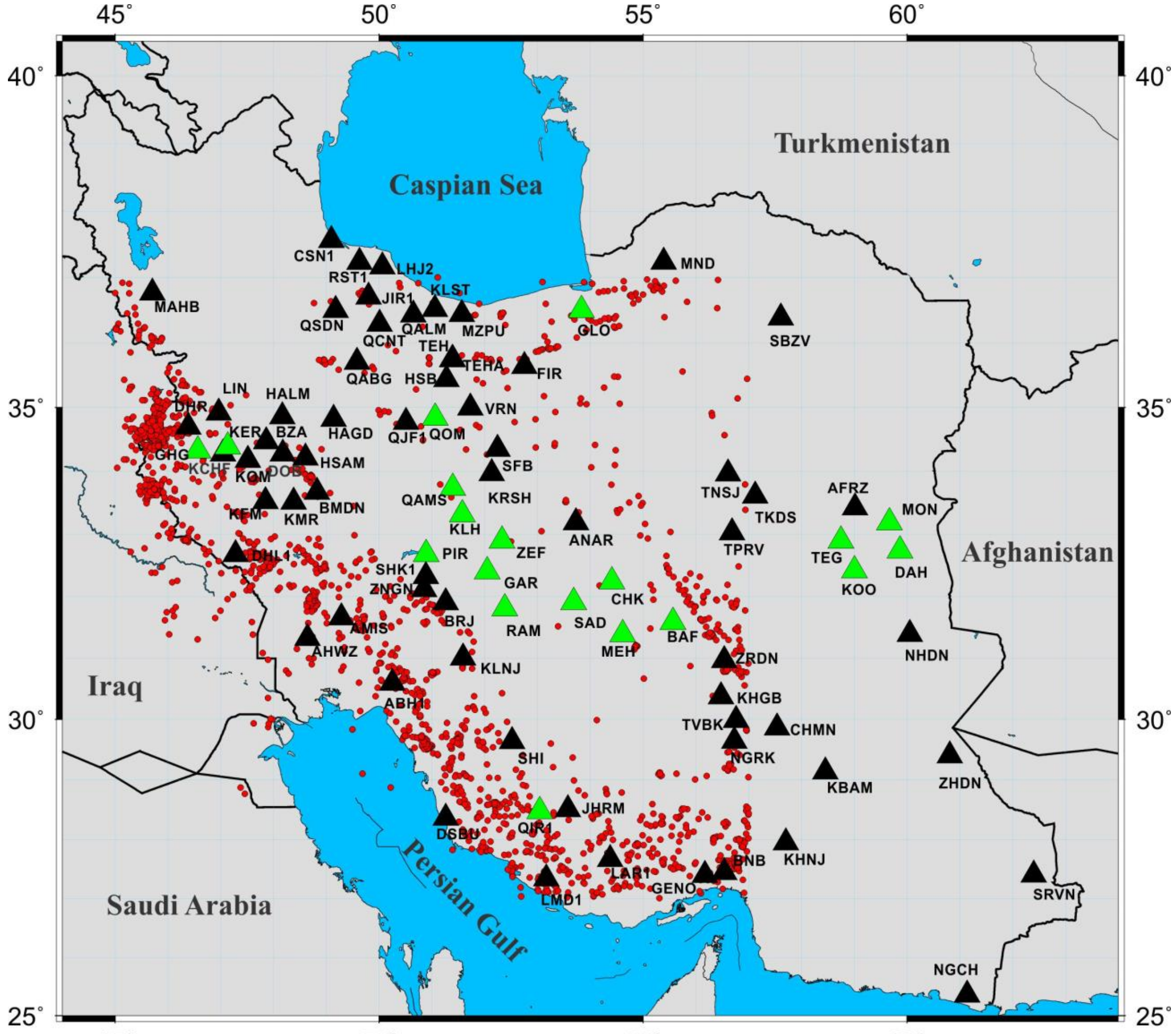

Figure 2.4. Location map of the study area (Iran). The seismic stations are shown by triangles (green: short-period, black: broad-band). The earthquakes are shown by red dots.

The stations were instrumented using different types of seismometers: short-period SS1 seismometers, medium-band Trillium-40s, and broad-band Guralp CMG3ESP-120s, CMG3T-360s and Trillium-240s seismometers. Sampling frequency was set equal 50 Hz for all records in this dataset.

2.3. Geological Setting

The tectonics of Iran is dominated by interaction between Eurasian and the Arabian Plates. The southwest of the Iranian plateau is trapped by the Arabian plate, and the northeast of the Iranian plateau trapped by Turan platform (Eurasia) (Berberian et al., 1981). Due to continuous relative movement of these plates, the Iranian plateau is affected by compressional deformation along the Alpine-Himalayan mountain belt (Mirzaei et al., 1998). Because of these geological conditions, Iran represents one of the most seismically active areas in the world and often experiences damaging earthquakes (Mirzaei et al., 1997), with human losses and extensive destruction.

In the following subsections, I describe the geological and tectonic structures of the two study areas used in this dissertation. I only focus on regional scales and near-surface conditions which are relevant in this dissertation.

2.3.1. Zagros area

As a part of the Alpine-Himalayan mountain belt, the Zagros fold and thrust belt is one of the most active regions of continental collision on the Earth (Snyder and Barazangi, 1986). The Zagros belt extends across approximately 1500 km from southeastern Turkey (Taurus mountains) to the Minab fault in the eastern part of the Strait of Hormuz located in southern Iran (Mirzaei et al., 1998). According to Vernant et al. (2004), the present-day crustal deformation through the Zagros orogen consists in a northward movement of the Arabian plate relative to Eurasia at the rate of 22±2 mm/yr at Bahrain (26.0667° N, 50.5577° E). Figure 2.5 shows a simplified geologic and tectonic map of Iran with locations of the Paleo-Tethys suture zone (PTS) suggested by several studies (e.g., Besse et al., 1998; Alavi, 1991; Hassanzadeh and Wernicke, 2016) and the Neo-Tethys suture zone (NTS) (e.g., Paul et al., 2006; Agard et al., 2011; Berberian, 1995).

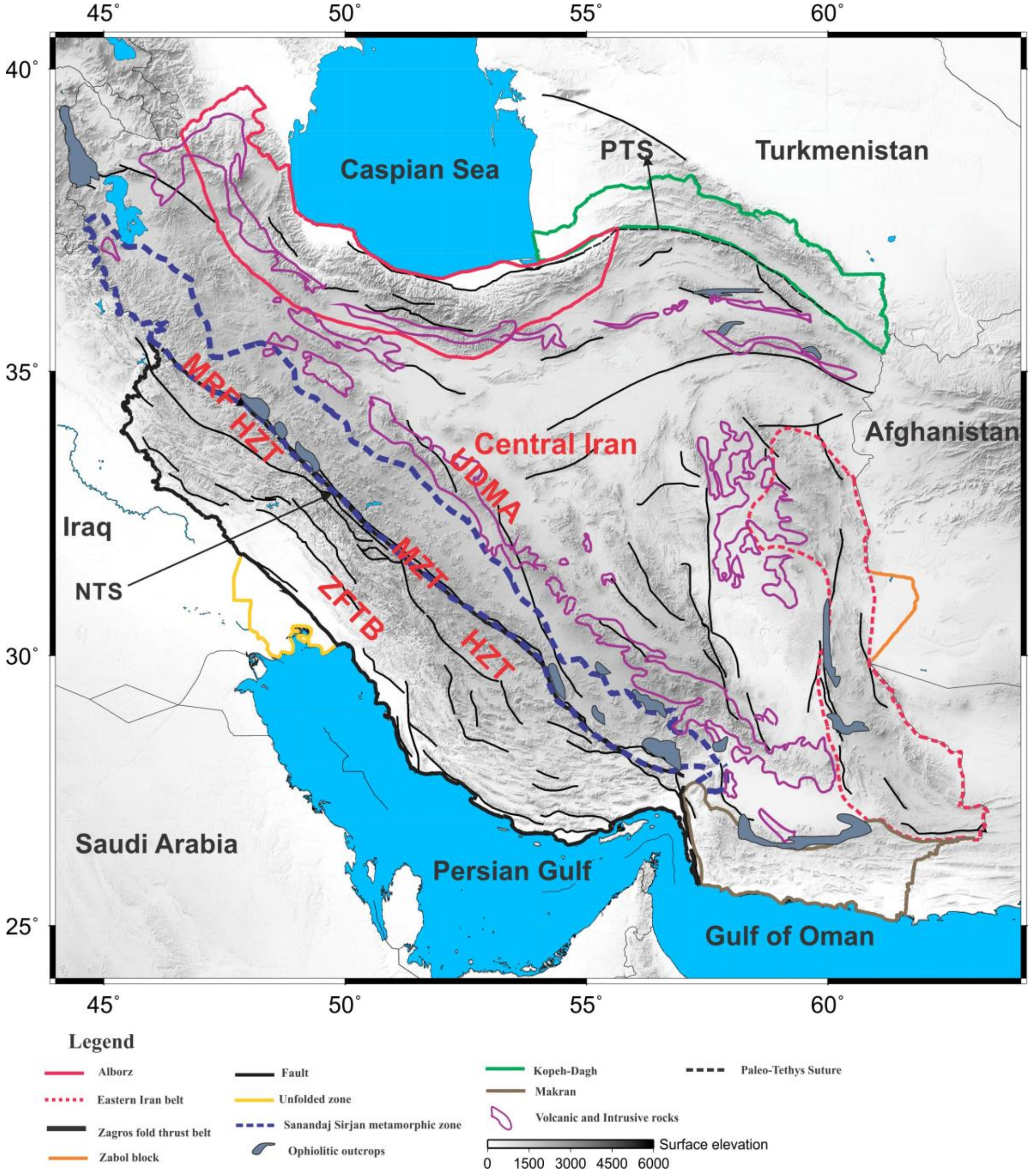

Figure 2.5. Simplified geological map of Iran showing locations of the major ophiolites, the major intrusive rocks, major faults (using Safarshahi, M., 2011), and main geological features (using Besse et al., 1998; Paul et al., 2010; Agard et al., 2011). Labels and lines indicate the Zagros fold and thrust belt (ZFTB; black irregular polygon), Sanandaj-Sirjan zone (SSZ; blue dashed irregular polygon), the main Zagros thrust (labeled MZT), the main recent fault (labeled MRF), Alborz (red irregular polygon), Makran (brown irregular polygon), Kopeh-Dagh (green irregular polygon), Central Iran, the Urmia-Dokhtar magmatic arc (labeled UDMA), Eastern Iran belt (red dashed irregular polygon) the Neo-Tethys suture (NTS; shown by the arrow) and the Paleo-Tethys suture (PTS; shown by the arrow).

During the Triassic period, the present territory of Iran was a set of continental blocks (the Cimmerian continent proposed by Sengör and Hsu, 1984) separated from Gondwana that came into collision with Eurasia (Stöcklin, 1968, as cited in Besse et al., 1998). In the Sinemurian time (200 Ma), the closure of the Paleo-Tethys caused an expansion of a large number of "molassic" basins in Iran, and the subduction-related volcanism within the Sanandaj-Sirjan and Lut block started in the north part of the Neo-Tethys (Stampfli and Borel, 2004). However, some authors argued that the closure time of the Paleo-Tethys Ocean occurred at the Late Triassic or even earlier time (e.g., Agard et al., 2011). Two sutures shown in Figure 2.5 were created, one related to closing the Neo-Tethys ocean in the south, and the other to the closure of the Paleo-Tethys ocean in the north (Besse et al., 1998; Alavi, 1991; Bagheri and Stampfli, 2008; Hassanzadeh and Wernicke, 2016). Precise locations of those two suture zones and the times of the opening and closure of the Neo-Tethys ocean is still controversial.

According to Stöcklin (1968), the Zagros orogenic system can be subdivided into five major subparallel tectonic elements shown in Figure 2.5: 1) the Zagros fold and thrust belt (ZFTB); 2) the Zagros thrust zone (ZTZ), which is recognized by the highest elevations in the whole Zagros mountain range; 3) the main Zagros thrust (MZT) or the main Zagros reverse fault (Berberian, 1995); 4) the Sanandaj-Sirjan metamorphic zone (SSZ); 5) the Urmia-Dokhtar magmatic arc (UDMA). Below, I briefly describe these tectonic elements separately.

The Zagros fold and thrust belt (ZFTB) contains 12-13 km thick shelf sediment deposits of the Permo-Triassic to Late Cretaceous/Paleocene age (James and Wind, 1965; Stöcklin, 1968; Berberian and King, 1981; Berberian, 1995; Agard et al., 2011). After the Mio-Pliocene, these deposits were folded into a sequence of NW-SE trending belts extending for about 1500 km from southeastern Turkey to the eastern part of the Strait of Hormuz (James and Wind, 1965; Stöcklin, 1968; Berberian and King, 1981; Berberian, 1995; Agard et al., 2011). Due to a collision of the Arabian Peninsula with central Iranian plate, this zone is still tectonically active with extensive shortening, uplifting, and thickening (Berberian, 1995). Several authors proposed different subdivisions within the ZFTB.

According to Berberian (1995), the ZFTB from NE to SW is subdivided to five key parallel trends located south of the MZT: 1) the Zagros thrust zone (ZTZ), 2) the simple folded belt, 3) the Zagros foredeep; 4) the Zagros coastal plain, and 5) the Persian Gulf-Mesopotamian lowland. By contrast, based on the structural style and topography, Agard et al. (2011) classified the ZFTB into two prominent domains from the SW to NE :1) the simple folded belt (SFB) bounded by the Persian Gulf at the south with hundreds of kilometers folding and constrained by several faults, and 2) the high Zagros consisting of higher topography, a sharp growth of elevation, and major thrusts.

The ZTZ (also called the high Zagros thrust belt (Berberian,1995) or the Crush Zone (Alavi, 1994; Mirzaei et al., 1998; Agard et al., 2005) is a narrow-thrust belt with width up to 80 km extending between the MZT and the ZFTB and subparallel to them (Berberian, 1995). The highest surface topography in Iran belongs to this zone. The ZTZ is characterized by widely overthrusted anticlines mostly consisting of allochthonous Jurassic-Cretaceous limestones of the Bisutun seamounts, obducted ophiolites and radiolarite from the Upper Cretaceous, and Eocene-Oligocene flysch deposits (Berberian, 1995; James and Wynd, 1965; Stöcklin, 1968). In the northeast of its margin, the ZTZ results in a sharp topography contrast with the central Iranian plateau (Mirzaei et al., 1998).

The main Zagros thrust (MZT), which is also called the main Zagros reverse fault (MZRF) (Berberian 1995), extends with NW-SE strike from the west of Iran to the north of Bandar Abbas. To the northwest of MZT, there is a group of right-lateral strike-slip faults called the main recent fault (MRF; Figure 2.5; Tchalenko and Braud, 1974). The MRF roughly follows the trace of the MZT (Berberian 1995). The MZT is known as the boundary between the ZFTB and the Sanadaj-Sirjan zone (SSZ; Stöcklin, 1968; Berberian, 1995). Due to the presence of ophiolites near the MZT, several studies suggested that the MZT is possibly rooted at Moho depths (Agard et al., 2005; Paul et al., 2006).

During the Mesozoic and Cenozoic times, the subducted Neo-Tethys oceanic plate produced volcanic arcs across the Iranian plateau in the UDMA, SSZ, and Alborz areas and Central Iran (Verdel et al., 2011). Among them, the SSZ is a metamorphic and igneous zone, extending approximately 1500 km from NE to SW with width up to 200 km. This zone is oriented parallel to the ZFTB, and its southern margin is bounded by the MZT (Stöcklin, 1968, Alavi, 1994). The SSZ is mostly made of Jurassic phyllites laid between other layers such as metamorphic rocks and sometimes containing massive volumes of calc-alkaline plutons of the Mesozoic period (Agard et al., 2005). The SSZ is characterized as an active Andean-type zone with calc-alkaline magmatic activity, which migrated to the north of the present-say Iran during the last half of the Mesozoic and later time (Berberian and King, 1981; Sengör, 1990; Agard et al., 2005; Verdel et al., 2011).

The UDMA is located between the SSZ and Central Iran, and parallel to Zagros and the SSZ (Figure 2.5). The calc-alkaline magmatic activity of UDMA continued from the Eocene to the present time, with the highest level of activity during the Oligo-Miocene (Berberian and Berberian, 1981; Berberian and King, 1981; Bina et al., 1986; Agard et al., 2005).

Many studies showed that the Zagros orogen experienced a long history of convergence consisting of multiple steps such as subduction, ophiolite obduction, and collision between the Eurasian and Arabian plates across the Neo-Tethys ocean. Agard et al. (2011) proposed the evolution of the Zagros orogen of these processes recorded from 150 Ma to 0 Ma. However, there are still several issues which are not understood and need to be discussed. I describe some of the main outstanding questions below.

In many studies, a slab break-off was suggested in the subducted oceanic lithosphere. For example, von Blanckenburg and Davies (1995) hypothesized that slab break-off occurred in this area, which means that some parts of the subducting oceanic crust were fragmented and sunk during the continental collision. However, the fate of the broken-off slab and the time of the collision are still being debated. This question could be elucidated by seismic methods because fragments of subducted crust may be detected as low-velocity anomalies at relatively shallow depths within the mantle.

The crustal break-off may have occurred in several stages. At the beginning of the continental collision, this subduction caused the Andean type Sanandaj-Sirjan volcanic zone (SSZ; Agard et al., 2005) and subduction started. According to Agard et al. (2011), in Late Paleocene (60-55 Ma), the first slab break-off in the north-central Zagros (ZTZ, Kermanshah region) occurred when the remaining Neo-Tethys ocean in this area had a width of around 1000 km then the second break-off of the slab occurred in the Late Miocene.

An important and still open question relates to the time of the continental collision and the evolution of the Zagros orogen. Agard et al. (2011) proposed a model for it consisting of three main periods:

1) From 115 to 85 Ma, subduction and fragmentation of the upper Eurasian plate took place;
2) From 60 to 40 Ma, slab break-off, crucial shifts of arc magmatism, and distributed growth in the upper Eurasian plate, and
3) After about 30 Ma, continental collision continues with a SW-dominant migration of deformation into several different zones. From 20 to 15 Ma, the SSZ was formed, from 12 to 8 Ma, the dominant deformation occurred at High Zagros, and from 5 to 0 Ma, the Simply Folded Belt was built. From 10 Ma to present, the second break-off of the crustal slab occurred.

In this scenario (Agard et al., 2011), the closure of Neo-Tethys ocean was suggested to occur in the mid-Miocene time, whereas other studies suggested that the Neo-Tethys was closed during the Miocene–Pliocene time (Glennie et al., 1973; Stoneley, 1981). However, Agard et al. (2005) reported that in the northern part of Zagros (Kermanshah-Hamadan area), the oceanic closure occurred in the Oligocene-Miocene period (25-23 Ma). Therefore, this time can be viewed as the start of the continental collision.

Another still unsolved geological problem is the location of the suture zone. Some authors argue that crustal deformation associated with the suture zone is located between the main Zagros thrust (MZT), which may be marked by possibly large Moho depth (e.g., Agard et al., 2005; Paul et al., 2006; Berberian, 1995), and the crush zone and the SSZ (Stöcklin, 1968; Agard et al., 2005; Hassanzadeh and Wernicke, 2016; Berberian, 1995). By contrast, other authors suggest that the suture zone runs northeast of the MZT between the SSZ and the UDMA (Alavi, 1994; Shafaii Moghadam and Stern, 2011).

The location of the suture largely depends on identifying large-scale variations of the crustal structure involving the entire crust and extending into the mantle. Such major tectonic features can be constrained by seismic methods. According to Motaghi et al. (2017), in the northern part of Zagros, the crustal thickness increases from 43 to 59 km beneath the main recent fault (MRF) and reaches 62 km between SSZ and UDMA, and then decreases to 42 km in the middle of the Central Iran. Paul et al. (2010) inferred Moho depth beneath the MZRF equal to 69±2 km and 56±2 km along two receiver function profiles across the central and northern Zagros, respectively, while beneath the ZFTB and in the central part of Zagros, the crustal thickness was estimated as 42±2 km. Several studies reported that earthquakes occurred in the Zagros are restricted to the upper continental crust with depths less than 20 km (Engdahl et al., 2006; Tatar et al., 2004). In central parts of Zagros, the crustal thickness was estimated as about 46±2 km (Hatzfeld et al., 2003). Snyder and Barazangi (1986) suggested that the depth of Moho beneath the MZT is near 65 km, although an interpretation of gravity data estimated the Moho depth of about 55 km in this area (Dehghani and Makris, 1984).

As shown above, similar to other areas around the world, seismic observations provide critical data for constraining the deep structure of the Zagros region. Based on earlier observations of earthquakes at depths exceeding 50 km, a model of active subduction of the continental crust of the Arabian shield underneath the Zagros was hypothesised in many studies (e.g., Nowroozi, 1971; Kadinsky-Cade and Barazangi, 1982). Nevertheless, later studies showed that the interpreted continental mantle earthquakes in this area largely resulted from source mislocations. Maggi et al. (2000) and Engdahl et al. (2006) suggested that almost all of Zagros earthquakes occurred at upper crustal depths less than 20 km. This controversy shows that accurate earthquake location is critical for interpreting the deep structure, and particularly crustal subduction and break-off within the upper mantle. I present my results of relocation of seismicity in the Zagros in the chapter 4, although this analysis does not extend to constraining the earthquake depths.

In addition to earthquake source locations, imaging of seismic velocities within the crust and the upper mantle can provide robust constraints on the geodynamic setting of the Zagros suture. For example, seismic Pn velocity tomography can effectively address problems such as determining the locations of the subducted oceanic slabs, whether it is attached or detached, and whether a lithospheric delamination is present.

2.3.2. Rigan area

Earthquake events in Iran are often accommodated by faults in Zagros, Alborz, Kopeh-Dagh and eastern Iran (Walker et al., 2003). The Central-east Iran as an intraplate region which is located between Zagros and Kopeh-Dagh and represents one of five principal seismo-tectonic provinces in this country (Mirzaei et al., 1998). The earthquakes in the Central-east Iran are also often accompanied by surface faulting (Berberian, 1979).

The Rigan study area of the second dataset of this dissertation is located within the Kerman plateau, which is a part of the Central-east Iran province. The Kerman plateau region experienced several large earthquakes with right-lateral strike-slip fault mechanism, located along the west part of the Lut block. This faulting mechanism accommodates the right-lateral shear occurring between the Central Iran and Afghanistan (Berberian et al., 2001). Due to the relative lack of seismicity and low topography of the plateau, the Lut block is known as a quite rigid and stable block almost in Tertiary period with approximately 400 km length and 200 km width (Berberian et al., 2001). However, the north-south zone surrounding the Lut block with major right-lateral strike-slip faults is known as a seismic active zone (Walker et al., 2003; Berberian et al., 2001). The Central-east Iran province is fragmented by a series of Quaternary fault systems (Berberian, 1976; Mirzaei et al., 1998) and covered by sedimentary and Quaternary volcanic rocks (Komak Panah et al., 2002).

Instrumental and historical earthquake catalogues show that Central-east Iran occasionally experienced large earthquakes such as the Bam earthquake in 2003, with magnitude M_w of about 6.6 (USGS estimate) and more than 32,000 deaths. Two other large earthquakes in the Rigan region occurred in 2010 and 2011 with moment magnitudes of $M_w = 6.5$ and 6.2 (also USGS estimates) respectively. The seismicity of the Central-east Iran is shallower than 20 km (Maggi et al., 2000; Engdahl et al., 2006).

Because for the Rigan area, a substantial part of the present work focuses on κ ("kappa") measurements and applications to engineering seismology, it is important to summarize what is known about the structure of the shallow near surface beneath the stations. Unfortunately, little of such data is available in this study. Because of the complexity of geology and tectonics of the region, bedrock depths and thicknesses of sedimentary deposits vary for different sites. For example, in the vicinity of Bam station (number 7 in Figure 2.3), soil profiles show sandy clay within the upper part and silty sand at the lowest part. Because of this thick soil deposits, Bam station was classified as class C site (Rayhani et al., 2008). According to Komak Panah et al. (2002), the Bam site is located on soft soil, Globaf station (number 2 in Figure 2.3) is on moderately soft soil, and Sirch site (number 1 in Figure 2.3) is on hard soil or weak bedrock. As it will be shown in section 2.4 and chapter 5, these site conditions somewhat correlate with the measured values of κ.

2.4. Results of Previous Analysis of Rigan Dataset

The Rigan-area dataset was used in my previous study (Safarshahi et al., 2013), which posed a number of questions revisited in this dissertation. The study by Safarshahi et al. (2013) focused on quantitative analysis of body S waves within the crust. Broadly, this analysis consists in measurements of the geometrical spreading, attenuation (measured by the Q-factor; chapter 1), and the high-frequency spectral parameter κ. In chapter 1, I described a significant controversy about the physical meanings of Q and κ. The key problem with these parameters is that they are not clearly separable from each other, and the values of both of them depend on the measurement methods employed. In standard approaches to earthquake data analysis, this problem is generally recognized and mitigated by using a set of carefully selected and fixed data processing parameters and model assumptions (e.g., Havskov et al., 2016). In the earlier study (Safarshahi et al., 2013), I adhered to such strictly conventional recipes for single-station measurements of Q and κ. The key results are summarized below.

In the conventional method, the Q and κ are determined separately. To estimate Q_S (subscript S denotes the shear waves) for body waves of ground acceleration records (e.g., Aki and Chouet, 1975), the spectral amplitude is presented as a function of distance (r) and frequency (f):

$$U_i\left(f,r\right)=S_i\left(f\right)r^{-1}\exp\left(\frac{-\pi f}{\beta Q_S}r\right) \quad . \tag{2.1}$$

In this relation, r^{-1} is the geometrical spreading for spherically-spreading body waves, and $S_i(f)$ is the source amplitude spectrum, and β denotes the S-wave velocity, and Q_S is the desired measure of attenuation (Aki and Chouet, 1975). In the single-station method, a set of fixed frequencies f (passbands of data filtering) are considered, and amplitude U in eq. (2.1) is viewed as a function of r. After multiplying both sides of eq. (2.1) by source-receiver distance and taking the natural logarithm then calculating the slope (denoted b) of its linear regression with respect to r (Figure 2.6), Q_S is obtained at each f as $Q_S=-\frac{\pi f}{\beta b}$. These values are labeled for each frequency band in Figure 2.6.

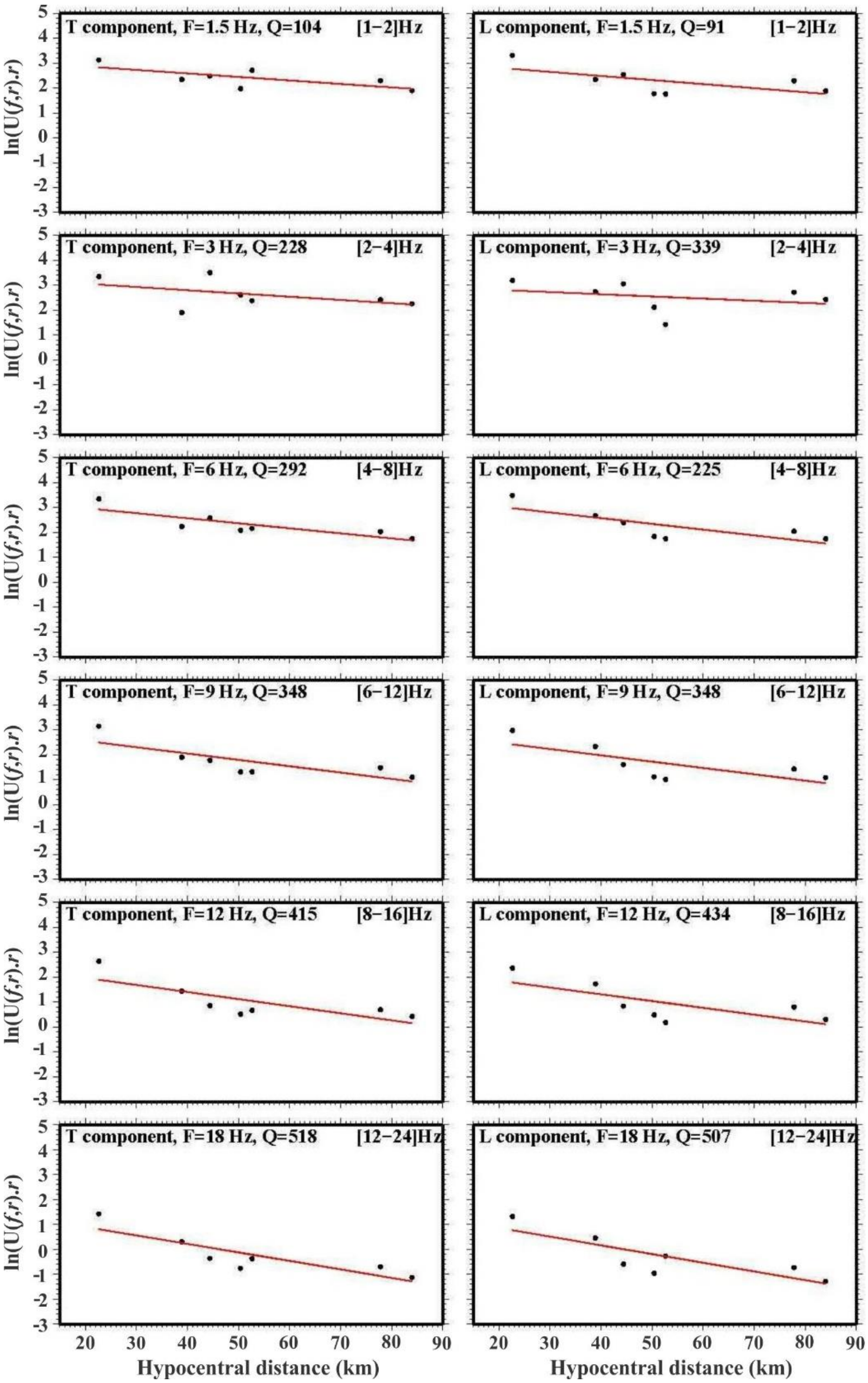

Figure 2.6. Logarithms of distance-corrected (multiplied by source-receiver distance) amplitudes for body S waves from Rigan earthquakes (Safarshahi et al., 2013). Each panel corresponds to one centre frequency indicated by labels F. Panels on the left are for the transverse horizontal component (labeled T), and plots on the right are for the longitudinal component (labeled L). Dots are the measured corrected amplitude values, and red lines show their linear regression with distance. Downward slopes of these lines give the *Q* values shown in labels.

Thus, the above procedure basically remaps the measured decrease of the amplitudes with distance (*b*) into a decay of the spectra with frequency (Q_S). Morozov (2008b, 2010a) criticized this remapping as nonphysical and arbitrary (controlled by unverifiable and inaccurate model assumptions). Plots similar to Figure 2.6 are not often shown in earthquake studies, but they provide important evidence in support for this critique. Note that the negative slopes of the red lines in Figure 2.6 (–*b*) increase with frequency much slower than proportionally to *f*. Consequently, the Q_S calculated from $Q_S = -\frac{\pi f}{\beta b}$ systematically increases with frequency. Safarshahi et al. (2013) approximated this increase as $Q_S\left(f\right) = 99 f^{0.58}$. Similar and often much steeper $Q_S(f)$ dependencies are reported by many authors and they are interpreted as a fundamental property of the Earth related to its "seismic absorption band" (Anderson, 1989). However, in chapters 5, 6 and 7, I describe a completely different approach to this problem, which will also explain the systematic increase of *Q*(*f*) with frequency.

In another application of the standard methodology to Rigan earthquake records, I calculated the parameter κ by the classical approach by Anderson and Hough (1984). This parameter characterizes the slope of the line fitted to the logarithm of the exponential decay of the spectral amplitude versus frequency: ($A\left(f\right) = A_0 e^{-\pi\kappa f}$, and therefore $\ln A\left(f\right) = const - \pi\kappa f$. Similarly to the distance dependence in eq. (2.1), spectrum *A*(*f*) in this equation must be corrected for the source spectrum *S*(*f*) and the *Q* along the wave propagation path (Anderson and Hough, 1984). By measuring this regression for amplitude spectra of individual S-wave records, Safarshahi et al. (2013) estimated $\kappa \approx$ 62.5 ms for the longitudinal and $\kappa \approx$ 57.7s for transverse components. Finally, after determining the $Q_S(f)$ and κ, Safarshahi et al. (2013) used these two parameters to simulate the time series for ground motion by using the stochastic finite-fault model by Motazedian and Atkinson (2005). This model is shown in Figure 2.7.

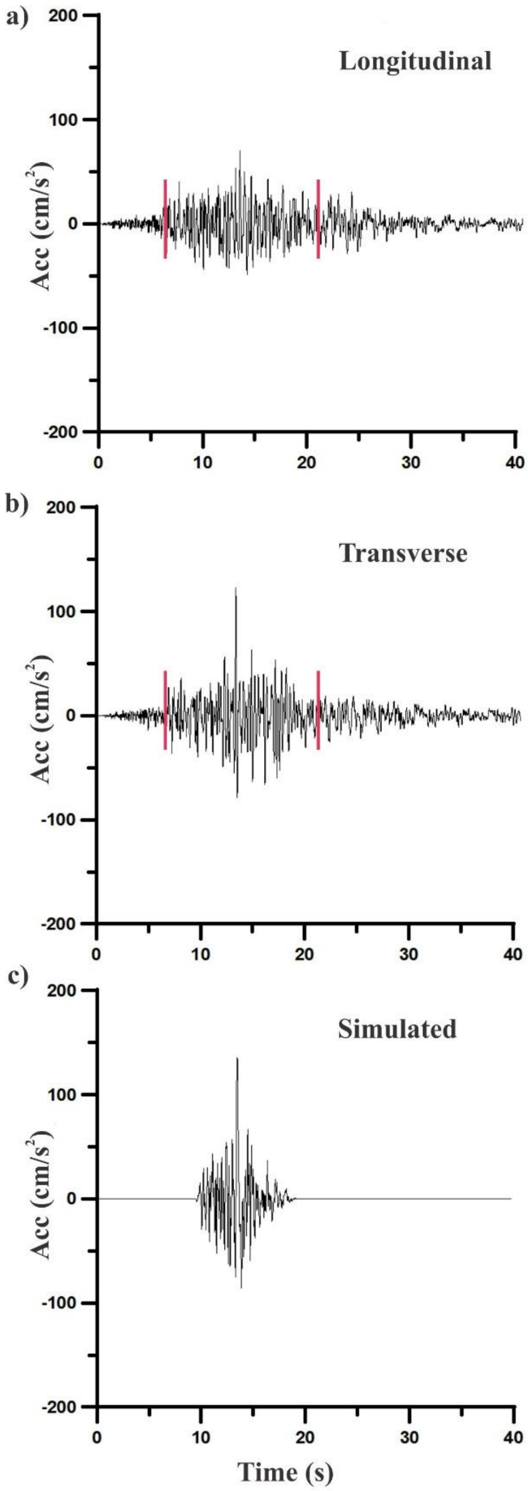

Figure 2.7. Two components of ground acceleration and simulated time series within the shear-wave window at station Rigan with epicentral distance 41 km (Safarshahi et al., 2013): a) longitudinal component; b) transverse component; c) simulated horizontal-component time series. Red vertical bars indicate the shear-wave time window.

As shown in the above summaries, the conventional *Q* factors and κ are not calculated simultaneously but instead corrected for each other in the two types of measurements. However, as argued in chapter 5 of this dissertation, this approach causes a great “hidden” uncertainty in both *Q* and κ, which is difficult to assess. It is better and much more reliable to invert parameters *Q* and κ jointly, and also together with parameters of geometrical spreading (chapter 5). When inverted jointly with other attenuation parameters, it turns out that κ describes most of the observed attenuation, and *Q* becomes large and nearly insignificant. In addition, parameters κ should also be associated with the earthquake source (Beresnev, 2019a, 2019b), which is also not considered in standard approaches (Anderson and Hough, 1984).

CHAPTER 3

EARTHQUAKE DATA PROCESSING

This chapter describes the general procedures for processing large earthquake datasets and their application to the Zagros dataset of this project. Earthquake data management and processing is a significant research subject by itself. In the following sections, I review the traditional and emerging methods for managing seismological data and software design and then describe a different approach, which is taken in this dissertation. This chapter is written in the form of a paper that may be submitted (in an abbreviated form) to The Seismic Record, which is the new open-access journal of the Seismological Society of America. The early stages of this work were described in the presentation by Safarshahi and Morozov (2019).

3.1. Introduction

In both exploration and earthquake seismology, substantial efforts for data organization and processing are required before an interpretable result can be obtained. Seismic imaging almost always involves combining multiple records obtained from heterogenous types of instruments operated by multiple operators, often in different countries, and at different times. Imaging procedures are almost always implemented by numerous computer algorithms, which need to be applied to the records in certain sequences, with numerous parameters that need to be properly documented. In addition to seismic waveform data ("time series" in chapter 2), seismic data analysis relies on "metadata", such as geographic coordinates of seismic stations and instrument responses, and also various "models", such as models of travel times for certain waves within certain parts of the Earth. Some of the data analysis tasks are performed interactively with the help of the human operator or analyst, and some of them are applied in unattended, large-volume "batch" processing. All of these diverse characteristics of modern seismic data analysis show that it requires a systematic approach to processing and imaging.

A number of distinct approaches exist, which are summarized in the following sections in this chapter. All of these approaches contain two key elements: 1) some method for organizing the heterogeneous dataset consisting of numerous files and data sources, and 2) methods for organizing complex sequencies of algorithms and applying them to the records. These two tasks are solved by complex software packages, which are usually called *seismic processing systems*.

In the early days of seismology, seismic processing was largely done by manual interpretation of seismogram plots or by processing individual records by programs written by the individual researchers. Over the past fifty years, this model of seismic processing has evolved greatly. With regard to the above requirements to processing systems, the challenge of data volume and complexity has increased tremendously, and numerous new types of data sources became available. For example, the Zagros dataset of this dissertation contains about 250,000 data and metadata files distributed over multiple directories, and they ideally need to be treated in a simple and common way. Another seminal recent development is the advent of web services automatically supplying seismic waveforms, metadata, documentation, and even pre-assembled and pre-processed datasets pertaining to important events, or historical data (e.g., https://ds.iris.edu/ds/nodes/dmc/data/#requests, last accessed April 21, 2021). With these recent developments, the notion of a data file is being replaced with a “cloud”, or some generalized data access mechanism.

With regard to the second aspect of the seismic processing system mentioned above (ways for combining tools and algorithms), the situation has been greatly improved, but in consequence it has also become somewhat complicated. A number of new and convenient computer languages have become available, and the increasing computer power now allows processing large datasets on a laptop. However, seismologists are all the more left with the choice of processing model based, for example, on the newest Python- or Julia-based software packages or the more traditional Matlab- or even Fortran-based software. Each of these paradigms offers certain advantages and disadvantages, but once a processing style is selected, switching to other styles may become difficult. As a solution to this problem, in this project, I employ a different approach, in which the integration of the different software tools is done by using a specialized seismic-processing (or even more general geophysical) data processing system called IGeoS (http://seisweb.usask.ca/igeos; last accessed April 21, 2021; Morozov, 2008a). This type of software design is standard in reflection seismology, in which a similar (and actually greater) variety of processing tasks is encountered. In this approach, the individual tools can be written by using any computer languages. The tools are free from most data search and input/output operations, and therefore they focus on the specific tasks.

In the following sections, I summarize the existing approaches to data organization and processing (sections 3.2 and 3.3), and then describe the IGeoS-based approach taken in this project (section 3.4).

3.2. Existing Approaches to Seismic Data Management

In seismic data processing at any scale, the waveform records are usually stored in data files (usually binary but sometimes ASCII), and the difference between the different processing models is in the way these files are accessed. In the older, classical approaches such as the Seismic Analysis Code (SAC; https://ds.iris.edu/files/sac-manual/, last accessed April 21, 2021) and SEISAN (http://seisan.info/, last accessed April 21, 2021) each record is represented by a file of the format specific to that software. The critical parameters such as the name of the station and channel are usually placed in file names, which have to be of a strictly defined format. The files are managed using these file names by the standard tools of the operating system. With modern datasets, the numbers of data files in such systems often become very large (many thousands in a directory), which causes numerous technical difficulties. The use of file names and directories limits the ability to sort the data and access them in variable ways. Thus, systems using single-record files are very restrictive and suitable only for small datasets.

A powerful alternative to keeping track of millions of individual files consists in using databases. A seismic database contains a table of all available waveform records, which may be in multiple individual or contiguous files of variable formats, and it also contains all of the metadata. By making calls to the database, the user is therefore able to retrieve any amount of data and make an arbitrary selection of it, without the need of knowing its internal structure and data formats. In commercial reflection seismic processing systems such as ProMAX, the database represents the core mechanism for data storage and retrieval. The first applications of databases in earthquake seismology were made at the University of Colorado at Boulder, in a system called DataScope. This system was later developed by Boulder Real Time Technologies into a commercial system for local seismic network management, named Antelope (https://brtt.com/software/, last accessed April 21, 2021).

The Antelope software uses a custom DataScope database, which is directly accessed by its codes. However, a much more general approach is to use the portable Structured Query Language (SQL) databases. There are two well-known and broadly used open-source (free) implementations of SQL databases called MySQL and PostgreSQL. These databases are accessed by forming SQL query strings describing the records requested by the user, and they return tables of metadata and indices of data files (or sometimes data files themselves). SQL databases can be queried by multiple remote users simultaneously by using Unix shells or graphical user interfaces (GUIs), and they usually also have application programming interfaces (APIs) to efficiently access them from software. A seismic database can return arbitrary subsets of the data sorted in various ways, and arbitrary processing can be performed with the returned data. In project Emerald (https://seiscode.iris.washington.edu/projects/emerald, last accessed April 21, 2021), a PostgreSQL database is used to perform the complete earthquake data processing and displays.

A natural (and relatively recent) extension of the database access to observational seismological data is in using web services. Web services currently represent the key data access mechanism at the IRIS (Incorporated Research Institutions for Seismology, a U.S.-based University consortium) Data Management Center (https://ds.iris.edu/ds/nodes/dmc/tools, last accessed April 21, 2021), and most other datacenters of the FDSN (International Federation of Digital Seismograph Networks; http://www.fdsn.org/datacenters/, last accessed April 21, 2021). Web services provide flexible data access methods to the centers' databases without knowledge of their SQL database schemas and without the need for handling variable file formats. Web requests can be made from any web browser or software working on any computer platforms and located anywhere in the world.

Most modern seismic toolboxes, such as described in the next section, are focused on the "file-centric" data-processing paradigm described at the beginning of this section. A data record is defined as one or several arrays of waveforms plus a structure of record headers with fixed names. The interaction between tools is performed by passing the data record from one tool to the other. In this way, for example, Matlab program serves as a shell script in SAC data processing. However, the more flexible code allows including tools which can access databases and web services.

The processing paradigm used in this dissertation (IGeoS) is significantly different from the "file-centric" model above. This paradigm can be described as "process-centric", or "stream"

(Morozov, 2008a), and it inherits from the way seismic datasets are usually processed in reflection seismology (e.g., the Seismic Un*x, https://cwp.mines.edu/software/, last accessed April 21, 2021). In this approach, the partitioning of the data into files is unimportant, and the data are processed as a continuous stream of records in a common, high-performance code. The databases and web services are also noncritical for the operation of the system, but they can be accessed by the individual tools as needed. More detail of this data processing paradigm will be given in the following sections.

3.3. Approaches to Data Analysis

In observational (earthquake) and exploration (reflection and controlled-source crustal) seismology, the approaches to data processing and software design are significantly different. To explain this difference, I will refer to a case of "custom", or "research" processing required when exploring new data or developing a new imaging approach. In observational seismology, such tasks are usually accomplished by custom software using some general-purpose programming language. Therefore, the flexibility, convenience, and power of such processing depends on the capabilities of this programming language, and also on the programming skills of the data analyst. By contrast, in reflection data processing, the data volume and software performance requirements are much higher, but the expectations of programming skills are reduced. In consequence, reflection seismic processing systems are based on specialized "data processing languages" allowing extensive parameterizations of processing flows without significant computer programming. I will briefly describe both of these models below.

At present, there exist numerous high-level, procedural-type programming languages suitable for seismological data analysis (see https://en.wikipedia.org/wiki/Comparison_of_numerical-analysis_software, last accessed April 21, 2021). Probably the most broadly used of such languages, particularly in the past, is Matlab (https://www.mathworks.com/products/matlab.html, last accessed April 21, 2021). Matlab is a simple, general-purpose language for scientific and engineering computing. In this language, the basic data structure is a multidimensional matrix, and most linear-algebra equations have a natural syntax, which makes this language convenient for handling seismic waveform records. Free, open-source implementations of this language are available, such as FreeMAT (http://freemat.sourceforge.net/, last accessed April 21, 2021) and GNU Octave (https://www.gnu.org/software/octave/index, last accessed April 21, 2021). In the data processing and inversion in this project, I use GNU Octave because of its free availability and slightly improved syntax containing elements of C++ (Figure 3.1).

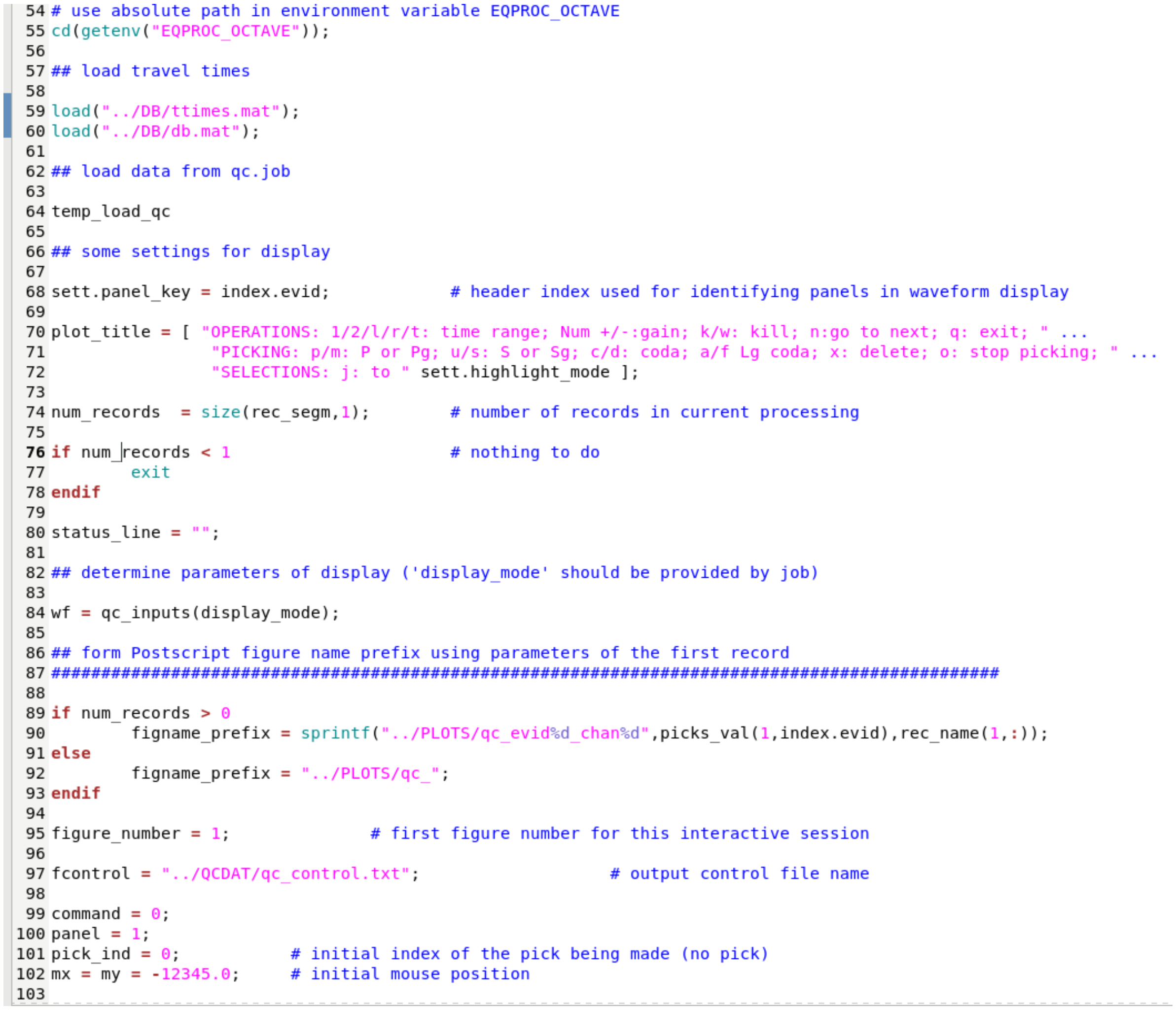

```
# use absolute path in environment variable EQPROC_OCTAVE
cd(getenv("EQPROC_OCTAVE"));

## load travel times

load("../DB/ttimes.mat");
load("../DB/db.mat");

## load data from qc.job

temp_load_qc

## some settings for display

sett.panel_key = index.evid;            # header index used for identifying panels in waveform display

plot_title = [ "OPERATIONS: 1/2/l/r/t: time range; Num +/-:gain; k/w: kill; n:go to next; q: exit; " ...
                "PICKING: p/m: P or Pg; u/s: S or Sg; c/d: coda; a/f Lg coda; x: delete; o: stop picking; " ...
                "SELECTIONS: j: to " sett.highlight_mode ];

num_records  = size(rec_segm,1);        # number of records in current processing

if num_records < 1                      # nothing to do
        exit
endif

status_line = "";

## determine parameters of display ('display_mode' should be provided by job)

wf = qc_inputs(display_mode);

## form Postscript figure name prefix using parameters of the first record
###############################################################################################

if num_records > 0
        figname_prefix = sprintf("../PLOTS/qc_evid%d_chan%d",picks_val(1,index.evid),rec_name(1,:));
else
        figname_prefix = "../PLOTS/qc_";
endif

figure_number = 1;              # first figure number for this interactive session

fcontrol = "../QCDAT/qc_control.txt";                   # output control file name

command = 0;
panel = 1;
pick_ind = 0;           # initial index of the pick being made (no pick)
mx = my = -12345.0;     # initial mouse position

```

Figure 3.1. A fragment of GNU Octave code used for interactive data quality control in this project.

In academic and nuclear-test monitoring seismology, large seismic processing toolboxes were created based on Matlab. One of the most notable of these projects is MatSeis developed at the Sandia National Laboratory (https://www.sandia.gov/MatSeis/, last accessed April 21, 2021). Numerous additional tools working in the Matlab command line interface are contributed by various researchers, for example the P-phase Picker for automatic or semi-automatic picking of P-wave arrival times in seismograms (https://www.usgs.gov/software/p-phase-picker, last accessed April 21, 2021). Such tools also usually work under GNU Octave.

Matlab-based toolkits were also developed for exploration-seismology applications, likely in almost every University seismology group. The simplicity and power of matrix language makes it a convenient method for teaching and quick prototyping of new algorithms. However, its performance is still significantly limited compared to codes compiled from C or Fortran, and the flexible syntax sometimes makes it error-prone. Also, for larger-scale and complex coding, object-oriented programming methods are highly beneficial, and these methods are also poorly represented in Matlab.

Starting from mid-1990's, IRIS sponsored a number of projects aiming to introduce modern object-oriented programming and distributed computations in seismological research. In particular, a number of tools for web data retrieval and processing by using Java language were developed (see packages beginning with 'j' at https://seiscode.iris.washington.edu/, last accessed April 21, 2021). The advantage of Java is that it is an object-oriented language that can be executed on practically any computer by using the Java Virtual Machine (JVM). Because of this cross-platform capability, Java is often used for developing interactive graphical user interfaces. However, it appears that the performance of the JVM is still limited for seismic data retrieval and significant processing tasks, and Java coding is still relatively complex.

It appears that the Python language is currently the most popular in the seismological and geophysical communities. Python is an object-oriented, general-purpose programming language, which also offers broad cross-platform functionality. Advantages of this language include the simplified syntax and easy linkages with codes written in Fortran and C, and with graphics toolkits. However, the original Python had no significant capability for processing arrays of data samples. This limitation was overcome in the package NumPy (https://numpy.org/, last accessed April 21, 2021).), which added Python classes for implementing operations with multidimensional arrays. These classes operate similarly to the basic data structures in Matlab. Further, project SciPy (https://www.scipy.org/, last accessed April 21, 2021) combined NumPy with packages for plotting, symbolic computations, libraries for scientific computations (such as optimization, integration, statistics, cluster analysis, interpolation, Fast Fourier Transform, and signal processing), and an enhanced interactive console for developers. SciPy also provides efficient tools (package scipy.weave) for including C/C++ codes within the Python code. This allows obtaining Python code with high numerical performance.

Based on SciPy, Krischer et al. (2015) developed the open-source project ObsPy (https://github.com/obspy/obspy/wiki, last accessed April 21, 2021), which is a Python library to facilitate earthquake data processing in seismology. The library supports all file formats broadly used in seismic processing and contains client programs to access the various data centers. The library also integrates the key algorithms developed for observational seismology. For example, ObsPy includes the computation of travel times in the IASPEI global-Earth model by using a cross-platform version of Kennett and Buland's "iaspei-tau" program, which was originally written in Fortran.

Other notable open-source programming languages which are rapidly becoming used in seismology are Perl (https://www.perl.org/, last accessed April 21, 2021), R (mostly for statistical applications such as model bootstrapping and cluster analysis; https://www.r-project.org/, last accessed April 21, 2021), and Julia (https://julialang.org/, last accessed April 21, 2021). In terms of convenience and performance, all of them seem to be comparable to Python, and they also have similar limitations related to the need of writing code in order to process the data. It appears that from the perspective of productive data analysis, the optimal language is the one offering most community expertise in terms of libraries and processing tools.

As mentioned at the beginning of this section, in reflection seismology, the paradigm of data processing is different from those described above. Although Java, Python, or Matlab programs are often used for prototyping, tests, and solving auxiliary tasks, large-scale data processing is performed using specialized software systems. No knowledge of computer programming is necessary to perform such processing. Generally, for any processing task (many more of which may be required than in average earthquake work), a custom executable program is created and executed. For example, in Seismic Un*x, the executable processing flow consists of multiple programs connected via the Unix pipeline (input/output stream) mechanism. In more sophisticated systems such as commercial reflection data processing systems (ProMAX, Echos) and IGeoS, the custom processing code is obtained by dynamic linking of “objects” from multiple libraries, producing a single computer code (Morozov, 2008a). This code operates within a single address space, and therefore it allows the fastest possible performance and close integration between the different tools. Hundreds of tools developed for previous projects can be directly utilized in processing any new data or developing new processing approaches.

The "back-propagation" design of the IGeoS system (Morozov, 2008a) is particularly advantageous in this regard, because it allows very general forms of processing, for example loading and removing (or introducing) any number of data records at any point within the processing flow. Unlike its commercial analogs, IGeoS can operate with no waveform data records at all. The concept of data records in IGeoS is also very general, including multicomponent records with variable time starts and durations, arbitrary user-named headers, and arrangement in structured data ensembles. Details of the different file formats and access to web data repositories are included in the corresponding input/output tools. Currently, the system can use combinations of any number of generic IGeoS files or files in SAC, SEED, miniSEED, SEGY, SEG2, or Seismic Unix formats, files retrieved in real time from IRIS web services, or from indexed SQL databases stored remotely or locally (Morozov and Pavlis, 2011a, 2011b). Currently, the system contains over 300 seismic processing tools, including data selections and sorting, filtering, displays, evaluation of distances and (back)azimuths on various models of ellipsoidal Earth, instrument response corrections from dataless SEED files, evaluation of IASP91 travel times, SQL and non-SQL database access, and other.

Finally, an important part of seismological data analysis consists in plotting of georeferenced data and creating maps. Because of the need to accurately account for the curvature of the Earth and multiple map projections, this is a significant problem for seismology and other areas of geophysics. Fortunately, for many years, the U.S. National Science Foundation supported development of the Generic Mapping Tools (GMT; https://www.soest.hawaii.edu/gmt, last accessed April 21, 2021), which serve as a free and open-source geographical information system for the geophysical community. GMT is a collection of Unix-based tools, which are now available on most computer platforms. These tools maintain a database of coastline shapes for the whole world, perform basic processing of gridded images (such as smoothing and interpolation), and plot them in high-quality PostScript files. The GMT tools were integrated in several of the plotting tools in the IGeoS system (Morozov, 2008a). These tools were also used for creating most illustrations in this dissertation (Figure 3.2).

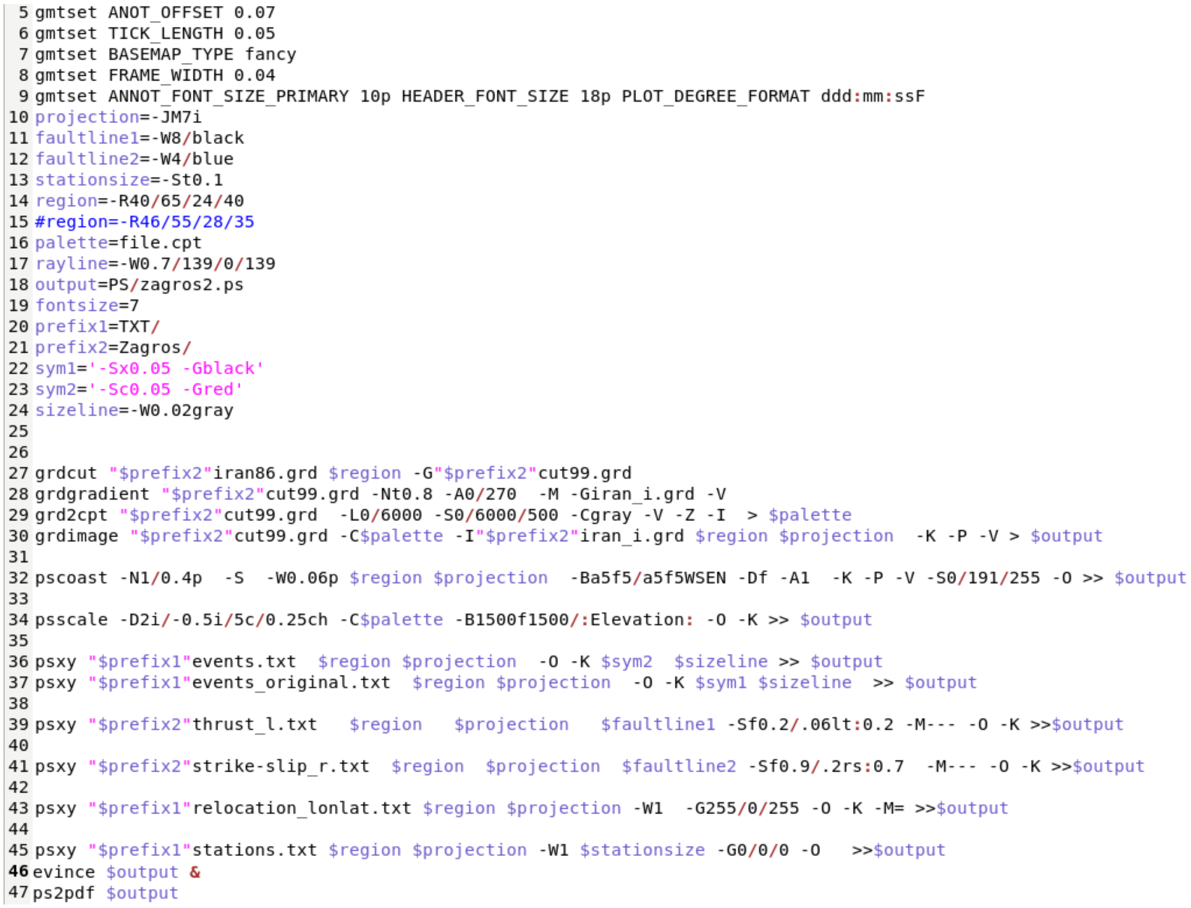

```
gmtset ANOT_OFFSET 0.07
gmtset TICK_LENGTH 0.05
gmtset BASEMAP_TYPE fancy
gmtset FRAME_WIDTH 0.04
gmtset ANNOT_FONT_SIZE_PRIMARY 10p HEADER_FONT_SIZE 18p PLOT_DEGREE_FORMAT ddd:mm:ssF
projection=-JM7i
faultline1=-W8/black
faultline2=-W4/blue
stationsize=-St0.1
region=-R40/65/24/40
#region=-R46/55/28/35
palette=file.cpt
rayline=-W0.7/139/0/139
output=PS/zagros2.ps
fontsize=7
prefix1=TXT/
prefix2=Zagros/
sym1='-Sx0.05 -Gblack'
sym2='-Sc0.05 -Gred'
sizeline=-W0.02gray


grdcut "$prefix2"iran86.grd $region -G"$prefix2"cut99.grd
grdgradient "$prefix2"cut99.grd -Nt0.8 -A0/270  -M -Giran_i.grd -V
grd2cpt "$prefix2"cut99.grd  -L0/6000 -S0/6000/500 -Cgray -V -Z -I  > $palette
grdimage "$prefix2"cut99.grd -C$palette -I"$prefix2"iran_i.grd $region $projection  -K -P -V > $output

pscoast -N1/0.4p  -S  -W0.06p $region $projection  -Ba5f5/a5f5WSEN -Df -A1  -K -P -V -S0/191/255 -O >> $output

psscale -D2i/-0.5i/5c/0.25ch -C$palette -B1500f1500/:Elevation: -O -K >> $output

psxy "$prefix1"events.txt  $region $projection  -O -K $sym2  $sizeline >> $output
psxy "$prefix1"events_original.txt  $region $projection  -O -K $sym1 $sizeline  >> $output

psxy "$prefix2"thrust_l.txt   $region   $projection   $faultline1 -Sf0.2/.06lt:0.2 -M--- -O -K >>$output

psxy "$prefix2"strike-slip_r.txt  $region  $projection  $faultline2 -Sf0.9/.2rs:0.7  -M--- -O -K >>$output

psxy "$prefix1"relocation_lonlat.txt $region $projection -W1  -G255/0/255 -O -K -M= >>$output

psxy "$prefix1"stations.txt $region $projection -W1 $stationsize -G0/0/0 -O   >>$output
evince $output &
ps2pdf $output
```

Figure 3.2. A fragment of Unix shell script for PostScript plotting using GMT codes.

3.4. Organizing and Processing Zagros Earthquake Data

In processing the large dataset from Zagros area, I use a hybrid approach combining the exploration- and earthquake-seismology style approaches described in the preceding section. The bulk of heavy-duty management, standard processing, and storage of the large dataset was performed by the large-scale and high-throughput processing system IGeoS (Morozov, 2008a). As all IGeoS processing (and similarly, for example, Seismic Un*x and Promax), the processing sequence may be quite complex, and are described by “job scripts”. This standard processing included operations commonly applied to any kinds of seismic records: loading and saving files in various formats, applying several types of filtering, rotation of components, operations with trace headers, measurement of amplitudes, and other operations. With the data prepared, the data stream was split into relatively small subsets (typically, 1 to about 100–200 records), which were processed by invoking GNU Octave scripts from within the IGeoS processing jobs. Details and examples of such scripts are given below. Any type of software using Matlab-type languages can be used, and we selected Octave because of its license-free operation and convenience in batch (command-line) operation. In a similar way, calls to Octave can be replaced with executing, for example, Python or Julia programs within the IGeoS processing flow.

To invoke the GNU Octave to perform dataset- and earthquake-seismology specific operations, I. Morozov wrote a new IGeoS tool called "procmat" (http://seisweb.usask.ca/igeos/index/index.html, last accessed April 21, 2021). With a given subset of data records, this tool extracts the selected record headers and time windows within the waveforms, and passes them into a Matlab-type code, which is further inserted in the desired Matlab/Octave code. In this way, arbitrary information from the IGeoS job can be passed to the Octave code performing the data analysis. On the other hand, the Octave code is completely unconcerned about the input and output if the data, formats of their records, and any basic operations such as filtering. The outputs of the Octave code are stored directly in the database, and they can be returned to the calling IGeoS job by using temporary files. Thus, from the user's perspective, this procedure works as a single IGeoS processing job.

The complete data processing sequence for all Zagros data consists of a set of IGeoS jobs, a set of GNU Octave codes, and a set of GMT scripts for plotting images. Some of the Octave codes are executed within the seismic processing jobs, and some of them are used for maintaining the database of earthquake records and travel-time and other picks, and also for the various types of inversion described in this dissertation. The scripts were designed so that in principle, the entire processing can be repeated by executing a single Unix shell script.

In this project, I chose to take a simplified approach to the database by using Matlab arrays and workspaces ("*.mat" files) to store all metadata tables and inversion results. With the number of records considered (about 250,000, with 62 stations), with a properly designed code (avoiding redundancies), this approach presented no difficulties on an average computer workstation. Similarly, I did not require random access to the waveform records (for which an SQL database would be needed). Instead of the random access, I created two copies of the dataset sorted by the recording stations (as in the original data) and by events. However, as described in the preceding sections, for larger projects, SQL databases such as PostgreSQL would be preferable. Such SQL databases could also be readily accessed from both within IGeoS and Matlab or Octave.

In the following subsection, I describe several key steps of the data preparation and analysis procedure. I group the variety of tasks into data reduction and quality control (QC) (subsection 3.4.1), advanced data analysis (subsection 3.4.2), and modeling and inversion (subsection 3.4.3).

3.4.1. Data reduction and quality control

The earthquake dataset from Zagros region of Iran provided by the Iranian Seismological Center (IRSC) in the form of approximately 250,000 miniSEED files distributed in several hundreds of subdirectories, 126 dataless SEED files with station response parameters, and a catalog of earthquake events in a text file. The waveform data were generally selected in order to capture the time windows corresponding to wave arrivals from the selected earthquakes. The data reduction procedure aimed at combining all of these data together and verifying that the earthquake times and locations match the time ranges in the waveforms. The data reduction also included assignment of geometry parameters, instrument corrections, and storage in the form suitable for further processing.

The data reduction was performed by one IGeoS job (“read_mseed.job”) executed in “batch” (unattended) mode for each station and acquisition year (2016 or 2017). For each relevant minSEED file, the job identified the source in the catalog, calculated the source-receiver distance, azimuth, and back-azimuth in the IASP91 Earth model, executed the IRIS SEED reader to obtain the instrument response parameters for the selected station, and applied the response corrections to each record. All records for that station were saved in a single IGeoS file (with the conventional name extension “.sia”). Thus after pre-processing, the dataset was saved in a smaller number of files (two per station) containing the complete waveform and metadata (trace header) information. These data files were used all subsequent processing.

Simultaneously with data pre-processing, by using IGeoS tool “procmat” described above, read_mseed.job invoked an Octave script “geometry.m” for groups of records. This script used the record information (source number and coordinates and other parameters, receiver and record parameters) to build up the database in Matlab/Octave workspace files. After loading a station, several quality-control operations were performed. Figure 3.3 shows source-receiver paths for earthquakes with magnitude above four occurred from January 2016 to December 2017. To reduce the density of pairs, a maximum of 10 paths for each station is shown. Figure 3.4 shows a histogram of source-receiver distances for the entire dataset. As one can see, the “regional” distance range from about 120 to 700 km is most commonly represented in the dataset. The azimuthal distributions of the source-receiver paths are quite uniform (Figure 3.5).

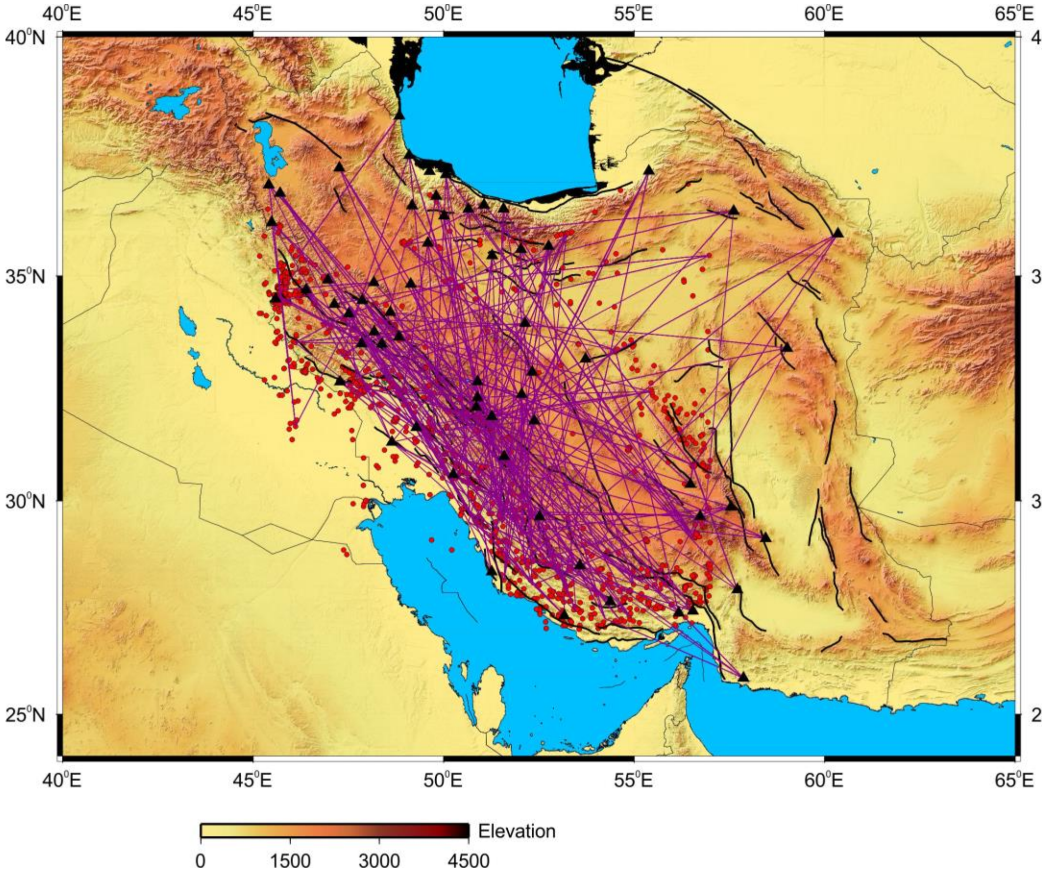

Figure 3.3. Locations of stations (black triangles), earthquakes with magnitudes above 4 (red circles), and source-receiver paths (purple lines) in Zagros dataset. For plot clarity, a maximum of 10 paths is shown for each station.

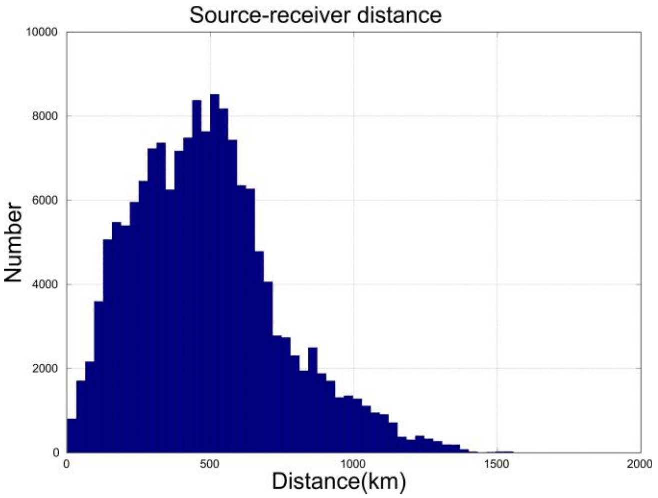

Figure 3.4. Histogram of source-receiver distance distribution from all stations.

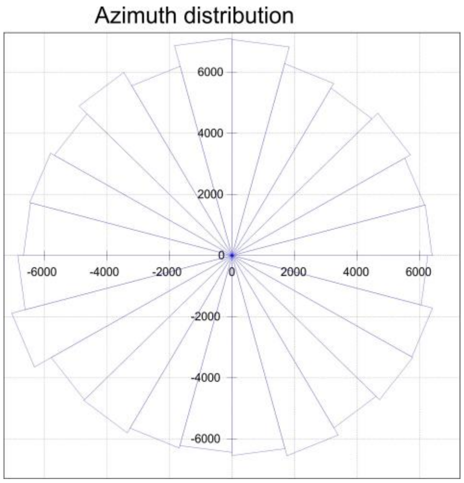

Figure 3.5. Rose diagrams of azimuth distribution from all stations of the dataset.

Figure 3.6, illustrates the interactive part of the initial data quality control (QC) and travel-time picking, which took most of the time of data processing, and also required the most complex of the interactive Octave codes. To perform this QC, another IGeoS job ("qc.job") was created, which executed an Octave script "qc.m" for one or two events recorded at the given station. The Octave scripts produces interactive displays showing all three components of seismic records, such as for station ZNGN in Figure 3.6. The records are displayed in black (default), green, or red colors corresponding to being selected as "good" (preferred for subsequent imaging, such as coda analysis) or "poor" quality (skipped in the analysis). These selections are made by the user, by using the mouse pointer and pressing keys on the keyboard. In addition to selections, time arrivals of the different seismic phases such as P, Pg, Sg, and optionally coda time windows are made interactively. These time picks are shown by the colored vertical bars in Figure 3.6. To guide the interpretation of seismic phases, the program displays the group velocities corresponding to the times of the seismograms. For example, note that the Pn wave (blue bars in Figure 3.6) arrives at group velocities of about 7.7 km/s in this area (labels in Figure 3.6). Note that the functionality of code “qc.m” allowing picking (and modifying) the times of seismic arrivals and selecting or deselecting records is also included in most other interactive tools for data analysis described in the next subsection.

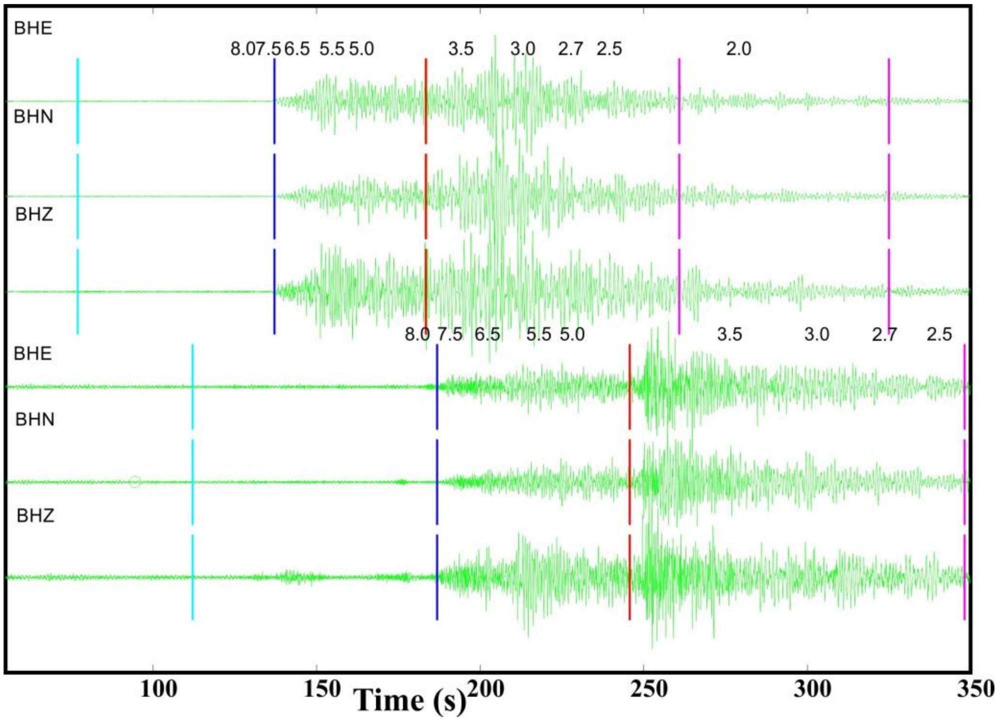

Figure 3.6. Quality control and picking times at station ZNGN for two events (M =5.2 and 4.2) with epicentral distances 400 and 561 km, respectively. Vertical bars are the times of events (cyan), P wave (blue), S-wave (red), and coda window (magenta) picks. Labels above the waveforms indicate the reference group velocities.

In Figure 3.7, I show another version of this interactive QC analysis using all vertical-component records recorded by a given station (ABH1) and displayed with spacings proportional to the source-receiver distances. This form of data presentation is typical in controlled-source seismology, and it allows observing the variation of wave velocities with depths and also checking consistency of travel-time picking. In this plot, travel times are reduced by using velocity 6 km/s, which means that the plotted times equal the travel time minus the source-receiver distance divided by six. An arrival at 6 km/s (roughly equal the crustal P-wave velocity) would appear as horizontal in this type of plot.

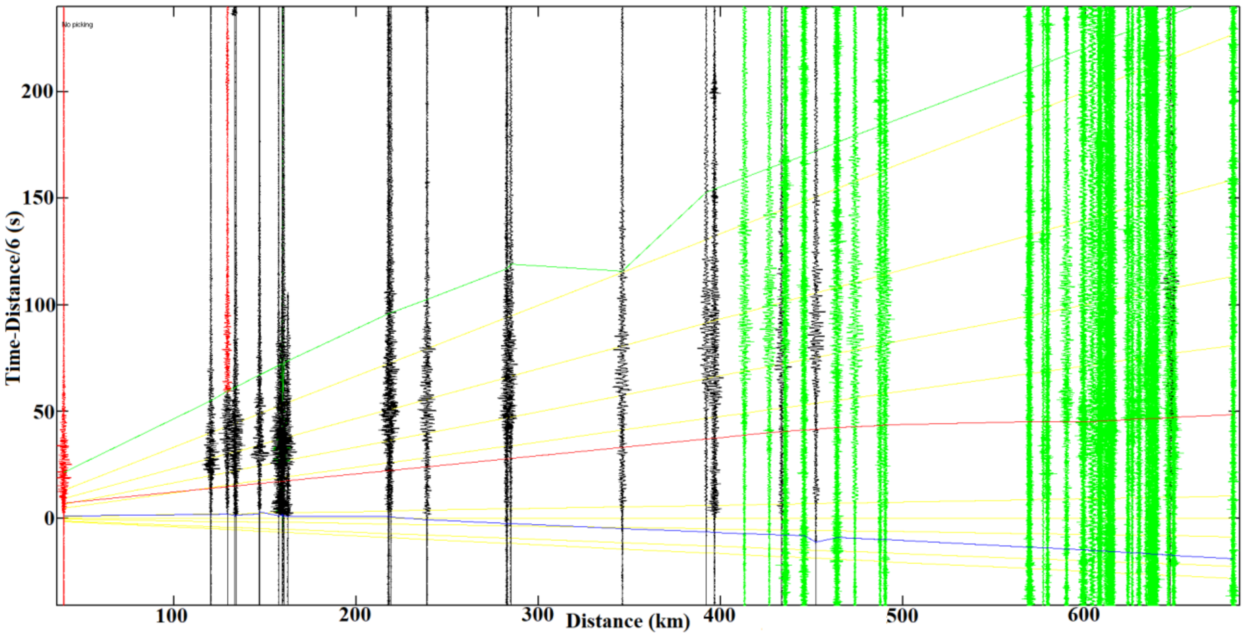

Figure 3.7. Distance section of the available 61 vertical-component records at station ABH1. Travel-time reduction with velocity 6 km/s is used. The original records shown in black, green records are selected for further analysis, red records are marked for deletion. Lines show the P-wave (blue), S-wave (red), and coda start (green) times. Yellow lines indicate the reference group velocities. Interactive time picking and record selections as in Figure 3.6 are also available in this display.

3.4.2. Advanced analysis

After the data reduction and QC, the data were processed by using IGeoS jobs which read portions of the prepared data, performed additional sorting or filtering as needed, and passed segments of the data to GNU Octave scripts. Several tasks of such advanced data analysis were performed in "batch" mode on the whole dataset, and some tasks were performed interactively with selected data. In particular, all good-quality data were sorted into files containing source locations within 0.5-degree coordinate bins. These data are convenient to display in section plots shown in Figure 3.7. Also, by using these binned records, another pass of interactive arrival-time refinement was performed in order to improve the accuracy of the time picks. In this improved picking, the estimated average travel-time model (subsection 3.4.3) was used to guide the identification of seismic-wave arrivals.

Figure 3.8 shows an illustration of spectral analysis of one three-component record from station ABH1. Note that above frequencies of about 7 to 10 Hz, all components show linear decreases in the logarithms of spectral amplitudes. These decreases are usually measured by parameter κ ("kappa"), which serve a valuable measure of the near-surface conditions in the vicinity of the receiver (Ktenidou et al., 2014). The interactive display shows the spectra within the Pn, Pg, and Sg-wave time windows, and also within the coda and Lg coda windows (Figure 3.8). By using the interactive functionality in this display, records can be selected for coda or H/V (horizontal- to vertical-component amplitude ratio) analysis.

As described in chapter 1, coda analysis is an important part of research with similar datasets. Raw coda envelopes are rarely shown in the literature, but in this study, I performed a detailed initial investigation of coda records by using another interactive display in the IGeoS – GNU Octave combination (Figure 3.9). In this display, note how the logarithms of amplitude within the coda and Lg coda window decrease with time. These amplitude decays represent the exponential decays of the recorded amplitudes, which are expected from coda. The logarithmic decrements of these amplitude decays are called the temporal attenuation coefficients (Morozov, 2008b), and these quantities are plotted in red in the bottom of Figure 3.9. Note that interestingly, these attenuation coefficients are near zero and often decrease with frequency (Figure 3.9). This observation has extensive consequences for explaining the nature of the coda, which will be discussed in chapters 6 and 7.

After the interactive examinations of selected three-component and coda records, I performed (for records deemed "good" only):

1) Measurements of the amplitudes within the seismic-phase arrival-time windows;
2) Polarization angle measurements;
3) Coda amplitude and logarithmic decrement measurements within several frequency bands;

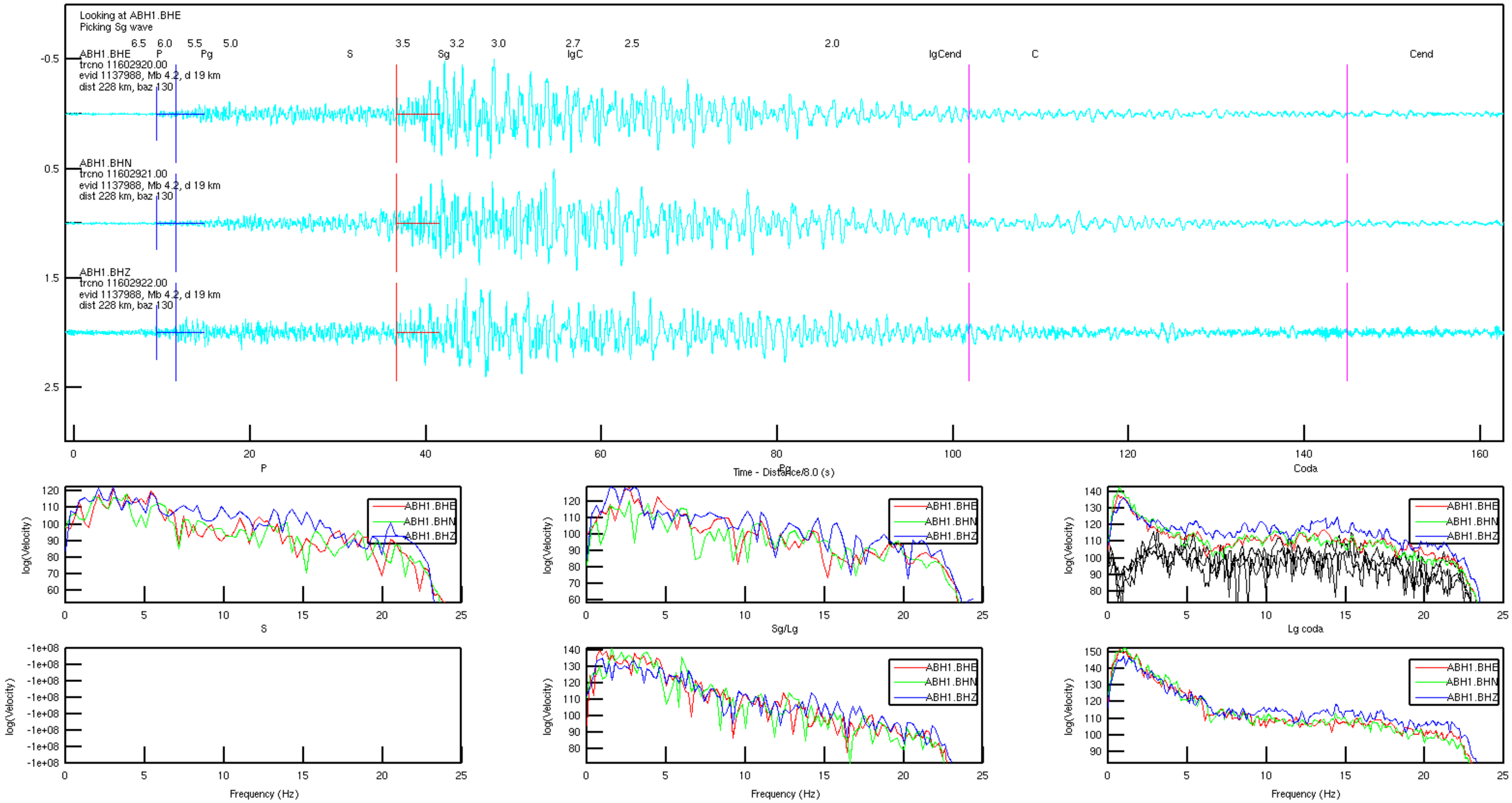

Figure 3.8. Interactive analysis of record spectra within the Pn, Pg, coda, Sg, and Lg coda windows (left, middle, and right columns in the top and the bottom) for one earthquake record at station ABH1.

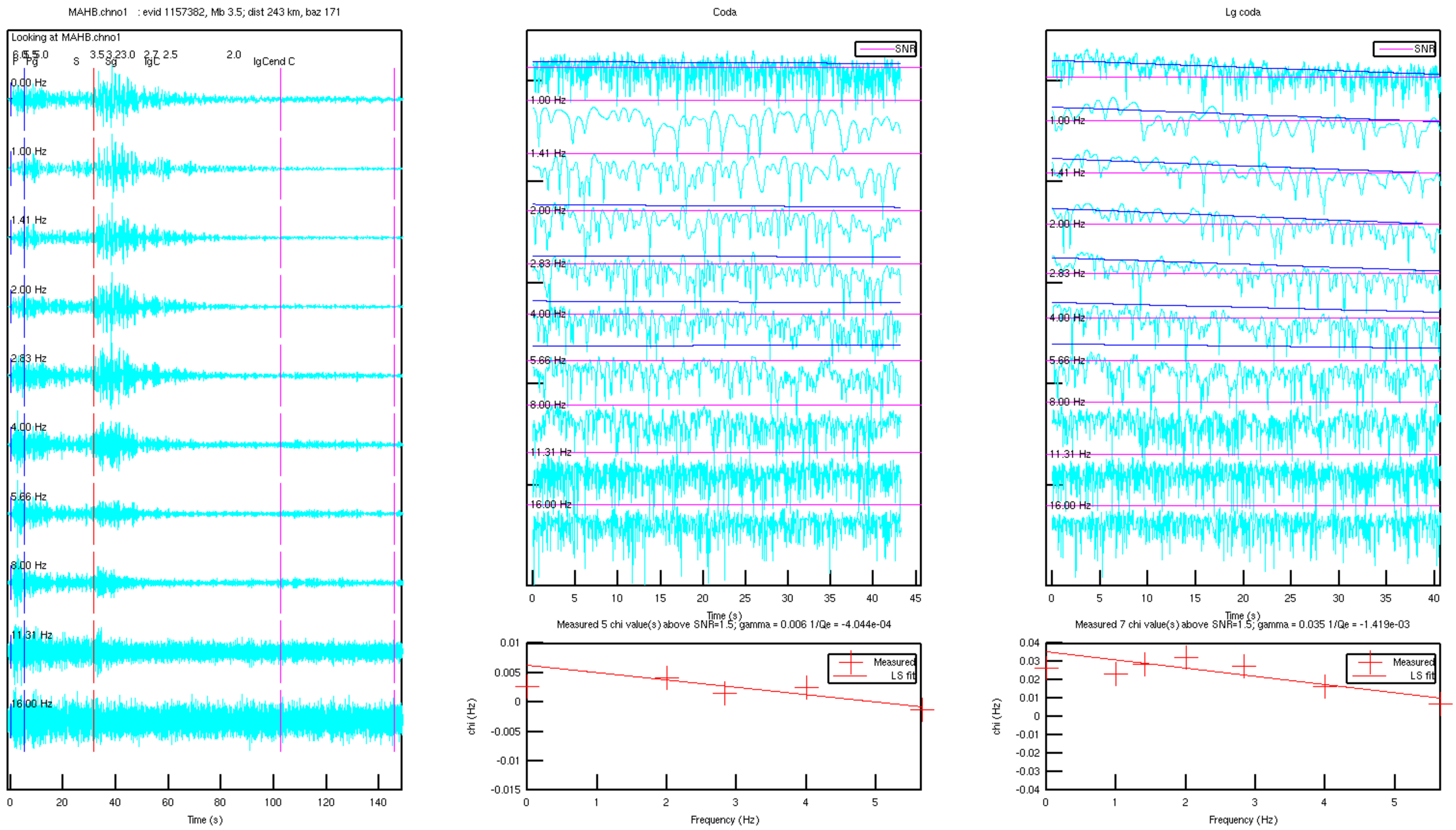

Figure 3.9. Interactive analysis of coda amplitude decays for one earthquake record at station KGS1. Left: vertical-component record unfiltered (top) and filtered within different frequency bands (labels). Middle and right: the corresponding amplitude envelope records for coda and Lg coda. Purple horizontal lines in these plots represent the minimum amplitude level required by the selected signal-to-noise ratio thresholds. In the bottom of each of these columns, measured values of attenuation coefficients (red crosses) and their trends with frequency (red lines) are shown.

4) Measurements of parameters kappa characterizing the slopes of the high-frequency spectral amplitudes;
5) Measurements of the ratios of spectral amplitude ratios of the horizontal and vertical (H/V) components for each record.

Results of these measurements were stored in the Octave workspace databases and used in the inversions described in chapters 7 and 8 of this dissertation.

3.4.3. Modeling and inversion

Similar to the conventional method of seismic data analysis (section 3.2), the main results of this study are obtained by a number of modeling and inversion methods applied to the measurements extracted from the waveform data. These inversions were implemented in a group of GNU Octave codes. These codes included:

1) Finalizing and plotting the geometry database;
2) Finalizing the database of arrival-time picks. This operation was repeated every time when a substantial amount of new data was added to the dataset. By using the current arrival-time picks, this code calculates the averaged dependencies of the travel times for each phase on the source-receiver distances (Figure 3.10). These regional-average travel times are then displayed in the QC and phase-time picking displays (subsection 3.4.1) and provide good guidance for future picking.
3) Several codes for correcting errors encountered from unexpected parameters in the input data files;
4) Several codes for plotting the various contents of the database;
5) Relocation and refinement of source times (chapter 4);
6) Codes for coda mapping and inversion (chapter 7);
7) Codes for analysis of wave polarizations (chapter 8).

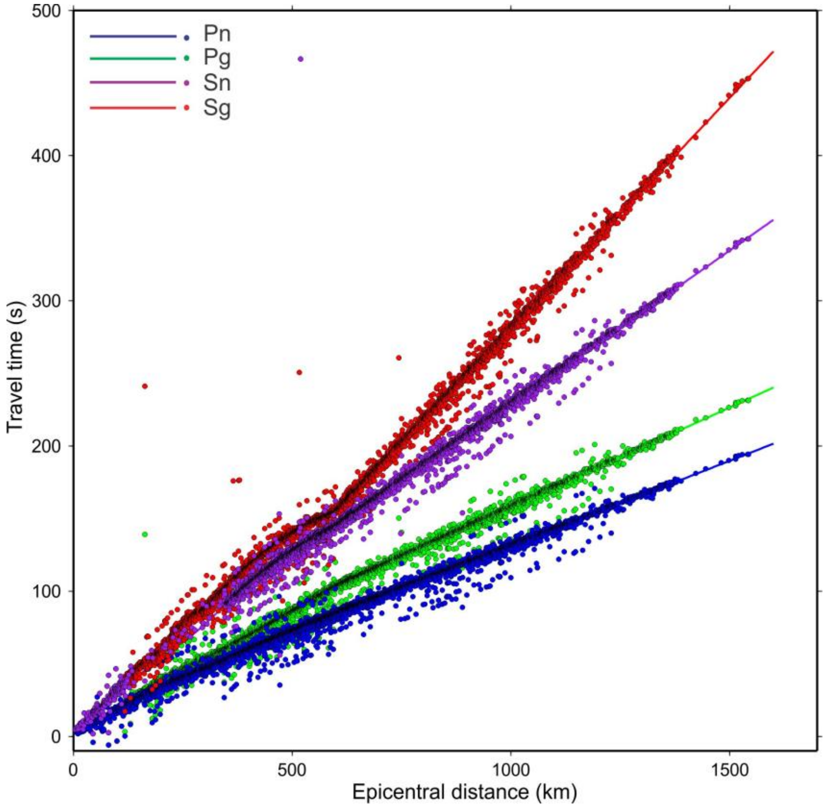

Figure 3.10. Travel times in Zagros dataset, plotted versus the source-receiver distances. Colored symbols are the interactive picks, and solid lines show the average distance dependencies of the travel times determined for each seismic phase (legend).

3.5. Conclusions

Large earthquake datasets can be conveniently and efficiently processed and inverted by sophisticated algorithms by using a combination of a high-throughput, exploration-style seismic processing system, which invokes specialized tools based on data analysis or programming packages such as Matlab (Octave), Java, Python, Julia, GMT, or other. This approach maximizes performance and flexibility of data analysis while minimizing the complexity of coding and the number of intermediate data files. In the present project, all steps of data analysis and inversion are done by using this approach, with the IGeoS seismic processing system with command lines on GMT and Octave interfaces. The resulting processing is completely self-documented and reproducible on any Unix system.

CHAPTER 4

EARTHQUAKE SOURCE RELOCATION

In this chapter, I describe a key part of earthquake data analysis, which consists in accurate determination of the times and locations of earthquake sources. This determination is a part of routine data processing, which is performed in several stages. First, soon after the earthquakes occur and the records are acquired, initial locations and times are calculated by the local seismographic networks operators and published in catalogs. These initial locations are used for further data archiving and processing. In particular, the initial location and event times from the IRSC catalog were used for extracting the record segments used in this study (chapter 2). However, for more detailed and accurate data analysis, improvements of the original locations and source times are often needed. These corrected locations are often referred to as event *relocations*.

In the following sections, I describe relocations performed for the Zagros area dataset (chapter 2). The relocation method is relatively simple (and standard) and only consists in adjustment of surface coordinates and times of seismic sources. In section 4.1, I give an introduction to several common relocation methods and a brief discussion of them. In section 4.2, I describe the relocation method used in this research, in section 4.3, I give the results, and in section 4.4, the resulting location errors are estimated. Finally, the chapter concludes with a discussion and conclusions (section 4.5).

4.1. Introduction

Earthquakes are unpredictable natural phenomena occurring at unknown locations and times, and therefore the determination of these parameters is a critical and fundamental problem in earthquake studies. In this dissertation, the datasets included catalogs of initial estimates of source coordinates and times (chapter 2), and therefore our task consisted in only improving these locations. This procedure of improving the earthquake locations and origin times presented in the catalog is called relocation.

The accuracy of event locations and origin times depends on several factors including travel time errors, accuracy of the model for seismic velocity structure, uncertainties in arrival time picks, or mathematical methods of location using, for example, only the arrival time picks or complete waveforms (Pavlis, 1986). In the simplest form used in this chapter, relocation can be performed by using the picked P-wave arrival times. This location or relocation by using arrival-time picks from individual records is called the absolute location method. This type of method is used in the following sections.

The absolute (re)location relies on accurate picking of seismic arrivals, which usually has to be done interactively by an experienced analyst. Such picking of P-wave onsets took a significant part of the time in this study (chapter 3). However, arrival picks often cannot be made accurately, particularly at larger distances or for weaker events. In such cases, event relocation can be solved through relative location methods. The idea of the relative relocation method consists in correcting the location and origin time of an event by comparing the waveforms to another event located sufficiently close to it. For closely spaced events of similar sizes and mechanisms, the waveforms may also be similar, which allows accurate measurement of the time difference between them by using waveform cross-correlations (Waldhauser and Ellsworth, 2000). If the hypocentral separation between the two events is insignificant compared to the hypocenter-station distance and the scale length of the velocity gradient, then the ray paths between the source and a common station are similar along the whole ray path. By using this similarity, the travel-time difference for the pair of events recorded at one station is related to their spatial separation and difference in origin times (Waldhauser and Ellsworth, 2000). The waveform cross-correlation procedure can be performed in the time domain (Deichmann and Garcia-Fernandez, 1992) or in frequency domain (Poupinet et al., 1984).

A powerful and popular technique for relative relocation of earthquakes is known as the double-difference method. This location algorithm uses pairs of absolute travel-time measurements or cross-correlation of pairs of waveforms of P and/or S waves. The relocation is performed by forming differential travel times and further minimizing their residuals (differences between the observed and theoretical travel-time differences for pairs of arrivals) (Waldhauser and Ellsworth, 2000). As in all location methods, it is important to know the velocity structure in the vicinity of the located events. In double-difference methods, the forward problem is usually solved by using 1D-layered velocity models. However, Michelini and Lomax (2004) showed that if a 1-D gradient model is used, it can result in substantial distortions and errors in the relative relocation results for closely spaced events.

Another common method for determining earthquake locations or relocations is the probabilistic non-linear approach, which represents modern implementation of classical graphical methods for locating earthquakes. In this method, the location is achieved by inverting for a set of points at which the location satisfying the given travel times could occur within a 1-D or 3-D layered model. When estimated from multiple travel-time picks, these sets of points give the posterior probability density function (p.d.f.), from which the location and its error estimates are obtained (e.g., Lomax et al., 2000). The estimation of this p.d.f. is subject to uncertainties due to assuming Gaussian distributions of time errors, network geometry, uncertainties in arrival time picks, and travel time computing errors. Due to non-linear relationships between the travel times and event location in the forward model, the location uncertainty area is often of non-ellipsoidal shapes (Lomax et al., 2001).

In this research, I perform relocation by using a simple method similar to the one described in the preceding paragraph. Because the Zagros dataset is dominated by regional-distance recordings, I only adjust the horizontal coordinates of source locations and leave the depths unchanged. Note that the determination of depths usually requires local-distance recordings and careful analysis of phases reflected from the surface. This analysis has likely not been performed with the present records, and most of the reported depth values in the catalog are likely filled with nominal (average for the area) values. I also perform relocation without considering any velocity model. Instead of constructing a velocity model and modeling travel times in it, I construct an average 1-D travel-time model (dependence *time*(*distance*)) by averaging all of the available P-wave travel times from 592 events.

4.2. Method

Each event within the dataset is relocated independently, by using all travel-time picks available for that event. The relocation is posed as an inverse problem with three unknown parameters, which are the shifts in the longitude and latitude of the event and a modification of its time. Therefore, when using more than three arrivals to constrain the event, the inverse problem is overdetermined and can be solved by least-squares inversion. Because the ray geometry depends on the location of the event, the location problem is nonlinear, and it would be solved by an iterative method as described below.

During one step of the iterative relocation, the travel-time fitting problem is linearized as follows. Denoting by (x, y, z) the coordinates and depth of the event, x_i and y_i the coordinates of i^{th} seismic station recording this event, Δx and Δy the unknown shifts in the coordinate of the source and Δt the shift of its origin time, the requirement of travel-time fitting for this event is written as

$$t_i + \Delta t = T_i\left(x + \Delta x, y + \Delta y, z + \Delta z\right), \tag{4.1}$$

where t_i is the travel time picked at station i, and $T_i(x,y,\mathrm{z})$ is the regional-average travel-time function. This function is determined prior to relocation and concurrently with interactive travel-time picking, by interpolating the time-distance curve of all available P-wave onset picks (chapter 3). When relocations are performed, the function $T_i(x,y,z)$ is re-calculated, which allows to improve the locations further. In the present simplified approach, I used the regional travel-time model in "1-D" form, as a single function $T_i\left(x,y,z\right) = T\left(d_i\right)$, where d_i is the source-receiver distance.

As mentioned above, because the dataset contains few local-distance recordings, I do not attempt hypocenter depth relocation (i.e., consider $\Delta z = 0$). The inverse problem consists in finding Δx, Δy, and Δt giving the best approximation of equation (4.1). This problem is nonlinear, and its solution is implemented by an iterative method. During each iteration, eq. (4.1) is linearized as

$$t_i + \Delta t \approx T_{0i} + \frac{\partial T_i}{\partial x}\Delta x + \frac{\partial T_i}{\partial y}\Delta y\ , \tag{4.2}$$

where $T_{0i} = T_i\left(x,y,z\right)$. The partial derivatives of travel time represent components of the ray-parameter vector $\mathbf{p}_i$ for waves from i^{th} station at the position of the source. Therefore, eq. (4.2) is

$$-\Delta t + p_{ix}\Delta x + p_{iy}\Delta y \approx t_i - T_{0i}\,. \tag{4.3}$$

During the n^{th} iteration of the inverse, this equation can be written in matrix form as

$\mathbf{L}\Delta\mathbf{m}^{(n)} = \Delta\mathbf{t}^{(n)}$, where the i^{th} row of matrix **L** equals $\begin{pmatrix}-1 & p_{ix} & p_{iy}\end{pmatrix}$, the i^{th} element of the right-hand side vector $\Delta\mathbf{t}^{(n)}$ equals $\Delta t_i^{(n)} = t_i - T_{0i}$, the model vector is $\Delta\mathbf{m}^{(n)} = \begin{pmatrix}\Delta t & \Delta x & \Delta y\end{pmatrix}^T$, and superscript '^{T}' denotes the matrix transpose. For more than two travel-time records *i*, this system can be solved for **m** in the form of a matrix multiplication of the data (the generalized linear inverse): $\Delta\mathbf{m}^{(n)} = \mathbf{L}_g^{-1}\Delta\mathbf{t}^{(n)}$. I use the ordinary least-squares method, in which $\mathbf{L}_g^{-1} = \left(\mathbf{L}^T\mathbf{L}\right)^{-1}\mathbf{L}^T$. Note that similar to $\Delta\mathbf{t}^{(n)}$, matrices **L** and $\mathbf{L}_g^{-1}$ are evaluated by using current positions of the relocated source, and therefore they also depend on the iteration *n*.

To evaluate the components of ray parameter in eq. (4.3), at this initial relocation stage, I take the 1-D form of the travel-time model: assume that regional travel times depend only on the source-receiver distance $d_i = \sqrt{\left(x_i - x\right)^2 + \left(y_i - y\right)^2}$,

$$T\left(x, y, z \mid x_i, y_i\right) = T\left(d_i\right). \tag{4.4}$$

With this travel-time function, $p_{xi} = -|p|\sin\varphi_i$ and $p_{yi} = -|p|\cos\varphi_i$, where φ_i is the azimuth to the i^{th} station (Figure 4.1), and $|p| = \partial T/\partial d$ is the ray parameter measured from *T*(*d*).

To solve the nonlinear travel-time inverse problem (4.1), I take the initial linear approximation (with $n = 1$) equal $\mathbf{m}^{(1)} = \Delta\mathbf{m}^{(1)}$ and obtain the next iteration as $\mathbf{m}^{(n+1)} = \mathbf{m}^{(n)} + \lambda\Delta\mathbf{m}^{(n)}$. This iteration converges when $\Delta\mathbf{m}^{(n)} \to \mathbf{0}$, i.e. when the travel-time misfits $\Delta\mathbf{t}^{(n)}$ can no longer be reduced by changing Δt, Δx, or Δy. Empirical factor $\lambda \le 1$ is included to "slow down" this convergence, in order to avoid oscillations due to "overshooting" of the optimal model. Parameter $\lambda = 0.5$ allows achieving stable convergence with 15 iterations in the present case.

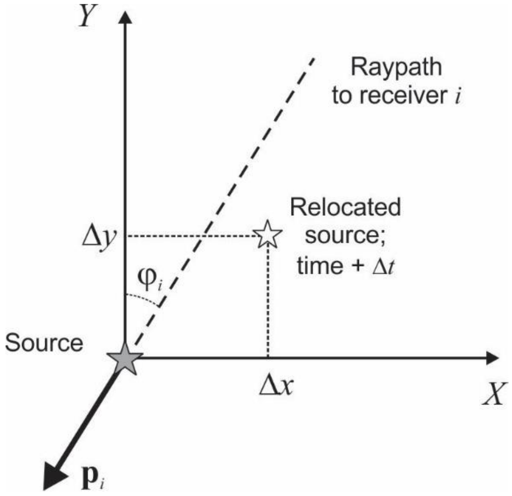

Figure 4.1. Schematic map of relocation and notation in eqs. (4.1)– (4.3).

4.3. Results

The relocation is applied only for events satisfying three criteria:

1) Producing at least three picked P-wave travel times.
2) The largest azimuthal gap is less than 240°. The requirement on the azimuthal gap is important in seismic location, because it allows avoiding one-sided distribution of ray paths causing large location errors in the transverse direction.
3) The inverted relocation distances are below 30 km in each step of the iterative procedure. This criterion removes events for which the P-wave picking errors are unreasonably large. These events likely require revisiting the quality control and picking operations (chapter 3).

The above selections resulted in 592 successfully relocated events out of the about 1300 events in the dataset. A histogram of relocation distances for the relocated events is shown in Figure 4.2.

Figure 4.2 shows that most events are shifted by less than 20 km by the relocation procedure. The amounts of source location shifts in the horizontal spatial directions for all relocated events are presented in Figure 4.3.

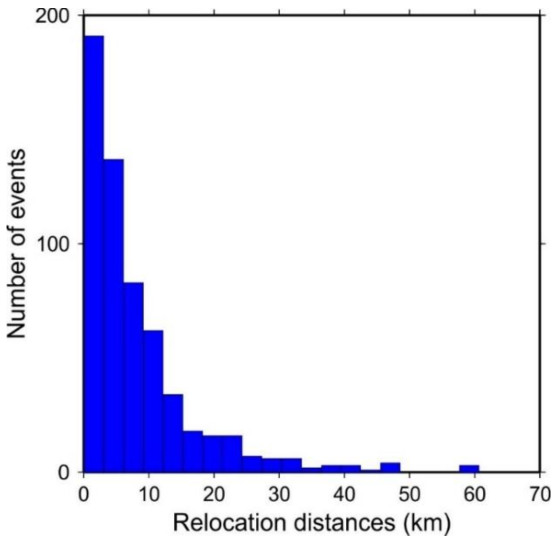

Figure 4.2. Histogram of relocation distances.

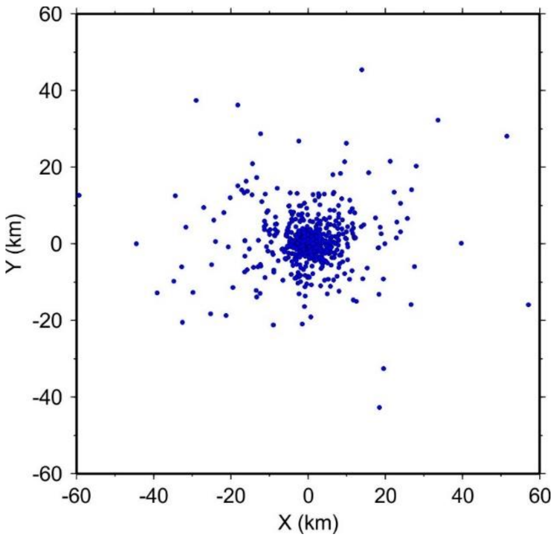

Figure 4.3. Longitudinal (X) and latitudinal (Y) shifts for all relocated events.

Figure 4.4 shows histograms of the distributions of the longitudinal and latitudinal shifts of the sources. The width of distributions of shifts for each of the horizontal coordinates is about 20 km. Larger estimated relocated distance for some events (outliers) such as near 60-km relocations in Figure 4.2 appear to result from travel time errors caused by several factors such as lower signal noise ratio, poor phase identification, and unfavourable azimuthal distribution of receiver stations.

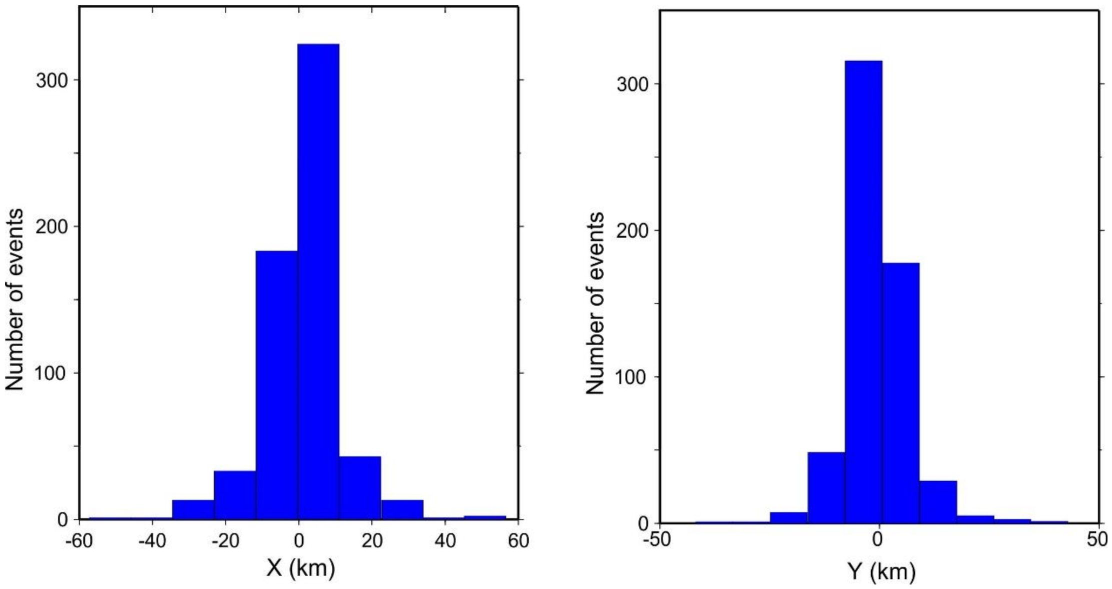

Figure 4.4. Histograms of relocation distances in the longitudinal (X) and latitudinal (Y) directions.

Figure 4.5 shows the distribution of event origin time shifts derived by the relocation procedure in the preceding section. Roughly, the time shifts are within about ±5 s. The time shifts are slightly (by about 1 s) shifted toward negative values, which suggests that our arrival-time picking was done (on average) somewhat later than in the original locations (which likely used mostly local-earthquake data).

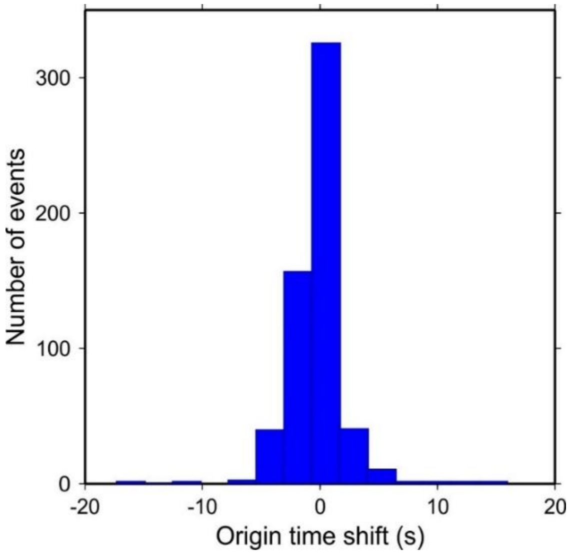

Figure 4.5. Histogram of estimated origin time shifts.

Another possibility for the time shifts may consist in the effects of topography (variable elevations of the stations) and variations of the velocity structure within this large region. All these observations show that the presented relocation is only a rough first approximation necessary for preconditioning the dataset for subsequent work. With the development of a 3-D tomographic model or a more accurate empirical travel-time model $T_i(x,y,z)$, relocation iterations can (and should) be continued, and its errors (next section) should reduce. Similarly, using the derived travel-time model and information about location errors above, additional quality control and correction of the travel-time picks can be performed. These operations would also improve the quality of event locations and origin times and reduce their errors.

As a geometrical criterion of the quality of location problems, a histogram of the numbers of paths used in each relocation is shown in Figure 4.6. Because at least three receivers are needed to calculate relocation, the smallest number of paths is three, and the largest is 17. For most relocated events, the number of paths ranges from five to nine.

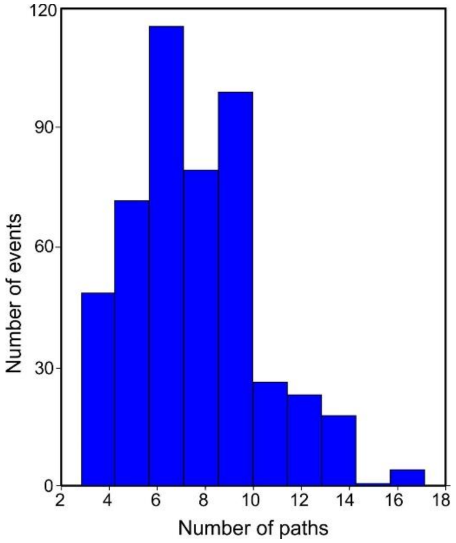

Figure 4.6. Histogram of the number of paths used in the relocation.

Figure 4.7 compares the initial time errors (black plus signs) with similar errors after relocation (stars). For each event, the time errors are measured by the root mean square (RMS) differences of all travel times from the available stations from the regional time $T_i(x,y,z)$ (preceding section). The reduction of the errors was achieved by shifting event coordinates (relocation) and changing the source times. As shown in Figure 4.7, the final travel-time errors are noticeably reduced compared to the initial ones, and both of the initial and final errors strongly vary for different events. As discussed above, these travel-time errors are affected by the velocity structures and elevations of the receivers, and therefore they would change with tomographic inversion and more accurate relocation.

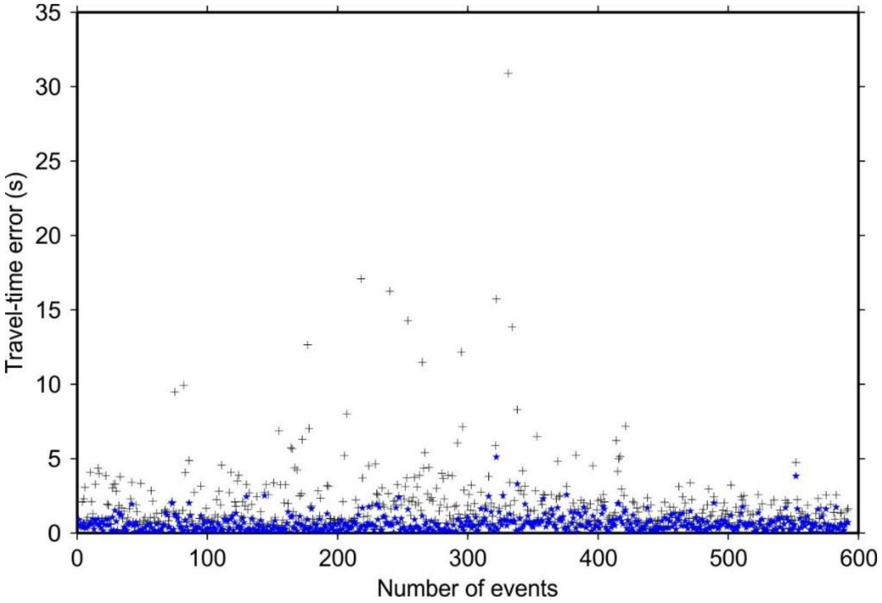

Figure 4.7. Travel time misfits versus the number of the performed relocation. The initial travel-time errors are shown by plus signs and the final travel-time error are shown by blue stars.

Because earthquakes are caused by crustal faulting, it is interesting to compare their locations with known active faults within the study area. In high-resolution local-earthquake studies, double-difference relocations often lead to relocated events tightly clustering near faults (e.g., Waldhauser and Ellsworth, 2000). For the present study, the relocated events with fault traces mapped at the surface are shown in Figure 4.8, and Figures 4.9 and 4.10 also show its zoomed-in versions. For comparison, the original origin locations from the IRSC catalog are also shown in Figures 4.9 and 4.10. Although the relocation improves the consistency of the travel-time dataset (Figure 4.7), the resulting locations (Figures 4.9 and 4.10) show no convincing associations with faults. Some of the relocated events appear to come closer to the mapped faults (red arrows in Figures 4.9 and 4.10), some get farther away from them, and some may become closer to a different

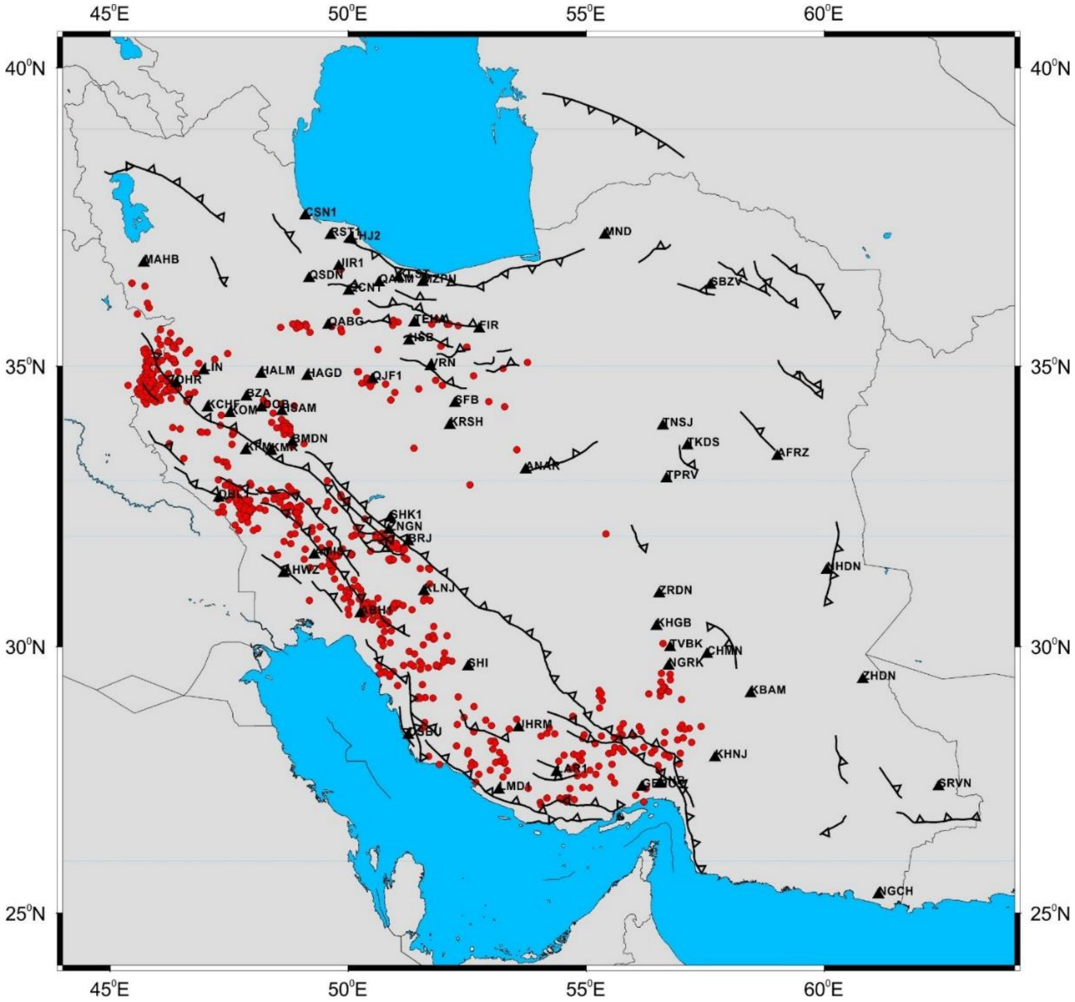

Figure 4.8. Coordinates of the relocated events (red dots) and mapped fault traces (black lines with indicators of slip directions). Triangles are the seismic stations of this study.

fault.This is not surprising, because earthquake sources are located at significant depths at which their locations may differ from surface projections of the faults. Also, many earthquakes may be produced by faults not reaching or not mapped at the surface. For the events in the recent catalog I used, there has been no studies associating them with specific faults. This task of event association with subsurface structures can be difficult and equivocal. For example, in my previous study (Safarshahi et al., 2013), I presented evidence for associating a known event with a fault different from the one with which it was previously associated. Finally, as shown in the next section, the accuracy of the simple relocation scheme above is likely insufficient for making such accurate associations with subsurface structure in this complex area.

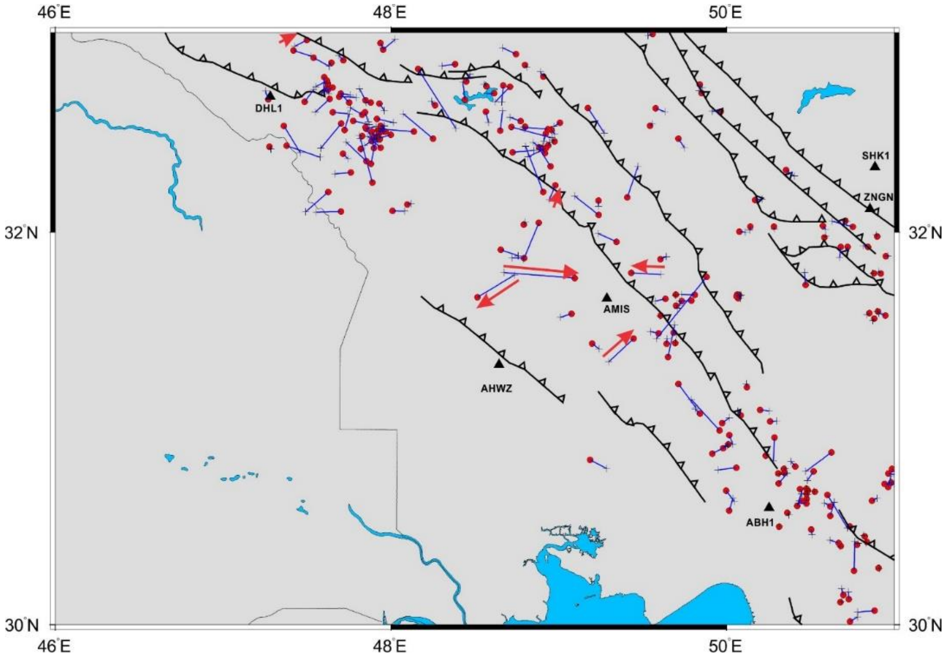

Figure 4.9. A zoom-in of Figure 4.8, additionally showing the original locations (small plus signs connected with relocated origins (red circle) by blue lines). Red arrows show the relocated events that get closer to the mapped faults.

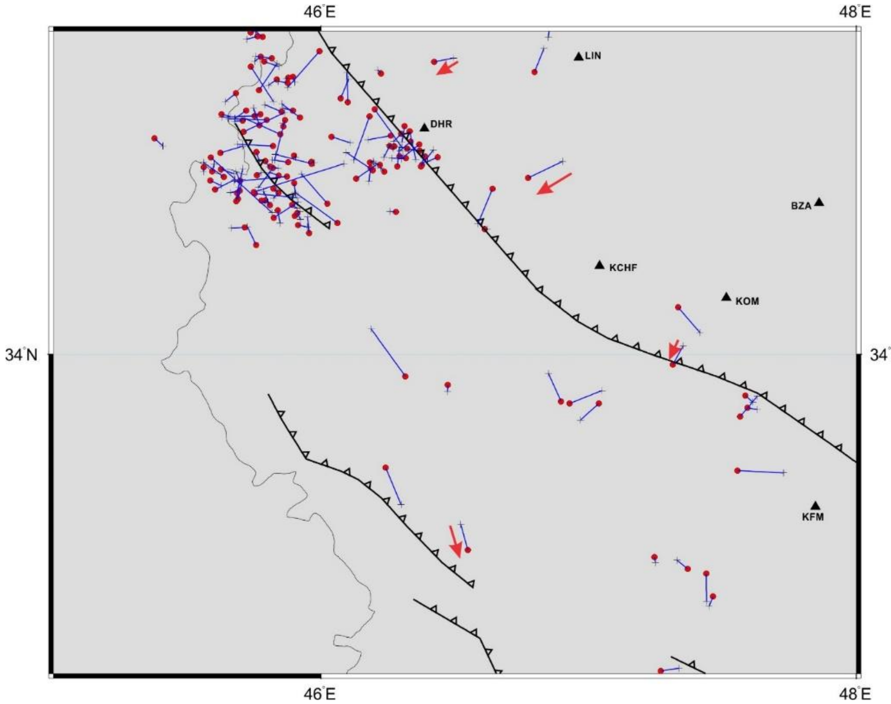

Figure 4.10. Another zoom-in of Figure 4.8, additionally showing the original locations. Symbols and lines are as in Figure 4.9.

4.4. Location Uncertainties

As in any physical measurement, the best-fit locations and origin times obtained by the procedure in the preceding section are subject to uncertainties. In particular, location uncertainties are caused by errors in travel-time measurements, inaccuracy of the regional travel time model (due to simplification of the 1-D structure), and uneven distribution of receivers (and particularly azimuthal gaps). These factors lead to appearance of a near-elliptical location uncertainty area for each event, whose shape and size I try estimating in this section.

For multi-parameter or nonlinear inverse problems, uncertainties of model parameters can be analyzed by the “Monte Carlo” (random sampling) method. To evaluate uncertainties of the location problem for one event (section 4.2), I performed a series of Monte Carlo tests by generating new travel time data equal $\tilde{t}_i = t_0 + T_i\left(x, y, z\right) + \delta t_i$ (eq. (4.1)), where t_0 is the origin time for this event and δt_i is a random time error. The time errors were assumed to belong to a Gaussian distribution with standard deviation equal the final travel time error (Figure 4.7). Using these random synthetic times as data t_i in eq. (4.1), the iterative relocation procedure was repeated giving an updated location of the earthquake. Such trials with random δt_i were repeated 250 times to obtain sampling of possible locations.

The method described above was applied to each of the relocated events in the dataset. Here, I present examples for two events for which the relocations were obtained. For one of these events, the deviations of locations caused by random time errors δt_i are shown by green dots in Figure 4.11. The average travel-time error is shown in this figure by the blue circle of radius $R = V_P \,\mathrm{stddev}\left(\delta t_i\right)$, where stddev() denotes the standard deviation of the time errors, and V_P = 5 km/s is the characteristic P-wave velocity within the crust. This circle shows a simple estimate of the expected level of location uncertainty due to travel-time uncertainties.

To obtain more rigorous and detailed measures of location uncertainty, the distribution of dots in Figure 4.11 can be approximated by a 2-D Gaussian distribution. Parameters of this distribution can be obtained by calculating the 2-D covariance matrix for source coordinates (x,y):

$$\mathbf{C} = \begin{bmatrix} v(x) & c(x,y) \\ c(x,y) & v(y) \end{bmatrix}, \tag{4.5}$$

where *x* and *y* are the components of the deviations of locations, and the variances and covariances of coordinate values are defined by the usual relations:

$$v(x) = \frac{1}{n}\sum_{i=1}^{n}(x_i - \bar{x})^2 , \tag{4.6}$$

$$c(x,y) = \frac{1}{n}\sum_{i=1}^{n}(x_i - \bar{x})(y_i - \bar{y}) . \tag{4.7}$$

Then, the standard deviational ellipse (SDE) can be drawn by using the eigenvectors of the covariance matrix **C**.

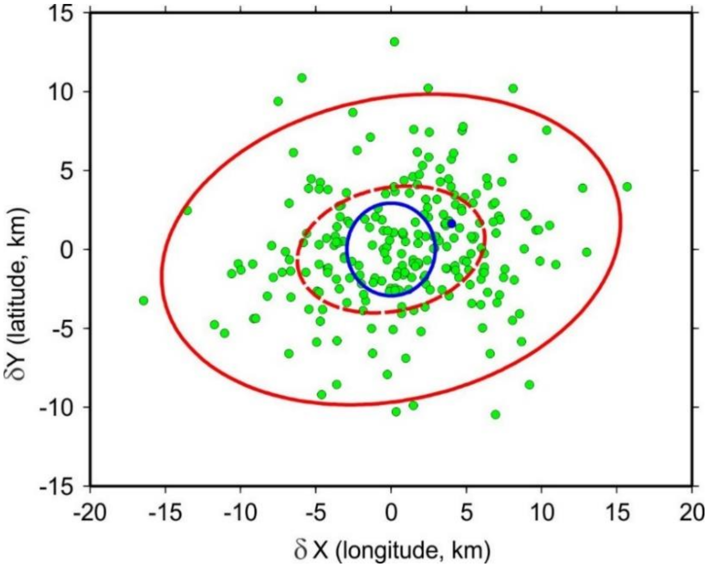

Figure 4.11. Evaluation of location uncertainty for event 1135452. Coordinated *δx* and *δy* are the deviations of location due to time uncertainties. Blue dot shows the amount of source relocation (section 4.2). Green dots show the deviations locations due to random travel-time errors. The blue circle average travel-time misfit. Red ellipses are the SDE (dashed line) and the 95% confidence ellipse (solid).

The semiaxes of this ellipse are given by square roots of the eigenvalues of **C** (variances of the principal components), and the directions of the semiaxes are those of the eigenvectors. The SDE is shown by the dashed red line in Figure 4.11. Approximating the distribution of random location errors by a 2-D Gaussian distribution, location accuracy can be described graphically by drawing ellipses centered on the best-fit location. These ellipses are obtained from the SDE by scaling both of its dimensions by a positive factor *r*, so that the value of *r* = 1 corresponds to the SDE. Denoting by *x* and *y* the coordinates in the directions of the principal axes of the SDE, the shape of the ellipse of size *r* are given by equation:

$$\left(\frac{x}{r\sigma_1}\right)^2+\left(\frac{y}{r\sigma_2}\right)^2=1, \tag{4.8}$$

where σ_1^2 and σ_2^2 are the eigenvalues of the covariance matrix for randomized locations (variances), and σ_1 and σ_2 or the semiaxes of the SDE. Relation (4.8) can also be expressed by replacing variables (*x*,*y*) with scaled Cartesian coordinates (x_1,x_2) as $x=\sigma_1 x_1$ and $y=\sigma_2 x_2$. In terms of these variables, the 2-D Gaussian distribution probability density function equals $p(x,y)=\frac{1}{\sqrt{2\pi}\sigma_1}\frac{1}{\sqrt{2\pi}\sigma_2}\exp\left(-\frac{x^2}{2\sigma_1^2}-\frac{y^2}{2\sigma_2^2}\right)$ and $p(x_1,x_2)=\frac{1}{2\pi}\exp\left(-\frac{x_1{}^2+x_2{}^2}{2}\right)$, respectively.

For any *r*, the confidence level of location is defined as the probability *P*(*r*) for a random location to be found within the error ellipse. Integrating over the interior of the ellipse, this probability is obtained as

$$P(r)=\iint\limits_{\substack{\text{interrior}\\ \text{of ellipse}}} p(x,y)\,dxdy=\frac{1}{2\pi}\iint\limits_{x_1{}^2+x_2{}^2\le r^2} e^{-\frac{x_1{}^2+x_2{}^2}{2}}dx_1dx_2=\frac{1}{2\pi}\int_0^{2\pi}d\theta\int_0^r\rho e^{-\frac{\rho^2}{2}}d\rho=1-e^{-\frac{r^2}{2}}, \tag{4.9}$$

where a further transformation into polar coordinates was used: $x_1=\rho\cos\theta$ and $x_2=\rho\sin\theta$.

Equation (4.9) shows that for *r* = 1, *P* = 39.35% of points are expected to be found within the 2-D SDE (dashed red ellipse in Figure 4.11). This level of confidence is usually insufficient, and instead of the SDE, error ellipses with confidence of $P = 95\%$ are typically used. By inverting eq. (4.9), the corresponding $r = \sqrt{-2\ln\left(1-P\right)} \approx 2.447$ (solid red ellipse in Figure 4.11).

As Figure 4.11 shows, there is an approximately 15-km location uncertainty at 95% confidence in the present dataset. The uncertainty area is extended in the E-W direction and approximately in the same direction as the relocation shift (blue dot in Figure 4.11). The relocation amount is smaller than the error ellipse, which suggests that the amount of relocation for this event was insignificant compared to the measurement error. Figure 4.12 shows another way for assessment of the location problem for the same event. In this figure, P-wave time misfits with respect to the regional travel-time model are shown for all stations recording this event. Each travel-time misfit Δt_i is shown by a segment in the direction of the back-azimuth to the corresponding station i, and the length of the segment equals $|\Delta t_i|$. Red lines indicate positive travel-time misfits $\Delta t_i > 0$ (suggesting that the source might be farther away from the station), and blue lines correspond to $\Delta t_i < 0$. Correlations of these errors with azimuths might indicate possible effects of geographical distribution of seismicity. The larger negative misfit (–2.1s) for station KLNJ with epicentral distance 342 km may be caused by a larger azimuthal gap.

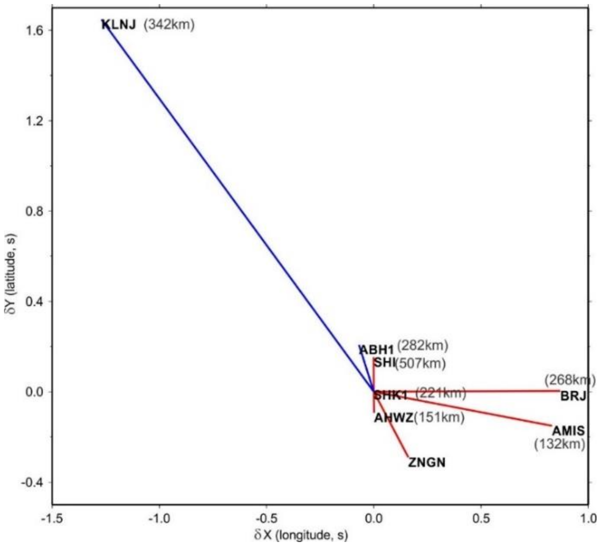

Figure 4.12. Travel-time misfits for each station recording event 1135452. Station codes and epicentral distances are labeled. The directions of the lines correspond to the directions to the stations used in relocation, and their lengths are proportional to the travel-time misfits. Red and blue lines indicate positive and negative travel-time misfits, respectively.

The relocation amount smaller than the 95% confidence interval and the combinations of travel-time misfits (red and blue lines in Figure 4.12) suggest that the source is indeed located (within measurement errors) close to the location reported in the catalogue.

Figures 4.13 and 4.14 show a similar Monte Carlo uncertainty analysis for event number 1137741. Because of the poorer coverage by seismic stations, the location uncertainty is much larger in this case. There is an over 100-km estimated location uncertainty (red ellipse) due to random time errors in this dataset. However, these estimates of the SDE and the 95% confidence ellipses are likely exaggerated by several outliers present in the data (green dots far from the main cluster in Figures 4.13), which are due to a small number of stations used for this event. The uncertainty area is extended in the NEE-SWW direction.The optimal relocation is located at north-east of original location. The relocation with relatively few stations and significant azimuthal gaps (Figures 4.12 and 4.13) can potentially be improved by detailed comparative analysis of the waveforms and improving the P-wave travel-time peaks t_i. Another improvement of this location could be made by using a more detailed travel-time model $T(x, y, z \mid x_i, y_i)$. Such a model can be obtained, for example, from travel-time tomography or by using regionally variable and/or anisotropic extension of the approximate time-field model in eq. (4.4).

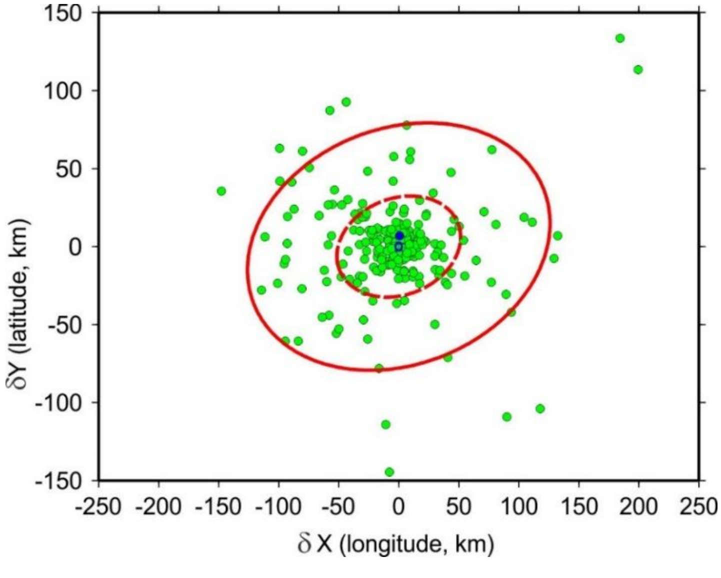

Figure 4.13. Evaluation of relocation uncertainty for event number 1137741. Symbols and lines are as in Figure 4.11.

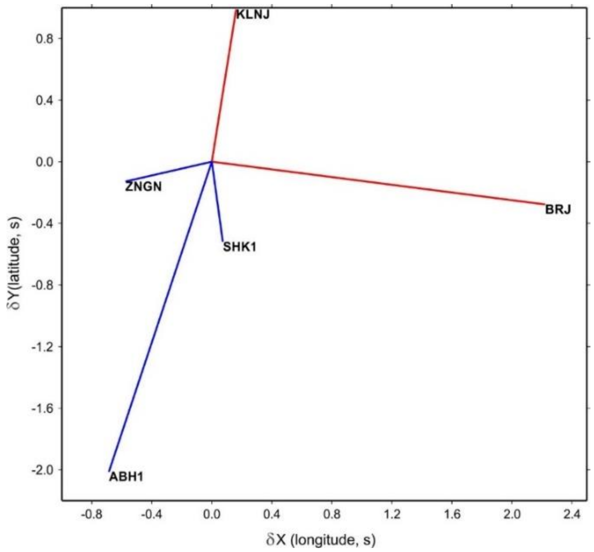

Figure 4.14. Travel-time misfits for each station recording event 1137741. The maximum time errors are +2.2 s and -2.1s for stations BRJ and ABH1, respectively. Lines and symbols are as in Figure 4.12.

4.5. Discussion and Conclusions

In this chapter, I performed a simple 2-D relocation of 592 events from in Zagros region by using a non-linear algorithm and a 1-D empirical model for travel times dependent on the source-receiver distances. The present event relocation results using picked P-wave travel times help to improve any further measurements of data analysis such as travel time tomography, and they provide significant geological information such as the origin time of the earthquake ruptures and their improved epicenters locations. However, the results can be improved in a number of aspects including improved quality control and travel-time picking, and also iteration of the relocation procedure with tomographic inversion of P-wave travel times. A more sophisticated probabilistic approach using 3-D velocity models could improve the accuracy of relocation results (chapter 8).

Most relocated earthquakes have horizontal spatial distributions in the range 10-25 km. The accurate relocations can provide us a better knowledge of seismicity pattern. Some of the relocated events suggest improved clustering near known mapped crustal faults. However, the information of depths is not inverted to provide a more detailed and accurate seismicity pattern. With the above improvements of the background travel-time model and relocation methods, the pattern of seismicity should definitely become more accurate, and it may suggest associations of the earthquakes with mapped or hitherto unmapped crustal faults.

CHAPTER 5

EMPIRICAL TIME–FREQUENCY RELATIONS FOR BODY S-WAVE SPECTRAL AMPLITUDES IN RIGAN AREA

This chapter describes a new method for deriving empirical time-frequency relations for body-wave seismic spectral amplitudes. Empirical distance- and frequency-dependent relations for body-wave spectral amplitude are extensively used in seismic regionalization and nuclear test monitoring, and these models are referred to as "standard models" below. This chapter proposes a much more accurate approach to such models. The approach is applied to the body S waves from Rigan area (chapter 2), but as argued in this chapter, it can be applied to much larger datasets from other areas. In addition, similar approaches can be used for other type of empirical amplitude models, such as for surface waves and coda.

The results of this chapter were published in the following papers:

- Safarshahi, M., and Morozov, I. B. (2021a). Robust empirical time-frequency relations for seismic spectral amplitudes, part 1: Application to regional S waves in southeastern Iran. Bulletin of the Seismological Society of America, **111**, 173-192, DOI: 10.1785/0120200172
- Safarshahi, M., and Morozov, I. B. (2021b). Robust empirical time-frequency relations for seismic spectral amplitudes, part 2: Model uncertainty and optimal parameterization. Bulletin of the Seismological Society of America, **111**, 193-205, DOI: 10.1785/0120200180

The copyright for these papers belongs to the Seismological Society of America, which allows authors to use their papers in their dissertations. The papers were modified and reformatted for inclusion in this dissertation. My contributions to the papers consisted in preparing the data, modeling, providing codes, participation in interpretation and writing.

The discussion in this chapter is rather extensive and organized as follows. In section 5.1, I describe the methodological difficulties of many existing standard models for seismic amplitudes. These problems originate in understanding the physical and mathematical meanings of the term “seismic attenuation”, the significance of the “frequency-dependent *Q*-factor”, separation of the different “attenuation effects”, and the “over-underdetermined character” of the inverse problems used for deriving standard models. The precise meanings of these terms are rarely considered in the literature, and they are considered in section 5.1.

In section 5.2, I develop a general parameterization for body-wave standard models and a general inverse method for them. A data-driven and physically meaningful parameterization for seismic-wave amplitudes is critical for formulating an accurate and stable standard model. Another key part of the proposed method consists in forming additional constraint equations to remove the biases observed within the model. By using different sets of constraints, the method also allows deriving the existing $A(t,f)$ models and $Q(f)$.

In section 5.3, I apply the new approach to the Rigan data. The most notable observation from this section is that after creating a robust model parameterization, *Q* values within the study area become frequency-independent and much higher (by over 20 times at frequencies near 1 Hz) than previously inferred by conventional analysis (Safarshahi et al., 2013). In subsections 5.3.1 and 5.3.2 I summarize the key findings, and in subsections 5.3.3 and 5.3.4 I give details of normalized source and site spectra and quantitative evaluation of the significance of the frequency-dependent *Q*-factor.

In section 5.4, I interpret the new standard model for Rigan area and point out some uncertainties inherent in interpreting similar models. Some of these uncertainties are conceptual (such as the differentiation between the source and receiver parameters kappa), and some are quantitative and related to the limited data coverage and data errors. These quantitative errors are measured in section 5.5.

In section 5.6, I propose an approach to parameterization of standard models for body-wave amplitudes that has also not been used before. Instead of using predefined mathematical forms of equations, the standard model is based on a statistical analysis of the obtained best-fit model for the given area. In section 5.7, I discuss the expected relation of this method to datasets of different types and volumes, and also implications for other studies. In particular, I show how the well-known standard model by Atkinson (2004) is reproduced as a special case of the approach in this study.

5.1. Introduction

Quantitative characterization of recorded seismic-wave amplitudes is among the key goals of seismic observations, and it is critical for estimating seismic hazard, measurement of attenuation, inverting for physical properties of earthquake and explosive sources, structure of the Earth, coda studies, constructing ground-motion prediction equations (GMPEs), and nuclear test monitoring. Empirical time and frequency dependencies of wave amplitudes are often referred to as "attenuation" in seismology (e.g., Castro et al., 1990; Atkinson, 2004). However, in physics, this term is understood more specifically, as hysteretic frictional phenomena within materials or damping in resonant systems. In this dissertation, I understand attenuation in this physical sense, and following Fisk and Phillips (2013a, 2013b), use the more general term "standard models" to describe the source-, site-, and particularly combined path and frequency dependencies of seismic amplitudes.

This chapter focuses on analyzing a general parameterization for time- (denoted t, or alternatively distance) and frequency- (f) dependent standard model $A(t,f)$ for S waves at local to regional distances. I use factorized time-frequency dependencies similar to those considered in many approaches, such as spectral decomposition, empirical Green's functions (EGF) (e.g., Trugman and Shearer, 2018), and GMPE. Although all these problems are closely related, spectral decomposition and EGF primarily focus on estimating the source and site spectra, whereas "standard models" mostly focus on the path and endpoint effects on wave amplitudes (e.g., Fisk and Phillips, 2013a, 2013b). In this chapter, my emphasis will be on reducing the mutual trade-offs between the Q factor, high-frequency site effects (kappa), parameters of geometrical spreading, and also on their relations to the selected form of the frequency-dependent Q (Morozov, 2008b). After evaluating the standard models, source and site spectra will also be estimated.

Ideally, the explicit mathematical form or computer code for calculating a time-frequency amplitude model should not be important as long as it accurately captures all significant features of the observed amplitude dependencies. Nevertheless, in practice, models used by different authors are often particular about their mathematical forms. These forms are motivated by theoretical considerations, simplicity, selections of inverse methods, and often by historic conventions evolved in various research or engineering areas. The commonly used parameterizations of wave amplitudes include power-law exponents of geometrical spreading (denoted ν here), parameters $f_{\max}$, κ and their distance dependences (in high-frequency spectral decay, or "kappa" studies), spatial, temporal, and "geometrical" attenuation coefficients (α, χ, and γ, respectively; Morozov, 2010a), t^* and Q (in body wave and coda studies), resonant frequencies f_0 and other site response parameters, the value of Q at 1 Hz (often denoted Q_0), and exponent η in the broadly used frequency dependence $Q\left(f\right)=Q_0 f^{\eta}$. The so-called "nonparametric" approaches (e.g., Castro et al., 1990; Oth et al., 2008, 2011) also utilize parameterizations of amplitudes by coefficients of polynomial spline functions in distance.

Atkinson (2012) summarized several forms of "parametric" standard models for seismic ground motion but noted that none of them achieves satisfactory data fitting at both local (< 80–100 km) and regional (> 100–150 km) distances. As shown in this chapter, the same problem occurs for "nonparametric" models across the transition between the local and regional distance ranges. These difficulties of the existing models are related to the common role of the frequency-dependent Q-factor in them. The Q (path effect) typically represents the key result of the inversion or the key parameter needed for isolating the source and/or site effects (e.g., Aki and Chouet, 1975; Castro et al., 1990; Edwards et al., 2008; Oth et al., 2008; Trugman and Shearer, 2018; Palmer and Atkinson, 2020). Most attenuation parameters (t^*, α, $f_{\max}$, κ, Q_{coda}) are explained by Q factors within portions of wave paths (e.g., Anderson and Hough, 1984; Ktenidou et al., 2014). However, the Q itself is only an intuitively defined phenomenological attribute of a seismic wave, and its meaning is strongly variable in different research areas (Morozov and Baharvand Ahmadi, 2015). As stated by Castro et al. (1990), in wave amplitude/attenuation studies, "… estimates of Q can only be obtained relative to some assumed geometrical spreading curve …" This observation means that this particular type of Q only represents the difference between the observed wave amplitudes and some reference model for them. This quantity contains the cumulative effect of the entire crustal structure, and its relation to physical attenuation is uncertain.

Because of reliance on assumed reference models and the empirical $Q(f)$, the key challenge of defining a standard model consists in achieving uniqueness, sufficient accuracy, and reliable physical meaning. As shown in this chapter, most existing models for $A(t,f)$ contain an important common problem, which can be described as "over-under-parameterization." This two-tier parameterization is expressed in a two- (or more) step approach to inversion. This problem can be seen even in pivotal studies, such as by Aki and Chouet (1975) and "parametric" approaches by Castro et al. (1990) and Atkinson (2004). In these models, an oversimplified form of reference geometrical spreading (i.e., an under-parameterized $A(t)$ dependence not fitting the data) is combined with a permissive (over-parameterized) model of arbitrarily frequency-dependent $Q(f)$. In most models (e.g., Aki and Chouet, 1975; Atkinson, 2004; Fisk and Phillips, 2013a, 2013b), the source and receiver couplings (usually a large number of parameters) are also excluded from the inversion for the geometrical spreading and $Q(f)$. Although the model turns out to be grossly under-parametrized and biased in its frequency-independent part, this bias is absorbed by Q values inferred independently at each measured frequency f. As a result of this two-step procedure, the bias caused by the assumed geometrical spreading is presented as an apparent $Q(f)$ with low $Q_0 = Q(1\ \text{Hz})$ and increasing with frequency. Such $Q(f)$ is found in practically all studies based on assumed geometrical spreading (e.g., Bowman and Kennett, 1991; Morozov, 2008b, 2010a; Morozov et al., 2018).

The key shortcoming of the tricky "over-under-parameterization" of standard models consists in excluding the basic case of elastic crustal and upper-mantle structure. For an elastic Earth with layering or velocity gradients, all amplitudes $A(t,f) \equiv A(t)$ are independent of f, and the measured attenuation should presumably equal $Q^{-1} = 0$. However, current models can practically never produce a $Q^{-1} = 0$. Because the actual geometrical spreading differs from $G(t) \propto t^{-1}$, single-station measurements based on Aki and Chouet's (1975) and similar approaches yield $Q(f) = Q_0 f$ (i.e., $\eta = 1$) in the elastic case, where $Q_0 < 0$ for ray focusing and $Q_0 > 0$ for defocusing (Morozov, 2008b, 2010a). Thus, a $Q(f)$ with $\eta \approx 1$ represents not as a Q-type attenuation but geometrical spreading $G(t) \propto A(f,t)\big|_{Q^{-1}=0}$ deviating from the assumed level (Morozov, 2008b). Conventionally, $Q(f)$ with $\eta > 0$ is attributed to "scattering attenuation" (Aki and Chouet, 1975). However, both of these interpretations are cumbersome for a layered elastic medium, because there are neither inelasticity nor Aki's (small-scale random) scattering in this case.

The missing zero-attenuation limit can be corrected by changing the parameterization of the path-related factor $A\left(f,t\right)\propto\exp\left[-\pi ftQ^{-1}\left(f\right)\right]$ to $\exp\left[-\chi\left(f\right)t\right]$, where $\chi\left(f\right)=\gamma+\pi fQ_e^{-1}$ is a two-parameter temporal attenuation coefficient, $\gamma=\chi\left(0\right)$ is the zero-frequency ("geometrical") attenuation, and Q_e measures the deviation from it ("effective Q" by Morozov (2008b, 2010a)). The conventional $Q(f)$ therefore equals $Q^{-1}\left(f\right)=\chi\left(f\right)/\left(\pi f\right)=c+d/f$ (where $c=Q_e^{-1}$ and $d=\gamma/\pi$). The latter form of frequency dependence was also used by Castro et al. (1990). This parameterization contains no singularity at $f\to 0$ and $Q^{-1}\to 0$, and it reveals another important elastic parameter γ. For these reasons, the $\chi(f)$ parameterization is stable and advantageous in practice (Morozov, 2008b, 2010a, 2010b).

When solving an "over-under-parameterized" inverse problem, the time/distance dependence of seismic amplitudes is underfitted during the first step of inversion whereas the Q part is overfitted during the second step. Model parameters related to frequency dependencies of amplitudes (Q_0, η, Q_c, κ, or f_{max}) mutually trade off, and they also trade off with parameters selected by convention, such as ν, γ, "prior" model, or model smoothness. This trade-off is difficult to measure in practical studies, but it is critical for understanding the meanings of the respective physical properties. In particular, the resulting $Q(f)$ trades off not only with the assumed value of ν (e.g., Kinoshita, 1994) but also with kappas, the entire source-receiver pattern in the data, and with equation weights applied in the inverse problems. Because the source-receiver distribution is unique to every dataset, I need to look for ways to exclude such trade-offs from final interpretation.

Despite the complex tangle of issues above, a robust inversion of wave amplitude data can be achieved by flexible parameterizations and rigorous quality control of the inverse problem. In this chapter, I perform such an inversion by integrating multiple broadly used parameterizations for $A(t,f)$. The chapter is organized as follows. In a previous analysis of these data, Safarshahi et al. (2013) used conventional methods and reported kappa and frequency-dependent Q values similar to those found in many other areas around the world. Thus, I expect that the methodology and key observations from these data should also be relevant to many other studies.

5.2. Method

To formulate a standard model for S-wave amplitudes in some study area, we should focus not on justifying a preferred mathematical expression but on finding a set of parameters sufficient for describing amplitude variations in the data. The mathematical form of the model is of secondary importance, but it is critical that: 1) the model captures all significant features of the data and 2) it makes no hypothetical assumptions such as an idealized body-wave spreading law, amplitudes monotonously decreasing with distance, scattering uniformly distributed within the crust and mantle, "smoothness" of amplitude dependences, proximity to known "prior" models, or even the intuitive relation $Q > 0$. With regard to requirement 2) above, the approach of this chapter is sharply different from conventional models (Aki and Chouet, 1975; Atkinson, 2004; Fisk and Phillips, 2013a, 2013b).

The definition of a frequency-dependent standard model for body S waves contains several aspects described in the following subsections. In subsection 5.2.1, I define the general functional form comprising most of the existing models as special cases. In subsection 5.2.2, I describe the most critical part of this model and compare it to existing non-parametric and parametric approaches to geometrical-spreading. In subsection 5.2.3, I outline the structure of the inverse problem. In subsection 5.2.4, I explain the general use of constraints in standard-model problems and specify the constraints preventing spurious spatial patterns of model parameters and data errors. Mathematical details of inversion with explicit constraints are given in Appendix A.

5.2.1. Generalized standard model

For given wave, let us denote its amplitude corrected for the source and receiver responses by symbol Φ. This amplitude represents the result of an idealized experiment with both the source amplitude and receiver response equal to one. Quantity Φ should only be dependent on the structure and physical properties of the Earth in the study area, and this dependence is called the standard model. In this dissertation, similar to many studies, the standard models is considered as only a function of the travel time t and frequency f, denoted $\Phi(t,f)$. Despite the variety of existing functional forms and notations for $\Phi(t,f)$ (e.g., Aki and Chouet, 1975; Anderson and Hough, 1984; Castro et al., 1990; Mayeda, 1993; Atkinson, 2004; Graizer, 2017), all of them represent the same physical property, which is the source- and receiver-normalized, time and frequency-dependent wave amplitude recorded from a given source at a given recording site:

$$\Phi\left(t, f\right) = \frac{A\left(t, f\right)}{A_{SR}\left(f\right)}, \qquad \text{where} \qquad A_{SR}\left(f\right) \equiv B\left(f/f_c\right) A_S\left(f\right) A_R\left(f\right) e^{-s\left(f\right)}. \tag{5.1}$$

Here, $A(t,f)$ is a smooth function approximating the amplitudes recorded in the appropriate component of ground motion, $B\left(\bar{f}\right) = \bar{f}^2 \big/ \left(1 + \bar{f}^2\right)$ is the normalized Brune's (1970) ground-acceleration spectrum, f_c is the source corner frequency, $\bar{f}$ is the normalized frequency, $A_S(f)$ denotes some additional variation of the normalized source spectrum, $A_R(f)$ is the receiver response spectrum, and $s(f)$ is an additional spectral shaping function. This function is used as a correction for unknown shapes of $A_R(f)$ and $A_S(f)$ during the linearized inversion for $\Phi(t,f)$. In this chapter, I use two functions $s(f)$ associated with the sources, but these functions turn out to be close and attributable to either $A_R(f)$ and $A_S(f)$ (section 5.3). Measurement of $A(t,f)$ from the data may include some types of averaging or, for example, evaluation of response spectra or the peak ground acceleration (PGA).

By including in eq. (5.1) contributions from source number j and receiver number i, let us consider the following generalized form for $\Phi(t,f)$:

$$\Phi_{ij}\left(t_{ij}, f\right) = S_j R_i G\left(t_{ij}\right) e^{-\pi\kappa_{Sj}\left(f - f_0\right)} e^{-\pi\kappa_{Ri}\left(f - f_0\right)} e^{-\pi f t^*}. \tag{5.2}$$

In this expression, $t^* = q t_{ij}$ is the cumulative attenuation along the wave path, $q \equiv 1/Q$ is the inverse quality factor, S_j is the source amplitude relative to spectrum $A_S(f)$ in eq. (5.2), R_i is the frequency-independent receiver site effect, G is the empirical geometrical spreading, and parameters κ and f_0 are explained below. With the above normalization of $A_S(f)$, the source and receiver amplitudes in eq. (5.2) equal

$$S_j = \frac{f_c^2}{4\pi\rho\beta^3}, \qquad \text{and} \qquad R_i = R_{\theta\phi} A_{FS} A_{red}, \tag{5.3}$$

where β is the shear wave velocity, ρ is the density near the source, $R_{\theta\phi}$ is the radiation pattern, A_{FS} is the receiver site amplification due to the free surface, and A_{red} is the amplitude reduction factor (Brune, 1970).

Model parameters in eq. (5.2) are differentiated exclusively by separating the path and endpoint effects and by the functional dependencies on variables t and f. The geometrical-spreading factor $G(t)$ depends only on the travel time t_{ij}, and it represents the "elastic" limit of $\Phi_{ij}(t,f)$ at $f \to 0$ or ($\kappa \to 0$, $Q^{-1} \to 0$). The exponential factors containing kappas denote the frequency-only dependencies, which are the high-frequency site effect κ_{Ri} for each receiver i (Anderson and Hough, 1984) and its (possible) source counterpart κ_{Sj}. Similarly to κ_R, parameters κ_S can contain effects of the Q and/or scattering within the near-source zone (Parolai, 2018). The factors containing kappas in eq. (5.2) are normalized so that they equal one at some reference frequency $f = f_0$. With $f_0 = 0$ and $\kappa_S = 0$, the conventional definition of $\kappa = \kappa_R$ (at zero distance) is obtained (Anderson and Hough, 1984). Note that factors S_j and R_i absorb any variations of scaling caused by selecting different f_0.

Parameters $A_R(f)$, R_i, and κ_R are mutually related and represent the local (path-independent) receiver site response. Similarly, $A_S(f)$, S_j, and κ_S constitute the source spectra. Because of mutual relations, these quantities should be carefully differentiated in eqs. (5.1) and (5.2). If taking parameter κ purely empirically, great uncertainty in its physical meanings is observed, with dependencies on distances, back-azimuths, sensor orientations, source and site properties, and measurement methods (Ktenidou et al., 2014). To render simple and unique physical meanings to κ_R and κ_S in eq. (5.1), we can interpret them as parameters of amplitude responses for the site and source, respectively. Because parameters S_i, R_j, κ_S, and κ_R are extracted from the spectra $A_S(f)$ and $A_R(f)$, these spectra must be normalized so that

$$\langle \ln A_S \rangle = \langle \ln A_R \rangle = 0, \qquad \text{and} \qquad \left\langle \frac{d \ln A_S}{df} \right\rangle = \left\langle \frac{d \ln A_R}{df} \right\rangle = 0, \qquad (5.4)$$

where the angle brackets represent the average values.

Finally, the factor containing q in eq. (5.2). is defined as the frequency-dependent path effect proportional to the product *ft* (number of wave periods). Its possible frequency dependence can be tightly constrained from the following, very general considerations. Eq. (5.2) can be understood as a Taylor series with respect to *t*, *f*, and *ft*:

$$\ln\Phi\left(t,\, f\right) = const + \ln G\left(t\right) - \pi\left(\kappa_{Sj} + \kappa_{Ri}\right) f - \pi qft \,, \qquad (5.5)$$

which is the perturbation-theory approximation (Morozov, 2010a). Thus, my restriction to a frequency-independent q (or Q) follows from the recognition that frequency-dependent effects are weak compared to elastic ones (Morozov, 2010a). For similar reasons, κ is also usually viewed as frequency-independent. If higher orders in f are indicated by the data, second-order terms $-\pi\left(\kappa'_{Sj} + \kappa'_{Ri}\right) f^2$ (i.e., frequency-dependent kappas) may need to be considered in eq. (5.5). Third-order terms $-\pi q' f^2 t$ (i.e., the frequency-dependent Q) would be even more redundant, particularly if considering regional variations of q (i.e., its dependencies on t). Subsections 5.3.3 and 5.3.4 contain a quantitative evaluation of such terms for this dataset.

The functional form for $\Phi_{ij}(t,f)$ (eq. (5.2)) includes most time-frequency relations used in the literature. Generally, $G(t)$ may contain the standard dependencies $G\left(t\right) \propto t^{-\nu}$, optionally within several source-receiver distance ranges and combined with the spatial attenuation coefficient by Bowman and Kennett (1991), coda amplitude exponent by Mayeda (1993), or “geometrical attenuation” $\exp\left(-\gamma t\right)$ by Morozov (2008b, 2010a). This parametrization is consistent with those by Aki and Chouet (1975), Atkinson (2004), and many other researchers, but extends them by treating ν as variable in the inversion. With allowing multiple variables, $G(t)$ is hybrid between the “non-parametric” and “parametric” models by Castro et al. (1990). In time-domain measurements, eq. (5.2) can be used for modeling seismic coda envelopes (Aki and Chouet, 1975; Morozov, 2010a; Jhajhria et al., 2017). In GMPE applications, eq. (5.2) can also be used with slightly different forms of $G(t)$ (Atkinson and Boore, 2006; Graizer, 2017; Kiuchi et al., 2019). Factors containing κ_R correspond to kappa studies (Anderson and Hough, 1984; Ktenidou et al., 2014; Parolai, 2018). Source-end values $\kappa_S > 0$ can also describe a source rupture occurring slightly slower than the idealized displacement across the entire fault area (Beresnev, 2019a).

Mayor et al. (2018) also measured a somewhat different $\kappa = t^*$ for coda waves by using a fixed t equal the coda lapse time. Distance dependencies of κ (Anderson, 1991) are not included in eq. (5.2) because such dependencies should be contained in the path-attenuation parameter q. In a spatially variable (e.g., tomographic) model, $G(t)$ and q should depend on coordinates (x,y) along the ray path. Parameters κ_R and κ_S can also be viewed as parts of the spatially-variable q within the receiver- and source-end blocks of the ray path.

The key difference of eq. (5.2) from most existing models is in using the data at all frequencies simultaneously and inverting for all parameters including κ, q, S_j, and R_i in joint inversion. The only exceptions are the normalized spectra $A_S(f)$ and $A_R(f)$ (eq. (5.1)), which are inverted for separately, after solving for the standard model. The complete $A_S(f)$ and $A_R(f)$ spectra can readily be included in joint inversion, such as done, for example, by Edwards et al. (2008). However, for more interpretable and better constrained results, I include in the main inversion only the key parameters of these spectra, which are the respective amplitudes S_j and R_i, and average spectral slopes κ_S and κ_R.

As illustrated in section 5.2, correlated variations of S_j and R_i and data errors are significant and may exceed the effects of κ and q. Therefore, strict error control is required for reliable inversion (subsection 5.2.4). The second major difference of the present method is that all available frequencies are considered together, and therefore the value of q is constrained more strongly than the conventional $Q(f)$. At the same time, a significant trade-off between parameters q, κ, S_i and R_j is also recognized (section 5.5.2).

5.2.2. Effective geometrical spreading

The frequency-independent amplitude dependence $G(t)$ in eq. (5.2) is not truly “geometrical spreading” in the sense of some simple mathematical model of spreading wavefronts. For the effective (empirical) function $G(t)$ in eq. (5.2), I use a five-parameter form (Figure 5.1a) encompassing several existing distance-range dependencies in the literature (e.g, Aki and Chouet, 1975; Atkinson, 2004; Drouet et al., 2008; Fisk and Phillips, 2013a, 2013b). This form of $G(t)$ can be readily recognized in the data by a local amplitude minimum at travel-time t_1

followed by a possible local maximum or inflexion at time $t_2 > t_1$ (Figure 5.1a). Algebraically, the frequency-independent amplitude in Figure 5.1a can be represented as

$$G(t) = \left(\frac{t}{\tau_1}\right)^{-\nu_{\text{near}}\psi_{\text{near}}(t)} \left(\frac{t}{\tau_2}\right)^{-\nu_{\text{far}}\psi_{\text{far}}(t)} e^{r\psi_r(t)}, \tag{5.6}$$

where r, ν_{near}, and ν_{far} are model parameters to be determined by data fitting, and $\psi_{\text{r}}(t)$, $\psi_{\text{near}}(t)$, and $\psi_{\text{far}}(t)$ are the respective basis functions (Figure 5.1b). Similar to many studies (e.g., Castro et al., 1990; Anderson, 1991; Atkinson, 2004; Fisk and Phillips, 2013a, 2013b), I could also use distances $X_1 = \beta t_1$ and $X_2 = \beta t_2$ (where β is the average S-wave velocity) for partitioning the geometrical spreading range.

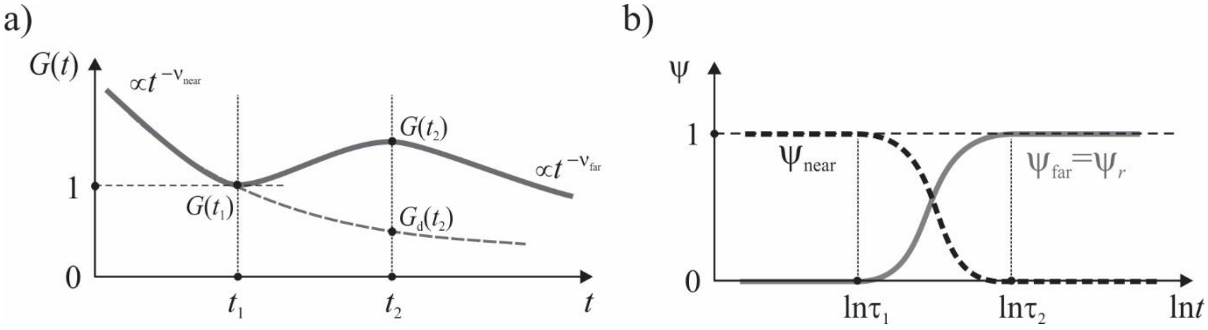

Figure 5.1. Geometrical spreading $G(t)$ parameterized by extremal times t_1 and t_2, near- and far-distance amplitude-decay exponents ν_{near} and ν_{far}, and relative-amplitude exponent r: a) schematic form of $G(t)$ showing the near-and far-distance asymptotes and extrema at travel times t_1 and t_2 (labels); b) basis functions in eq. (5.6) (gray and dashed lines and labels). In plot a), $G_d(t_2)$ denotes the amplitude extrapolated to t_2 by the power law from times $t < t_1$.

The above parameterization for $G(t)$ is selected purely empirically, to ensure that the model captures all important observations in the data. As it will be shown in section 5.3, a significant increase in the amplitudes is indeed seen across a relatively short interval $[t_1, t_2]$ in Rigan-area data. To illustrate that such amplitude variation is not unique to these data, Figure 5.2 shows S-wave amplitudes from an event within the Guerrero subduction zone (Mexico). These data are from Figure 5 by Castro et al. (1990), which was modified by normalizing all amplitudes by their average levels within 100-km epicentral distances and overlaying all frequency bands in one plot.

In the nonparametric spectral decomposition (e.g., Castro et al., 1990; Oth et al., 2011), amplitude decays are treated as independent at each frequency but smooth across the entire distance range (lines in Figure 5.2a). However, because of this required smoothness, the estimated amplitude trends are strongly affected by the single data point beyond 120 km (Figure 5.2a). If not assuming a uniform smoothness of amplitudes, the same data suggest a steeper and nearly frequency-independent amplitude decrease to about 100 km and a relative amplitude increase or plateau beyond this distance (black lines in Figure 5.2b). Such a plateau or small amplification in $G(t)$ are also present in "trilinear" distance dependencies by Atkinson (2004, 2012) and also in nonparametric attenuation curves by Oth et al. (2008).

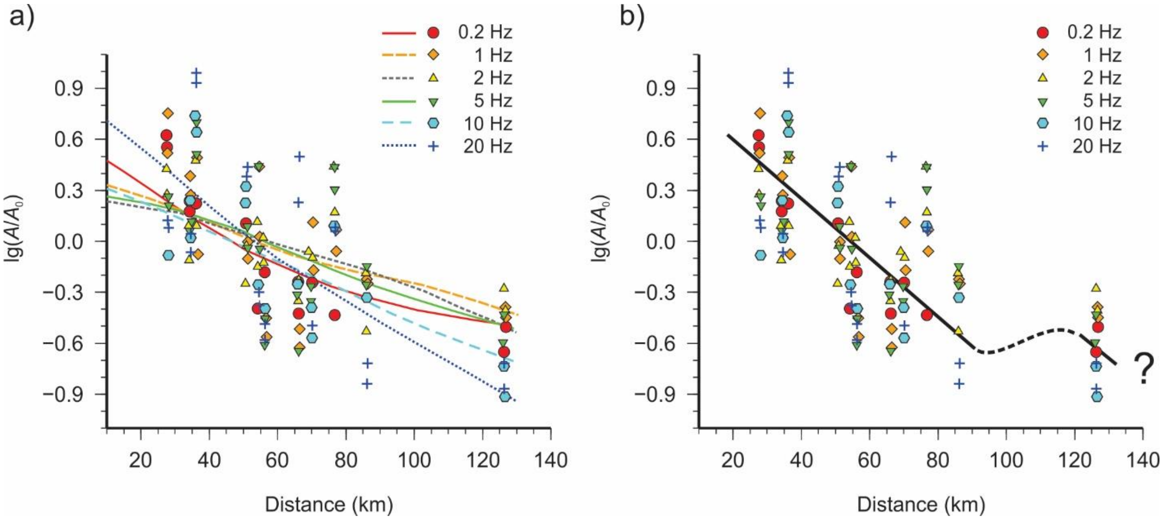

Figure 5.2. Distance dependence of logarithms of normalized S-wave amplitudes from the 25 April 1989 event recorded at stations along the Guerrero subduction zone in Mexico ($M_s = 6.9$; data from Figure 5 in Castro et al. (1990)): a) spectral amplitudes within six frequency bands (labeled in the legend) and non-parametric models for them by Castro et al. (1990) (lines); b) the same data points with an alternate, frequency-independent distance dependence (black lines).

Theoretically, non-monotonous amplitude amplifications corresponding to $r > 0$ in eq. (5.6) are expected beyond about 80 to 150-km distances. Such amplifications should come from the onsets of near- and post-critical reflections from the Moho (hence my notation of r). For Sg/Lg waves, such effects due to layered crustal structure were modeled by Bowman and Kennett (1991) and other authors. These reflections are most coherent at lower frequencies, and therefore they are also seen by the increases in the values of empirical κ near 100–120 km

(Anderson, 1991). Such effects can be included in the frequency-dependent geometrical spreading (Yang et al., 2007), which is, however, not considered in this chapter.

The basis functions $\psi_r(t)$, $\psi_{\text{near}}(t)$, and $\psi_{\text{far}}(t)$ in eq. (5.6) are selected so that function $G(t)$ and its derivatives are continuous across the entire time interval, is of power-law forms for $t < t_1$ and $t > t_2$, and shows extrema or inflections at times t_1 and t_2 (Figure 5.1a). The values of t_1 and t_2 are determined by inspecting the amplitude-decay curves prior and after the inversion for $G(t)$ (section 5.3). To match the times t_1 and t_2 observed in the data, the characteristic times τ_1 and τ_2 are determined by solving equation $d\ln G(t)/d\ln t = 0$, which should have two roots located at $t = t_1$ and t_2 (Figure 5.1a). The resulting values of τ_1 and τ_2 are close to t_1 and t_2 respectively, but slightly shifted from them.

For practical characterization of the shape of $G(t)$ in eq. (5.6), it is convenient to use values directly seen in the time-amplitude plots: the power-law exponents ν_{near}, ν_{far}, and inflection or extrema times t_1 and t_2. To visualize the value of r, it is convenient to use the amplitude ratios measured from the data, for example (Figure 5.1a):

$$b_{21} = \frac{G(t_2)}{G(t_1)} \quad \text{and} \quad b_{22} = \frac{G(t_2)}{G_d(t_2)} = G(t_2)\left(\frac{\tau_1}{t_2}\right)^{\nu_{\text{near}}}. \tag{5.7}$$

Here, $G_d(t_2)$ is the “direct-wave” amplitude that would have been observed if the near-distance power law (at $t < t_1$) continued to time t_2. Quantity b_{21} in eq. (5.7) is the ratio of the largest and smallest amplitudes across the interval $[t_1, t_2]$, and b_{22} can be interpreted as the amplification of the “direct wave” by reflections and other waves at time t_2 (Figure 5.1a).

5.2.3. Linear forward model and inverse

Similar to kappa and Q studies and for consistency with the exponential parameterization in eq. (5.2), the selected frequency intervals in the data should be sufficiently broad, contain consistent spectral slopes $\partial^2(\ln\Phi)/(\partial t\partial f)$, and be unaffected by near-surface resonances (Parolai, 2018; Pilz et al., 2019). To form a linear inverse problem for parameters S_j, R_i, ν_{near}, ν_{far}, r, κ_R, κ_S, and q (eq. (5.2)), I divide the observed amplitudes by the normalized source and receiver spectra in eq. (5.1): $a_{ij} = A_{ij}^{\text{obs}}(t, f) / A_{SR}(f)$ and combine all model variables in a model vector

$$\mathbf{m} \equiv \left(\left\{ \ln S_j \right\} \quad \left\{ \ln R_i \right\} \quad \kappa_S \quad \kappa_R \quad \nu_{\text{near}} \quad \nu_{\text{far}} \quad r \quad q \right)^T, \tag{5.8}$$

where the first two elements are groups of logarithms of all source and receiver factors. Taking logarithms of eqs. (5.2) and (5.6) gives

$$\begin{aligned} \ln a_{ij}(f) = \ln S_j + \ln R_i - \\ - \pi(f - f_0)\kappa_S - \pi(f - f_0)\kappa_R - \\ - \psi_{\text{near}}(t_{ij})(\ln t_{ij} - \ln \tau_1)\nu_{\text{near}} - \psi_{\text{far}}(t_{ij})(\ln t_{ij} - \ln \tau_2)\nu_{\text{far}} + \\ + \psi_{\text{r}}(t_{ij})r - \pi f t_{ij} q, \end{aligned} \tag{5.9}$$

where t_{ij} is the travel time from source j to receiver i. These equations can be written in matrix form:

$$\mathbf{d} = \mathbf{Lm}, \tag{5.10}$$

where matrix **L** consists of the coefficients with which the above variables enter the right-hand side of eq. (5.9). The data vector **d** consists of all values of $\ln a_{ij}(f)$ selected for inversion.

The linear inverse problem in eq. (5.10) usually contains more equations than unknowns (202 vs. 35 in this dataset), and therefore it has to be solved in an approximate sense. Such approximate solutions are often obtained by minimizing some data-misfit norm (Menke, 1984). However, it is difficult to construct a single norm representing all model-quality criteria for a given dataset. The approximate inverse of eq. (5.10) is also non-unique because variables $\ln R_i$ trade off with $\ln S_j$, variables ν trade off with spatial patterns of $\ln R_i$ and $\ln S_j$, and variables κ trade off with q. Once these issues are noted for the specific dataset, they can be resolved by requiring that together with eq. (5.10), the model satisfies some additional constraints related to the volume and structure of the dataset. These constraints can also be written in matrix form:

$$\mathbf{Bm} = \mathbf{c}\,. \tag{5.11}$$

Different selections of matrix **B** and vector **c** allow implementing multiple derivations of standard models. Some of these selections are described in section 5.7 (for existing models) and subsection 5.2.4 (for my model).

The procedure for the least-squares inversion of linear eq. (5.10) while exactly satisfying the constraint eq. (5.11) is described in Appendix A. By using vector **m** (eq. (5.8)) obtained from this inversion, the predicted data for all earthquakes, stations, and frequencies can be calculated as $\hat{\mathbf{d}} = \mathbf{Lm}$. Finally, data errors (misfits, or residuals) are obtained as

$$\boldsymbol{\varepsilon} = \mathbf{d} - \hat{\mathbf{d}}\,. \tag{5.12}$$

5.2.4. Constraints on standard-model quality

Figures 6 to 9 by Atkinson (2012) and my results for Rigan data in section 5.3 show that after conventional multi-step inversions of equations (5.10), site parameters $\ln R_i$ and data errors exhibit intervals of systematic correlations with epicentral distances. Although hypothetically possible, such correlations are unlikely in real data and suggest that propagation of errors has occurred due to inaccurate weighting of the least-squares inverse. To remove such spurious correlations of $\ln R_i$ with epicentral distances, I selected four distance ranges $0 < x_i \le 100$ km, $100 < x_i \le 150$ km, $150 < x_i \le 200$ km, and $x_i > 200$ km, where x_i is the distance to the nearest earthquake for receiver i. For each of these ranges, I include in matrix **B** and vector **c** eight rows representing the following equations for $\ln R_i$:

$$\sum_{i \in \text{distance range}} \ln R_i = 0\,, \quad \text{and} \quad \sum_{i \in \text{distance range}} \left(x_i - \langle x \rangle\right) \ln R_i = 0\,, \tag{5.13}$$

where $\langle x \rangle$ denotes the average of x_i within this distance range. These constraints mean that no constant terms and no correlations with x are expected for $\ln R_i$ within each of these distance intervals. Note that the first of these equations also removes the general $\ln R_i \to \ln R_i + c$ invariance described in the preceding subsection.

After including constraints (5.13), the rank of the matrix that needs to be inverted in order to obtain the constrained solution (this matrix is denoted **K** in Appendix A), was still strongly deficient for the present dataset. This rank deficiency arose because of almost all stations recording only a single earthquake. By experimenting with the inverse, I found that the correct rank could be obtained by adding constraints $\kappa_R = 0$ for all receivers, or simply by removing variables κ_R from the model vector **m** (eq. (5.8)). However, one of the uncertainties of κ_R is fundamental and appears in any dataset. This common uncertainty relates to the invariance of eq. (5.2) with respect to shifting all kappas as

$$\kappa_R \to \kappa_R + \bar{\kappa} \quad \text{and} \quad \kappa_S \to \kappa_S - \bar{\kappa} , \tag{5.14}$$

with an arbitrary $\bar{\kappa}$. After application of these constraints, only two parameters κ remained. Thus, with the present dataset and because of the ambiguity (5.14), kappa values can be attributed to either the sources (as κ_S) or to the corresponding receivers (as κ_R), or shared among them (section 5.3). By taking $\kappa_S \equiv 0$, the conventional interpretation is obtained (Anderson and Hough, 1984).

With the above constraints imposed, the linear system was still lacking one constraint, which was again due to the limited ray coverage causing trade-off between parameters κ_S for the two earthquakes (or with κ_R if considered). To remove this trade-off, I hypothesize that the two kappas are proportional to the characteristic times of the earthquakes $\tau_c = 1/f_c$, where f_c is the corner frequency. This hypothesis appears to be reasonable if viewing κ_S as a part of the source spectrum (Beresnev, 2019a) because in this case, τ_c is the only time scale (or spatial dimension) of the source zone. Although the source-kappa interpretation is generally not favored (Frankel, 2019), it is viable in many cases (Beresnev, 2019b) and cannot be excluded for the present data. For the two earthquakes, the proportionality $\kappa_S \propto \tau_c$ can be written as one equation in matrix **B**:

$$f_{c1}\kappa_{S1} - f_{c2}\kappa_{S2} = 0 . \tag{5.15}$$

Alternate forms of constraints on kappa values can also be imposed, such as $\kappa_{S1} = \kappa_{S2}$, or setting $\kappa_{S1} = \kappa_{S2} = 0$ and using a common κ_R for all receivers. These selections lead to only minor differences in the results and are not shown here.

The above constraints yielded matrix **B** (eq. (5.11)) with $N_\lambda = 9$ rows, which allowed performing an initial inversion by the method in Appendix A. However, further examination of the resulting data errors at higher frequencies showed that the errors still contained correlations with source-receiver distances similar to those shown in subsection 5.7.1. To remove such spurious correlations, I added two more pairs of constraint equations in matrix **B** and vector **c**. These equations are similar to eq. (5.13) and require that data errors do not correlate with distances x_i within ranges $x_i < 100$ km and $x_i > 100$ km:

$$\sum_{i \in \text{distance range}} \left(d_i - \hat{d}_i \right) = 0 , \qquad \text{and} \qquad \sum_{i \in \text{distance range}} \left(x_i - \langle x \rangle \right) \left(d_i - \hat{d}_i \right) = 0 . \tag{5.16}$$

As mentioned in the preceding subsection, these equations can be alternately implemented by carefully constructed data weights depending on distances x_i. Finally, all of the above constraints allowed obtaining a good-quality solution described in the following section.

5.3. Results

By using all spectral amplitudes within the selected frequency ranges as vector **d** in eq. (5.10), the resulting best-fitting models **m** for the transverse, radial, vertical, H2C, and 3C amplitudes are shown in Tables 5.1, 5.2, 5.3, and 5.4. In these tables, for each model parameter, I show the optimal values obtained by solving eqs. (5.10) and (5.11) and also their 90% confidence ranges. These confidence ranges were obtained by data bootstrapping described in 5.5.2.

The principal objective of this chapter is in ensuring consistency of the path- and endpoint-related standard model $\Phi_{ij}(t,f)$ (eq. (5.2)). In the following subsections, I therefore start from quality control and then describe the resulting time-frequency dependencies $\Phi(t,f)$. Once the $\Phi_{ij}(t,f)$ model is determined and assuming that it extends to the entire observation frequency band, the source and receiver site spectra are estimated by solving another linear inverse problem for ln$A$ data residuals, similar to Castro et al. (1990) and other authors. This inversion is relatively straightforward and given in subsection 5.3.3.

Table 5.1. Optimal values and 90% confidence ranges[1] of source- and path-related model parameters for single-component S-wave amplitudes.

	Transverse-component		**Radial-component**		**Vertical-component**	
parameter	***value***	***range***	***value***	***range***	***value***	***range***
$\ln C_1$	3.27	3.19 – 3.35	3.28	3.20 – 3.35	2.91	2.85 – 2.98
$\ln C_2$	2.06	1.92 – 2.22	1.93	1.79 – 2.06	1.39	1.26 – 1.51
κ_1 (s)	0.051	0.047 – 0.055	0.044	0.041 – 0.048	0.006	0.003 – 0.009
κ_2 (s)	0.032	0.030 – 0.035	0.028	0.026 – 0.030	0.004	0.002 – 0.006
ν_{near}	1.77	1.64 – 1.89	1.60	1.49 – 1.73	1.21	1.11 – 1.32
ν_{far}	2.52	2.21 – 2.83	2.38	2.08 – 2.67	1.99	1.99 – 2.51
r	1.17	1.03 – 1.30	1.02	0.90 – 1.15	0.89	0.78 – 1.01
q, 10^{-4}	2.39	1.19 – 3.52	2.56	1.42 – 3.74	6.41	5.40 – 7.40
b_{21}	3.5	3.1 – 4.0	2.7	3.4 – 3.0	2.6	2.3 – 2.9
b_{22}	5.4	4.7 – 6.2	3.9	3.9 – 5.1	3.5	3.1 – 4.0

[1]) Estimation of statistical confidence ranges is described in subsection 5.5.2.

Table 5.2. Optimal values and 90% confidence ranges[1] of estimated model parameters for receiver site coupling.

	Transverse-component		**Radial-component**		**Vertical-component**	
parameter	***value***	***range***	***value***	***range***	***value***	***range***
$\ln R_1$	0.22	-0.04 - 0.47	0.44	0.20 - 0.68	0.11	-0.13 - 0.33
$\ln R_2$	-0.38	-0.65 - -0.12	-0.68	-0.94 - -0.43	-0.63	-0.87 - -0.41
$\ln R_3$	0.13	-0.07 - 0.32	0.21	0.01 - 0.40	0.23	0.07 - 0.40
$\ln R_4$	0.4	0.21 - 0.58	0.29	0.11 - 0.46	0.37	0.21 - 0.52
$\ln R_5$	-0.18	-0.41 - 0.05	-0.13	-0.37 - 0.09	-0.28	-0.48 - -0.08
$\ln R_6$	0.13	-0.03 - 0.29	0.09	-0.06 - 0.25	0.19	0.06 - 0.33
$\ln R_7$	-0.05	-0.29 - 0.18	-0.06	-0.30 - 0.17	-0.32	-0.53 - -0.11
$\ln R_8$	0.28	0.03 - 0.52	0.33	0.09 - 0.56	0.42	0.21 - 0.63
$\ln R_9$	0.54	0.30 - 0.76	0.45	0.24 - 0.66	0.47	0.27 - 0.66
$\ln R_{10}$	-0.27	-0.48 - -0.07	-0.31	-0.52 - -0.10	-0.3	-0.49 - -0.13
$\ln R_{11}$	0.09	-0.15 - 0.33	-0.22	-0.45 - 0.00	0.2	-0.01 - 0.40
$\ln R_{12}$	0.01	-0.28 - 0.29	0.2	-0.07 - 0.47	0.23	-0.03 - 0.47

$\ln R_{13}$	-0.17	-0.39 - 0.05	-0.07	-0.29 - 0.14	-0.28	-0.49 - -0.08
$\ln R_{14}$	-0.42	-0.65 - -0.20	-0.29	-0.51 - -0.09	-0.1	-0.29 - 0.09
$\ln R_{15}$	-0.04	-0.21 - 0.14	-0.12	-0.29 - 0.04	0.29	0.13 - 0.44
$\ln R_{16}$	0.05	-0.02 - 0.13	0.04	-0.03 - 0.11	0.08	0.02 - 0.15
$\ln R_{17}$	0.03	-0.14 - 0.20	0.27	0.11 - 0.43	0.13	-0.02 - 0.27
$\ln R_{18}$	1.03	0.83 - 1.22	1.3	1.11 - 1.50	0.83	0.66 - 1.00
$\ln R_{19}$	0.12	-0.13 - 0.37	0.07	-0.17 - 0.30	0.21	-0.01 - 0.43
$\ln R_{20}$	-0.04	-0.24 - 0.15	0.07	-0.12 - 0.25	-0.06	-0.23 - 0.11
$\ln R_{21}$	-0.05	-0.29 - 0.18	-0.12	-0.35 - 0.10	-0.05	-0.26 - 0.15
$\ln R_{22}$	-0.04	-0.28 - 0.19	-0.07	-0.31 - 0.17	-0.3	-0.52 - -0.11
$\ln R_{23}$	-0.45	-0.64 - -0.25	-0.61	-0.79 - -0.43	-0.56	-0.73 - -0.39
$\ln R_{24}$	0.2	-0.05 - 0.44	0.29	0.07 - 0.50	0.2	-0.00 - 0.39
$\ln R_{25}$	-0.26	-0.43 - -0.11	-0.2	-0.35 - -0.05	-0.17	-0.31 - -0.03
$\ln R_{26}$	0.04	-0.19 - 0.27	-0.08	-0.31 - 0.14	0.05	-0.16 - 0.25
$\ln R_{27}$	-0.9	-1.15 - -0.65	-1.08	-1.32 - -0.85	-0.96	-1.18 - -0.76

[1]) Estimation of statistical confidence ranges is described in subsection 5.5.2.

Table 5.3. Optimal values and 90% confidence ranges[1] of source- and path-related model parameters for multicomponent S-wave amplitudes.

	H2C amplitudes		**3C amplitudes**	
parameter	***value***	***range***	***value***	***range***
$\ln C_1$	2.62	2.55 – 2.70	3.82	3.76 – 3.89
$\ln C_2$	2.37	2.24 – 2.51	2.49	2.37 – 2.61
κ_1 (s)	0.049	0.045 – 0.052	0.028	0.025 – 0.031
κ_2 (s)	0.031	0.028 – 0.033	0.018	0.016 – 0.020
ν_{near}	1.70	1.59 – 1.82	1.49	1.39 – 1.59
ν_{far}	2.44	2.16 – 2.73	2.22	1.97 – 2.48
r	1.10	0.98 – 1.23	1.06	0.94 – 1.17
q, 10^{-4}	2.36	1.24 – 3.51	5.39	4.41 – 6.38
b_{21}	3.3	2.9 – 3.7	3.1	2.8 – 3.5
b_{22}	5.0	4.4 – 5.7	4.5	4.0 – 5.0

[1]) Estimation of statistical confidence ranges is described in subsection 5.5.2.

Table 5.4. Optimal values and 90% confidence ranges[1] of estimated model parameters for receiver site coupling.

	H2C amplitudes		**3C amplitudes**	
parameter	***value***	***range***	***value***	***range***
lnR_1	0.36	0.11 - 0.59	0.28	0.06 - 0.50
lnR_2	-0.52	-0.78 - -0.28	-0.6	-0.82 - -0.38
lnR_3	0.13	-0.06 - 0.32	0.23	0.07 - 0.39
lnR_4	0.34	0.18 - 0.51	0.3	0.15 - 0.45
lnR_5	-0.18	-0.41 - 0.04	-0.18	-0.37 - 0.02
lnR_6	0.13	-0.03 - 0.29	0.12	-0.02 - 0.26
lnR_7	-0.05	-0.28 - 0.17	-0.13	-0.34 - 0.06
lnR_8	0.3	0.06 - 0.52	0.38	0.17 - 0.58
lnR_9	0.49	0.28 - 0.70	0.48	0.29 - 0.66
lnR_{10}	-0.22	-0.42 - -0.02	-0.38	-0.55 - -0.21
lnR_{11}	-0.04	-0.27 - 0.18	0	-0.20 - 0.19
lnR_{12}	0.09	-0.19 - 0.35	0.11	-0.13 - 0.35
lnR_{13}	-0.14	-0.36 - 0.06	-0.1	-0.29 - 0.08
lnR_{14}	-0.34	-0.55 - -0.14	-0.34	-0.53 - -0.17
lnR_{15}	-0.08	-0.25 - 0.08	0.04	-0.11 - 0.19
lnR_{16}	0.06	-0.01 - 0.12	0.05	-0.01 - 0.11
lnR_{17}	0.15	-0.01 - 0.30	0.13	-0.01 - 0.27
lnR_{18}	1.17	0.98 - 1.35	1.13	0.96 - 1.29
lnR_{19}	0.09	-0.15 - 0.32	0.16	-0.05 - 0.36
lnR_{20}	0	-0.19 - 0.17	-0.05	-0.22 - 0.11
lnR_{21}	-0.05	-0.27 - 0.17	0.02	-0.18 - 0.21
lnR_{22}	-0.1	-0.32 - 0.12	-0.15	-0.36 - 0.04
lnR_{23}	-0.53	-0.72 - -0.35	-0.5	-0.67 - -0.35
lnR_{24}	0.24	0.02 - 0.44	0.2	0.00 - 0.38
lnR_{25}	-0.22	-0.37 - -0.07	-0.24	-0.37 - -0.11
lnR_{26}	-0.04	-0.27 - 0.18	0.01	-0.20 - 0.20
lnR_{27}	-1	-1.23 - -0.76	-0.95	-1.16 - -0.76

[1]) Estimation of statistical confidence ranges is described in subsection 5.5.2.

5.3.1. Quality control

Quantitative characterization of model uncertainties allows validating the model. In particular, the important question is whether the small level of attenuation q can be differentiated from zero and from the effects of kappa. Data residuals (misfits) evaluated for the transverse-component optimal models (Tables 5.1 and 5.2) are shown in Figure 5.3. As described in section 5.2, such plots are critical for quality control and final formulation of the inversion procedure. The final data residuals should show correlation with neither distance (Figure 5.3a) nor frequency (Figure 5.3b). To obtain the results in Figure 5.3a and b, a preliminary inversion by using Brune's (1970) spectra (with $s(f) = 0$ for both sources in eq. (5.1)) was performed first (Figure 5.3c). The median data residuals resulting from this inversion show noticeable correlations with frequency, which are shown by gray diamonds in Figure 5.3c. By iterative adjustment of $s(f)$ functions (eq. (5.1)), median data errors are corrected to near zero (Figure 5.3b). The resulting functions $s(f)$ for the two sources are shown by lines in Figure 5.3c. Broadly, these functions can be interpreted as resonance peaks at frequencies 10 to 12 Hz in the receiver site spectra, or similar variations of source spectra.

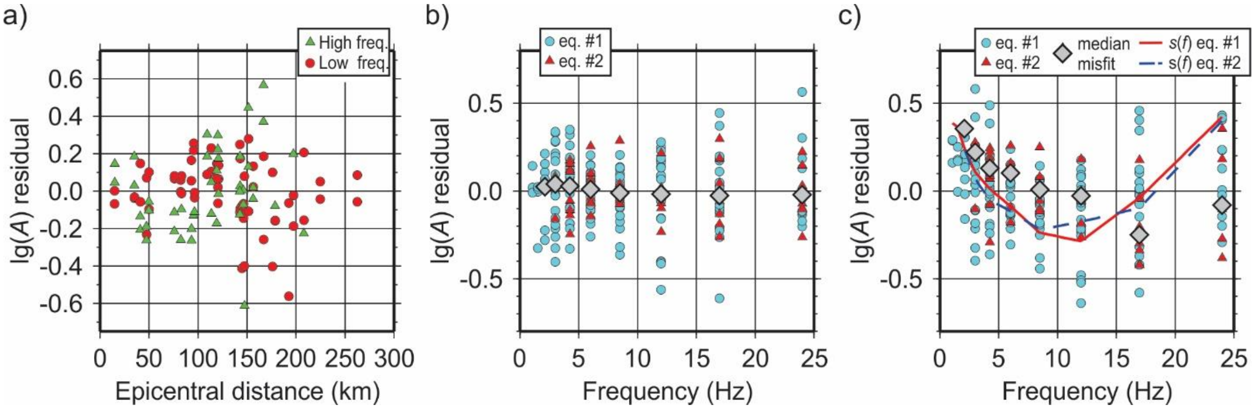

Figure 5.3. Data residuals (decimal log-amplitude misfits) for all records using transverse-component amplitudes: a) dependence on source-receiver distances, b) final dependence on observation frequencies after correcting for the $s(f)$ function; c) data residuals from preliminary inversion by using Brune's (1970) spectrum. Lines in plots c) show the $s(f)$ functions (eq. (5.1)) estimated for the two earthquakes.

The adjustment of functions $s(f)$ can be compared to iterative inversion for source and site spectra (Drouet et al., 2008) or to the procedure of deriving constrained site spectra and κ_0 by

Klimasewski et al. (2019). However, Klimasewski et al. (2019) performed spectral corrections by adding Fourier amplitudes instead of their multiplication in eq. (5.1).

Another important standard-model quality criterion is the distribution of receiver-coupling values lnR_i, shown by decimal logarithms in Figure 5.4. Due to the explicit constraint equations (eq. (5.13)), lnR_i values show no trend with source-receiver distance (Figure 5.4).

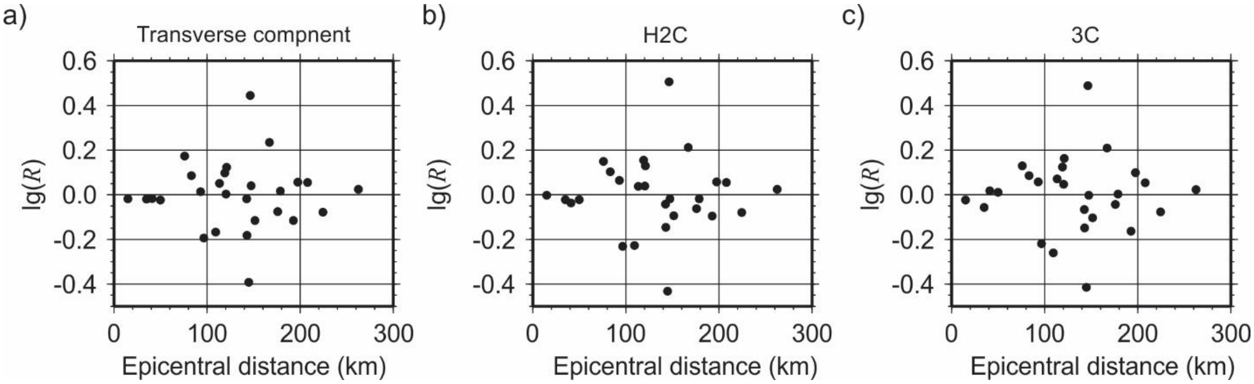

Figure 5.4. Station coupling terms lgR_i for a) transverse component, b) H2C, and c) 3C amplitudes.

Due to fitting the data without unrealistic correlations between model parameters and spurious trends in data errors, the evaluated distance dependencies (geometrical-spreading and q-related factors) in eq. (5.2) should be reliable. Note that as an initial test of the algorithm, I performed inversion without explicit constraints on lnR_i (eq. (5.13)). In that test, systematic (unacceptable) trends in lnR_i were obtained. In a much larger dataset, similar trends can also be seen in attenuation-corrected data by Atkinson (2012; Figure 3 in that paper).

After estimating the detailed $G(t)$, $s(f)$, κ and q, the total standard deviations of lg$A$ residuals equal approximately 0.18 for the transverse-component amplitudes and H2C, and 0.15 for 3C amplitudes (error bars in Figure 5.5). This quantity indicates the degree of overall consistency of the observations with the selected model (eq. (5.2)). These variances are somewhat smaller than those from fitting conventional models and in comparable studies (e.g., Atkinson, 2004, 2012). These data variances can be further reduced by adding parameters to the model, such as including azimuth- or frequency-dependent geometrical spreading in eq. (5.2). More detailed models would also be less portable, and they would also be weaker constrained. For these reasons, more detailed models are not considered in this study. However, the most important observation from this quality control is that data errors alone do not uniquely characterize the accuracy of the model, and additional quality criteria need to be considered.

5.3.2. Time-frequency dependencies

To extract from the predicted-data vector $\hat{\mathbf{d}}$ the distance and frequency dependencies that are of the most interest in this study, let us consider another forward-model matrix $\mathbf{L}_s$, which is obtained from $\mathbf{L}$ by retaining only the columns corresponding to variables lnR_i and lnS_j (eq. (5.8)) and zeroing out all other columns. The data predicted by this matrix $\hat{\mathbf{d}}_s = \mathbf{L}_s\mathbf{m}$ are analogous to the travel-time "statics" (additive local effects) well-known in reflection seismology. Vector $\hat{\mathbf{d}}_s$ comprises all effects of source and receiver couplings in the data and omits all path effects. By subtracting these statics from the observed data ($\mathbf{d}' = \mathbf{d} - \hat{\mathbf{d}}_s$) and from the predicted data ($\hat{\mathbf{d}}' = \hat{\mathbf{d}} - \hat{\mathbf{d}}_s$), the path-related part of the standard model is isolated (Figure 5.5).

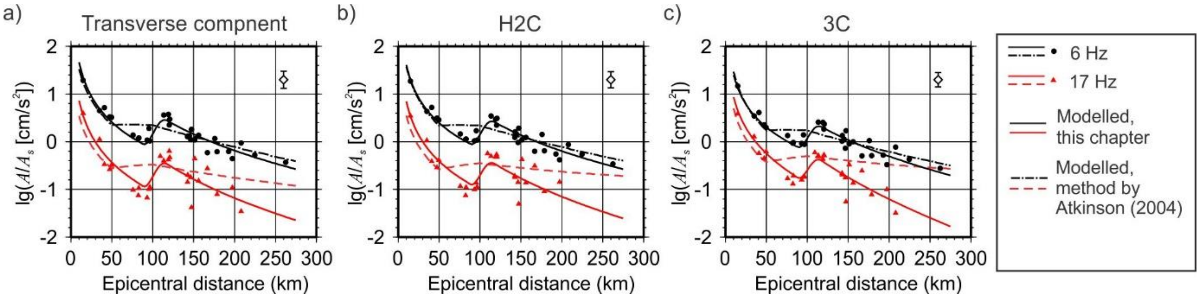

Figure 5.5. Distance dependencies of amplitudes at frequencies 17 Hz (red or gray in print) and 6 Hz (black). Symbols are the data corrected for the source and receiver effects, and lines are the inverted standard models: a) Model for transverse-component amplitudes; b) for H2C amplitudes; c) for 3C amplitudes. Error bars in the upper-right corners of each plot show the total standard deviations of ln$A$ misfits.

As it is apparent from Figure 5.5, the data themselves (black dots and red/gray in print triangles) clearly indicate an amplitude increase from about 90 to 115-km distances. This amplification justifies my use of two characteristic travel times t_1 and t_2 (Figure 5.1a). The resulting estimates of this amplitude amplification are $b_{21} \approx 3.5$ and $b_{22} \approx 5.4$ for transverse-component S-wave spectral amplitudes, $b_{21} \approx 3.3$ and $b_{22} \approx 5.0$ for H2C amplitudes, and $b_{21} \approx 3.1$ and $b_{22} \approx 4.5$ for 3C amplitudes (eq. (5.7)). These values indicate significant contributions from near-critical reflections (from the Moho and/or deep crust) entering the S-wave time windows at these distances.

5.3.3. Source and receiver site spectra

Estimation of the source and receiver site spectra was performed by the same algorithm as described in eqs. (5.10) and (5.11) with the following modifications: 1) parameters $\ln S_j$ and $\ln Ri$ replaced with $A_S(f)$ and $A_R(f)$ spectra sampled at 11 frequencies $\{f_s\}$ of data sampling, 2) model vector (eq. (5.8)) truncated to source and receiver parameters only, and 3) the input data modified by correcting for the path and kappa factors (eqs. (5.1), (5.2), and (5.5)):

$$d_{ij}\left(t, f\right) = \frac{1+\left(f/f_c\right)^2}{\left(f/f_c\right)^2} \times \frac{A\left(t, f\right)}{e^{-s(f)} G\left(t\right) e^{-\pi\kappa_{Sj}\left(f-f_0\right)} e^{-\pi\kappa_{Ri}\left(f-f_0\right)} e^{-\pi f t^*}} . \qquad (5.17)$$

These Brune's spectrum, path- and kappa-corrected amplitudes are modeled as products of source and receiver site spectra:

$$d_{ij}\left(t_{ij}, f_s\right) = A_{Ri}\left(f_s\right) A_{Sj}\left(f_s\right). \qquad (5.18)$$

To select the numerical inversion method for nonlinear equations (eq. (5.18)), it is necessary to consider whether it is appropriate to solve them for *d* directly or to linearize them first by taking logarithms. This question is answered by considering the expected distribution of measurement errors (data residuals). To produce an unbiased solution from the least-squares inversion method, the data residuals should possess zero means and be distributed close to the normal (Gaussian) distribution. Errors in the recorded amplitudes are principally due not to random site noise but to signal-related effects such as scattering and multipathing. Therefore, the amplitude errors δd scale with the values of *d*, and they are distributed not normally but closer to the log-normal distribution. Consequently, we can expect that errors $\delta \ln d$ should be close to a normal distribution, and the linearized equations for $\ln d$ can be solved by the least-squares method.

After taking logarithms of eq. (5.18), linear system in eq. (5.10) is obtained and solved in the least squares sense, subject to the receiver-scaling constraint $\sum_{f_s}\sum_{i}\ln A_{Ri}\left(f_s\right)=0$ (Castro et al., 1990). Note that the conventional approach to solving eq. (5.18) independently at each frequency f_s (e.g., Castro et al., 1990) is generally unsafe, because it does not guarantee satisfying conditions $\left\langle d\ln A_S/df\right\rangle=\left\langle d\ln A_R/df\right\rangle=0$ (eq. (5.4)). These conditions are required in order to consistently interpret the values of κ_S and κ_R as the high-frequency slopes of the source and receiver spectra, respectively. To ensure such consistent interpretation, I included the above equations as additional constraints on the inversion.

The resulting spectra are shown in Figures 5.6 and 5.7 for four end-member cases, which attribute the spectral filtering functions $\exp\left[-s\left(f\right)\right]$ and $\exp\left(-\pi\kappa f\right)$ to either sources or receivers (see eqs. (5.1) and (5.2) and explanations in section 5.3). Line colors in these figures are complementary, so that the same color corresponds to $A_S(f)$ and $A_R(f)$ spectra that would be present simultaneously.

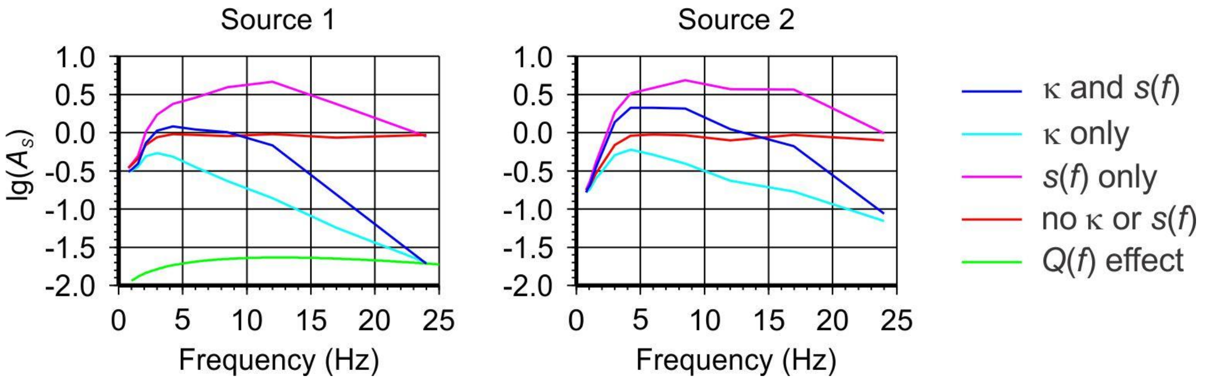

Figure 5.6. Spectral responses $A_S(f)$ for two earthquake sources of this study. Line colors show different combinations of κ and $s(f)$ functions included in the source spectra (legend). The variation of the $Q(f)$ effect by less than 0.3 (green line; P_η in eq. (5.19)) shows the low importance of the selection of a frequency dependent Q in this model.

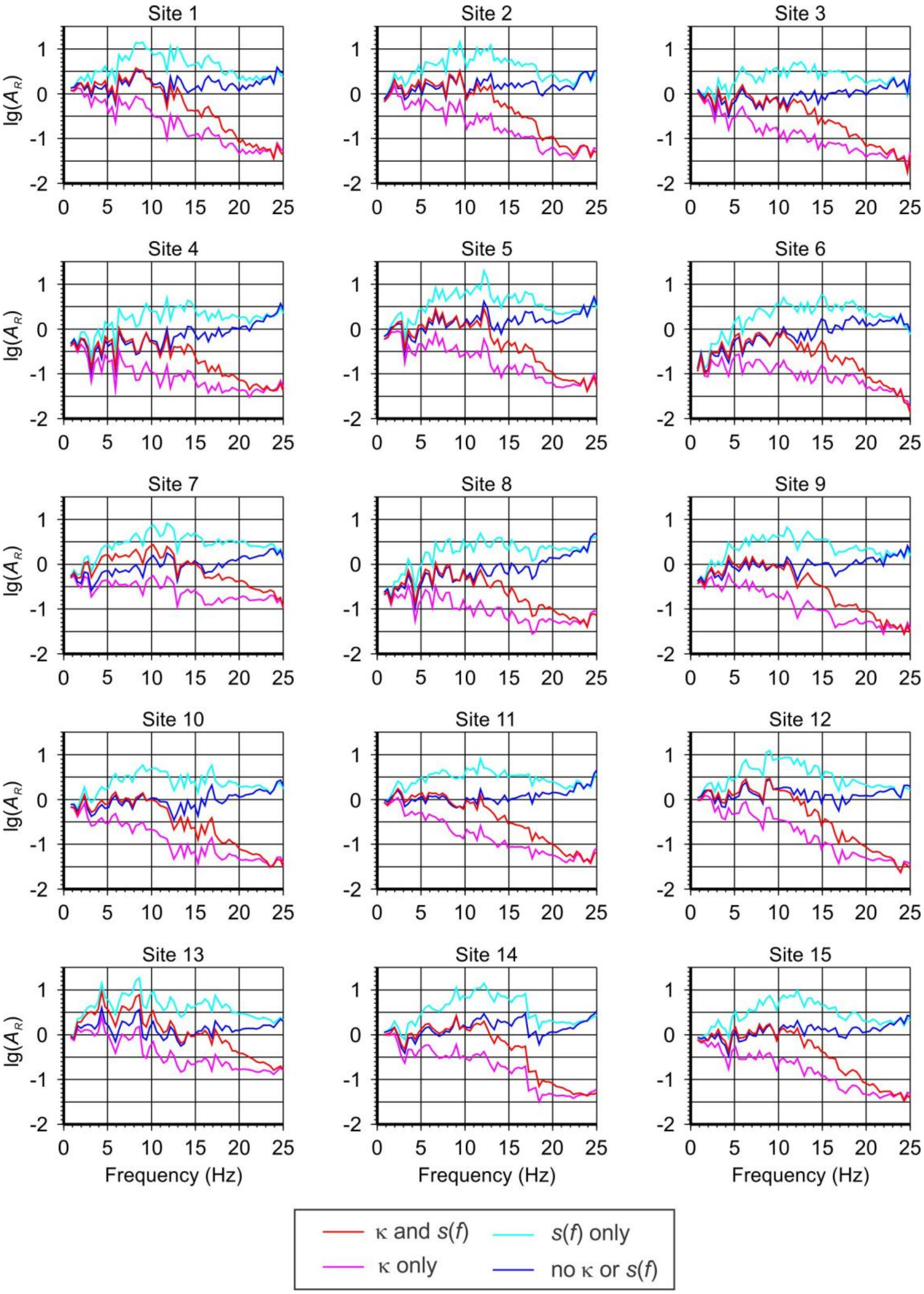

Figure 5.7. Spectral responses $A_R(f)$ for all stations of this study. Line colors show different combinations of κ and $s(f)$ functions included in the spectra (legend).

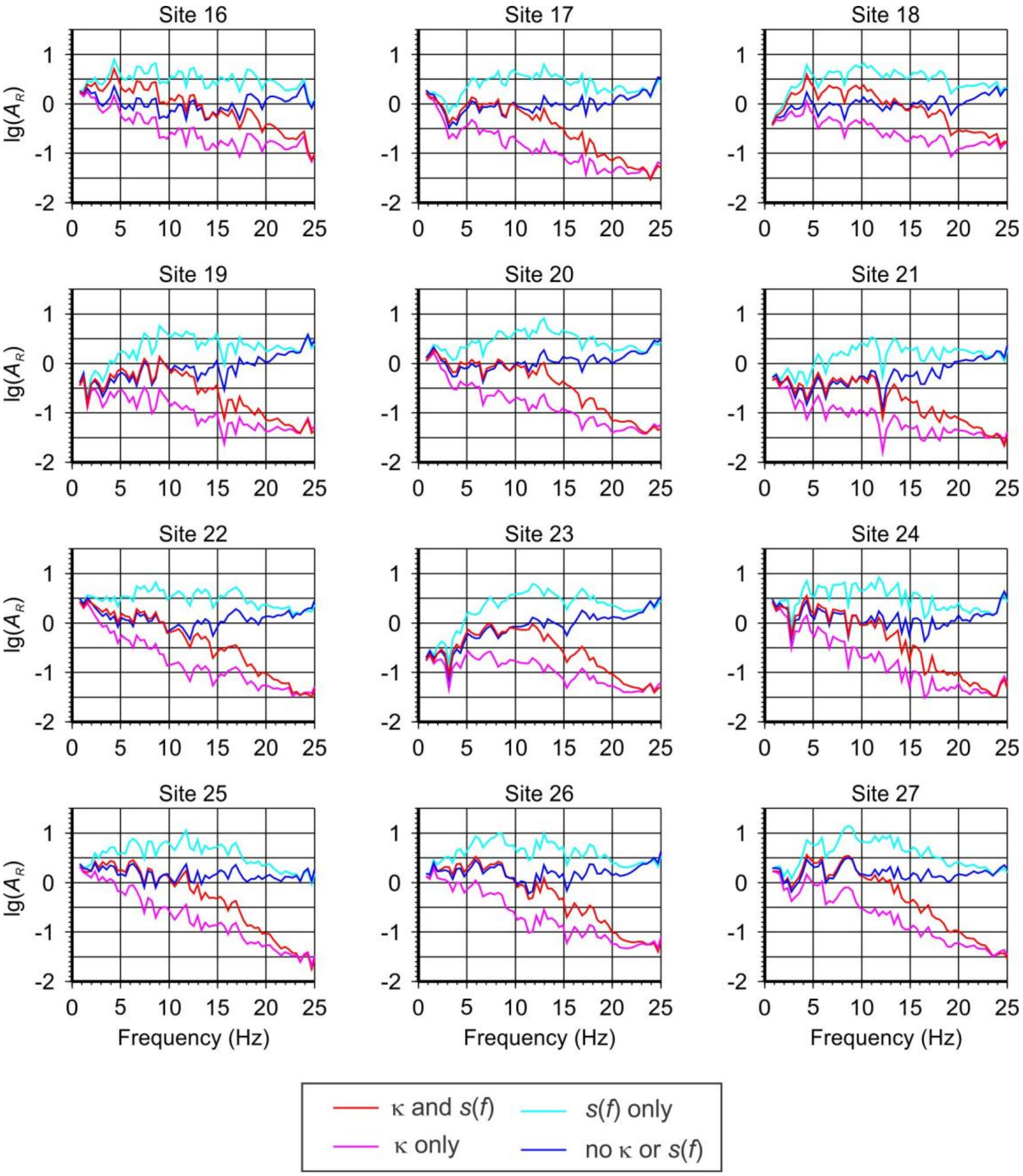

Figure 5.7, continued.

The case of both κ and *s*(*f*) attributed to site spectra (red lines in Figures 5.6 and 5.7) represents the conventional interpretation assuming all high-frequency effects being caused by site effects (Anderson and Hough, 1984). This interpretation is plausible, although the alternate interpretation with *s*(*f*) function belonging to the source (magenta in Figures 5.6 and 5.7) also appears likely. In this dataset, the trade-off between κ_R and κ_S cannot be excluded from consideration, and therefore, the alternate solutions shown by blue and cyan colors in Figures 5.6 and 5.7 are also possible.

For interpreting the results of κ and Q measurements, knowledge of near-surface receiver-site conditions is most important. Unfortunately, this information is limited in the present study. Due to the complexity of geology and tectonics of the region, bedrock depths and thicknesses of sedimentary deposits vary for different sites. For example, in the vicinity of Bam station (#7 in Figure 2.3 in chapter 2), soil profiles show sandy clay within the upper part and silty sand at the lowest part. Due to these thick soil deposits, Bam station was classified as site class C (Rayhani et al., 2008). According to Komak Panah et al. (2002), the Bam site is located on soft soil, Globaf station (#2 in Figure 2.3 in chapter 2) is on moderately soft soil, and Sirch site (#1) is on hard soil or weak rock (Table 5.5). However, the high-frequency slopes of the spectra (with overlying resonance peaks) shown by the red and magenta lines in Figures 5.7 appear to be expected for the soft-rock sites of this survey. After the site spectra are estimated, parameters kappa can be measured from them for each site. Table 5.6 shows these kappa values for each site and for each of the single-component and multicomponent amplitudes within the S-wave window. These values were measured between 10-Hz and 25-Hz frequencies in the conventional interpretation of kappa effects (red in Figures 5.6 and 5.7). Interestingly, the vertical-component kappas are systematically much lower, and in a few cases, they are negative. Among other factors, lower signal-to noise ratios in vertical-component records could be one potential reason for such values.

Table 5.5. Available site classification data in the study area (Komak Panah et al., 2002).

Soil description	**Geological conditions**	**Sites**
soft soil	Thick soft clay or silty sandy clay. Mostly alluvial plain.	Bam (#7)[1]
moderately soft soil	Interbedded fine and coarse material, alluvium terraces with weak cementation.	Golbaf (#2) [1]
hard soil, weak rock	Well cemented and compacted soil, old Quaternary outcrop.	Sirch (#1) [1]

[1]) Numbers of sites adopted in Figure 2.3 in chapter 2.

Table 5.6. Values of κ (in seconds) measured from site spectra for single-component amplitudes (Figure 5.7).

Site #	***Transverse***	***Radial***	***Vertical***	***H2C***	***3C***
1	0.042	0.035	-0.003	0.057	0.035
2	0.044	0.037	0.001	0.033	0.012
3	0.032	0.025	-0.012	0.052	0.026
4	0.019	0.013	-0.023	0.056	0.042
5	0.041	0.034	-0.003	0.059	0.028
6	0.031	0.023	-0.01	0.037	0.02
7	0.019	0.014	-0.007	0.028	0.014
8	0.016	0.01	-0.027	0.023	0.013
9	0.035	0.029	-0.007	0.067	0.052
10	0.027	0.02	-0.018	0.052	0.025
11	0.033	0.024	-0.011	0.059	0.047
12	0.05	0.044	0.007	0.037	0.023
13	0.019	0.016	-0.004	0.049	0.035
14	0.056	0.051	0.012	0.017	-0.003
15	0.046	0.04	0.004	0.056	0.032
16	0.014	0.011	-0.005	0.031	0.021
17	0.031	0.025	-0.009	0.018	-0.018
18	0.02	0.017	0.002	0.043	0.033
19	0.023	0.016	-0.02	0.049	0.035
20	0.036	0.029	-0.007	0.069	0.061
21	0.019	0.015	-0.021	0.04	0.017
22	0.032	0.024	-0.011	0.058	0.04
23	0.033	0.024	-0.008	0.043	0.015
24	0.038	0.032	-0.005	0.05	0.041
25	0.052	0.045	0.009	0.031	0.002
26	0.032	0.024	-0.01	0.065	0.045
27	0.049	0.044	0.007	0.061	0.028

5.3.4. (Un)Importance of the frequency-dependent *Q*(*f*)

The green line in the first plot in Figure 5.6 additionally demonstrates the general lack of significance of the frequency-dependent *Q*(*f*) in seismology, as discussed in this chapter and also by Morozov (2008b, 2010a, 2010b, 2011a). If we assume a frequency-dependent $Q(f) = Q_0 f^{\eta}$ for an S wave, then its effect within a limited frequency band (attenuation coefficient) can still be approximated by a frequency-independent Q-factor Q_e (Morozov, 2008b, 2010a). For $Q_0 = 99$ and $\eta \approx 0.58$ estimated for the study area by Safarshahi et al. (2013) and frequency range from 1 to 30 Hz, this $Q_e \approx 1025$ (Morozov, 2008b). The ratio of the frequency-dependent and constant-Q_e effects equals

$$P_{\eta}(t, f) = \exp\left[-\frac{\pi f t}{Q(f)}\right] \Big/ \exp\left(-\frac{\pi f t}{Q_e}\right). \tag{5.19}$$

For t corresponding to 100-km distance, this function is shown by the green line in Figure 5.6 (panel on the left). This line shows that the total variation of P_{η} across the measured frequency band is less than 0.3, which is much smaller than the variations and uncertainty of the source and site responses (Figure 5.6). Therefore, even with this modest Q_e (compared to values $Q \approx 4000$ in Tables 5.1 and 5.3), and also by Atkinson (2004) and Palmer and Atkinson (2020), selection of the functional form of $Q(f)$ is insignificant and hardly measurable. The effect of $Q(f)$ is also within the error due to the under-parameterization of $G(t)$ (sections 5.1 and 5.5; Morozov, 2008b, 2010a; Morozov et al., 2018).

5.4. Interpretation

Both conventional (frequency-dependent $Q(f)$ based) and my new (q = const) models can be easily evaluated and fit to the observed seismic amplitudes with similar average errors. Both approaches can generally be used as empirical standard models $\Phi(t,f)$, along with many selections for background geometrical spreading. However, from the viewpoints of its more detailed accuracy, independence of assumptions, and consistent physics, the model of this chapter is strongly preferable. Note that this model (section 5.3):

1) Achieves a better data fit across the local to regional distance ranges (solid and dashed lines in Figure 5.5);

2) Inverts for the source (S_j) and receiver site (R_i) factors in one step and eliminates their correlations with epicentral distance;
3) Eliminates unexpected spurious correlations of data residuals with distances and frequency, which bias the results of conventional models; compare Figure 5.3a (for this model) to Figure 5.20b in subsection 5.7.1 and Figures 6 to 9 in Atkinson (2012) (for conventional models);
4) Uses a physically well-defined and more strongly constrained frequency-independent parameter $q \equiv 1/Q$ instead of the method-dependent apparent $Q(f)$;
5) Overall, simplifies and facilitates a detailed and quantitative analysis of the resulting model without unverified hypotheses about the natures of recorded waves and their characteristics such as geometrical spreading and $Q(f)$.

Compared to the conventional analysis of the same and similar datasets (subsection 5.7.1 and Safarshahi et al. (2013)), several significant observations can be made. These observations appear to be general and should apply to other areas. First, the geometrical-spreading exponents ν are much larger than those often used for both the near and far distance ranges (Aki and Chouet, 1975; Atkinson, 2012; Safarshahi et al., 2013). For the transverse, H2C, and 3C spectral amplitudes, I estimate $\nu_{\text{near}} \approx 1.77$, 1.70 and 1.49, respectively, with statistical confidence intervals shown in Tables 5.1 and 5.3. For ν_{far}, I obtain values of 2.52, 2.44, and 2.22, respectively (Figure 5.5). The lower values of both ν_{near} and ν_{far} for 3C amplitudes correlate with their comparatively low values for vertical-component amplitudes ($\nu_{\text{near}} \approx 1.21$ and $\nu_{\text{far}} \approx 1.99$; Table 5.1). The values of $\nu_{\text{far}} > 2.2$ are in a particularly stark contrast with the usual assumption of $\nu_{\text{far}} = 0.5$ (e.g., Atkinson, 2004; Fisk and Phillips, 2013a, 2013b).

Compared with $\nu = 1$ for body waves in a homogenous half-space (Aki and Chouet, 1975), increased values of ν_{near} should be expected from crustal velocity gradients and layering. Velocity gradients and reflections cause curvatures of body-wave paths and reflections, which consequently increases the values of ν or γ (see the explanations of the forms of $G(t)$ following eq. (5.2)). Large values of ν_{far} show that propagation of regional S-waves beyond the critical reflection distance (~115 km in this area) is far from spreading of surface waves in a homogeneous half-space (e.g., Bowman and Kennett, 1991). Long propagation within the crustal waveguide encounters significant small-scale scattering, which principally occurs from surface topography and shallow subsurface (Jhajhria et al., 2017). This scattering should lead to ν values much larger than in a homogenous half space (Morozov, 2010a, 2010b).

The second major observation from the model in eq. (5.2) is that the "geometrical" $G(t)$ for S waves is non-monotonous and contains an amplification between about 90 and 115 km. The amount of this increase is significant, which can be expressed by transverse-component amplification factors $b_{21} \approx 3.5$ and $b_{22} \approx 5.4$ (eq. (5.7), Table 5.1, and Figure 5.1a). This amplification can again be explained by reflections and anisotropic (upward and forward-directed) scattering from and near the base of the crust. This strong amplitude variation is present but appears smoothed over in models averaged over large areas in North America by Atkinson (2004, 2012). This amplification is clearly seen in the source/site corrected data (Figure 5.5), and it is also suggested by other data (Figure 5.2b).

The third general observation from this inversion is that the frequency-independent attenuation in southeastern Iran is much weaker than the one inferred by the conventional methods ($Q_0 \approx 99$ by Safarshahi et al. (2013)). From my q estimates (Tables 5.1 and 5.3), the Q is about 1500 for the vertical component, about 4000 for horizontal components, and 1800 for 3C. Even taking the largest q within the estimated confidence bounds for H2C (Table 5.3), the smallest Q for this area would be about 2800. This range of attenuation is consistent with the estimates by Atkinson (2012), and particularly with the recent study of the Q-corrected kappa in Canada (Palmer and Atkinson, 2020). This weak attenuation supports the premise of my model (eq. (5.5)) stating that seismic wave amplitudes are dominated by elastic effects.

Fourth, owing to the clear functional separation between the effects of $G(t)$, κ, and Q in eq. (5.2), parameters κ are measured concurrently with Q. The inverted values of $\kappa_S \approx 51$ and 32 ms for transverse-component (for the two earthquakes or stations recording them), and 49 and 31 ms for H2C (Table 5.3) are close to those typically observed for soft-rock sites (Ktenidou et al., 2014). Interestingly, for vertical component, these values are much lower (6 and 4 ms; Table 5.1), and these low values contribute to the reduced $\kappa \approx 28$ and 18 ms for 3C amplitudes (Table 5.3). For all components, the kappas likely include both source and site effects (subsection 5.3.3). If the source κ is produced by the time signature of the rupture (Beresnev, 2019a, 2019b), then it might be common to all components and therefore limited by the smallest value measured above. Thus, κ_S could be limited to 6 and 4 ms for the two earthquakes, although this conjecture still needs to be examined in modeling studies.

The slower decay rates ν, smaller kappas, and larger q for vertical-component and 3C ground motions within S-wave records could be explained by several factors: a) dependencies of refractions and reflections within the crust on incidence angles, b) coupling between the horizontally and vertically-polarized S-waves within the crust, and c) S-wave coupling with P-waves occurring during propagation through the layered and/or scattering crust.

In summary of the interpretation, the new model shows that all data can be explained by much steeper frequency-independent geometrical spreading $G(t)$, site effects, source spectra $S(f)$ possibly different from Brune's (1970), and only weak path-related attenuation ($Q > 2000$ with average of $Q \approx 4000$ for horizontal ground motions). Considering that many studies such as by Atkinson (2004, 2012) and Safarshahi et al. (2013) fit similar wave-amplitude data by using much lower values of ν and much lower but frequency-dependent Q, these results may appear disturbing. This uncertainty illustrates the difficulty of attenuation measurements and also the great subjectivity embedded in conventional interpretations of wave attenuation. By contrast, the present results are based on a rigorous method with detailed error checking, and they are well supported by the available data.

5.5. Model Uncertainty

In the following subsections, I differentiate between two types of model uncertainties that are present both in preceding section and all other standard models. The first of these types is the most harmful and difficult uncertainty caused by a customary or subjective selection of mathematical parameterization, particularly with the use of an under-parameterized function $G(t)$. The second type of model uncertainty is typical for all physical measurements and caused by random data measurement errors.

5.5.1. Uncertainties due to model parameterizations

Figure 5.8 illustrates the strong uncertainty of standard models arising from different approaches to their parameterization. In this figure, two models derived from my S-wave data are shown: (1) Figure 5.8a obtained by using simultaneous inversion for all 35 parameters describing the functional form of $G(t)$, q, κ, S_j and R_i (eq. (5.2)), and (2) an alternate model (Figure 5.8b) derived by the conventional parameterization and multi-step inversion procedure by Atkinson (2004). In the first of these approaches, the parameterization of $G(t)$ is based on summarizing the $A(t,f)$ observations in the data and viewing q as a single constant. In the second approach, the shape of $G(t)$ is under-parameterized (based on the fixed "trilinear" power-law model by Atkinson (2004, 2012)), but the Q (i.e., q) is allowed to freely vary with frequency. As one can see, the modeled $\Phi(t,f)$ dependencies are strongly different, particularly at higher frequencies and local-distance ranges (solid lines in Figures 5.8a and 5.8b). In particular, regarding the amounts of amplitude amplification from 90 to 115 km and beyond 250 km, the wave-amplitude predictions differ by about three times in these models. The models also strongly differ by the inferred Q factors (Figure 5.8c), which is partly because the model of Figure 1a also contains the high-frequency spectral decay parameters κ (eq. (5.2)). Thus, from most user's and interpreter's perspectives, the models are significantly different. However, the root-mean square (RMS) average log-amplitude residuals for these models are nearly identical and equal $\left\langle \delta \ln A\left(t, f\right)\right\rangle_{\mathrm{RMS}} \approx 0.42$ for the model in Figure 5.8a and 0.43 for Figure 5.8b. These close average errors can be seen from the similar ranges of data misfits (vertical axes in Figures 5.8d and 5.8e). Therefore, the traditional total-RMS misfit of log-amplitude data provides practically no differentiation between these models, which means that both of them fall within the trade-off of this model parameterization. Note that this RMS least-squares data fit is currently the only criterion used for model validation (e.g., Castro et al., 1990; Atkinson, 2004, 2012; Fisk and Phillips, 2013b).

Despite the insensitivity of the RMS criterion described in the preceding paragraph, the two models in Figures 5.8a and 5.8b are nevertheless clearly separable by the more detailed patterns of data misfits (plots d and e in Figure 5.8) and by the distributions of receiver coupling parameters $\ln R_i$ vs. distance from the nearest earthquake (plots f and g).

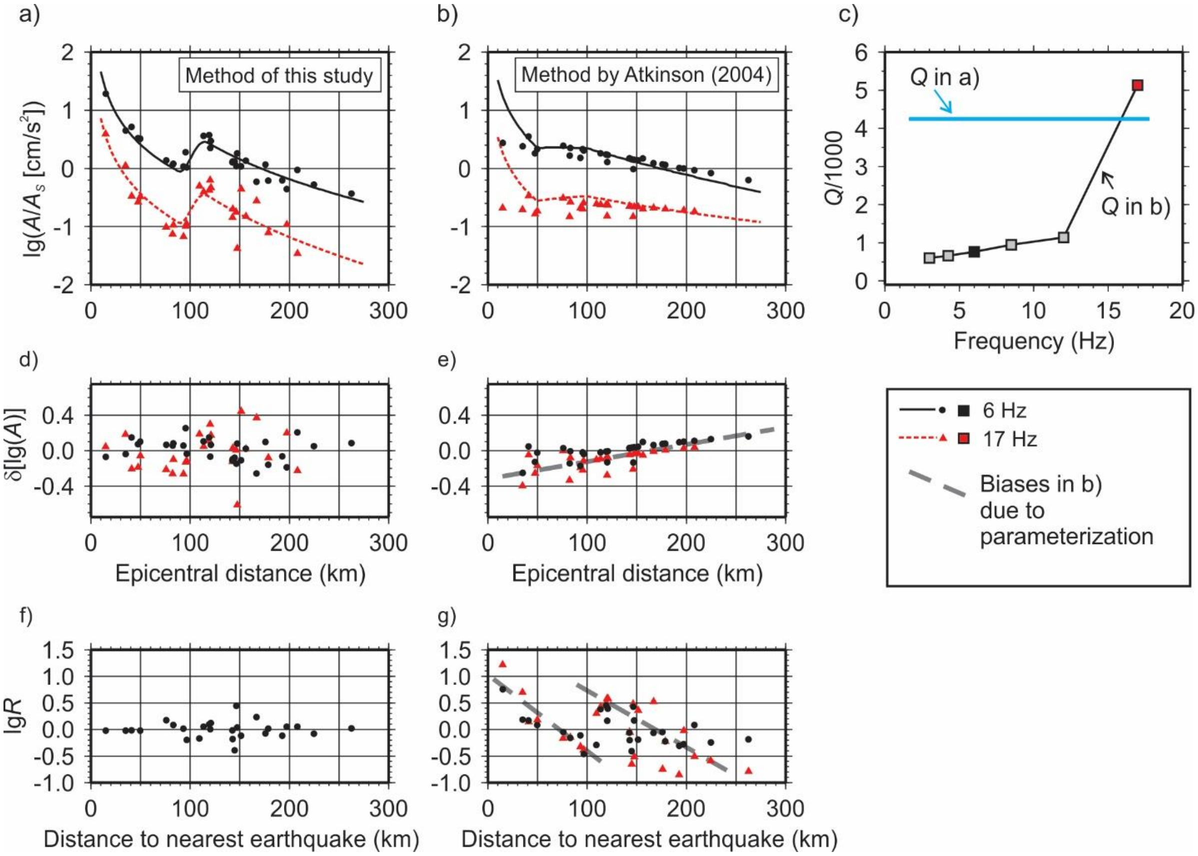

Figure 5.8. Summaries of source-and receiver coupling corrected standard models derived using the conventional and my new estimation method: a) Modeled lg $\Phi(t,f)$ dependencies (lines; eq. (5.2)) and source-receiver corrected data (symbols) on distance at frequencies 6 (black color) and 17 Hz (red, gray in print), obtained by joint inversion of section 5.3. Here and in plots b), d), and e), travel times t are converted to distances $x = \beta t$, where $\beta = 3.5$ km/s is the average S-wave velocity. b) The same using the conventional method (Atkinson, 2004). c) Q-factors from the two methods. d) and e) lg$A$ data misfits corresponding to the models in plots a) and b), respectively. f) and g) Corresponding receiver coupling terms $\ln R_i$ (eq. (5.2)). Dashed gray lines in e) and g) indicate spurious correlations of data errors and receiver terms with distance.

First, the model in Figure 5.8a fits the local-distance range much more accurately and does not overfit the regional distances.Such uniform fitting of both local and regional ranges is the key quality requirement for models of this kind (Atkinson, 2012). Second, to satisfy the model in Figure 5.8b, receiver terms $\ln R_i$ must possess two systematic trends with distance from the nearest earthquake (gray dashed lines in Figure 5.8g). Note that these trends are very close to the distance trend of the "attenuation" model $\ln A(t,f)$ itself (Figure 5.8b). Third, the measurement errors of $\delta[\ln A(t,f)]$ turn out to be non-random, because they exhibit an increase with epicentral distance (dashed line in Figure 5.8e). This pattern of data errors is particularly clear (and therefore questionable) at regional distances, and it indicates a data overfitting at regional distances. This systematic bias of errors is also contrary to the key assumption of the least-squares inversion. Because of these spurious patterns, the model in Figure 5.8b is clearly unacceptable in general, although it might of course occur incidentally due to a "fortuitous" selection of receiver sites and behavior of seismic instruments. Such models assuming systematic trends in site and instrumental conditions can hardly be portable to other measurements and study areas. Rather than allowing such patterns of site terms, the trends shown in Figures 5.8e and 5.8g can be more naturally explained as deficiencies of the "over-under-parameterized" model (Morozov, 2008b, 2010a).

Although rarely examined in such detail, problems similar to those of Figures 5.8b, 5.8e, and 5.8g may be present in many existing "attenuation" models. For example, Atkinson (2012) pointed out that none of the existing models adequately matches the wave-amplitude data at both local and regional epicentral distances, and also across the transition between these distance ranges. Models are dominated ("pegged" in the terminology by Atkinson (2012)) by regional distances containing most data points and where the amplitude variation with distance is smoother (see Figure 5.8b). Amplitude decay rates at regional distances determine the frequency-dependent $Q(f)$ because within this range, a fixed $G\left(t\right)\propto t^{-0.5}$ is always assumed (Atkinson 2004; Fisk and Phillips, 2013b).

Clearly, a $Q(f)$ dependence inferred for regional distances cannot be expected to also work at local ranges. Better data fitting can be achieved by considering distance- (time-) range dependent $Q(t,f)$ (Bora et al., 2017; Graizer, 2017). However, this modification is practically equivalent to allowing a more flexible $G(t)$, which is my approach in Figure 5.8a. With removed under-parameterization of $G(t)$, the entire distance range can be fit adequately and without artifacts with only a single, frequency-independent q value (eq. (5.2); Figures 5.8d and 5.8f). Finally, data residuals correlated with source-receiver distances similar to Figure 5.8b can be seen in published models, such as in Figures 6 to 9 by Atkinson (2012).

Due to its allowing a frequency-dependent $Q(f)$, the model in Figure 5.8b represents only one possible selection out of an infinite set of models producing identical $A(t,f)$ dependencies. To characterize the whole set of such equivalent models, we can use simultaneous transformations

$$\begin{cases} q \to q(t, f) = q - c/f - d/t, \\ \kappa \to \kappa + d, \\ G \to G\exp(-\pi ct), \end{cases} \tag{5.20}$$

with arbitrary constants *c* and *d*. Since parameters *c* and *d* do not affect eq. (5.2), they cannot be determined from distance and frequency dependencies of seismic amplitudes. Selections of certain values for *c* and *d* are usually made by either mathematical convention (such as preference of a power law for *G*(*t*)) or by certain construction of the inversion algorithm (such as taking a fixed *G*(*t*) and $\kappa = 0$ when measuring *Q*(*f*); Aki and Chouet, 1975). In practical observations (e.g., Campbell (2009), this chapter, and most field studies in reflection seismology), time- and frequency-independent *Q* is often preferred, which means $c = 0$ and $d = 0$). In an opposite approach, by expecting both $c > 0$ and $d > 0$, *Q*-factors increasing with both *t* and *f* are often found in coda studies (e.g., Calvet and Margerin, 2013) and also for response spectra (Graizer, 2017). Another practical choice is $d = 0$ (distance-independent *Q*) and $c \neq 0$ (usually $c > 0$). With this selection, the shapes of the "frequency-dependent *Q*" curves $Q(f) = 1/(q - c/f)$ are close to $Q(f) = Q_0 f^{\eta}$ with $0 < \eta \leq 1$, which are reported in many studies (Morozov, 2008b). Finally, Bora et al. (2017) used yet another selection of $c = 0$ and $d \neq 0$, which gave a frequency-independent but distance-dependent *Q* close to $Q(t) = 1/(q - d/t)$. In a recent article, Haendel et al. (2020) utilize even broader trade-off relations than eq. (5.20) by considering the *q* as frequency-dependent ($q = (Q_0 f^{\eta})^{-1}$) and transferring its effect into a travel-time (distance) and frequency-dependent kappa: $q \to 0$ and $\kappa \to \kappa + qt = \kappa + t\, f^{-\eta}/Q_0$. For the alternate (conventional) interpretation of this dataset in Figure 5.8b, the uncertainty related to varying parameter *c* is illustrated in Figure 5.9. In this figure, bold lines are the *q*(*f*) and *G*(*t*) for the model Figure 5.8b. Starting from this model, I applied transformations in eq. (5.20), with $d = 0$ and *c* varying from –0.01 to 0.01 Hz (thin lines in Figure 5.9). Each of these models is completely equivalent to all others in terms of the time/frequency dependencies of wave amplitudes (eq. (5.2)). Note that since the *q* at each frequency is derived from distance (time) dependencies that can be complex and non-monotonic, this apparent *q* should not be expected to be strictly non-negative.

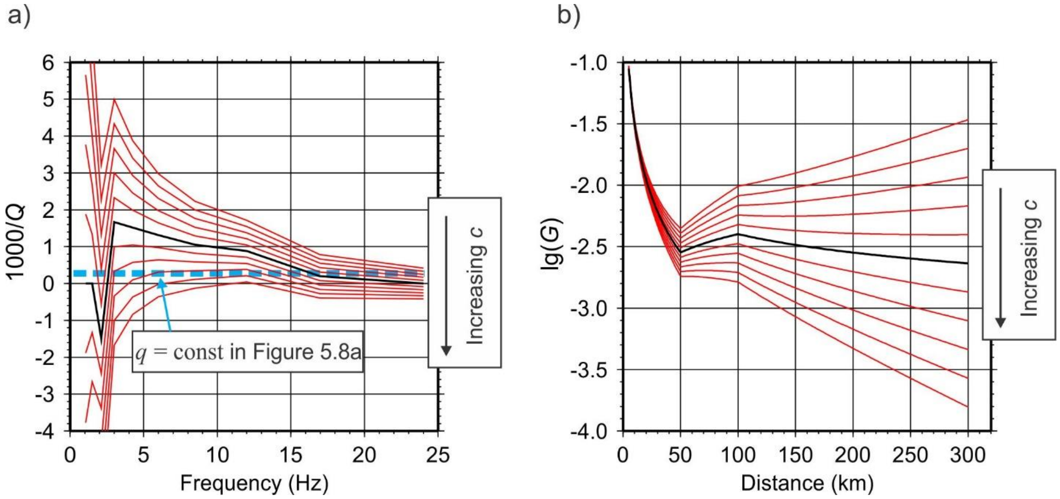

Figure 5.9. Ambiguity of models and the trade-off between $G(t)$ and $q(f)$ in the conventional interpretation of the dataset: a) variations of the frequency-dependent q for various values of parameter c (eq. (5.20)); b) the corresponding variations of $G(t)$ making identical $\Phi(t,f)$ dependencies. Arrows indicate the increase of parameter c, with thick black lines corresponding to c = 0. Thick dashed line in a) shows the constant-q level used in the model in Figure 5.8a.

The ambiguity of "over-under-parameterized" standard models such as shown in Figure 5.8b and eq. (5.20) is not emphasized and often unnoticed in conventional approaches, because of certain construction of their multi-step inversion methodologies (e.g., Fisk and Phillips, 2013b). Specifically, during the first step of the inversion, factors S_j, R_i, and often κ in eq. (5.2) are not considered when inverting for Q, which leads to omitting important constraints on the model. Based on an intuitive association with Q-factors of mechanical or electrical resonators, the inverted quantity is denoted "Q" and loosely interpreted as "anelastic attenuation" (e.g., Atkinson, 2004, 2012; Fisk and Phillips, 2013b; Bora et al., 2017). However, traveling seismic waves are not resonators, and this association is unfounded. The principal contributions to the seismic Q-factor come from the elastic earth's structure such as layering and small-scale heterogeneity. Therefore, most of the effects of the Q are actually elastic and dependent on the travel time (distance) and not on the numbers of wave periods. These time-only dependent effects are indistinguishable from the similarly empirically defined geometrical spreading $G(t)$. Note that the geometrical spreading within a layered earth is also frequency-dependent (Yang et al., 2007). Thus, the Q (or q) in eq. (5.2) is the "apparent" attenuation, which is only an empirical parameter used for approximating the amplitude data (Morozov and Baharvand Ahmadi, 2015;

Graizer, 2017). The same apparent character applies to parameters κ (eq. (5.2)), particularly when they are viewed as time- or epicentral-distance dependent (e.g., Ktenidou et al., 2014).

5.5.2. Statistical data uncertainties

In the model of Figure 5.8a, the uncertainties and trade-off caused by the "over-under-parameterization" should be absent. The major uncertainty in eq. (5.20) is removed by requiring q = const (thick dashed line in Figure 5.9a). However, this model still contains smaller uncertainties and parameter trade-offs related to statistical data errors and possibly factors not accounted for in eq. (5.2), such as regional variations of q or the frequency-dependent geometrical spreading $G(t,f)$. These remaining model uncertainties are measured in this subsection.

The inverse of eq. (5.10) is obtained in the form of a generalized inverse (see Appendix A)

$$\mathbf{m} = \mathbf{L}_g^{-1}\mathbf{d} + \mathbf{m}_g \, , \tag{5.21}$$

where $\mathbf{L}_g^{-1}$ is a matrix and $\mathbf{m}_\mathrm{g}$ is a vector dependent on the structure of the dataset. By using this solution, $\ln\Phi_{ij}(t,f)$ data predicted for all earthquakes, stations, and frequencies are calculated by the matrix product $\hat{\mathbf{d}} = \mathbf{Lm} = \mathbf{LL}_g^{-1}\mathbf{d} + \mathbf{Lm}_g$. Finally, the data misfits (or residuals shown for two frequencies in Figure 5.8d) are mentioned as eq. (5.12).

By using eqs. (5.8), (5.10), (5.12), and (5.21), model uncertainty analysis is performed by the following procedure of data bootstrapping with resampled residuals. By using the data $\hat{\mathbf{d}}$ and residuals $\boldsymbol{\varepsilon}$ predicted by the optimal model, I construct a new data vector $\mathbf{d}^*$ with kth element equal $d_k^* = \hat{d}_k + \varepsilon_l$, where index l is selected randomly from the list $1,\ldots,N_d$ (where N_d is the total number of data points). This data vector $\mathbf{d}^*$ represents the result of a hypothetical measurement in which the earth (i.e., the standard model) is the same but new measurement errors are randomly drawn from the distribution of data errors found in the present model. By using the randomized data $\mathbf{d}^*$, a new solution $\mathbf{m}^*$ is found by eq. (5.21). The procedure is repeated 5000 times, giving a multi-dimensional empirical distribution of model parameters $\ln R_i$, $\ln S_j$, κ_S, ν_near, ν_far, and r (eq. (5.8)).

Figures 5.10 to 5.13 show simple assessments of the model trade-off by cross-plotting pairs of model parameters $\mathbf{m}^*$. In each of these cross-plots, two measures of model uncertainty are shown. First, by taking 5% and 95% quantiles of the distribution of each model parameter regardless of the values of other parameters, total confidence ranges for each variable is quantified (lines in Figures 5.10 to 5.13; Tables 5.1 to 5.4). These confidence ranges show the bounds on parameter values expected in the present dataset. The probabilities of model variables being below or above these ranges are close to 5%. Second, the shapes of these 2-D scatterplots indicate the mutual covariances, or trade-offs between the different model parameters. In particular, Figure 5.10 shows that q negatively trades off with κ_S (note the negative slopes of the clouds of bootstrapped models). Interestingly, both the q and κ_S are distinctly different for time-frequency amplitude variation models inverted from the horizontal-component and three-component vector (3C) amplitude data (compare Figures 5.10a and 5.10b to 5.10c). This difference is due to the much smaller κ and larger q for vertical-component amplitudes within the S-wave window. An important observation from Figures 5.10 to 5.12 is that although the median q values are small (corresponding to large $Q \approx 4170$ for transverse component, $Q \approx 4230$ in the H2C model, and $Q \approx 1850$ for 3C), they are distinctly different from the zero-attenuation level $q = 0$.

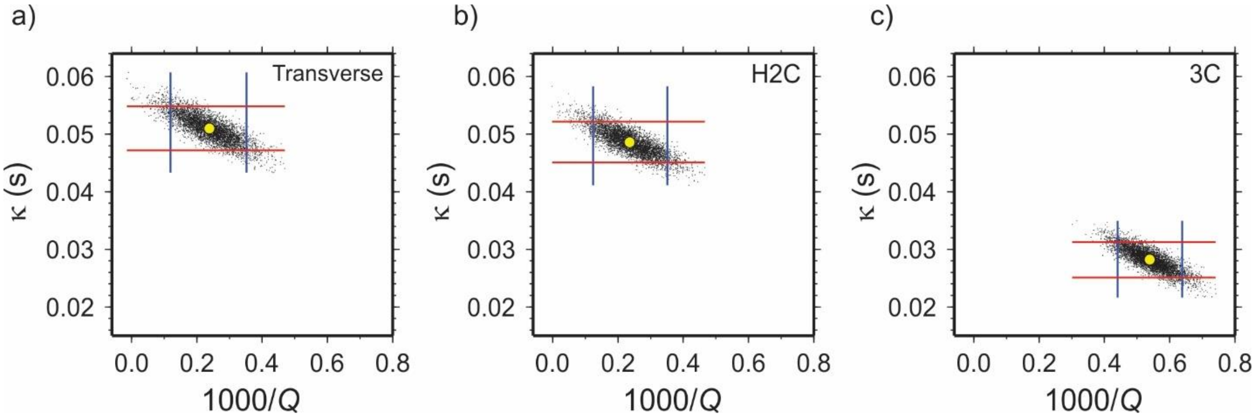

Figure 5.10. Scatterplots of κ (interpreted as κ_S for earthquake #1) values versus $1000q = 1000/Q$ from 5000 randomized inversions: a) for transverse-component amplitudes; b) H2C amplitudes; c) 3C amplitudes. Yellow (almost white in print) dots show the corresponding optimal model parameters, and lines indicate their 90% confidence intervals.

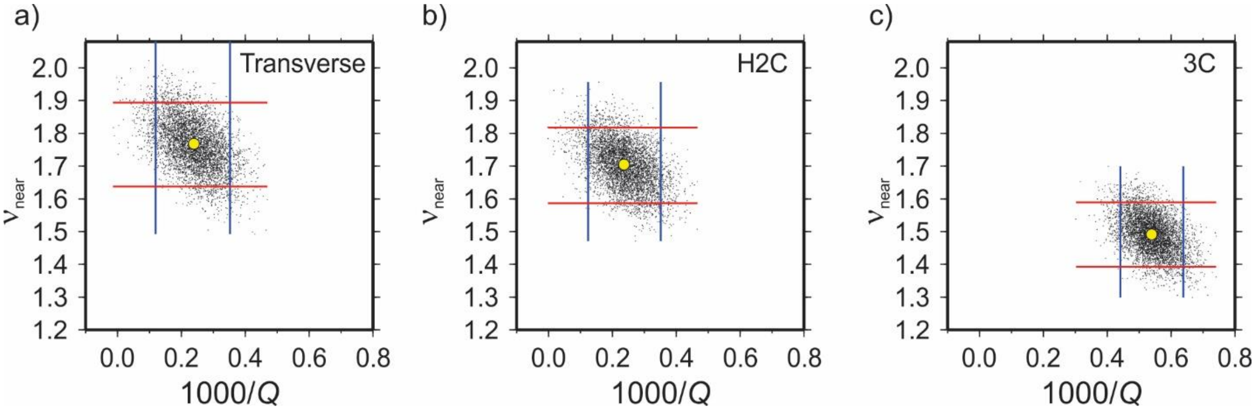

Figure 5.11. Scatterplots of parameters ν_{near} versus $1000q = 1000/Q$ from 5000 randomized inversions: a) for transverse-component amplitudes; b) H2C amplitudes; c) 3C amplitudes. Symbols and lines are as in Figure 5.10.

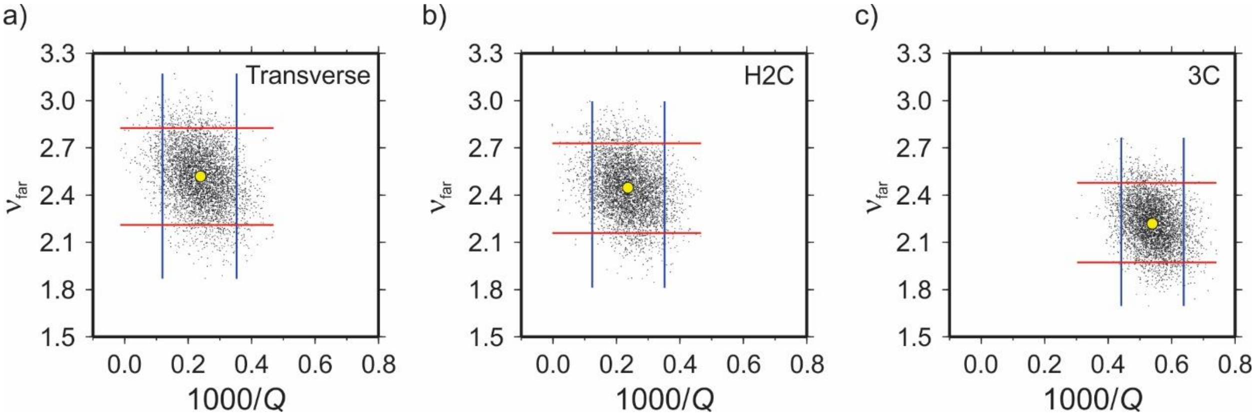

Figure 5.12. Scatterplots of parameters ν_{far} versus $1000q = 1000/Q$ from the randomized inversions: a) for transverse-component amplitudes; b) H2C amplitudes; c) 3C amplitudes. Symbols and lines are as in Figure 5.10.

In Figures 5.11 and 5.12, negative correlations of q with parameters ν_{near} (local geometrical spreading) and ν_{far} (regional geometrical spreading) are seen, although these correlations are weaker than with κ_S. The values of median ν_{near} are also different for the transverse-component ($\nu_{near} \approx 1.77$), H2C ($\nu_{near} \approx 1.70$), and 3C-amplitude models ($\nu_{near} \approx 1.49$). Both of these values are much larger than those used in existing standard models (Atkinson, 2004). For the median ν_{far}, the difference between the different types of S-wave amplitudes is smaller, but the values are large and exceed about 2.52 (for transverse component), 2.44 (for H2C), or 2.23 (for 3C) with 95% confidence (Figure 5.12). Note that these values are consistent with the geometrical-spreading exponents measured for coda waves by Jhajhria et al. (2017), which ranged from 1 to 3 with an average of 1.93. Finally, parameter *r* (characterizing the change of *G*(*t*) across the transition from local to regional distances) positively correlates with ν_{far} and is nearly the same for transverse-component, H2C, and 3C S-wave amplitudes (Figure 5.13).

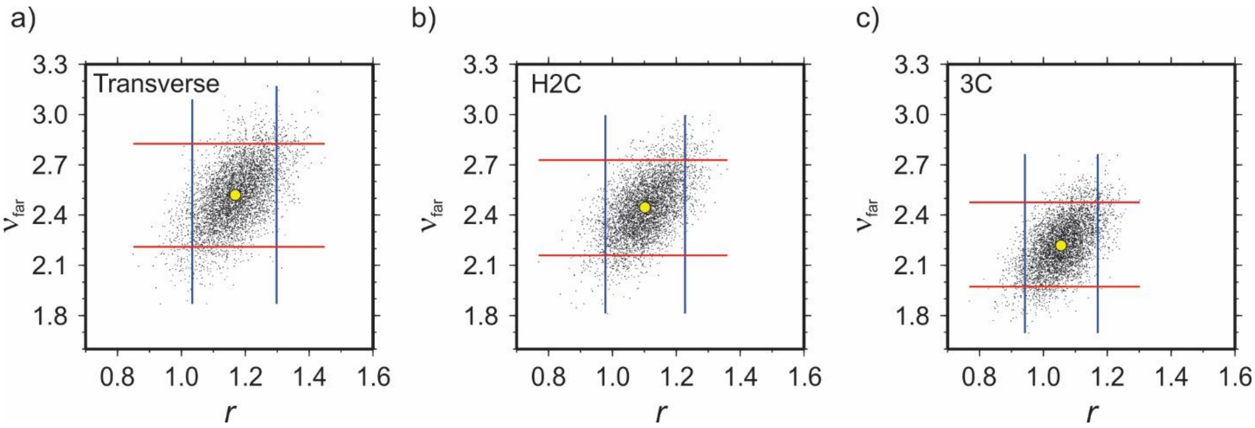

Figure 5.13. Scatterplots of parameters ν_{far} versus *r* from randomized inversions: a) for transverse-component amplitudes; b) H2C amplitudes; c) 3C amplitudes. Symbols and lines are as in Figure 5.10.

In addition to the single- and two-parameter variances, the complete model uncertainty can be characterized by the principal-component (PC) analysis. PC eigenvectors represent the directions of the strongest trade-offs (covariances) within the distribution of bootstrapped random models. These PC directions are obtained by calculating the covariance matrix for the ensemble of models $\mathbf{m}^*$:

$$M_{ij} = \sum_{n=1}^{N} s_i s_j \left(m_i^{*n} - \left\langle m_i^* \right\rangle\right)\left(m_j^{*n} - \left\langle m_j^* \right\rangle\right), \qquad (5.22)$$

where n is the model number, N is the total number of bootstrapped random models, $\left\langle m_i^* \right\rangle$ denotes the mean of all m_i^{*n} and $s_i = \sum_{n=1}^{N} \left[\sum \left(m_i^{*n} - \left\langle m_i^* \right\rangle \right)^2 \right]^{-1/2}$. The principal components of the distribution are given by normalized eigenvectors of this matrix sorted by decreasing eigenvalues.

Figure 5.14 shows ten largest PC eigenvalues accounting for the strongest variances of combined model parameters. In this figure, note that PCs #2 and #3 contribute variances of about 75% of that of the largest PC, and the rest of the PCs are below about 50% of the largest variance. The distribution of eigenvalues is nearly identical for all measures of wave amplitude (Figures 5.14a to c). Figure 5.15 shows how the two largest PCs are oriented among the parameters of the model. The leading PC principally consists of the coupling factor for the second source ($\ln S_2$), two kappa values (κ_{S1} and κ_{S2}), the values of ν_{near} and ν_{far}, and the q (marked by asterisks in Figure 5.15a). These six parameters represent the principal trade-off within the model. To summarize this trade-off, I observe that the least-constrained model perturbation (largest-variance eigenvalue) consists of approximately equal positive shifts in κ_{S1}, κ_{S2}, ν_{near}, a somewhat smaller shift in ν_{far}, and simultaneous negative shifts in q and $\ln S_2$. Interestingly, within the PC #1, parameters $\ln R_i$ show several correlated groups of 5–7 receivers (Figure 5.15a). These correlated groups could represent imperfectly constrained model-parameter trends as in Figure 5.8g (also seen in Figure 5.8f). In the PC #2, the trade-off mostly occurs between three site factors (asterisks in Figure 5.15b). To examine the interactions between only the earth-structure related parameters, I further extract from matrix **M** (eq. (5.22)) rows and columns corresponding to parameters κ_{S1}, ν_{near}, ν_{far}, r, and q. This extraction yields a simplified 5×5 covariance matrix in which the effects of all other variables are averaged.

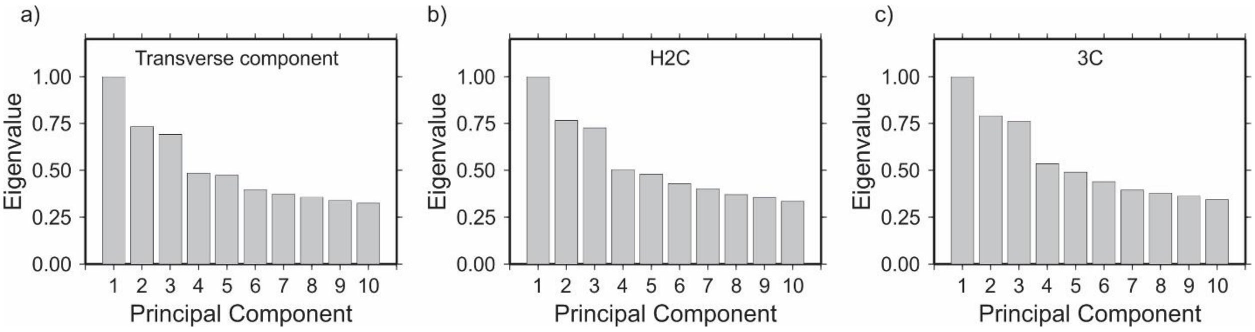

Figure 5.14. Eigenvalues corresponding to principal components of model uncertainty, relative to the largest eigenvalue: a) for the model based on transverse- component amplitudes; b) for model based on H2C amplitudes; c) for model based on 3C amplitudes.

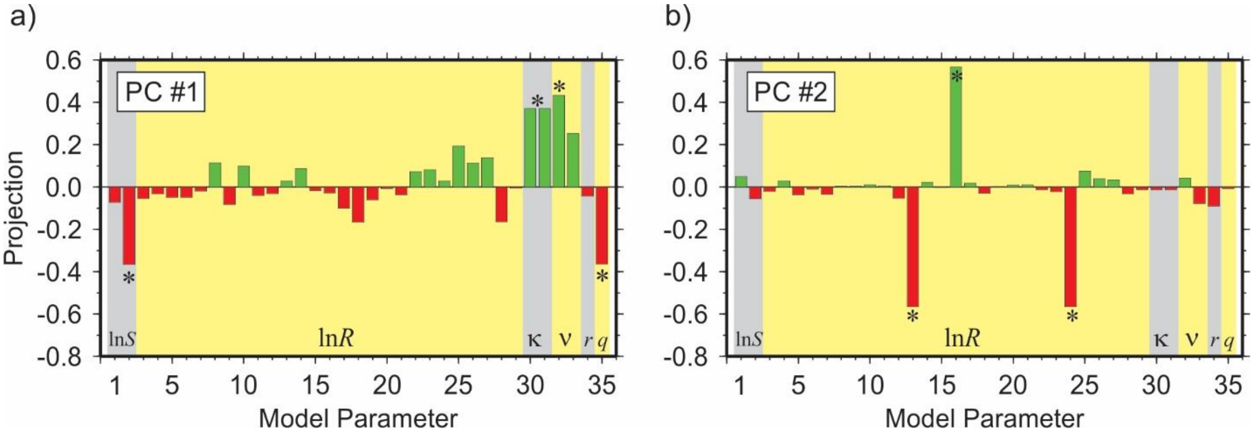

Figure 5.15. Two leading principal components of covariance matrix for the model of transverse-component amplitudes: a) and b) projections of the first and second largest principal components, respectively. Color/gray backgrounds and labels indicate groups of similar model variables, and asterisks indicate the most significant contributions to the principal-component vectors.

For this matrix, results of PC analysis are shown in Figures 5.16 and 5.17. These results are similar to the observations from the leading PCs of the full matrix (Figures 5.14 and 5.15). The distribution of leading variances (Figures 5.16) and mutual relations of the uncertainties of parameters (Figure 5.17) can be interpreted as principally related to the earth's crust and not to the distribution of sources and receivers. Thus, these five PCs represent an important part of the $\Phi(t,f)$, together with eq. (5.2) and the inverted values of model parameters.

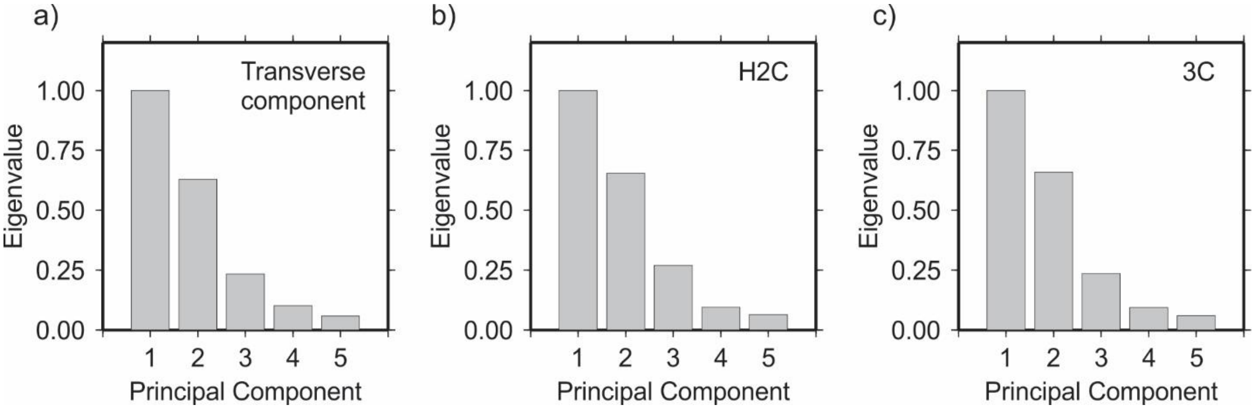

Figure 5.16. Eigenvalues of the five-parameter covariance matrix, relative to the largest eigenvalue: a) for the model based on transverse- component amplitudes; b) for model based on H2C amplitudes; c) for model based on 3C amplitudes.

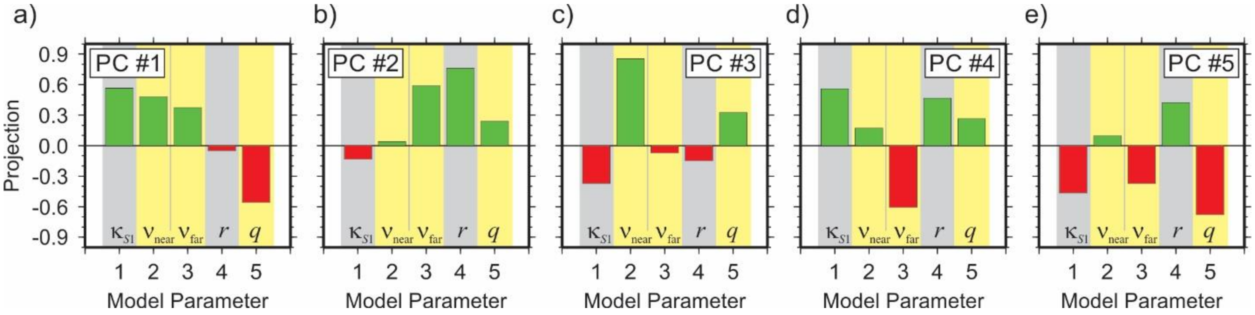

Figure 5.17. Principal components of the five-component covariance matrix for transverse-component amplitudes (panels a) to e)). The backgrounds and labels are as in Figure 5.15.

As shown in Figure 5.17a, the principal trade-off consists in a correlation between κ, ν_{near}, and ν_{far}, and an anti-correlation of these parameters with q. The second principal component contains a positive trade-off between parameters ν_{far} and r (Figure 5.17b).

5.6. Optimal Parameterization

The reduced 5×5 covariance matrix and its eigenvectors described at the end of section 5.5 allow deriving a new parameterization of the model that can be called optimal, or "data-driven." In contrast to eq. (5.2), this parameterization does not reduce to a product of elementary functions of *t*, *f*, and *tf*. Instead of this functional simplicity, the new parameterization consists of five factors that are statistically uncorrelated and do not mutually trade off.

To obtain the optimal parameterization, let us denote **V** a matrix combining the five normalized principal-component vectors (Figure 5.17) as columns. Next, let us present eq. (5.2) as

$$\ln \Phi_{ij}\left(t, f\right) = \ln \bar{\Phi}_{ij}\left(t, f\right) - \boldsymbol{\xi}\left(t, f\right)\left(\boldsymbol{\mu} - \bar{\boldsymbol{\mu}}\right), \tag{5.23}$$

where $\boldsymbol{\xi}$ is a time-and frequency-dependent, five-element matrix row (basis function) specified in the next paragraph, $\boldsymbol{\mu}$ is the earth-related part of the model vector in eq. (5.8):

$$\boldsymbol{\mu} \equiv \left(\kappa_S/\kappa_0 \quad \nu_{\text{near}} \quad \nu_{\text{far}} \quad r \quad q/q_0\right)^T, \tag{5.24}$$

$\bar{\boldsymbol{\mu}}$ is its value for some average model in the study area, and $\bar{\Phi}_{ij}(t, f)$ is the complete average standard model. For the average model, I can use the best-fit model derived in preceding sections or some "reference" model obtained, for example, from existing regional studies (e.g., Atkinson, 2012). In eq. (5.24), parameter κ_0 is introduced in order to make all elements of $\boldsymbol{\mu}$ dimensionless. It is convenient to select its value as $\kappa_0 = q_0 t_0 = q_0 x_0 / \beta$, where x_0 is the characteristic distance at which the ln$A(t,f)$ dependencies are compared (further in this section, I use x_0 = 10 km), t_0 is the corresponding characteristic time, β is the average (characteristic) S-wave velocity, and q_0 is the characteristic attenuation, for which I take $q_0 = 10^{-4}$.

The matrix-row basis function $\boldsymbol{\xi}$ in eq. (5.23) consists of the elements of matrix **L** related to the selected five model parameters (eq. (5.9))

$$\begin{aligned}
&\xi_1(t, f) = \pi\kappa_0(f - f_0), \\
&\xi_2(t, f) = \psi_{\text{near}}(t)(\ln t - \ln\tau_1), \\
&\xi_3(t, f) = \psi_{\text{far}}(t)(\ln t - \ln\tau_2), \\
&\xi_4(t, f) = -\psi_{\text{r}}(t), \\
&\xi_5(t, f) = \pi q_0 f t.
\end{aligned} \tag{5.25}$$

In these expressions, the reference frequency f_0, the travel-time interval of amplitude amplification $[t_1,t_2]$, and basis functions ψ_{near}, ψ_{far}, and ψ_{r} are defined in section 5.2.2 (where I also take $f_0 = 10\ \text{Hz}$). Note that the selections of f_0, x_0, and q_0 only affect the units and numerical values of the model parameters but not the functional dependencies of ln$\Phi_{ij}(t,f)$. The deviation of model $\boldsymbol{\mu}$ from $\bar{\boldsymbol{\mu}}$ is a linear combination of the principal components, which can be written as matrix product

$$\boldsymbol{\mu} - \bar{\boldsymbol{\mu}} = \mathbf{V}\boldsymbol{\mu}^{\text{opt}}. \tag{5.26}$$

In this notation, elements of vector $\boldsymbol{\mu}^{\text{opt}}$ represent contributions from the individual principal components. Substituting eqs. (5.23) and (5.26) into eq. (5.2), I obtain the desired optimal parameterization of $\Phi_{ij}(t,f)$:

$$\Phi_{ij}\left(t,f\right)=\bar{\Phi}_{ij}\left(t,f\right)e^{-\boldsymbol{\xi}\left(t,f\right)\mathbf{V}\boldsymbol{\mu}^{\text{opt}}}. \tag{5.27}$$

This expression can be interpreted in a very general sense of a perturbation- (scattering-) theory approximation (Morozov, 2010a). Equation (5.27) also reveals the origins of both the conventional Q and kappa models. For example, if $\bar{\Phi}_{ij}\left(t,f\right)$ is adopted as a reference model (containing some form of geometrical spreading, Brune's source spectra and hypothetical delta-function site responses), then factor $e^{-\boldsymbol{\xi}\left(t,f\right)\mathbf{V}\boldsymbol{\mu}^{\text{opt}}}$ represents the deviation from this reference model, or "perturbation." Parameters $\boldsymbol{\mu}^{\text{opt}}$ in this equation represent both elastic and anelastic effects and include the conventional $q \equiv Q^{-1}$, κ, and also variations of ν.

As noted in section 5.5, parameters q, κ, and ν trade off with each other, but parameters μ_k^{opt} (k^{th} elements of vector $\boldsymbol{\mu}^{\text{opt}}$) do not. Therefore, parameters μ_k^{opt} and eq. (5.27) represent a unique and "natural" parameterization of the standard S-wave amplitude model independent of mathematical conventions and subjective theoretical assumptions. Analogously to the sine and cosine functions in the Fourier transform, these functions are "orthogonal" in the sense of representing mutually uncorrelated model parameters for the given earth structure and source-receiver geometry.

For comparison with conventional models, matrix products in eq. (5.27) can be written explicitly as

$$\begin{aligned}\Phi_{ij}\left(t,f\right)=\bar{\Phi}_{ij}\left(t,f\right)\exp\Big[&-p_1\left(t,f\right)\mu_1^{\text{opt}}-p_2\left(t,f\right)\mu_2^{\text{opt}}-p_3\left(t,f\right)\mu_3^{\text{opt}}-\\&-p_4\left(t,f\right)\mu_4^{\text{opt}}-p_5\left(t,f\right)\mu_5^{\text{opt}}\Big].\end{aligned} \tag{5.28}$$

In this form, parameters μ_1^{opt} through μ_5^{opt} are analogous to parameters b_1, b_2, b_3, and c_4 by Atkinson (2004, 2012), and functions $p_k\left(t,f\right)$ replace the power-law functions within the corresponding distance intervals. Although these functions are not represented by simple mathematical expressions, they can be easily evaluated numerically as shown in Figure 5.18.

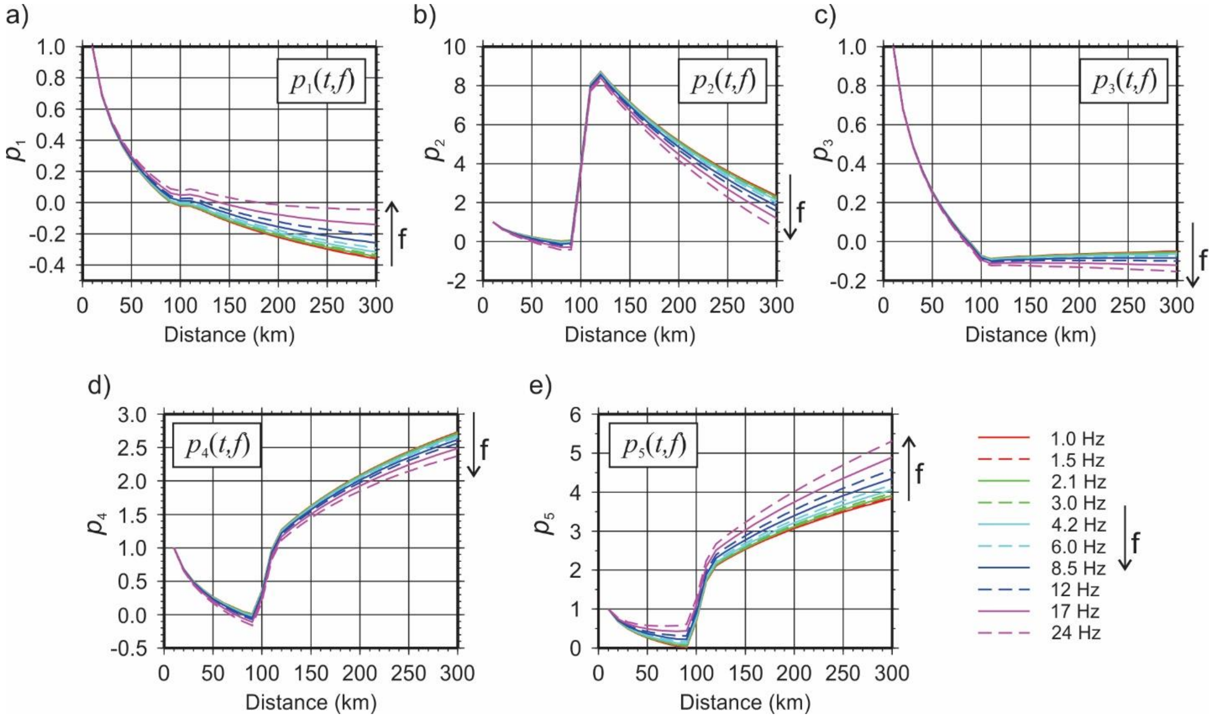

Figure 5.18. Distance dependencies of the principal components of optimal parameterization (plots a) to e)) at different frequencies (line colors; legend). All dependences are normalized at epicentral distance 10 km. To aid in gray-scale viewing, on the right of each plot and legend, arrows labeled ‘f’ indicate the directions of increasing frequency for the different curves.

With all $\mu_k^{\text{opt}} = 0$, the best-fit model $\bar{\Phi}_{ij}\left(t, f\right)$ is obtained (solid lines in Figure 5.8a), and nonzero μ_k^{opt} give independent variations of this model. As Figure 5.18 shows, the first and third principal components (parameters μ_1^{opt} and μ_3^{opt}; plots a) and c)) dominate the local distance region ($x < 90$ km), and the second component (μ_2^{opt}; Figure 5.18b)) is strong near the beginning of the regional-distance interval ($x > 115$ km).

Frequency dependencies are combined with time dependencies in these functions. The strongest frequency dependencies are seen at the largest distances for the first and fifths principal components (Figure 5.18a and Figure 5.18e). This observation again shows that as mentioned in the *Introduction* section, the frequency-dependent amplitude decay rates are different at the local and regional distances, and therefore they cannot be described by a common *Q*(*f*). This assumption of a common *Q*(*f*) appears to be the principal difficulty of conventional parametrizations (Atkinson, 2012; Fisk and Phillips, 2013b).

5.7. Discussion

Following Morozov (2008b, 2010a, 2010b), the methodological recommendation from the above analysis for standard-model studies is to avoid under-parameterization of their frequency-independent parts and to allow the elastic limit $Q^{-1} = 0$. Model parameterizations should be data-driven and represent the observations from the dataset. “Feature-agnostic” parameterizations using no specific knowledge of the wave-propagation problem can be used, such as the “nonparametric” parameterizations of $G(t)$ (eq. (5.2)). However, nonparametric models also consist of selections of sampling, regularization strategies, and smoothing parameters that may be difficult to select and verify (section 5.2). In this chapter, I used a five-parameter model for $G(t)$ reflecting the shapes of the observed $A(t,f)$ dependencies (Figure 5.1). Note that while being more economical than nonparametric sampling of the distance range (e.g., Castro et al., 1990; Oth et al., 2011), this parameterization considers more detailed forms of $G(t)$ (Figure 5.2) and requires no smoothing.

It is often assumed that “data-driven” inversion always requires large data volumes (e.g., Trugman and Shearer, 2018). However, the effect of data volume is not always so simple. For under-parameterized and underfitted models such as the $G(t)$ part of eq. (5.2), using larger datasets may complicate identification of important features in the data and even make them unrecognizable. For example, if considering a large dataset such as in Figure 4 in Atkinson (2004), the short $[t_1,t_2]$ amplitude-amplification interval may become difficult to recognize due to different locations of ray paths and variable source and receiver terms. Similarly, if numerous station terms R_i are disregarded when inverting for $G(t)$, the resulting data misfits are large and create a distribution of errors in which the $[t_1, t_2]$ interval would again be smeared. Inversions of large datasets also contain implicit weighting of the contributions from different epicentral distance ranges. For example, most existing standard models for ground motion are dominated by regional distances (beyond 150 km, where the observations are abundant) and poorly match the $A(t,f)$ at local distances (< 100 km). Atkinson (2012) also showed this regional dominance in Figure 4 in that paper.

Thus, smaller and localized datasets with non-uniform source-receiver coverage are useful for designing model parameterizations, weighting, regularizations, constraints, and for testing inversion techniques. For a large dataset, it may also be useful to examine parts of it (such as common-receiver or common-source subsets) separately in order to recognize wavefield patterns and determine the optimal parameterizations and inverse methods.

Another general recommendation from this chapter and also from Morozov (2008b, 2010a, 2010b) is to use the frequency independent q and to combine its inversion with inverting for κ. The constraint q = const is key for deriving a robust solution. This constraint appears to be the only way to render uniqueness and a simple physical meaning to q as a measure of the frequency- and wave-path related part of $\Phi(t,f)$. By contrast, if treating Q as frequency- and even travel-time dependent (Graizer, 2017; Calvet and Margerin, 2013), or κ as distance-dependent (Anderson, 1991), almost any part of the observed $\Phi(t,f)$ (eq. (5.2)) can be attributed to either $Q = \pi f / \left(const - \ln \Phi \right)$ or $\kappa = const - \ln \Phi / \pi$. As illustrated in the above discussion of the source and site spectra (5.3.3), the net effect of the frequency-dependent Q is smaller than the uncertainties inherent in the $s(f)$ and kappa filters. The effect of the frequency-dependent Q on $\ln A$ is also close to data residuals (Figure 5.3). These comparisons show that the $Q(f)$ in standard models generally represents an over-parametrization that can and should be avoided.

The model of this chapter represents only the basic 1-D case and requires additional detail and extensions in other studies. In particular, in larger geographical areas, path effects (G and q) need to be replaced with tomographic models and may become anisotropic. To account for the observations of frequency-dependent near-critical reflections appearing in $\Phi(t,f)$ dependencies at about 100–120 km distances (Oth et al., 2011, and this chapter) frequency-dependent geometrical spreading $G(t,f)$ (Yang et al., 2007) may be needed in eq. (5.2). Such effects may be suggested by the increased $\ln A$ residuals from ~100 to 200-km distances in the present data (Figure 5.3a). Source and receiver site effects (κ_S and κ_R) may similarly become anisotropic, and path bending and multipathing may need to be included at longer source-receiver distances.

Although illustrated on a single and relatively small dataset, key observations of this chapter is methodological and apply to the general approach to constructing standard model by factorization of recorded amplitude spectra (eq. (5.2)). Because of inverting many model parameters from a single least-squares measure of log-amplitude data fit, the values of the resulting parameters and their uncertainties and trade-offs depend on how the models are constructed. For an adequately parameterized model, its uncertainties are of statistical nature, similar to any other physical measurement. This type of uncertainties can be used to produce a model-independent parameterization determined by the structure of the available dataset (eqs. (5.27) and (5.28)). Estimates of statistical uncertainties can also be used for designing seismic experiments. However, for under-parameterized and “over-under-parameterized” models, strong trade-offs occur with parameters fixed by convention, such as the geometrical-spreading exponent $b_3 = 0.5$ at regional distances by Atkinson (2004, 2012). Allowing a frequency-dependent $Q(f)$ reduces but does not completely remove the effects of such under-parameterization and leads to models with hidden biases and “footprints,” such as shown by the distance-correlated site coupling (amplification) terms and data errors (Figures 5.8e and 5.8g). For practical applications, the most important detrimental effect of such under-parameterization is in inaccurate data fitting at local distances (Atkinson, 2012). To remove these biases and inaccuracies, more flexible parameterizations should be used.

Unfortunately, the problematic “over-under-parameterization” feature can be seen in most current models for wave amplitudes. Parametric models (e.g., Aki and Chouet, 1975; Atkinson, 2004, 2012; Fisk and Phillips, 2013a, 2013b) postulate stringent forms of geometrical spreading, and consequently they suffer from parameter trade-offs most. The “nonparametric” approaches (e.g., Castro et al., 1990; Drouet et al., 2008; Oth et al., 2011) also contain an aspect of under-parameterization in the form of selected smoothing operators (see detailed discussion of this point and of the general model-constraining methodology in section 5.2). Another limitation of most existing models is in attaining the solution by minimizing only a single number, which is the least squared data error, sometimes modified by smoothing or proximity to “prior” models. Nevertheless, seismic data are complex and usually require multiple data-fit and model-quality criteria.

Thus, my general recommendation for many types of studies in various areas around the world is to: 1) start from a parameterization of $G(t)$ (eq. (5.2)) that would allow a near-elastic (with small Q^{-1}) interpretation of the data, and then 2) improve the data fit by using a constant Q and employing additional model-quality criteria. Inferences of a frequency-dependent $Q(f)$ can often be viewed as indicators of uncontrolled trade-offs in model parameterization and insufficiently detailed data fitting (Morozov, 2008b, 2010a). Models with constant Q have well-defined physical meanings supported by perturbation-theory rationale (Morozov, 2010a), and they often yield more accurate and detailed data fitting than $Q(f)$ models. For example, as shown in Figure 5.8, the same data are fit more closely (and across the entire epicentral-distance range) by the constant-Q (q) model (Figure 5.8a) than by a model with a frequency-dependent Q (Figures 5.8b and 5.8c). This comparison means that the entire frequency dependence of Q lies within the unconstrained statistical parameter trade-off. For example, assume that I create an analog of Figure 5.11 for q taken at a fixed frequency, such as for $Q(1\text{ Hz}) = Q_0 \approx 99$ derived from these data by conventional methods (Safarshahi et al., 2013). Because both models satisfy the least-squares criterion for $\ln A(t,f)$ data, parameter trade-off extends from this Q_0 and its assumed counterpart of $\nu = 1$ all the way to the point ($Q = 4000$, $\nu = 1.77$) in Figure 5.11. In a different way, the unconstrained character of $Q(f)$ for these data is illustrated in subsections 5.3.4.

5.7.1. Multi-step procedures and constraint equations

In this subsection, I show that although rarely examined explicitly, certain forms of constraints (eq. (5.11)) determine the forms of most existing attenuation models (e.g., Castro et al., 1990; Atkinson, 2004, 2012; Fisk and Phillips, 2013a, 2013b; Graizer, 2017). These constraints are also responsible for insufficient accuracy of many existing models across the local to regional distance ranges, which was noted by Atkinson (2012).

All of the conventional approaches can be reproduced by the general eqs. (5.10) and (5.11). The implicit constraints are often implemented by multi-step procedures, in which only a subset of model parameters is varied during each step. For a specific example, let us consider "parametric" standard models with frequency-dependent $Q(f)$, such as by Castro et al. (1990), Atkinson (2004), Fisk and Phillips (2013a, 2013b), or Graizer (2017). In the notation by Atkinson (2004), during the first two inversion steps, the source factors S_j are related to earthquake magnitudes M as $\lg S_j = c_1 + c_2(M-4) + c_3(M-4)^2$, and receiver factors R_i and factors containing kappas are disregarded. These assumptions mean that constraints $\ln R_i = 0$ and $\kappa_S = \kappa_R = 0$ are imposed on the inverse, and eq. (5.8) reduces (in terms of decimal logarithms) to

$$\lg \Phi_{ij} = \lg S_j - b \lg x - c_4 x \,. \tag{5.29}$$

In this equation, $x = \beta t$ is the source-receiver distance, β is the average S-wave velocity, and $b = \nu_1$, ν_2, and ν_3 within each of the three selected distance ranges $x < X_1$, $X_1 < x < X_2$ $x \in \left[X_1, X_2\right]$, and $x > X_2$, and c_4 is an additional model parameter. Parameters b are interpreted as properties of the geometrical spreading $G(t)$ (eq. (5.9)), but c_4 is (by convention) attributed to the Q-factor as: $c_4 = q\left(f_b\right)\pi f_b \left(\lg e\right)/\beta$, where f_b is the fixed measurement frequency. Note that due to such definition, the Q obtains a built-in increase with frequency $Q\left(f_b\right) \propto f_b$:

$$Q\left(f_b\right) \equiv q^{-1}\left(f_b\right) = f_b \frac{\pi \lg e}{\beta c_4}. \tag{5.30}$$

In the first step of the inversion by Atkinson (2004), parameters b_1 and b_2 are estimated by using only the data at frequencies below 10 Hz, keeping $c_4 = 0$, and fixing the value of $b_3 = 0.5$ at distances $x > 150$ km. To implement this step with the current dataset, I similarly set $\nu_3 = 0.5$ and minimize the data error by grid search varying v_1 between 1.0 and 1.6, ν_2 between –0.5 and 0.5, X_1 between 50 and 100 km, and X_2 between 100 and 200 km (Atkinson, 2004). For each amplitude type, an optimal combination of these parameters is found by minimizing the following misfit function:

$$F\left\{\varepsilon_i\right\} = w \times median\left\{\left|\varepsilon_i\right\|_{\varepsilon>0}\right\} + median\left\{\left|\varepsilon_i\right\|_{\varepsilon\le 0}\right\}, \tag{5.31}$$

where $\varepsilon_i \equiv \ln A_i^{\text{data}} - \ln A_i^{\text{model}}$ is the fitting error of i^{th} data point. The use of statistical (median) measures reduces the sensitivity of F to data outliers and anomalous values of receiver site effects. Weight w in eq. (5.31) causes this optimization procedure to prefer models close to the upper bound of $\ln A_i^{\text{data}}$ (Figure 5.19a). Such fitting along the upper limit of $\ln A_i^{\text{data}}$ is usually achieved by using larger (more uniformly distributed) datasets with fixed $\nu_3 = 0.5$ (b_3 in Atkinson (2004)). By using weight $w = 2$ (eq. (5.31)), I obtain a $G(t)$ dependence similar to Atkinson's (2004) (Table 5.7). However, as Figure 5.19a clearly shows, the constraint $\nu_3 = 0.5$ is *ad hoc* and not well justified beyond 100-km epicentral distances.

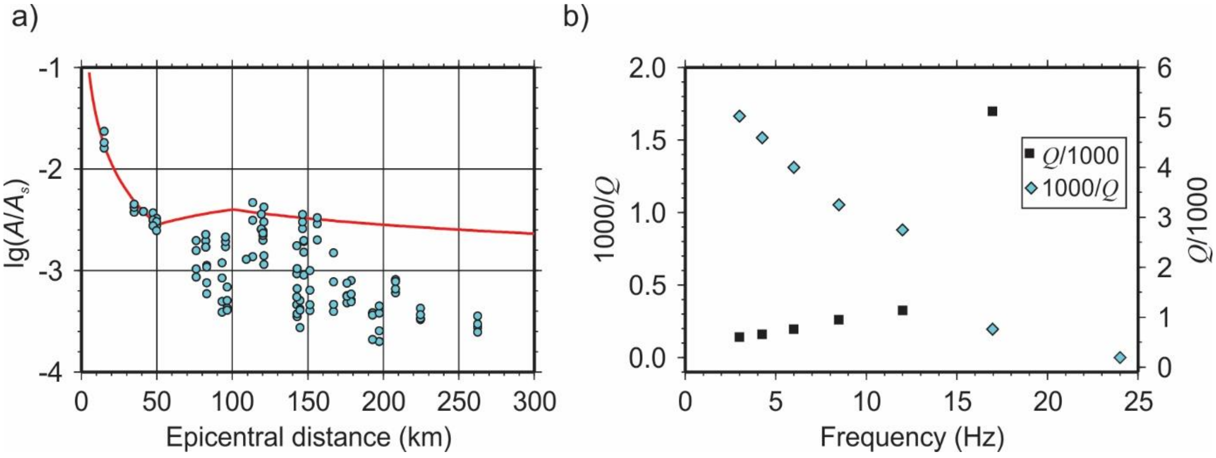

Figure 5.19. Inversion of $A(t,f)$ data for transverse-component amplitudes using the method by Atkinson (2004): a) Geometrical-spreading model (red line) obtained by fitting ln$A$ data at frequencies below 10 Hz (circles); b) $q = 1/Q$ (diamonds) and Q (squares) obtained by inversion for q at individual frequencies.

Table 5.7. Parameters of optimal geometrical-spreading models for S waves of this study.

Amplitude type	X_1	X_2	b_1	b_2	b_3
Transverse-component	50	110	1.2	-0.5	0.5
H2C	50	110	1.0	-0.1	0.5
3C	80	150	1.2	-0.3	0.5

The second and key step of conventional inversion consists in: 1) considering each individual frequency f_b separately, 2) subtracting the interpreted geometrical spreading from the data (eq. (5.9)) as $\ln a'_{ij} \equiv \ln a_{ij} - \ln G\left(t_{ij}\right)$, 3) constraining $\ln R_i = 0$, $\nu_{\text{near}} = \nu_{\text{far}} = 0$, and $\kappa_R = \kappa_S = 0$ in eqs. (5.8) and (5.9), and 4) inverting for only $\ln S_j$ and q (i.e., c_4 in eq. (5.29)). By implementing these constraints in eq. (5.11), the values of q and $Q \equiv q^{-1}$ values are obtained, as shown in Figure 5.19b. Similar to Atkinson (2004) and Safarshahi et al. (2013), the resulting $Q(f_b)$ steeply increases with f_b.

Lines in Figure 5.20a show the variations of $\ln A(t,f_b)$ predicted by this model. These lines are closer to the data than $\ln G(t)$ in Figure 5.19a, which is usually viewed as an effect of Q (Atkinson, 2004). However, a plot of ln$A$ data errors versus source-receiver distance and frequency (Figure 5.20b) reveals problems with this two-step, "over-under-parameterized" inverse. The data residuals correlate with both distance (gray line in Figure 5.20b) and frequency (symbols). The effect of the Q (vertical span of model lines in Figure 5.20a) is comparable to the correlated data errors (line in Figure 5.20b), which shows that the Q may represent a remapping of errors in the under-parameterized part of the model. Note that similar correlations of data residuals with source-receiver distances are present in published models, for example in Figures 6 to 9 by Atkinson (2012).

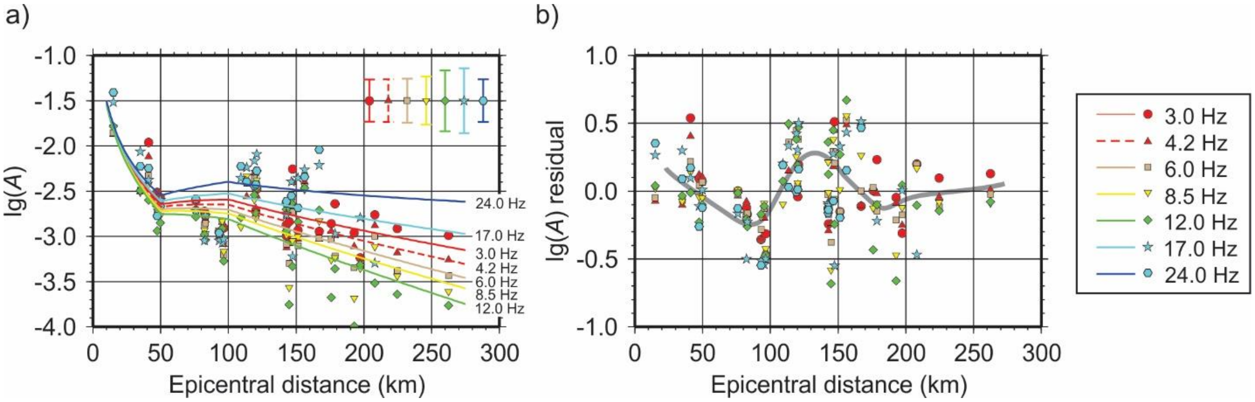

Figure 5.20. Inversions of transverse-component S-wave amplitudes with fixed $G(t)$ (Figure 5.19a) and frequency values f_b: a) Distance dependencies at several f_b (labeled lines). Symbols are the lg$A$ data with source terms subtracted. Standard deviation of data residuals are shown by error bars in the upper-right corner. b) Data residuals vs. source-receiver distance. Thick gray line in b) indicates a trend of the lg$A$ data residual with distance. Frequencies f_b are given in the legend.

Oth et al. (2008) gave another interesting example of real and synthetic data showing how nonparametric inversion for a frequency-dependent Q produces unstable results in cases of non-uniform source-receiver distributions. By separating the attenuation laws at closer and farther distances (i.e., effectively increasing the parameterization of ln$G(t)$), Oth et al. (2008) achieved stability and obtained reasonable (from their point of view) results of $Q(f) \approx 114 f^{0.96}$ and $Q(f) \approx 72 f^{1.12}$ for S waves in a region of Romania.

The observations in the preceding two paragraphs suggest the general meaning of the widespread frequency dependence of $Q(f)$ – it represents a correction for under-parameterized elastic-wave (geometrical) spreading (Morozov, 2008b, 2010a). For example, the mentioned $Q(f)$ by Oth et al. (2008) are nearly proportional to f, which means (combined with $\kappa = 0$ assumed during this step) that the source-receiver response corrected wave amplitudes $\Phi(t,f)$ are practically frequency-independent (eq. (5.2)). Therefore, wave propagation within this region is nearly elastic, and the “physical” Q for the crust should be much larger than $Q_0 = 114$ and 72 above. The contribution of the “true” q of the Earth’s crust is still unclear in these results.

In kappa studies, the second step of inversion is performed differently, by normalizing the amplitude spectra, setting $q = 0$, but allowing a distance-dependent κ_R instead of the frequency-dependent Q (Anderson, 1991). Nevertheless, the fundamental structure of the model (eqs. (5.8) and (5.9)) remains the same. Distance dependences of κ_R are still explained by Q along crustal wave paths (Anderson, 1991; Ktenidou et al., 2014).

In the third common step of conventional approaches to wave-amplitude models (eq. (5.2)), parameters S_i and R_i, source spectra, corner frequencies, and kappas are inverted from data residuals (Castro et al., 1990; Atkinson, 2004; Oth et al., 2011; Fisk and Phillips, 2013a, 2013b). However, due to coupling between most of the parameters S, R, ν, κ, q, and spectra $A_S(f)$ (eqs. (5.1) and (5.2)), results of these procedures again contain intricate remappings of data errors, such as shown in Figure 5.20b. Strong algorithm dependencies of multi-step inversion procedures were also noted by Oth et al. (2008), who combined the second and third steps above.

Thus, the outcomes of conventional multi-step inversions depend on the sequences of operations, theoretical assumptions, selection of weighs, and other details of algorithms. Because of the uniqueness of each dataset, it seems hardly possible to rigorously compare different inversions or to propose a universal recipe for such multi-step inversion. It appears that the only way to achieve a simple and consistent procedure is to utilize joint inversion for all parameters S_j, R_i, ν, κ, q, and source functions $A_S(f)$ simultaneously. In addition, we should not only rely on simple data averaging and least-squares inversion but need to consider explicit criteria of model quality, as done in this chapter.

5.8. Conclusions

By using a flexible and assumption-free time/frequency parameterization, rigorous inversion method, and taking measures to control the spurious biases within the model, empirical time/frequency dependencies of S-wave amplitudes are measured from a dataset in southeastern Iran. The resulting model predicts the amplitude data with better or similar accuracy compared to the conventional models, and it also shows a better distribution of data residuals uncorrelated with distance and frequency. The model also exhibits significant differences from a previous model for the same area. These general observations may likely apply to other areas around the world.

Specifically, the frequency-independent and frequency-dependent (kappa and Q-type) attenuation for orientation-independent horizontal (H2C) and three-component (3C) S-wave amplitudes is somewhat weaker than for transverse-component amplitudes. The geometrical (frequency-independent) spreading of S waves is much faster than usually assumed and depends on the travel time t (for orientation-independent horizontal component of ground motion) as about $t^{-1.7}$ at distances less than 90 km and $t^{-2.45}$ at greater than 115 km. Between these distances, the amplitude increases by a factor of about three, which is interpreted as an effect of reflections from the deep crust and/or the Moho. High-frequency spectral parameters kappa range within approximately 30–50 ms. The kappa may be associated with either receiver site responses or source spectra. With accurate geometrical-spreading, kappa, and source-spectral models, the apparent Q-factor is nearly frequency independent and exceeds 2000, with the maximum-likelihood value of about 4000. For vertical-component ground motions within the S-wave window, the Q is lower (about 1500) and kappas are much lower (4 – 6 ms).

Extending the results of the model, I argue that in order to obtain a robust model for time- and frequency dependent seismic-wave amplitudes, the frequency-independent part of the model (effective geometrical spreading) should be parameterized more flexibly. In particular, the transition between local and regional distance ranges may contain a relative amplification and a change in the geometrical-spreading decay rate. With sufficiently flexible geometrical spreading, data fitting is improved at both local and regional distances. Only a frequency-independent Q is needed to explain the amplitudes across the entire epicentral-distance range.

In section 5.5, two types of model parameter trade-offs are evaluated for the model. The first type of trade-off is related to the common practice adopted in most current studies, in which an under-parameterized model for geometrical spreading is combined with a frequency-dependent Q-factor. In this case, strong parameter trade-offs are always inherent in the resulting model. These trade-offs involve parameters that are rarely analyzed, such as correlations of receiver coupling with epicentral distance and biases in median data residuals. To control these unacceptable trade-offs, additional constraints can be imposed on the model.

The second type of model-parameter trade-off occurs with sufficient parameterizations and is due to the usual random measurement errors in the data. This trade-off is clearly seen in the model but moderate in magnitude. Detailed statistical analysis shows that all inverted properties are adequately resolved. By using the principal-component analysis, an optimal (trade-off free) parameterization of the time- and frequency dependent seismic amplitudes is derived.

CHAPTER 6

ANALYSIS OF SEISMIC CODA I: EAST INDIAN SHIELD

In this chapter and the following chapter 7, I describe two cases of detailed analysis of seismic coda in Iran and India. Coda waves form long, slowly decaying tails of seismic records which are often used for characterizing the physical properties of the crust beneath the receiver (chapter 2). Because coda measurements require only a single station and not many earthquakes, they represent one of the most common seismic observations. However, as noted by Morozov (2008b, 2010a), a significant controversy exists about the key property used in coda interpretation, which is called the "frequency-dependent coda *Q*", or Q_c. This controversy of the concept of the *Q*-factor extends far beyond the coda research area. For example, frequency dependencies of seismic *Q* are important for the analysis of body waves (chapter 5), measurements of the high-frequency parameter kappa, attenuation corrections in reflection seismic imaging, and even for laboratory measurements of seismic *Q* in rock samples.

In this chapter, I describe the current methodology of coda measurements, explain its controversy and problems, and present an alternate approach using the concept of temporal attenuation coefficients (Morozov, 2008b). This approach was also the basis of the data analysis in chapter 5. Using this approach, I re-interpret the results of a single-station study from eastern India, recently published by Singh et al. (2019). The new interpretation is drastically different from the one proposed by Singh et al. (2019), and it reveals a nearly elastic (low-attenuation) character of wave seismic propagation within the Indian Craton. Similar observations for the tectonically active area of Zagros will be made in chapter 7. The near-elastic character of codas is a novel and most important observation which has still not been recognized in earthquake studies.

The results of this chapter were published in the following paper:

- Morozov, I. B, and Safarshahi, M. (2020). Elastic character of seismic coda envelopes within east Indian shield. Pure and Applied Geophysics, **177**, 5799–5818, DOI: 10.1007/s00024-020-02600-2

The copyright for this paper belongs to Springer Nature Switzerland AG, which allows authors to use their papers in their dissertations. My contributions to the paper consisted in preparing the data, modeling, and participation in interpretation and writing. The text of the above paper was expanded, modified, and reformatted for inclusion in this dissertation.

6.1. Introduction: Meaning of the Seismic *Q*-factor

In a continuously growing number of studies of seismic codas from local and regional earthquakes, frequency-dependent coda Q (denoted $Q_c(f)$ here) is measured for numerous areas. The observed Q_c is usually explained by a similar "quality-factor" property of the Earth, which is further subdivided into S-wave and P-wave, intrinsic, scattering, and other types of Q. However, despite the long history and routine use of seismic quality factors, their physical meanings and particularly frequency dependencies are still poorly understood. Apart from the general trust in the "Q" notation, physical interpretations of Q_c are only supported by theoretical models of scattering on small random heterogeneities in macroscopically-homogenous media (e.g., Fehler and Sato, 2003). Application of these models to practical Q_c measurements always involve a major approximation, which consists in disregarding the key elastic structures of the study areas, such as the crust-mantle boundary, crustal layering, and velocity gradients. The impact of this approximation on Q_c measurements is rarely examined. Nevertheless, in cases where such assessment was performed (Morozov, 2008b, 2010a), selections of the elastic-structure model and other processing parameters were shown to dominate the resulting $Q_c(f)$ dependencies. With more accurate elastic structure, the values of $Q_c(f)$ at $f = 1$ Hz often increase by 20–30 times, and its frequency dependence changes from nearly proportional to f to a constant (Morozov, 2008b).

Unraveling the physical meanings and frequency dependencies of seismological Q-factors is a difficult task that is far from completion. Eleven years ago, Pure and Applied Geophysics initiated a discussion of this topic (Mitchell, 2010), and the present study (Morozov and Safarshahi, 2020) is a continuation of this discussion inspired by a recent paper in the same journal (Singh et al., 2019). As a careful implementation of the current coda Q methodology, the results by Singh et al. (2019) clearly highlight its problems, even though these authors did not point these problems out. The paper by Singh et al. (2019) was notable for its detail of model presentation and for attempting tomographic inversion to constrain the spatial variations of the frequency-dependent

Q_c. Similar to most researchers, Singh et al. (2019) summarized their frequency-dependent $Q_c(f)$ by an empirical scaling relation, $Q(f) = Q_0 f^{\eta}$ where f is the observation frequency in Hertz, $Q_0 = Q(1\text{ Hz})$, and exponent η is close to one. Therefore, revisiting these results should also help understanding the causes of such commonly found behavior of the Q-factor.

The notation 'Q' and the common usage of the term "attenuation" in physics usually refer to amplitude decays $A(f,t)$ in some oscillatory processes in which the relative mechanical-energy loss is proportional to the number of oscillation cycles. This proportionality is represented by defining the inverse Q-factor as (chapter 7; Aki and Richards, 2002)

$$Q^{-1} = \frac{1}{2\pi}\frac{\Delta E}{E}, \tag{6.1}$$

where E is some measure of average mechanical energy of a rock volume (specifically, Aki and Richards (2002) use the peak elastic energy), and ΔE is its reduction after one loading/unloading cycle $\Delta T = 1/f$. In practice, quantities E and ΔE are difficult to measure and even to evaluate theoretically, but Q^{-1} is nevertheless recognized by the characteristic dependence of wave amplitude on the travel time t and frequency f: $A(f,t) = A_0 \exp\left(-\pi Q^{-1} f t\right)$. In this dissertation, I refer to such amplitude decays as "Q-type" attenuation, and call "non-Q" any other variations of $A(f,t)$ depending on f or t separately.

Seismic coda is clearly produced by waves reflected and scattered within the crust or mantle, but is it due to some "scattering Q" property of the Earth? The key difficulty of using scattering-theory models for coda (e.g., Aki and Chouet, 1975; Aki, 1980; Singh et al., 2019) consists in assuming that the measured Q_c must also be caused by a Q of the medium. In other words, within an elastic medium ($Q^{-1} = 0$ in eq. (6.1)), the coda is expected to be infinite $(Q_c^{-1} = 0)$. Nevertheless, this premise is clearly not true in even the simplest real cases. For example, a single-layer crust overlaying a uniform half-space mantle produces a coda consisting of reverberations within the layer (Bouchon, 1982). The amplitude decay rate within this coda is determined by the reflectivity and two-way reflection time within the layer (Figure 6.1):

$$A(t) = A_0 t^{-\beta} r^{\frac{Vt}{2L}}, \qquad (6.2)$$

where t is the time after the primary-wave onset at the station, L is the one-way distance between successive reflections, V is the wave velocity, r (with $r < 1$) is the average absolute value of the reflection coefficient at the bottom of the layer, and $t^{-\beta}$ is the average geometrical spreading for waves reflected (scattered) within the layer. The amplitude decay in Figure 6.1 and eq. (6.2) is frequency-independent, and it is hardly useful to attribute a "*Q*-factor" to it by using eq. (6.1). This amplitude decreases with time only, which is analogous to geometrical spreading and unrelated to the product *ft*.

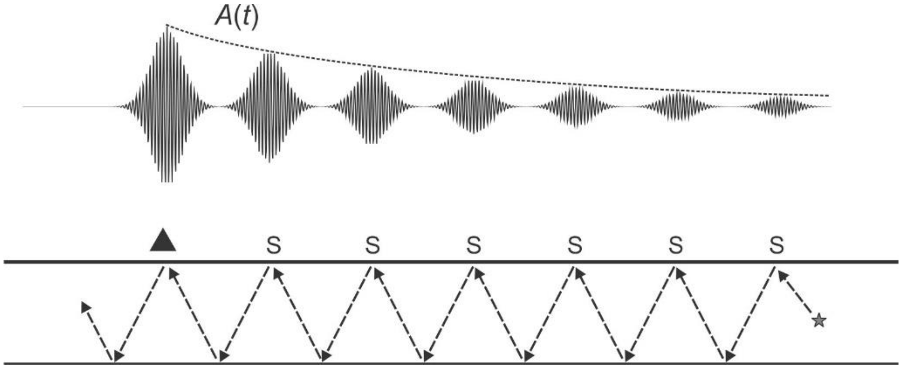

Figure 6.1. Schematic frequency-independent coda envelope $A(t)$ (eq. (6.2)) produced by reflections within a single-layer crust or sedimentary basin. Triangle is the seismic station, star is the source, near-surface scatterers for different orders of multiple reflections are labeled 'S'. Source waveforms are schematically modeled by Gabor wavelets. Note that the scattering points are not necessarily located on a straight line.

However, if interpreting this $A(t)$ by the method of Aki and Chouet (1975), the derivative of the logarithms of the normalized and corrected amplitudes $\frac{\partial}{\partial t}\ln\left(\frac{A}{A_0}t\right) = \frac{V}{2L}\ln r - \frac{\beta - 1}{t}$ is approximated as $\left(-\pi f / Q_c\right)$ taken at the average observation time $\langle t \rangle$. Consequently, the resulting apparent Q_c equals

$$Q_c\left(f,\langle t\rangle\right)=\frac{\pi f}{\pi f_r+\dfrac{\beta-1}{\langle t\rangle}}\approx\frac{f}{f_r}\left(1-\frac{\beta-1}{\pi f_r\langle t\rangle}\right), \tag{6.3}$$

where the approximate relation is for larger observation times $\langle t\rangle \gg |\beta-1|/(\pi f_r)$, and the characteristic frequency is

$$f_r \equiv \frac{V}{2\pi L}|\ln r| \quad , \tag{6.4}$$

(because $r<1$, $\ln r=-|\ln r|$). Thus, the purely elastic coda yields $Q_c\left(f,\langle t\rangle\right)$ proportional to *f*, i.e. η = 1 in the power law $Q(f)=Q_0 f^{\eta}$. Since β > 1 at local distances (approximately 1.3 to 1.6; e.g., Atkinson, 2004), the empirical Q_c also increases with $\langle t\rangle$ (second relation in eq. (6.3)). Such increases of Q_c with both *f* and $\langle t\rangle$ are often reported for seismic coda (Singh et al. (2019) and many references in Morozov (2008b) and Morozov et al. (2018)). The increase of Q_c with frequency is usually attributed to the "scattering *Q*" (Dainty 1981), and larger $\langle t\rangle$ are associated with greater depths of scattering (Singh et al. 2019). However, these interpretations are clearly invalid for the example in Figure 6.1. The measured $Q_0 \approx (1\,\mathrm{Hz})/f_r$ principally represents the elastic structure: thickness of the crust (parameter *L* in eq. (6.4)) and average velocity of wave modes dominant within the coda (*V*). The factor |ln*r*| in eq. (6.4) may be viewed as a justification for interpreting eq. (6.3) as a "scattering" (more precisely, "multiple-reflection") *Q*. However, this Q_c relates to the whole crust and cannot be attributed to the medium at any locations or depths within it. This Q_c cannot be used at all without knowledge of the specific elastic structure (Figure 6.1).

The assumption that Q_c^{-1} is caused by an "in-situ" Q^{-1} (which is also dominated by the S-wave Q_S^{-1}) was introduced by Aki (1980) from earlier observations by Tsujiura (1978). These observations showed that site amplification for coda waves correlated with S-wave amplification factors. Nevertheless, this observation only means that shear waves are dominant within the coda

(Figure 6.1), but their contribution into Q_c^{-1} is not necessarily due to a Q_S^{-1}. Shear waves dominate the "elastic" coda by virtue of large reflection and mode-conversion amplitudes r near critical angles (eq. (6.2)), existence of two S-wave polarizations (versus one for P waves), and also because of their coupling with surface waves. For near-vertically propagating crustal S waves (L equal the crustal thickness H= 35 km, V = 3.5 km/s, r = 0.1, and $\langle t \rangle = 100$ s), the first term in eq. (6.3) gives $f_r \approx 0.037$ Hz and $Q_c \approx 30f$. For near-critical S waves comprising the Lg phase, $L \approx 1.1H$, and eq. (6.2) can be approximated by the power-law $A(t) \propto t^{-0.83}$ (Campillo, 1987), from which the average reflection coefficient can be estimated as $r \approx 0.5$ to 0.8. With such r, Q_c in eq. (6.3) varies within a broad range from about 120f to 3000f, which covers the range of typical Q_c values including the results by Singh et al. (2019).

Seismic scattering theories (Aki, 1969; Sato, 1977) refer to an idealized case of a boundless homogenous half-space with random, subwavelength-scale heterogeneities statistically uniformly distributed in space. In this case, the geometrical spreading can be determined theoretically, and the coda would indeed have infinite length if $Q^{-1} \to 0$ (although also of infinitesimal amplitude; Frankel and Wennerberg, 1987). However, this case of homogeneous media is far from reality, and adopting this model as a background produces the characteristic behavior of $Q_c(f)$ nearly proportional to f. Morozov (2008b, 2010a) and Morozov et al. (2018) reviewed many observational studies based on Aki and Chouet's (1975) approach and showed that the frequency-dependent Q and particularly Q_c can often be explained as artifacts of this inaccurate background model. As in eq. (6.3), the frequency-dependent Q_c typically represents not a Q-type "attenuation" in the sense of the statistical scattering models (Aki 1969; Sato 1977) but the deterministic elastic structure of the Earth: crustal thickness, velocity gradients, layering, major reflectors within the crust and mantle, and velocity contrasts near the surface, coastlines and sedimentary basins (Morozov, 2010a; Jhajhria et al., 2017; Morozov et al., 2018).

To make the assumption-sensitive $Q_c(f)$ dependencies comparable for different geographic areas, standardized selections of processing parameters have been recommended (Havskov et al., 2016). However, comparisons of standardized $Q_c(f)$ dependencies are hardly more informative than comparing the temporal decay rates of amplitudes $a(f,t) \equiv \partial \ln A(f,t) / \partial t$ themselves. Functions $Q_c(f)$ derived by the procedure of Aki and Chouet (1975) can be viewed as mathematical transformations of time dependencies predominant in $a(f,t)$. This transformation includes multiplication by f, which causes the leading frequency dependence shown in eq. (6.3) (Morozov, 2008b). Moreover, transforming $a(f,t)$ into a $Q_c(f)$ obscures the most valuable observation from coda envelopes – namely that $a(f,t)$ is usually nearly frequency-independent (as in eq. (6.2)).

If we are interested not merely in documenting $Q_c(f)$ curves for a geographic region but also in revealing its physical properties, then a more empirical and assumption-free model is needed. As shown in this chapter, the codas observed in the study by Singh et al. (2019) are nearly elastic, and they can be more reliably described not by the delicate concept of $Q_c(f)$ but by an alternative, frequency-independent property of the subsurface that I denote γ and call effective geometrical attenuation (Morozov, 2008b). This property corresponds to the limit $Q^{-1} \rightarrow 0$ and therefore represents the elastic structure. As illustrated by eq. (6.2), this elastic structure is likely dominated by large-scale crustal features, but it may also contain subwavelength-scale layers and scatterers (Morozov 2010a, 2011a).

In the following sections, I show how the γ and effective (model- and frequency-independent) Q_c can be approximately obtained from published $Q_c(f)$ results without redoing the complete data analysis. In section 6.2, I review the conventional $Q_c(f)$ coda model and highlight some of its theoretical and observational problems. In section 6.3, I re-interpret the Q_c model by Singh et al. (2019) by using the attenuation-coefficient approach by Morozov (2008b, 2010a, 2010b, 2011a, 2013). The regionalized $Q_c(f)$ model by Singh et al. (2019) gives a unique opportunity to examine the spatial patterns of geometrical attenuation γ and to recognize the "footprint" of the conventional $Q_c(f)$ method. One of the most interesting results of sections 6.2 and 6.3 is that the effective Q_c within the eastern Indian Shield turns out to be extremely high, in contrast to the $Q_c(f)$ found by Singh et al. (2019) and many similar studies, which is low at 1 Hz and steeply increases with frequency. The high effective Q it can be explained by the Earth's crust being principally *elastic* (section 6.4). In section 6.5, I describe a preliminary empirical model for geometrical spreading for coda, also inspired by the mapping procedure by Singh et al. (2019). In section 6.6, I discuss the resulting model, compare it to tectonic features of the study area, and also discuss some limitations and possible extensions of the approach. In section 6.7, I give the conclusions of this chapter.

6.2. Conventional Approach to Q_c

The model by Aki and Chouet (1975) inverts for a frequency-dependent coda Q-factor $Q_c(f_b)$ by approximating the recorded coda envelopes $A(f_b,t)$ as functions of time t at each of the selected band-pass frequencies f_b:

$$A(f_b,t)=S(f_b)R(f_b)G(t)\exp\left[-\frac{\pi f_b t}{Q_c(f_b)}\right], \tag{6.5}$$

In this relation, $S(f)$ is the source amplitude spectrum, $R(f)$ is the receiver response, $G(t)$ is the geometrical spreading selected in the form $G(t)=t^{-\beta}$, and β is the geometrical spreading parameter (notation as in Singh et al. (2019)). Singh et al. (2019) specify the assumptions of this model, which are standard in local-coda studies:

1) Spherical direct- and scattered-wave wavefronts,
2) Single, weak, isotropic scattering on a homogenous statistical distribution of small-scale, random heterogeneities,
3) Constant scattering amplitude (absence of factors related to the scattering point in eq. (6.5)), and
4) Both forward-traveling and scattered waves within the coda dominated by body S waves.

This combination of assumptions leads to selecting $\beta = 1$, which is also similar to many multiple-scattering and radiative transfer models (e.g., Frankel and Wennerberg 1987; Zeng et al. 1991). However, because this $\beta = 1$ underestimates the actual geometrical spreading in an inhomogeneous crust and this error increases with t, the resulting $Q_c(f_b)$ increases with f_b, t, and consequently with the source-receiver distance. These increases are seen in the single-station $Q_c(f_b)$ values by Singh et al. (2019) (Figure 6.2).

In the following subsections, I use the $Q_c(f_b)$ results by Singh et al. (2019) (Figure 6.2) to explain the observational and theoretical problems with the above model (eq. (6.5)). For readers only interested in the alternative approach that is free from these problems (section 6.3), these subsections can be skipped.

6.2.1. Problems with $Q_c(f)$ interpretations

A key observation from the model by Singh et al. (2019) is that their Q_c increases not only with frequency and lapse time but also radially, away from the seismic station (Figure 6.2). Because of the use of only one seismic station, this observation is particularly clear in this study.

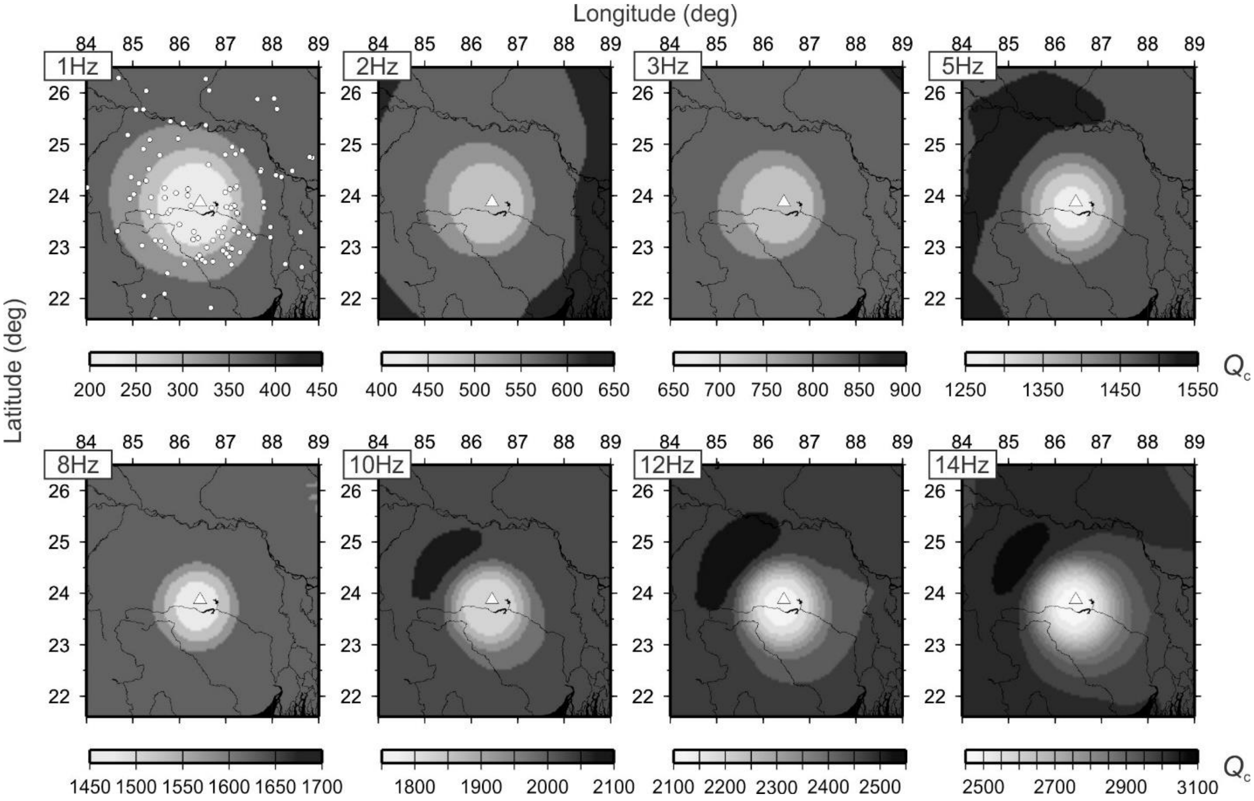

Figure 6.2. Maps of Q_c by Singh et al. (2019; their Figure 6) within eight frequency bands (labels). Triangle indicates the Dhanbad seismic station used for deriving this model, and dots in the first plot are the locations of 112 earthquakes. Major rivers and coastline are shown for geographical reference. Note the systematic increases of Q_c with distance from the station, and also near proportional increase with frequency.

Although this spatial pattern may be due to a fortuitous selection of station location, it is far more likely that it represents an “acquisition footprint” due to direct correlation of Aki and Chouet’s (1975) Q_c with the source-receiver distance. Although weaker, similar increases of Q_c with distances were also shown by Blanke et al. (2019). The strong and symmetric increase of Q_c both into the Indian craton (west and south-west of the station in Figure 6.2) and into the continental collision zone (northeast) shows that this increase should not be interpreted geologically. At lower frequencies, the conical pattern of Q_c is slightly shifted west of the station (Figure 6.2), which suggests a relative decrease of Q_c into the craton. This trend is again contrary to the expected higher Q for stable, older, and colder tectonic structures.

Also similar to many other studies, Q_c values by Singh et al. (2019) increase near linearly with the length of coda windows (Figure 9 in that paper). Lapse-time (t_{lapse}) dependencies of Q_c are usually attributed to the depths of scattering increasing with t_{lapse} in Aki and Chouet's (1975) model. Nevertheless, the schematic example in Figure 6.1 again contradicts this assumption – scattering times (even if viewing Moho reflections as "scattering") may generally be unrelated to the depths of scattering. The largest velocity contrasts are located near the free surface, and this is likely the zone of strongest wave scattering for all lapse times.

Another conspicuous difficulty with the model by Singh et al. (2019) is that their $Q_c(f)$ is almost proportional to frequency f (the power-law exponent η between 0.9 and 1.02; Figure 6.3). This behavior is often found in the literature (with η sometimes as high as 1.7) and unfortunately, most authors do not view frequency dependence as problematic. Nevertheless, if understanding the $Q_c(f)$ according to the original scattering theories, as a "quality factor" of some effective medium (Aki 1969; Sato 1977), then cases of $\eta \geq 1$ present major difficulties for physical interpretation. With $\eta > 1$, dependencies $Q(f) = Q_0 f^{\eta}$ mean a relative increase of high-frequency amplitudes with distance, they cannot be implemented by reasonable equations of continuum mechanics, and imply peculiar causality properties (Morozov et al., 2018). As in eqs. (6.2) and (6.3), the case $\eta = 1$ represents an amplitude decrease with time only, which means that this is not Q-type attenuation at all. Thus, the part of the model shaded gray in Figure 6.3 is nonphysical or is at least dominated by non-Q type attenuation. The rest of this model with $\eta > 0.9$ is also close to these conditions, which means that the Q-type attenuation in the study area is actually much weaker than suggested by the low values of Q_0 (Morozov, 2008b).

The fourth striking observation from the results by Singh et al. (2019) is in the very strong anti-correlation between the values of Q_0 and η (arrow in Figure 6.3). The scatter of the inverted (Q_0, η) points across this trend direction suggests an estimate of measurement errors, which are minor compared to the trend. The anti-correlation between Q_0 and η means that only one of these parameters is significant, so that, for example, Q_0 can be inferred from η at any point within the study area. More likely, both of these parameters represent a single physical factor within the Earth's crust, and I need to investigate what this underlying factor may be. As suggested by eq. (6.3) and the results in section 6.3, these controlling factors are the large-scale elastic structure of the crust and the acquisition footprint. Thus, the variations of Q_0 and η along the arrow in Figure 6.3 represent, for example, variable crustal thickness and not what is traditionally understood as "attenuation" of the subsurface.

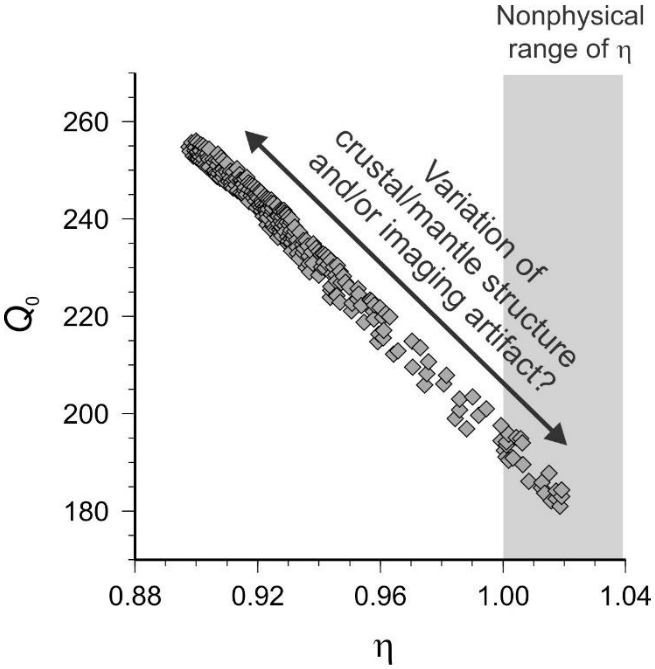

Figure 6.3. Trade-off between parameters Q_0 and η (diamonds) for 30-s coda window in the model by Singh et al. (2019; part of their Figure 13). Nonphysical range of parameter $\eta > 1$ is shown by gray background.

In the following subsection, I show that all four of the correlated trends in Q_c values (with frequency, distance, lapse time, and coda window length) represent a common effect of an inaccurate background model assumed during data analysis (represented by fixed parameter $\beta = 1$ in eq. (6.5)). This spurious effect is again seen particularly clearly in the results by Singh et al. (2019) because of their use of long source-receiver distances (up to about 350 km).

6.2.2. Theoretical shortcomings of the conventional coda model

The theoretical models by Aki (1969) and Sato (1977) with many extensions to multiple-scattering regimes represent applications of the scattering theory to traveling waves. Generally, these models show that in a macroscopically-homogenous medium with sub-wavelength scale heterogeneities, the amplitude decay of a harmonic wave can be described by a frequency-dependent Q-factor (Dainty 1981). However, application of these models to practical observations of seismic coda (e.g., Aki and Chouet, 1975; Aki, 1980) contains a subtle but important fallacy, which explains the observational anomalies described in the preceding subsection. This fallacy can be seen by comparing the standard use of the scattering theory in physics with its application to seismic coda (Figure 6.4).

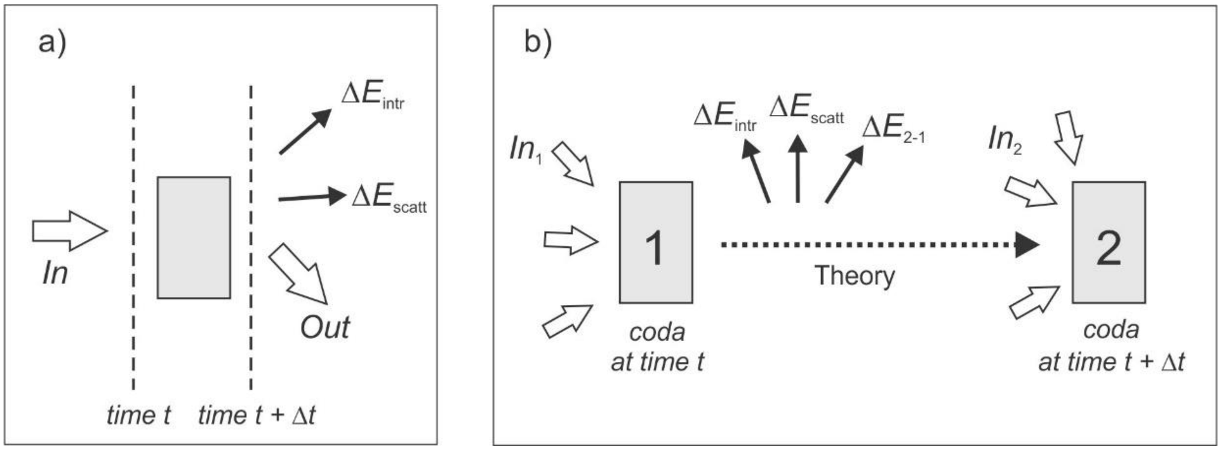

Figure 6.4. Uses of scattering theory: a) conventional in physics, comparing two wavefields within the same volume; b) in coda Q measurements, comparing two different parts of the wavefield (Aki and Chouet 1975). Gray rectangles indicate the volumes considered, block arrows labeled “In” and “Out” are the incident and resulting wavefields, solid arrows labeled ΔE_{intr} and ΔE_{scatt}, denote the mechanical-energy loss due to intrinsic and scattering attenuation. In plot b), ΔE_{2-1} denotes the relative energy difference between wavefield states 1 and 2, and the dotted arrow represents the assumed theoretical model connecting the two states.

In the conventional scattering-theory problem, some “incident” wavefield interacts with a volume of the medium and produces an “outgoing” wavefield (Figure 6.4a). During this interaction, mechanical energy may be lost either in the form of heat (“intrinsic” attenuation, denoted ΔE_{intr} in Figure 6.4a) or in the form of scattered waves that are not counted in the “outgoing” wavefield. The portion of energy of these secondary waves is called the “scattering” attenuation (eq. (6.1); $\Delta E_{\mathrm{scatt}}$ in Figure 6.4a). Note that the identification of scattered waves is subjective and depends on the detail of the model for the outgoing field. For example, the outgoing and scattered waves may or may not include reflections, mode conversions, and scattering on certain structures. Since the models in Figure 6.4a are considered for harmonic waves in a macroscopically-homogenous effective medium (Aki, 1969), the average energy dissipation rates are constant, and the time-average decrements ΔE_{intr} and $\Delta E_{\mathrm{scatt}}$ can be attributed to any point and any wave period. This formal definition gives the inverse *Q*-factors Q_{total}^{-1}, Q_{intr}^{-1}, and Q_{scatt}^{-1} by eq. (6.1). From the energy balance ($\Delta E_{\mathrm{total}} = \Delta E_{\mathrm{intr}} + \Delta E_{\mathrm{scatt}}$), these *Q*-factors are related as

$$Q_{\mathrm{total}}^{-1} = Q_{\mathrm{intr}}^{-1} + Q_{\mathrm{scatt}}^{-1} . \tag{6.6}$$

However, it is rarely noted that the definitions of the various *Q*-factors by eqs. (6.1) and (6.6) only rigorously apply to cases in which the “in” and “out” states refer to the same volume, so that $\Delta E_{\mathrm{total}}$ represents the energy loss from it. This case is only achieved for free oscillations, laboratory measurements with rock samples, or in theoretical models of effective media. By contrast, in most field seismic-*Q* measurements, the observational environment is different, as schematically shown in Figure 6.4b. The two compared states refer to *different parts* of the wavefield, which are, for example, coda waves recorded at different times t_1 and t_2 or body waves recorded at different points x_1 and x_2. For the two states, the “in” waves are different, such as waves arriving along different raypaths or traveling different distances from the source. When evaluating the energy difference between these states, we need to include not only ΔE_{intr} and $\Delta E_{\mathrm{scatt}}$ but also the energy difference $\Delta E_{2\text{-}1}$ occurring in the absence of any attenuation (Figure 6.4b). For example, $\Delta E_{2\text{-}1}$ contains the difference of wave amplitudes at different distances from the source or scattering points (Morozov, 2008b, 2010a). For coda, this energy also contains contributions of the form $\Delta E_{2-1} = E\left(s_2 - s_1\right)$, where s_1 and s_2 are the strengths of scattering at points producing coda states 1 and 2 (Figure 6.4b; Nishigami (1997)). Consequently, the inverse *Q*-factor inferred from coda and body-wave measurements based on Aki and Chouet’s (1975) procedure is

$$Q_{\mathrm{total}}^{-1} = Q_{2\text{-}1}^{-1} + Q_{\mathrm{intr}}^{-1} + Q_{\mathrm{scatt}}^{-1} . \tag{6.7}$$

Thus, the conceptual problem with Aki and Chouet's (1975) approach consists in omitting the elastic-limit term $Q_{2\text{-}1}^{-1}$ in eq. (6.7) and interpreting Q_{intr}^{-1} and Q_{scatt}^{-1} as properties of the medium. As shown by Morozov (2008b, 2010a, 2010b) and in section 6.3, $Q_{2\text{-}1}^{-1}$ often dominates the resulting $Q_c^{-1}(f)$ images (Figures 6.2 and 6.3). This term absorbs all (inevitable) errors of the theoretical model relating the two states being compared (dotted arrow in Figure 6.4b).

Finally, the name "quality factor" and notation '*Q*' for the ratio in the right-hand side of eq. (6.1) is inspired by analogy with quality factors of electrical or mechanical resonators. However, this analogy is somewhat misplaced for boundless wave-propagating media, because they lack the principal property of a resonator, which is the resonant frequency. The *Q*-factors in eqs. (6.1) and (6.6) are meaningful only for finite structures with resonant frequencies, such as the whole of the Earth, crustal column, or a group of sedimentary layers. For a region within a nearly homogenous crust (as in Aki and Chouet's (1975) model), the energy ratio in eq. (6.1) is not a material property and depends on the specific wave-mode content. To avoid such imprecise associations with resonators, it would be best to avoid notation '*Q*' for this ratio, as done in section 6.3.

6.3. Attenuation-Coefficient Approach to Coda

In contrast to the model by Aki and Chouet (1975), the coda amplitude model of this chapter does not assume any specific structure of the crust, observation geometry, distribution of scatterers, or scattered wavefield dominated by body or surface waves. Instead of these theoretical hypotheses, the model is purely empirical and only focuses on a sufficient parameterization of the observed coda envelopes $A(f,t)$. This parameterization is based on three general requirements:

1) Both time-dependent ($G(t)$) and frequency-dependent factors in coda envelopes ($\exp\left(-\pi Q_c^{-1} ft\right)$; eq. (6.5)) should be measured without assuming a known elastic background, i. e. some fixed form for $G(t)$. The parameterization should also be not preferential in favor of the *Q* model of wave attenuation (eq. (6.1)).
2) The parameterization should be able to explain the baseline case of zero attenuation ($Q^{-1} = 0$) within the crust and mantle. As coda envelopes (Figures 6.5 and 6.6) and

many other seismic observations suggest, Q-type attenuation is a secondary effect compared to the effects of the Earth's elastic structure (geometrical spreading, refractions, reflections).

3) In contrast to eq. (6.5) using each f_b independently, I look for a common frequency dependence within the model. This principle allows obtaining a tightly constrained and unambiguous measure of Q-type attenuation.

A rigorous model satisfying these requirements should predict absolute coda envelopes $A(f,t)$ by considering variable geometrical spreading, Q-type attenuation within the medium, and variable distribution of scatterers. With regard to spatially-variable strengths of wave scattering, such models for coda envelopes were developed by Nishigami (1997, 2006). At the end of section 6.5, I propose a model which could provide such a general and useful alternative to eq. (6.5) in coda studies. However, in the absence of sufficient field data from east Indian shield, inversion of complete coda amplitudes is unfeasible. Instead of this detailed inversion and similarly to existing studies (Aki and Chouet 1975, Singh et al. 2019, and many other), I utilize coda parameters derived from individual coda envelopes $A(f,t)$ by using eq. (6.5). However, two important modifications are made in this parameterization (Morozov, 2008b): 1) a more general form of geometrical spreading

$$G(t) = t^{-\beta} e^{-\gamma t}, \tag{6.8}$$

with variable "geometrical attenuation" parameter γ, and 2) parameter Q_c^{-1} treated as frequency-independent and expected to be small. After deriving parameters γ and Q_c^{-1} from each record, they are empirically regionalized as in Singh et al., (2019).

Also as in most inversions for coda Q (Aki and Chouet, 1975), I eliminate the source and receiver factors in eq. (6.5) ($S(f_b)$ and $R(f_b)$) by using normalized coda amplitudes $A(f,t)/const$, so that the results are insensitive to this *const*. This normalization is achieved by using the window-averaged temporal decay rates $\langle \partial \ln A/\partial t \rangle$ as data when inverting eqs. (6.5) and (6.8) for γ and Q_c^{-1}. These decay rates should normally be measured from field data (e.g., Jhajhria et al., 2017).

However, in this chapter, field records are unavailable, and I extract $\langle \partial \ln A / \partial t \rangle$ values from the apparent $Q_c(f_b)$ values reported by Singh et al. (2019) (Figure 6.2). This data preparation procedure is described in subsection 6.3.1.

In subsection 6.3.2, instead of the conventional parameters Q_0 and η, I show how an alternate pair of in-situ γ and effective-Q_c^{-1} properties can be attributed to the Earth's subsurface. In subsection 6.3.3, I show how these properties are derived from $\langle \partial \ln A / \partial t \rangle$ data and interpret the results. In sections 6.4 and 6.5, I further discuss the intricate question of geometrical spreading for coda envelopes and suggest a more rigorous alternative for the empirical relation (eq. (6.8)). Finally, also in section 6.5, I give a more complete model of coda envelopes that could be useful in future studies.

6.3.1. Measured coda attributes

As noted in section 6.2, within each of the eight frequency bands f_b considered by Singh et al. (2019), spatial distributions of Q_c are dominated by "conical" patterns centered on the seismic station (Figure 6.2). These patterns are hardly geological but likely caused by the selected form of the model (eq. (6.5)) applied to data from a single station (Figure 6.2). To reduce this "footprint" of the transformation $A(f_b, t) \rightarrow Q_c(f)$ (eq. (6.5)), I need to return to the raw quantity actually measured from coda envelopes. As I show below, this quantity is the frequency-dependent temporal attenuation coefficient, which was denoted $\chi(f)$ by Morozov (2008b, 2010a).

In the classic Aki and Chouet's (1975) method of coda analysis, the $A(f_b,t)$ data are first transformed into the derivatives of $\ln A$ with respect to time:

$$\left\langle -\frac{\partial \ln A}{\partial t} \right\rangle = \beta \left\langle t^{-1} \right\rangle + \pi Q_c^{-1} f_b , \qquad (6.9)$$

where $\langle \ldots \rangle$ denotes averaging over the coda time window and frequency band centered at frequency f_b. This time derivative can be written as a combination of some reference (or "background") model of geometrical spreading with a "temporal attenuation coefficient" $\chi(f_b)$ (Morozov, 2010a). The temporal attenuation coefficient for coda is analogous to the spatial attenuation coefficient α commonly used for traveling waves (Aki and Richards 2002; sometimes denoted η as by Zeng et al. 1991). By taking the reference geometrical spreading in the form $G(t) \propto t^{-\beta_0}$, we have

$$\left\langle -\frac{\partial \ln A}{\partial t} \right\rangle \equiv \beta_0 \left\langle t^{-1} \right\rangle + \chi\left(f_b \right), \tag{6.10}$$

where the temporal attenuation coefficient is

$$\chi\left(f_b \right) = \gamma + \pi Q_{\mathrm{c}}^{-1} f_b, \tag{6.11}$$

and its frequency-independent term is denoted by

$$\gamma \equiv \left(\beta - \beta_0 \right) \left\langle t^{-1} \right\rangle. \tag{6.12}$$

This γ is the "geometrical attenuation" in eq. (6.8). By measuring this parameter (subsection 6.3.2), the power-law exponent β can be estimated as

$$\beta = \beta_0 + \gamma \big/ \left\langle t^{-1} \right\rangle. \tag{6.13}$$

With the conventional selection of $\beta_0 = 1$ (Aki and Chouet, 1975), the logarithms of amplitudes decrease approximately linearly with time t, as $\ln\left[A\left(f,t \right) t^{\beta_0} \right] \approx const - \chi\left(f_b \right) t$. For a single seismic event, $\chi(f_\mathrm{b})$ derived from Figure 3 in Singh et al. (2019) is shown in Figure 6.5. As this figure shows, the negative slopes ($-\chi\left(f_b \right)$) are almost equal for all f_b, which means that $\partial \ln A / \partial t$ is nearly frequency-independent (similar to Figure 6.1). Although such plots are rarely presented, *all* of them that we have seen to date (Parvez et al., 2008; Morozov, 2010a; Langston, personal communication, 2012; Escudero et al., 2016; Jhajhria et al., 2017) show weak frequency dependencies of the temporal amplitude decay rates $\partial \ln A / \partial t$. Thus, near frequency independence of temporal decay rates appears to be a common observation with seismic coda.

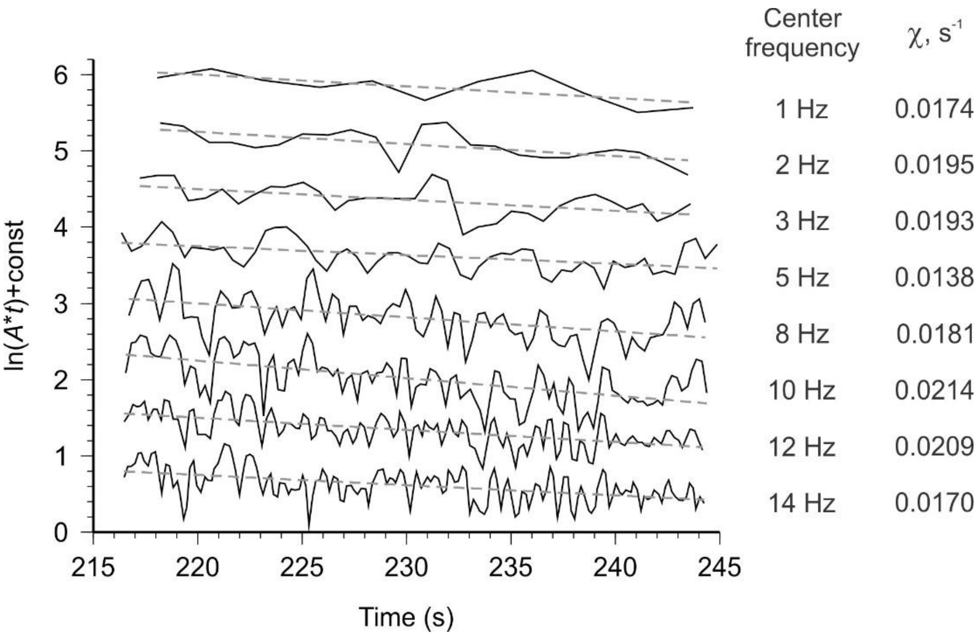

Figure 6.5. Spherical geometrical-spreading corrected logarithms of coda amplitudes $a(t) = \ln\left[A(f,t)t^{\beta_0}\right] + C$ (with $\beta_0 = 1$) for one event (solid lines; derived from Figure 3 in Singh et al. (2019). Arbitrary constants C are added in order to display all frequency bands in one plot. Gray dashed lines show linear regressions of $a(t)$ by using least-squares regressions. Frequency bands and the values of χ (slopes of regression lines) are listed on the right.

Figure 6.6 shows that the principal contribution to $\chi(f_b)$ comes from the frequency-independent term $\gamma \approx 0.018$ s^{-1}, and therefore, by taking $t \approx 230$ s (Figure 6.5), eq. (6.13) gives $\beta \approx 5.1$. The causes of such large β are discussed in subsection 6.3.3.

The slope of the linear trend in $\chi(f_b)$ (black dashed line in Figure 6.6) corresponds to an extremely high $Q_c \approx 30500$. Without formal analysis of its uncertainty, it is clear from Figure 6.6 that this Q_c is indistinguishable from a complete absence of Q-type attenuation. The dominant contribution to $\chi(f)$ comes from γ, and the total effect of Q_c at 14 Hz is only about 8% of γ. Much stronger variations of $\chi(f_b)$ come from the attenuation peaks at about 2 Hz and 10 Hz and a trough near 5 Hz (gray dashed line in Figure 6.6). These variations may be due to near-surface resonances beneath the seismic station. These resonances can be included in the receiver site response $R(f)$ in eq. (6.5).

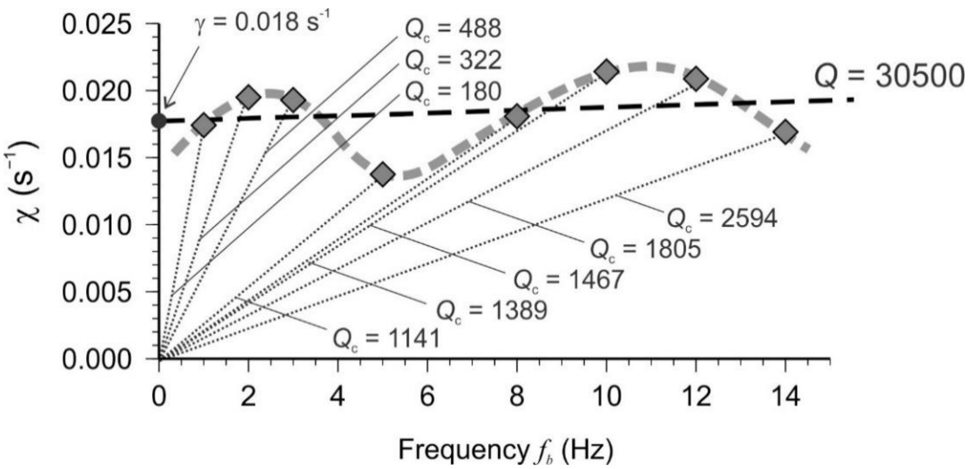

Figure 6.6. Frequency dependence of the temporal attenuation coefficient for coda. Diamonds are the values χ at eight frequencies listed in Figure 6.5, and thick gray dashed line is the interpreted $\chi(f)$ with two peaks. Black dashed is shows a linear approximation (eq. (6.11)), with intercept $\gamma \approx 0.018$ s^{-1} and inverse slope $Q \approx 30500$ labeled. Dotted lines with labels Q_c show the slopes (assuming $\gamma = 0$) used by Singh et al. (2019) to estimate the frequency-dependent Q_c values (labels).

By contrast to the detailed interpretation above, in a conventional approach to the same data, the $\chi(f_b)$ trend with resonances is disregarded, β is assumed to equal $\beta_0 = 1$, and γ is set equal zero (Singh et al. 2019). The resulting Q_c absorbs all of these arbitrary selections, and consequently, it is found to strongly increase with frequency, source-receiver distance, and lapse time. Graphically, the conventional (apparent) Q_c^{-1} values are shown by the slopes of dotted lines in Figure 6.6. From these slopes, we can see that Q_c^{-1} actually represents γ divided by the arbitrarily selected filtering frequency: $Q_c^{-1}(f_b) \approx \gamma/(\pi f_b)$. Therefore, this Q_c contains a built-in proportionality to f_b ($\eta \approx 1$ in Figure 6.3; eq. (6.3)). Clearly, since all information extracted from coda-envelope data consists in the $\chi(f_b)$ dependence (thick dashed line in Figure 6.6, deriving a Q_c by connecting each point to the coordinate origin (dotted lines) is only a mathematical transformation of this $\chi(f_b)$. The physical meaning of this apparent $Q_c^{-1}(f_b)$ is clearer and more directly expressed by relation $\gamma \approx const$.

6.3.2. Earth's attenuation coefficient and Q_c

Despite similar notations, the spatially distributed (regionalized) Q_c in Figure 6.2 is a physical quantity different from the measured Q_c discussed in the preceding subsection. This important question is complicated and will be extensively discussed in chapter 7. Here, I only briefly outline the basic relation between the "measured" (i.e. inferred from the attenuation coefficient) and the "in situ" (assumed to be present with in the subsurface) Q_c's.

The regionalized Q_c (Figure 6.2) was obtained by Singh et al. (2019) using the back-projection method by Xie and Mitchell (1990) independently at each frequency f_b. This back-projection was originally formulated for *Lg* coda *Q* (Xie and Mitchel, l990), and it represents a tomographic inverse for a forward model assuming that the Q_c^{-1} measured for a source-receiver pair is an areal average of a similar in-situ property of the Earth, which I denote $Q_{c,\mathrm{Earth}}^{-1}$:

$$Q_c^{-1} = \frac{1}{S_W} \iint_S dxdyW\left(x,y\right) Q_{c,\mathrm{Earth}}^{-1}\left(x,y\right). \tag{6.14}$$

In this equation, the integrals are evaluated over an elliptical area *S* containing all scattering points with travel times smaller than the maximum time considered within the coda window, weights *W*(*x*,*y*) = 1 and $S_W = \iint_S dxdyW\left(x,y\right)$. The inverse of eq. (6.14) similarly represents $Q_{c,\mathrm{Earth}}^{-1}$ at any point (*x*,*y*) as a linear combination of Q_c^{-1} for source-receiver ellipses covering that point (Xie and Mitchell 1990):

$$Q_{c,\mathrm{Earth}}^{-1}\left(x,y\right) = \sum_n K_n\left(x,y\right) Q_{c,n}^{-1}, \tag{6.15}$$

where *n* is the number of coda observation and $K_n(x,y)$ is the pseudo-inverse kernel for the n^{th} observation.

Eq. (6.14) with *W*(*x*,*y*) = *const* within the scattering ellipse represents only an *ad hoc* areal averaging formula, and eq. (6.15) is one of its generalized inverses. Several forms of integration weights *W*(*x*,*y*) in eq. (6.14) were proposed, such as by Del Pezzo et al. (2016) and Giampiccolo and Tuvèt (2018). These approaches also start by assuming that scattering and intrinsic *Q*-factors exist within the subsurface, and that the observed Q_c^{-1} is obtained by their averaging across distributions of single or multiple scattering points within a homogenous half-space. However, a correct forward model should not consist of only Q-factors because it should be able to explain the case of $Q_{\mathrm{Earth}}^{-1} = 0$ and consider multiple scattered-wave types. The model should also differentiate between site and propagation-path effects, frequency dependences of scattering amplitudes, and spatial distributions of scatterers (Nishigami, 1997) without mixing all of these properties into a Q (Jhahria et al. 2017). In this chapter, I do not explore any possible alternatives to eq. (6.14) but assume instead that eq. (6.15) and the images in Figure 6.2 represent some useful in-situ quantity $Q_{c,\mathrm{Earth}}^{-1}\big|_{\beta=\beta_0}$, which determines the frequency-dependent part of coda envelope decays. By this notation, I indicate that this quantity is obtained from eq. (6.5) by using (an inaccurate) assumption $\beta = \beta_0 = 1$. In the following subsection, I try estimating a similar quantity $Q_{c,\mathrm{Earth}}^{-1}$ independently of this assumption.

6.3.3. Data processing for attenuation coefficient

Existing $Q_c(f_b)$ estimates at multiple frequencies f_b such as provided by Singh et al (2019) can be inverted for the effective geometrical attenuation $\gamma_{c,\mathrm{Earth}}$ and Q-type attenuation $Q_{c,\mathrm{Earth}}^{-1}$ of the study area by using the following processing sequence:

1) "Reverse-processing" of $Q_c(f_b)$ into $\chi(f_b)$ in each record, in a way similar to other types of $Q(f)$ data (Morozov, 2008b, 2010a, 2010b, 2011a, 2013).
2) Correction of the dependencies of the resulting $\chi(f_b,x,y)$ on observation time t at each point (x,y) within the image. This correction is specific to the regionalized coda Q problem and is related to spurious increases of Q_c with distance from the station (Figure 6.2).
3) Inversion of $\chi(f_b,x,y)$ for $\gamma_{c,\mathrm{Earth}}(x,y)$ and $Q_{c,\mathrm{Earth}}^{-1}(x,y)$ for every point (x,y) within the final image.
4) In addition, estimation of the frequency-dependent residual in the temporal attenuation coefficient $\Delta\chi(f_b,x,y)$ representing local coda-attenuation effects.

Details of these operations are as follows. Step 1) is performed by noting that since the reported Q_{c}^{-1} (Figure 6.2) was obtained from $\chi(f_{\mathrm{b}})$ (eq. (6.11)) by assuming $\beta = \beta_0$ (i.e., $\gamma = 0$), the attenuation coefficient for a given record can be reproduced by an inverse transformation:

$$\chi\left(f_{\mathrm{b}} \right) = \pi Q_c^{-1}\left(f_{\mathrm{b}} \right) f_{\mathrm{b}} . \tag{6.16}$$

Ideally, if field records were available, these $\chi(f_{\mathrm{b}})$ obtained for each source-receiver pair could be interpolated and regionalized to obtain a spatially-distributed $\chi(f_{\mathrm{b}},x,y)$. This approach is taken in chapter 7. However, for Singh's et al. (2019) data, only the regionalized $Q_c(f_{\mathrm{b}},x,y)$ is available (Figure 6.2). Therefore, I simply estimate the regionalized $\chi(f_{\mathrm{b}},x,y)$ at each point (x,y) by the same transformation

$$\chi\left(f_{\mathrm{b}}, x, y \right) = \pi\, Q_{c,\mathrm{Earth}}^{-1}\left(f_{\mathrm{b}}, x, y \right)\Big|_{\beta=\beta_0} f_{\mathrm{b}} . \tag{6.17}$$

To justify step 2) above, note that the values of $Q_c(f_{\mathrm{b}},x,y)$ by Singh et al. (2019) contain spurious increases with t, which look like a "conical" footprint in the spatial image (Figure 6.2). In the single-station transformation (eq. (6.16)), the actual $\chi(f_{\mathrm{b}},t)$ of the record would be recovered, but when using the regionalized $Q_c^{-1}\left(x, y\right)$ (eq. (6.17)), the footprint is averaged over multiple records and is impossible to undo. However, for geologic interpretation, $\chi(f_{\mathrm{b}},x,y)$ is expected to have no trend with t, and therefore this arbitrary drift should be removed. For simplicity, I estimate this drift by the coefficients γ_0 and γ_0' of linear regression

$$\chi\left(f_{\mathrm{b}}, x, y \right) \approx \gamma_0 + \gamma_0' r\left(x, y\right) , \tag{6.18}$$

where $r(x,y)$ is the distance from point (x,y) to the seismic station. By fitting eq. (6.18) in the least-squared sense for the entire area, we obtain γ_0' and de-trend the values of χ as

$$\chi_{\mathrm{detrend}}\left(f_{\mathrm{b}}, x, y \right) = \chi\left(f_{\mathrm{b}}, x, y \right) - \gamma_0' r\left(x, y\right) . \tag{6.19}$$

Note that this assumption of coda properties being independent of the source-receiver distance is also made (although not specially enforced or verified) in the model by Aki and Chouet (1975). Safarshahi and Morozov (2021a) also showed that similar constraints are important to include in the inversion procedure for measuring β and body-wave Q^{-1}.

As shown in Figure 6.7, the spatially de-trended attenuation coefficients (6.19) lie between about 0.01 to 0.02 s^{-1} and oscillate with frequency f_b. At each f_b, most of these variations occur in the vicinity of the seismic station, showing that the footprint of the source-receiver distribution has not been completely removed. However, spatial variations of χ_{detrend} at each f_b are below 20% (Figure 6.7), compared to ~100% variation of the apparent Q_c at 1 Hz (Figure 6.2). This footprint could be significantly reduced by 2-D wavenumber filtering; however, it has minor impact on the final result, and I perform no such filtering in this study. Ideally, the footprint should not occur when directly deriving the $\chi(f_b,x,y)$ (eq. (6.17)) from raw data.

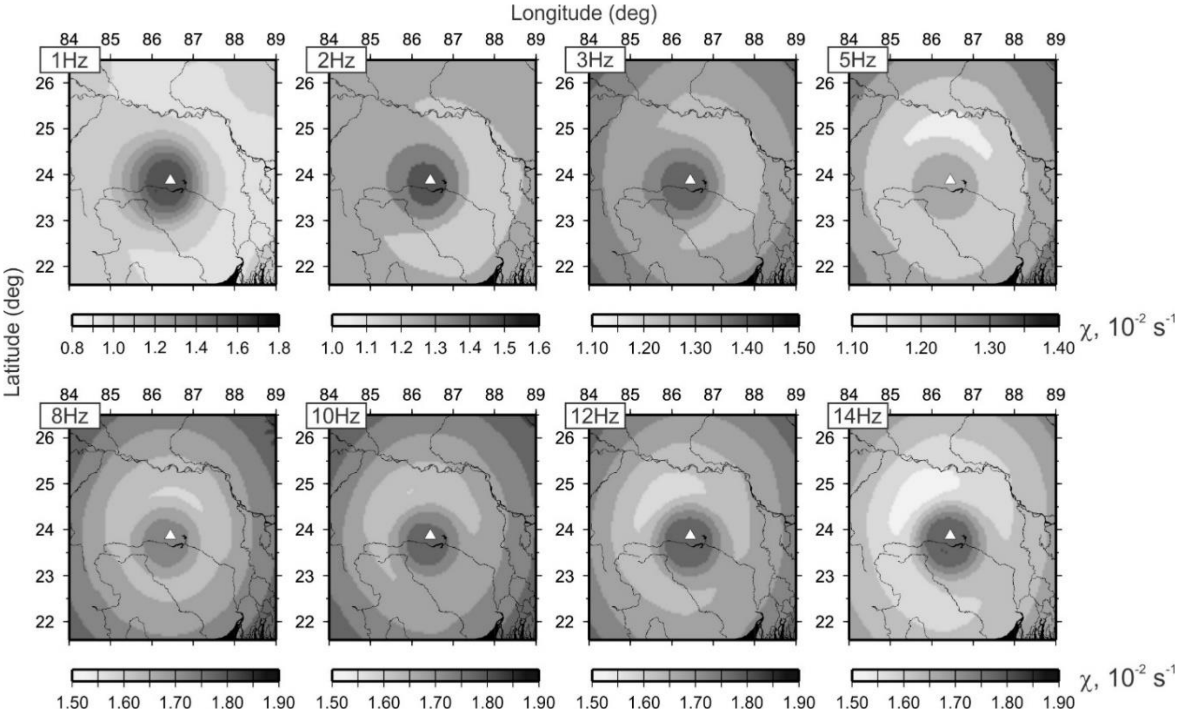

Figure 6.7. Attenuation coefficients χ_{detrend} within eight frequency bands (labels) with regional trend with distance removed. Triangles show the seismic station used in this study. Note that the values and spatial patterns of χ are close at all frequencies, indicating frequency-independent coda-envelope decays.

Step 3) in the processing procedure above is performed by approximating $\chi_{\text{detrend}}(f_{\text{b}},x,y)$ at each point (x,y) by a linear regression model with respect to f_b:

$$\chi_{\text{detrend}}\left(f_{\text{b}},x,y\right)\approx\chi_{\text{linear}}\left(f_{\text{b}},x,y\right), \tag{6.20}$$

where

$$\chi_{\text{linear}}\left(f,x,y\right)\equiv\gamma_{c,\text{Earth}}\left(x,y\right)+\pi Q_{c,\text{Earth}}^{-1}\left(x,y\right)f\ . \tag{6.21}$$

In this relation, $\gamma_{\text{c,Earth}}$ and $Q_{\text{c,Earth}}^{-1}$ are regression coefficients with meanings of geometrical attenuation and in-situ coda Q_c^{-1} at point (x,y), respectively. These quantities have consistent and mutually complementary physical meanings representing the frequency-independent and dependent parts of coda amplitude decays, i.e., the non-Q and Q-type attenuations defined in section 6.1. Subscripts '$_\text{c}$' in these notations indicate that these medium properties refer to the seismic coda, and they may differ from analogous quantities for body or surface waves. In particular, the "coda" properties $\gamma_{c,\text{Earth}}$ and $Q_{c,\text{Earth}}^{-1}$ should be highly sensitive to the magnitudes and spatial distributions of wave reflectors and scatterers in the study area.

Thus, instead of eight independent models for apparent Q_c at each f_b (Figure 6.2) loosely related by scaling law $Q\left(f_{\text{b}}\right)=Q_0 f_{\text{b}}^{\eta}$, I obtain two frequency-independent quantities $\gamma_{c,\text{Earth}}$ and $Q_{c,\text{Earth}}^{-1}$ (Figure 6.8). Although these quantities are still empirical, they are better constrained (utilize all $\chi_{\text{detrend}}\left(f_{\text{b}},x,y\right)$ data), independent of the selection of $G(t)$ in eq. (6.5), and therefore much more physical than Q_0 or η, or than the original $Q_c(f)$ (Figure 6.2). In particular, in contrast to the original Q_c^{-1} controlled by the assumed value of β_0 in Aki's (1969) model, $Q_{c,\text{Earth}}^{-1}$ can be unambiguously viewed as a coefficient in the Taylor series for $\chi(f_\text{b},x,y)$ with respect to f_b (eq. (6.21); Morozov, 2010a). In the final step 4) of the above procedure, data residuals are evaluated for regression (6.20):

$$\Delta\chi\left(f_{\text{b}},x,y\right)=\chi_{\text{detrend}}\left(f_{\text{b}},x,y\right)-\chi_{\text{linear}}\left(f_{\text{b}},x,y\right). \tag{6.22}$$

These quantities can be interpreted as frequency-dependent coda attenuation (deamplification) factors for locations (*x*,*y*) (Figure 6.9). As discussed in section 6.6, these quantities may be useful for seismic site characterization.

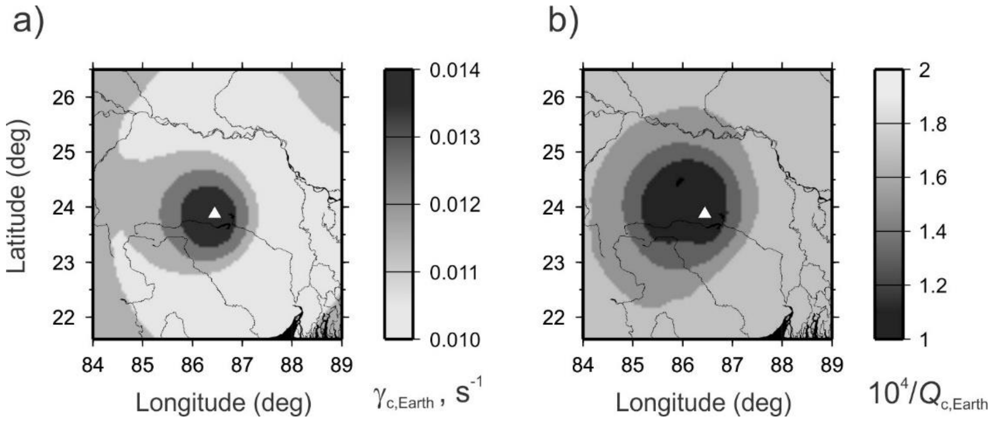

Figure 6.8. Coda envelope model derived from χ maps in Figure 6.7: a) geometrical (frequency-independent) attenuation; b) inverse effective $Q_{c,Earth}$. Triangles show the seismic station.

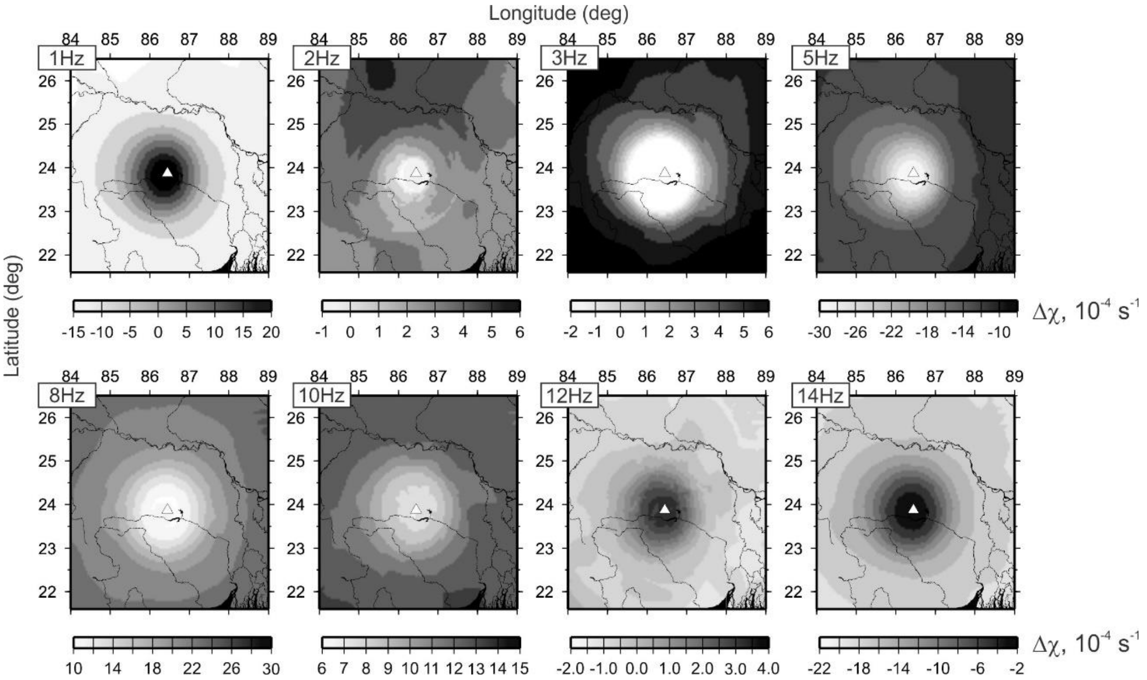

Figure 6.9. Coda deamplification factors $\Delta\chi$ at eight frequencies used in Q_c measurements (labels).

6.4. Near-Elastic Character of Coda Envelopes

The above analysis allows making an important general observation about the seismic codas in the East Indian Shield: most of the observed coda behavior can be explained by wave propagation within an *elastic* Earth's crust. Despite the usual understanding of the seismic Q as an indicator of wave "attenuation" caused by fluids, elevated temperatures, and zones of small-scale scatterers within the crust (Aki, 1969), the observed $Q_c(f)$ dependencies are readily explained by time-only (or travel-distance only) dependent wave amplitude decays. Such time-only dependencies can be caused by the effects of varying velocities, layering, and reflections and mode conversions on major discontinuities, such as the base of the sedimentary deposits and the crust. This observation also applies to numerous studies in many areas around the world, in which the Q-factor steeply increases with frequency (Morozov, 2008b, 2010a; Morozov et al., 2018). The observation of near-elastic S-wave propagation within the crust is also supported by other results of this dissertation (chapters 5 and 7).

With regard to the proposed elastic character of seismic coda, two types of evidence were given in this chapter. First, the simple theoretical model in Figure 6.1 shows that even a one-layer, purely elastic crust will produce a $Q_c(f)$ that is quantitatively close to the observed dependencies. In numerous publications (e.g., Aki and Chouet, 1975) it is stated that parameter Q_0 in the empirical law $Q_c(f) \approx Q_0 f^{\eta}$ represents "seismic attenuation", and the low value of $Q_0 \approx 100$ is thought of representing a significant attenuation at seismic frequencies. However, the model in Figure 6.1 shows that the value of Q_0 can be naturally explained by the thickness of the crust (or layer) and reflection coefficient at its base. This model may explain, for example, why Q_0 is usually larger for older and colder crust within stable cratons – in these areas, the crust and sediments are thicker and reflectivity is lower.

The second key argument for the elastic character of coda is observational. As shown by the attenuation-coefficient approach (section 6.3; Figures 6.5 and 6.6), the decays of the normalized coda amplitudes with time are nearly frequency-independent. Therefore, there appears to be little contribution from frictional processes within the medium. Frictional mechanisms such as viscosity or pore-fluid friction would cause the phenomenon of mechanical hysteresis, in which certain fraction of mechanical energy would be lost during every wave cycle. Such phenomena are characterized by mechanical-energy loss increasing with frequency, which is *not seen in the data* (Figures 6.5 and 6.6).

The origin of the observed $Q_c(f)$ in the near-elastic mechanisms explains why steeply increasing $Q(f)$ dependencies are so commonly reported. As Morozov (2008b, 2010a, 2010b, 2011a) illustrated for many types of waves, the increase of Q with frequency is explained by the fact that the actual ray paths bend upward or reflect (like in Figure 6.1), which causes the amplitude decay with distance to occur faster than in radial waves assumed in the standard model by Aki and Chouet (1975). These phenomena are known as wave defocusing, and they cause geometrical attenuation $\gamma > 0$. When interpreted by the Aki and Chouet's (1975) approach and many of its modifications, the positive γ is then seen as an artificial $Q(f)$ increasing with frequency.

6.5. Preliminary Model for Coda Amplitudes

Determination of a suitable form of the "reference" or "background" geometrical spreading for coda waves is a difficult problem, and no universal solution for it likely exists. In this section, I only suggest an empirical model for geometrical spreading for coda inspired by the mapping procedure by Xie and Mitchell (1990) and Singh et al. (2019).

From eqs. (6.8) and (6.18), a reasonable empirical form of $G(t)$ additionally dependent on distance from the station r can be suggested:

$$G\left(t,r\right) = t^{-\beta_0} \exp\left(-\gamma_0' r t\right). \tag{6.23}$$

This relation follows the average trend of frequency-independent coda amplitudes within the study area, and the χ_{detrend} and $\chi_{c,\mathrm{Earth}}$ values are determined with respect to this form (Figures 6.7 and 6.8a). By combining the effective geometrical spreading (6.23), attenuation (6.21), and the surface-consistent site terms (6.22), the measured decay rates of coda envelopes (shown by $Q_c(f_{\mathrm{b}})$ maps in Figure 6.2) are accurately reproduced.

As shown by eq. (6.23), the geometrical spreading for coda cannot be rigorously represented by a single time dependence $G(t)$ as in eq. (6.5). The coda consists of waves traveling within a broad area surrounding the source and receiver, and its geometrical (elastic) spreading depends on the entire structure within this area. In particular, the coda depends on the source-receiver distance, at least for wider separations between them. This dependence can be seen from the difference between parameters $\beta = 1$ modeled in a boundless homogeneous half-space and likely valid for an immediate vicinity of the source (Aki and Chouet, 1975), $\beta \approx 2$ measured at local distances (Jhajhria et al., 2017), and $\beta \approx 5$ at near-regional distances estimated in subsection 6.3.1. The geometrical spreading for coda should also depend on the selected coda start time and window length. Note that even at 300–350-km distances, Singh et al. (2019) use the definition of coda start times recommended for local-earthquake studies: $t_{\text{coda start}} = 2t_S$ (where t_S is the direct S-wave time) but not definitions by group velocities, such as 3.15 km/s for Lg coda by Xie and Mitchell (1990).

To understand the strong sensitivity of β to the source-receiver distance and other parameters of the data, note that the geometrical spreading has different meanings for traveling waves and codas. For a traveling wave (body or surface), the purpose of the geometrical spreading function is to describe the amplitude of the wave at time t, such as represented by factor $G(t) \equiv t^{-\beta}$ in eq. (6.5). By contrast, for coda, the amplitude itself is unimportant and only its time derivative $G'(t) \equiv \partial G / \partial t$ is used (eq. (6.9)). For a power law $G(t) \propto t^{-\beta}$, these two functions are closely related as

$$G'(t) = -\beta G(t)/t \ . \tag{6.24}$$

However, this relation cannot be used for seismic coda, in which local variations of amplitudes are not simply proportional to $G(t)/t$. Large values of β derived from $G'(t)$ in coda measurements refer to such local scattered-wave amplitude variations (as in eq. (6.24)), and they should not be replaced with simplistic body-waves $G(t)$ models. Numerical modeling (Morozov, 2010a) shows that power-law wave amplitude decays are close to the $t^{-\beta}$ form (still with $\beta > 1$) only to about 50 – 100-km distances. Beyond these distances, amplitude variations are more complex and may be non-monotonous. Note that unlike β, the attenuation coefficient γ appears to always attain stable values ranging from zero to about 0.1 s^{-1}, with consistent correlations with tectonic types of the crust (Morozov, 2008b, 2010a). This is because γ is a differential quantity evaluated locally, similar to function $G'(t)$ above.

Although the geometrical spreading for coda is not a function of time alone, the model in subsection 6.3.2 allows writing it for each earthquake/station pair as an integral over the interior of the scattering ellipse:

$$G = t^{-\beta_0} \exp\left[-\frac{t}{S_W} \iint_S dxdyW(x,y)\gamma_{c,\text{Earth}}(x,y) \right]. \tag{6.25}$$

Here, eq. (6.14) was used to express G through the observed γ, which further predicted from $\gamma_{\text{c,Earth}}$ similarly to predicting Q_c^{-1} in eq. (6.20). This empirical expression should explain coda amplitudes in the absence of attenuation, and therefore it can facilitate measurement of Q when moderate attenuation is present. The complete location-, time-, and frequency-dependent model replacing eq. (6.5) is

$$A(f,t) = S(f)R(f)G\exp\left[-\frac{\pi ft}{S_W} \iint_S dxdyW(x,y)Q_{\text{c,Earth}}^{-1}(x,y) \right]. \tag{6.26}$$

where G is the regional geometrical spreading in eq. (6.25).

6.6. Discussion

Although much weaker than in Q_c models (Figure 6.2), the footprint of the procedure by Singh et al. (2019) still dominates the near-station area in the final images (Figures 6.8 and 6.9). This footprint consists of the area in which *all* of the scattering ellipses overlap (see Figure 5 in Singh et al. (2019)). In this area, the approximation of the heuristic forward model for Q_{c}^{-1} is most problematic (section 6.3). With such non-uniform acquisition geometry, regionalization as attempted by Singh et al. (2019) is likely impossible without detailed knowledge of the mechanism of the coda, which is unavailable. However, outside of the footprint area[1], the average values of γ and Q_e can probably be trusted in these images.

For comparisons with existing coda models (e.g., Singh et al., 2019), the change of parameterization from the conventional (Q_0, η) to (γ, Q_e) can be viewed as an alternate way to describe $Q_c(f)$ dependencies. However, parameters (γ, Q_e) yield new insights into the earth's structure that are difficult to glean from (Q_0, η) or from the frequency-dependent $Q_c(f)$. The (γ, Q_e) parameterization encourages more specific and quantitative interpretations than usually achieved by reporting $Q_c(f)$ values. In particular, elastic structures generally correspond to $Q_e^{-1} = 0$, and variable γ represents the complexity of crustal structure. As described in section 6.4, larger γ values (i.e., faster geometrical spreading) to increased crustal velocity gradients, pronounced layering, and stronger small-scale reflectivity and scattering. These effects were modeled numerically for realistic media and structures with and without attenuation (Morozov et al., 2008; Morozov, 2011a). When the attenuation is "turned on," quantity $Q_e^{-1} > 0$ becomes a measure of all frequency-dependent effects including the anelasticity of the crust. As shown in this chapter, these effects are relatively weak within the eastern Indian Shield. Since coda envelope decay rates are often nearly frequency independent (section 6.1), crustal Q_e^{-1} is likely low in many areas around the world.

Due to the consistent physical background and unambiguous separation between parameters γ and Q_e, these parameters can be expected to be comparable for different types of waves. Morozov (2008b, 2010a, 2010b, 2013) and Morozov et al. (2008) reinterpreted a number of Q_c and other types of Q studies by using this pair of parameters instead of the conventional Q_0 and η. Figure 6.10 shows a summary of this interpretation of *Lg* coda Q combined with the results from this chapter. Although producing nearly identical dependencies of wave amplitudes $A(f,t)$, the (γ, Q_e) parameterization reveals a simple correlation with tectonic and geological features of the study areas (Morozov, 2008b). Tectonically stable areas are characterized by $\gamma \langle \gamma_D = 0.008$ s^{-1},

---

[1] Singh et al. (2019) provide a resolution estimate that appears comparable to the footprint area (their Figure 8). However, this estimate refers only to their inverse approach within the same footprint area and does not account for the non-uniform weighting of the forward model (chapter 5 in this dissertation).

and in active tectonic areas, γ is above this level and extends to about 0.1 s^{-1} (Figure 6.10b). Across the entire range of tectonic ages, γ decreases with age (gray line in Figure 6.10b). Morozov (2008b) explained this reduction of γ by lower crustal velocity gradients, weaker reflectivity, and thicker crust in older tectonic regions. The effective attenuation quality factor Q_e exceeds about 800–1000 in most cases. For tectonically stable areas, Q_e is generally higher, and its values are difficult to measure and scattered (principally because the corresponding attenuation per one wavelength $Q_e^{-1} \ll 1$) (Figure 6.10a).

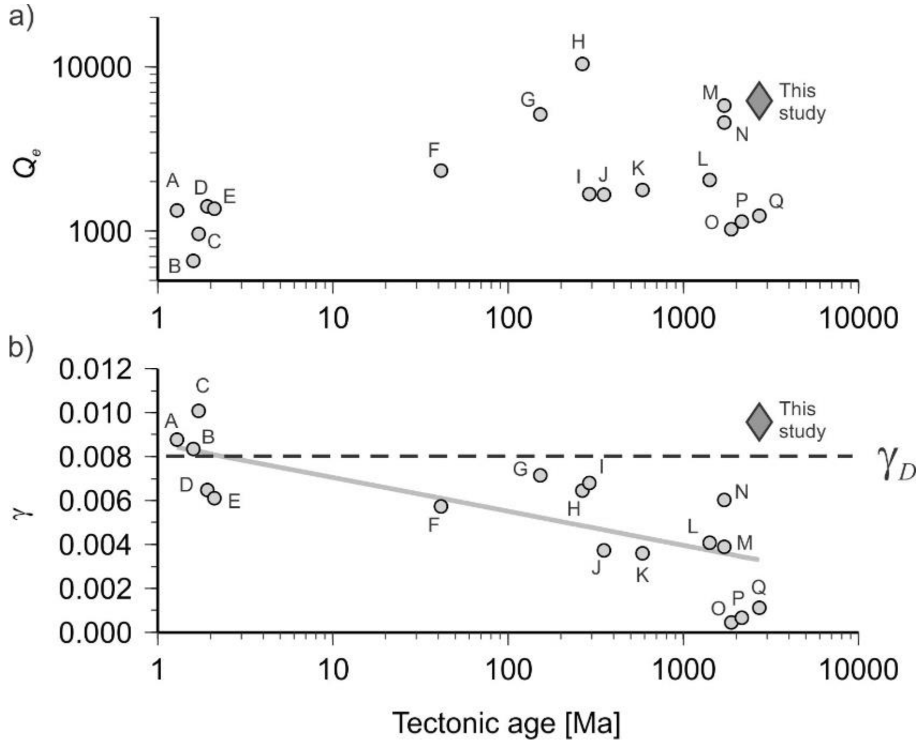

Figure 6.10. Compilation of (γ, Q_e) results for different areas by Morozov (2008b) (labeled circles) with the average value for eastern Indian Shield by Singh et al. (2019) (diamond labeled "This study"), as functions of time since the most recent tectonic activity: a) effective inverse attenuation (Q_e) and b) geometrical attenuation (γ).The thick dashed line shows the discriminant γ_D = 0.008 s^{-1} (Morozov, 2008b), and the gray line is the interpreted trend of γ with tectonic age). Letters indicate the tectonic regions (Mitchell and Cong 1998): A – The Andes Mountains; B – Basin and Range Province of north America; C – Tethys region (the area of convergence of the Eurasian, African, Arabian, and Indian plates), D – the Arabian Peninsula; E – the East African Rift; F – the Rocky Mountains; G – northeastern China; H – the eastern Altaid belt of Eurasia; I – the Tasman province of Australia; J – the Atlantic Shield of South America; K – the African Fold Belts; L – the North American Craton within the United States; M – the Australian Craton; N – Eurasian cratons; O – African shields, P – the Brazilian Shield; Q – the Indian Shield. The tectonic age of this study was taken the same as for point Q.

In relation to the interpreted level of γ_D, the ~20% magnitudes of acquisition/inversion footprints in $\gamma_{c,\mathrm{Earth}}$ and $Q_{c,\mathrm{Earth}}$ do not affect the principal conclusions about γ values. The geometrical attenuation $\gamma_{c,\mathrm{Earth}}$ is between 0.01 and 0.013 s^{-1}, which is above γ_D and within the range characteristic for active tectonic areas (Figure 6.10b). These increased values of γ may be due to the structural complexity caused by extensive folding and faulting in the foothills of Himalaya (Singh et al., 2019). Outside of the near-station footprint, the values of $\gamma_{\mathrm{c,Earth}}$ slightly increase into the interior of the Indian Shield west and south-west of the seismic station (Figure 6.8a). However, the amount of this increase is below 0.001 s^{-1} and may be insignificant. Overall, spatial variations of the model appear to be not reliably resolved by these data.

Q-type coda attenuation within the study area is typical for stable tectonic regions, with the lowest $Q_{c,\mathrm{Earth}}$ of about 5700 (Figures 6.8b and 6.10a). Note that the inverted values are about 20 to 30 times larger than $Q_0 = Q(1\ \mathrm{Hz})$ by Singh et al. (2019) (Figure 6.2). This relation between Q_e to Q_0 is typical for coda studies (Morozov, 2008b). As mentioned above, Q_e has the meaning of a Q-factor for waves within the crust, and similar values of Q are found in body-wave attenuation studies (e.g., Atkinson 2004). Similarly to the observations in section 6.2, effects of $Q_{c,\mathrm{Earth}}$ are weak compared to those of $\gamma_{c,\mathrm{Earth}}$ and the frequency-dependent site deamplification factors $\Delta\chi$ (Figure 6.9). Therefore, the inverted $Q_{c,\mathrm{Earth}}$ values may be within fluctuations of these primary factors.

The spatial pattern of the attenuation-coefficient residuals $\Delta\chi$ is dominated by the acquisition footprint (Figure 6.9). Interestingly, this footprint is positive at 1 Hz and above 10 Hz but negative between these frequencies (Figure 6.9). These variations are likely caused by resonances beneath the recording station. Farther away from the recording site, spatial variations and contrasts between close frequencies are present, such as at 1, 2, and 3Hz frequencies (Figure 6.9). However, these variations are weak (about $3\cdot10^{-4}\ s^{-1}$, or ~3% of γ; Figure 6.9) and difficult to interpret. These patterns may be affected by measurement uncertainties due to the distribution of earthquakes and the regionalization method by Singh et al. (2019). These patterns may also contain contributions from source effects and near-surface resonances, which may corroborate the suggestions by Jhajhria et al. (2017) that coda is dominated by near-surface scattering. Potentially, with footprint-free $\chi(f_{\mathrm{b}},x,y)$ data derived directly from coda envelopes, $\Delta\chi(f_{\mathrm{b}},x,y)$ would contain useful information for site amplification maps.

As discussed in section 6.3, along with the relatively straightforward inversion procedure, regionalization of the observed $\chi(f)$ (i.e., forward model for this inversion) remains a difficult open question. This question equally applies to the present as well as to the conventional coda Q methods such as by Xie and Mitchell (1990). Rigorous physics-based models directly explaining $\chi(f)$ and/or coda amplitude envelopes are needed. Such models could follow the single- or multiple-scattering energy transport theories (e.g., Zeng et al., 1991; Nishigami, 1997) or numerical ray-theory or waveform modeling (Fehr et al., 2019; Morozov et al., 2008).

6.7. Conclusions

The frequency-dependent coda Q results by Singh et al. (2019) for the eastern Indian Shield are reinterpreted by using two new properties of the Earth's subsurface: geometrical attenuation denoted γ and an alternate (effective) Q-factor. Both of these parameters are frequency-independent, which makes these quantities better constrained and easier to compare for different geographic areas. In chapter 7, mapping of these parameters will be derived from a much larger dataset in Zagros area of Iran.

The inverted level of $\gamma \approx 0.010$ to 0.013 s^{-1} is similar to those in other areas of active tectonics around the world. The effective Q_c is above 5700, and the Q-type attenuation may be below the detection level. In addition to γ and effective Q_c, maps of frequency-dependent and spatially-variant coda amplification and deamplification are obtained. Effects of these resonances on coda spectra also exceed those of the effective coda Q_c.

Thus, coda amplitudes in the study area are principally determined by the structure of the crust and not by Q-type (intrinsic or small-scale random scattering) attenuation effects. This observation is corroborated by observations of raw spectral amplitudes of the coda, in which the time derivatives of the logarithmic coda envelopes are nearly frequency-independent. These general conclusions are supported by the results from Zagros dataset (chapter 7) and are likely relevant to many other areas around the world.

CHAPTER 7

ANALYSIS OF SEISMIC CODA II: Lg CODA ENVELOPES IN ZAGROS AREA

In this chapter, I describe the analysis of seismic coda in Zagros area of Iran. As mentioned in the preceding chapter, coda waves are used for characterization of the physical properties of the Earth. When done for an extended area, results of coda measurements are often presented by maps of the frequency-dependent coda Q, denoted Q_c. However, mapping results and even the definition of Q_c depends on multiple variables: the source and receiver locations, measurement time, and reference model for geometrical spreading. Therefore, Q_c cannot be rigorously represented by a function of only one point within the subsurface, as it is commonly assumed.

This chapter reviews the existing methods and proposes several new methods for coda mapping. In addition or replacement for Q_c, new, physically better justified parameters of the subsurface are proposed: exponents of geometrical spreading (denoted γ here), effective attenuation (denoted q_e), and scattering intensities (denoted $\delta\phi$). I compare several methods for mapping parameters γ, q_e, and $\delta\phi$ by using Lg coda records from Zagros dataset (chapter 2). The presentation is based on the following paper submitted to the Geophysical Journal International:

- Safarshahi, M., and Morozov, I. B. Quantitative interpretation of Lg coda envelopes: Several types of mapping and spatial interpolation in Zagros area of Iran.

My contributions to the submitted paper in processing the data, providing codes, inversion, and participation in interpretation and writing.

7.1. Introduction

The goal of seismic coda studies consists in characterizing the Earth's crust by the properties of scattered waves. With numerous computational enhancements, the principle of coda imaging remains the same since its original inception, and it consists in utilizing the shapes of normalized coda envelopes within several frequency bands (Aki, 1969). Envelope normalization removes the effects of the source and receiver and reduces coda measurements to deriving a single quantity denoted the coda Q, or Q_c. This quantity is typically found to be steeply increasing with frequency (denoted f here) and often with coda lapse times (Aki and Chouet, 1975; Calvet and Margerin, 2013).

By now, frequency-dependent $Q_c(f)$ curves have been documented in hundreds of studies within many areas around the world. However, the fundamental question about the meaning of Q_c and its relation to physical properties of the crust and/or uppermost mantle is still far from clarity. It is even unclear whether the Q_c is purely a measured attribute of coda shape, phenomenological property of the crust, or both. In numerous models originating from the scattering-theory approach by Aki and Chouet (1975), these questions are answered by hypothesizing phenomenological P- and S-wave Q-factors of the crustal and mantle layers. These Q-factors are further subdivided into the P- and S-wave Qs, intrinsic and scattering Qs, and sometimes into more subtle types of Q related to wavefield fluctuations, boundary effects, or pore flows within rock samples (Morozov and Baharvand Ahmadi, 2015). Q-factors are commonly found to be frequency-dependent, which is often approximated by the power law $Q\left(f\right)=Q_0 f^{\eta}$. For seismic codas, values $\eta > 0$ and often close to $\eta = 1$ are commonly reported. However, neither such steep $Q(f)$ dependencies nor parameters Q_0 and η necessarily represent “attenuation” in physical sense related to small-scale heterogeneity, temperature, fluids, and melts within the medium. For example, $Q(f)$ dependencies with $\eta \approx 1$ are observed for purely elastic crust containing velocity gradients and reflecting boundaries such as sedimentary layers and the Moho (chapter 6). The physical meanings of the measured Q_0 and η need to be examined in each specific case.

Establishing the physical reality and meanings of the frequency-dependent $Q(f)$ is a complex task, which is not considered here. Instead, in this chapter, I follow the convention made in most studies and assume that the measured Q_c possesses *some* meaning as an empirical property of the Earth. With this assumption, I only focus on the ways this empirical property is attributed to the continuum of surface or subsurface locations $\mathbf{x} = (x,y)$. I show that this mapping procedure is generally only a mathematical operation which can be performed in multiple different ways, and suggest how it can be improved by physical considerations.

The procedure for distributing the Q_c measured in a finite set of coda records to a continuous function $Q_c(\mathbf{x})$ is called mapping, regionalization (Singh and Herrmann, 1983), or spatial weighting (e.g., Del Pezo et al., 2016). In Q_c mapping, the desired “in-situ” $Q_c^{-1}\left(\mathbf{x}\right)$ at an arbitrary point **x** is sought as a linear combination of values measured from a discrete set of coda records $\left(Q_c^{-1}\right)_k$:

$$Q_c^{-1}(\mathbf{x}) = \sum_k w_k(\mathbf{x})\left(Q_c^{-1}\right)_k , \tag{7.1}$$

where k is the number of an observation, and $w_k(\mathbf{x})$ is some spatial weighting function (Del Pezzo et al., 2016). The same spatial weights are used for different types of inverse Q, such as the intrinsic or scattering parts of Q_c^{-1} (Del Pezzo et al., 2016).

Although eq. (7.1) looks like spatial interpolation, it is not interpolation because there exists no specific coordinate $\mathbf{x}_k$ for a given measurement k, so that the mapped $Q_c^{-1}(\mathbf{x}_k)$ would equal the measured $\left(Q_c^{-1}\right)_k$. Instead, coda measurements are performed in a four-dimensional (4-D) space of receiver and source coordinates, which I denote $\mathbf{x}_i$ and $\mathbf{x}_j$, respectively. The meaning of eq. (7.1) can be seen from the "back-projection" method by Xie and Mitchell (1990), in which the weights $w_i(\mathbf{x})$ are derived by solving an inverse problem with the observed $\left(Q_c^{-1}\right)_k$ serving as data. Such inversion requires a forward problem predicting the coda measurement k from the in-situ Q of the subsurface: $Q_c^{-1}(\mathbf{x}) \rightarrow \left(Q_c^{-1}\right)_k$. However, no rigorous forward model of such kind exists, and as shown in section 7.4, no such model is generally possible. The meaning of mapping by eq. (7.1) is rather specific: it represents a form of 4-D interpolation-extrapolation of the data with respect to the source and receiver coordinates. The success of this mapping can only be verified by predicting the *measured data* $\left(Q_c^{-1}\right)_{k'}$ for some source-receiver combinations k', by using the same eq. (7.1). Therefore, quantity $Q_c^{-1}(\mathbf{x})$ in eq. (7.1) is not guaranteed to be an in-situ property of the subsurface, but it is an auxiliary, "apparent" quantity used in this mathematical interpolation-extrapolation. In section 7.4, I show that several simpler (including more accurate) forms of such 4-D data interpolation can be constructed without assuming an "in-situ" $Q_c^{-1}(\mathbf{x})$.

In the absence of a physically justified forward model for the observed $\left(Q_c^{-1}\right)_k$, functions $w_i(\mathbf{x})$ in eq. (7.1) are usually selected by some rules based on the experiment geometry. For example, Calvet et al. (2013) design these functions so that for any model cell at point **x**, $Q_c^{-1}(\mathbf{x})$ is an average of all readings $\left(Q_c^{-1}\right)_k$ for which the great-circle arc connecting the source and receiver crosses the cell. However, for local coda, this intuitive rule is hardly justified because most scattered waves do not travel along the source-receiver great arc (Aki and Chouet, 1975). In the method by Xie and Mitchell (1990), the measured $\left(Q_c^{-1}\right)_k$ is predicted by averaging the model $Q^{-1}(x)$ over a 2-D surface area enclosed within the scattering ellipse for *k*th source-receiver pair. This areal averaging is also a hypothesis assuming that some "in-situ Q_c^{-1}" at point **x** equally contributes to all measurements whose scattering ellipses cover this point. This hypothesis is difficult to explain, and Xie and Mitchell (1990) gave no argument for it. For Lg phase *Q* (not coda), Xie et al. (2004) used a similar rule with $Q^{-1}(\mathbf{x})$ averaged along the Lg ray path. The subjectivity of such *ad hoc* rules is further increased by the variety of back-projection type (row-action) inverse methods and spatial filtering (such as smoothing) utilized when evaluating the inverse in eq. (7.1) (Xie and Mitchell, 1990). Finally, Del Pezzo et al. (2016) and others proposed numerical models for functions $w_i(\mathbf{x})$ from Monte Carlo simulations of a multiple-scattering energy transport the coda. Del Pezzo et al. (2016) also gave approximations of the weights $w_i(\mathbf{x})$ by Gaussian functions.

Regardless of the detail of weights $w_i(\mathbf{x})$ (eq. (7.1)), from the physics point of view, all of the above mapping approaches contain a common and serious flaw. These models attempt explaining the measured coda Q^{-1} by postulating a namesake property Q^{-1} of the medium (or sometimes the intrinsic and scattering Q^{-1}, or mean free paths in multiple-scattering models; Sato, 1978). However, the notion of an in-situ *Q*-factor is only meaningful in the very abstract model of a quasi-homogeneous medium with small random scatterers. In realistic cases, this approximation ignores all first-order physical factors such as the structure of the crust. For a useful analogy, in reflection seismology, it is well known that the near-source and receiver structure (velocity gradients, low-velocity layers, reflectors) is responsible for most features of the seismic record, and Q^{-1} represents only a small correction to it. Scattering-theory concepts such as the effective *Q* and the mean free path are suitable in quasi-homogeneous media *with no spatial variation* (for more on this, see Morozov and Baharvand Ahmadi, 2015). However, this approximation is insufficient for local and particularly Lg coda mapping, in which spatial variations of crustal properties are sought.

Thus, I argue that for Lg coda mapping, the interpretation should not reduce to the conventional transformation of the measured coda envelope $A(t,f)$ into a $Q_c^{-1}\left(f\right)$, which is further mapped into a $Q_c^{-1}\left(f,\mathbf{x}\right)$. Instead of this procedure, in sections 7.4 and 7.5, I explore two new and one little used old type of approaches:

1) Empirical mapping similar to the one by Xie and Mitchell (1990) but with explicit recognition of the elastic (frequency-independent) and anelastic (frequency-dependent) parts of $A(t,f)$. Instead of $Q_c^{-1}\left(f\right)$ at multiple frequencies f, I use only two simpler, frequency-independent attributes suggested by Morozov (2008b, 2010a, 2011b): the geometrical attenuation denoted γ(x) and effective attenuation factor denoted $q_e = Q_e^{-1}$. These quantities are assumption-independent, and possess a more straightforward interpretation than the frequency-dependent Q_c^{-1}. I explore two alternate mapping schemes: one based on the areal coda averaging model by Xie and Mitchell (1990), and another using averaging over the circumferences of the coda-scattering ellipses rather than their interiors.
2) Alternatively, mapping can be performed not for coda models but any coda data attributes directly, by their interpolation in the 4-D space of source and receiver coordinates. This yields a simple, accurate, and practical approach suitable for predicting coda observations from new source-receiver combinations.
3) Mapping regions of scattering within the near surface using fluctuations of coda power based on the method by Nishigami (1997) (section 7.5).

The empirical maps for Lg coda $\gamma(\mathbf{x})$ and $q_e(\mathbf{x})$ are illustrated by using the Lg coda data from Zagros area in Iran (Figure 7.1). From the Zagros dataset (chapter 2), I extracted 1968 vertical-component, 2146 orientation-independent horizontal-component (H2C), and 1975 three-component (3C) records from 777 earthquakes. Lg coda windows were selected as starting at group velocity 2.6 km/s and extend for 45 s, and records with signal to noise ratios above 1.5 are included in coda mappings.

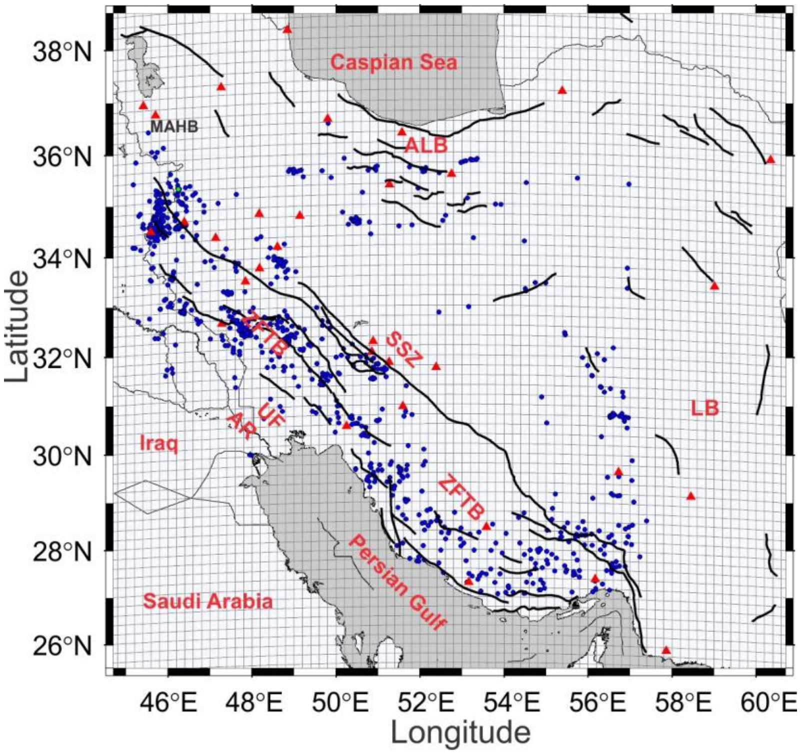

Figure 7.1. Study area showing the seismic stations (red triangles) and source locations (dots) of the Lg coda dataset. The earthquake shown by green dot and station labeled MAHB are used in Figure 7.2. Grid shows the discretization of the area into 0.2° by 0.2° blocks for back-projection inversion and mapping. Lines show major faults. Labels indicate geological features discussed further in this chapter: LB –Lut block, ALB – Alborz, SSZ – Sannadaj-Sirjan zone, ZFTB – Zagros fold thrust belt, UF – unfolded zone, and AR – Arvand Rud river.

Prior to discussing the mapping methods, in section 7.2, I define the attenuation-coefficient parameterization of coda data. As shown in chapter 6 and also on many examples by Morozov (2008b, 2010a, 2010b, 2011b), this parameterization allows achieving model-assumption free results for many types of waves. In section 7.3, I use the attenuation coefficient to make a key observation directly from the data. This observation consists in the predominantly *elastic* (frequency-independent) behavior of the observed coda amplitudes, which can be expressed as $\partial \ln A(t, f)/\partial t \approx const(f)$. This elastic character is rarely noted in the literature, apparently because of the established practice of immediate transformation of $\ln A(t,f)$ into a $Q_c^{-1}(f)$ (Aki and Chouet, 1975). Nevertheless, the nearly frequency-independent time derivatives of $\ln A(t,f)$ appear to be common in many datasets, and they suggest that coda amplitude decay *is not* a *Q*-type process. We can therefore expect that the elastic structure of the crust should be responsible for most of the observed coda envelopes. As shown in section 7.4, the “physical” attenuation (described by parameter q_e) is only a relatively small correction to elastic effects.

7.2. Data Parameterization

As with any data, parameterization of coda observations should be objective (represent the data and not our theories or assumptions) and insensitive to complicating factors which I would like to avoid, such as source magnitudes and local variations of receiver coupling (Mayeda, 1993). Aki’s (1969) classical coda model was motivated by exactly these considerations. By taking time derivatives of the logarithms of coda amplitudes $\ln A(t,f)$, all scaling factors are removed, and local variations of the crustal structure are averaged out by considering sufficiently large scattering times.

As a result of these normalization operations, the raw quantity measured in this method is the temporal attenuation coefficient $\chi(t,f)$,which can be written it two forms (Morozov, 2008b):

$$\chi(t,f) \overset{\text{def}}{=} -\frac{\partial}{\partial t}\ln A(t,f) = -\frac{\partial}{\partial t}\ln\left[G(t)e^{-\frac{\pi f t}{Q_c(f)}}\right]. \quad (7.2)$$

The first of these equations is the definition of χ, and the second is its conventional transformation into the frequency-dependent Q_c by using some reference factor denoted $G(t)$ (e.g., Aki and Chouet, 1975). Function $G(t)$ has the meaning of geometrical spreading in the absence of “attenuation,” which means that $G(t) \overset{\text{def}}{=} A(t,f)$ in the hypothetical case of $Q_c^{-1} = 0$. For Lg coda, the geometrical spreading is taken as a function of time t and the source-receiver distance d (e.g., Xie and Mitchell, 1990). Note that $G(t)$ in eq. (7.2) is not measured but only defined theoretically for some simple reference model. Morozov and Safarshahi (2020) showed that the geometrical spreading for real coda cannot be reduced to a function of only t and/or d. However, in the present chapter, it is only important that: 1) the attenuation coefficient χ is independent of any selection for $G(t)$, and 2) using the second eq. (7.2), function $Q_c^{-1}(f)$ can always be viewed as a recalculation of $\chi(t,f)$.

Of the two forms of eq. (7.2), the first one is unambiguous and most useful for data analysis below. By contrast, the second eq. (7.2) is only *a limited theoretical model* assuming that $G(t)$ is accurately known, and scattering occurs by some perfectly known mechanism, such as a quasi-homogeneous medium with single or multiple scattering, and scatterers distributed in certain way. For example, in local coda studies, the geometrical spreading is usually taken for spherical body waves: $G(t) \propto t^{-1}$ (e.g., Aki and Chouet, 1975), and an analogous model of pure surface waves is used for Lg coda (Xie and Mitchell, 1990). Consequently, the inferred frequency dependence of $Q_c(f)$ is largely determined by the adopted model for $G(t)$. However, specifying the reference $G(t)$ plus inferring a Q_c at independent frequencies f is equivalent to simply reporting the original $\chi(t,f)$ (first eq. (7.2)). Such reverse transformations of $Q(f)$ curves into their parent $\chi(t,f)$ were shown for coda in chapter 6 and for other wave types by Morozov (2008b, 2010a, 2011b). The use of the attenuation coefficient χ encourages measuring and inverting the coda data directly, without referencing subjective and unrealizable models such as quasi-homogeneous crust or following strict conventions in data processing (Havskov et al., 2016).

Because published coda amplitudes (e.g., Aki and Chouet, 1975) usually use geometrical-spreading corrections, let us also define the corresponding modified attenuation coefficient by χ_G:

$$\chi_G \overset{\text{def}}{=} -\frac{\partial}{\partial t}\left(\ln\frac{A}{G}\right) = \chi + \frac{\partial \ln G}{\partial t}. \tag{7.3}$$

This attenuation coefficient is related to the reported frequency-dependent Q (of any kind, not only Q_c) as $\chi_G(t,f) = \pi f Q^{-1}(f)$ (second eq. (7.2)). Note that with this Q-type parameterization, it is expected that $\chi_G(t,f)$ is strictly proportional to t. Thus, for any reference $G(t)$ function, $Q_c^{-1}(f)$ and the two forms of χ (eqs. (7.2) and (7.3)) can be transformed into each other. The first eq. (7.2) is clearly more convenient for Lg coda, because in this case, the accurate function G is unknown. As argued in chapter 6 this function cannot be inferred from simple models of waves in a homogeneous crust. Once the zero-frequency limit $\chi(t,f\rightarrow 0)$ is measured from the data, the geometrical spreading can be obtained from eq. (7.2) as $G(t,f) = G_0(f)\exp\left[-\int^t \chi(t',0)\,dt'\right]$, where G_0 is an arbitrary and generally frequency-dependent factor (Yang et al., 2007; Morozov, 2010a).

Time dependences of $\chi(t,f)$ and $\chi_G(t,f)$ need to be carefully considered further. With relatively short coda time windows and in the presence of random noise and significant amplitude fluctuations, both $\ln A(t,f)$ and $\ln\left[A(t,f)/G(t)\right]$ are usually approximated by linear functions of t for a fixed f. Therefore, the differential quantities χ and χ_G are approximately independent of time, and they can be viewed as functions of frequency alone and written as $\chi(f)$ and $\chi_G(f)$ (Morozov, 2008b). This approximation of short measurement windows is made in most coda studies, and I also use it further in this chapter. However, in some studies, longer time intervals allow observing (for a fixed f) $\chi_G(t,f)$ different from proportional to t, and therefore $Q_c(f)$ variable with t. In the Q-based terminology, this observation is described as the "lapse-time dependence of $Q_c(f)$" (e.g., Calvet and Margerin, 2013) and explained by variations of scattering properties at different crustal or mantle depths. Nevertheless, eqs. (7.2) and (7.3) show that the variation of $\chi_G(t,f)$ with t only indicates that the selected function $G(t)$ is insufficiently accurate in match with the observed $A(t,f)$. This inaccuracy of $G(t)$ comes from grossly oversimplified models and is almost certainly unrelated to the scattering properties of the subsurface.

7.3. Elastic Character of Coda Envelopes

This section continues the discussion of the near-elastic character of coda envelopes started in section 6.4. Figure 7.2 shows the time dependencies of the logarithms of Lg coda envelopes $\ln A(t,f_b)$ measured within several frequency bands denoted f_b, and the corresponding $\chi(f_b)$ within Lg coda window for one earthquake. As seen from the plots on the left in Figure 7.2, the slopes of $\ln A(t,f_b)$ with time t are negative and similar for all f_b. The reduction of coda amplitudes occurs predominantly with time, which is different from Q-type attenuation (which is expected to show slopes steeply increasing with frequency f_b). The time-only dependent amplitude reduction is naturally explained by the geometrical spreading and reflections of seismic waves. For a useful analogy, note that coda waveforms closely resemble reflection seismic records in controlled-source seismology.

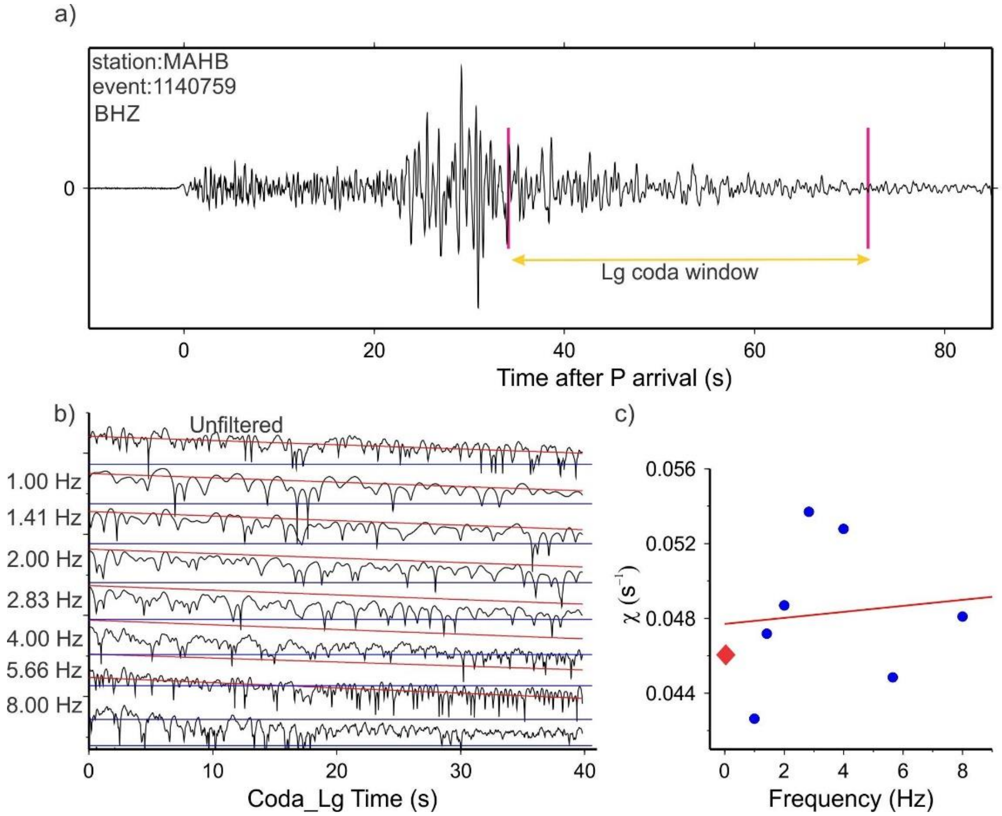

Figure 7.2. Lg coda from earthquake number 1140759 in the database recorded on station MAHB at source-receiver distance 165 km and backazimuth 163°: a) Vertical-component waveform. magenta bars indicate the Lg coda window. b) Logarithms of band-pass filtered coda envelopes (frequencies shown in labels). Red lines show the average slopes representing the attenuation coefficients χ; c) Attenuation coefficients χ versus frequency (blue dots), χ for unfiltered record (red diamond), and their average trend $\chi(f)$ (red line). The location of earthquake (a green dot) and station (labeled MAHB) are shown in Figure 7.1.

Unfortunately, time-only dependent amplitude decays can also be explained by one ambiguity of the *Q* model, which makes the interpretations ambivalent and/or biased (for a review, see Morozov et al., 2018). A frequency-independent $\chi(t)$ can be explained by a $Q_c(f)$ proportional to *f* in the second eq. (7.2), so that the ratio $f/Q_c(f) = const$. Thus, dependencies close to $Q(f) \propto f$ are equivalent to geometrical spreading with no *Q*-type attenuation at all (Morozov, 2008b, 2010a). However, using $Q(f) \propto f$ or even steeper frequency dependencies is clearly an artificial and physically inappropriate way of describing frequency-independent phenomena. A much simpler and more natural view consists in analyzing and reporting the functional dependencies of $\chi(t,f)$ directly (first eq. (7.2)).

By using the χ parameterization of the coda, two observations can be made directly from the plots on the lower right corner in Figure 7.2: 1) the attenuation coefficient is nonzero (usually positive) and nearly constant within the coda windows, and 2) it only weakly varies with frequency. To parameterize such dependencies, I can use the two leading terms in the Taylor series with respect to f (now considering t fixed as the coda window time):

$$\chi(f) \approx \gamma + \pi q_e f \,, \tag{7.4}$$

where γ is the "geometrical" attenuation coefficient, $q_e \overset{\mathrm{def}}{=} Q_e^{-1}$, and Q_e denotes the "effective" (apparent) Q-factor (Morozov, 2008b, 2010a). Similar parameters can be defined for $\chi_G(f)$.

Across the measurement frequency band, the contribution from the geometrical term γ dominates the values of $\chi(f)$ for Lg coda (plots on the lower right corner in Figure 7.2). These observations are similar in many other coda studies (Morozov, 2008b, 2011b; Jhajhria et al., 2017; Morozov et al., 2018; chapter 6 of this dissertation). Therefore, we can expect that the elastic structure should explain most of the $A(t,f)$ dependencies. In addition to this weak or moderate trend with frequency, $\chi(f)$ contains strong variations due to the partly coherent scattering and near-surface resonances (chapter 6). Similar to the scattering-theory coda model (Aki, 1969), I disregard these variations here and focus on the averaged linear trend $\chi(f)$ in eq. (6.11).

The attenuation-coefficient data collected from 1968 vertical-component Lg coda windows of this study are summarized in Figure 7.3. The values of γ range from about -0.01 to 0.07 s^{-1}, and q_e ranges from about -0.004 to 0.004. The mean q_e is small and negative ($-6 \cdot 10^{-4}$), and the one standard deviation range includes the point $q_e = 0$ (green lines in Figure 7.3b). Thus, the deviation of q_e from zero appears to be statistically insignificant. The data show a slight trend of the (negative) q_e reducing with increasing γ (thick red line Figure 7.3b), which might be due to the additive background noise in the seismograms. By empirically subtracting this trend, noise-corrected (γ, q_e) data are obtained (Figure 7.3c). The mean value of this corrected q_e is low: $q_e \approx 8.35 \cdot 10^{-5}$, suggesting that the characteristic Q-factor for coda waves within the study area is about $Q \approx 12000$. Note that with uncorrected q_e (Figure 7.3b), the average Q would be higher or even negative.

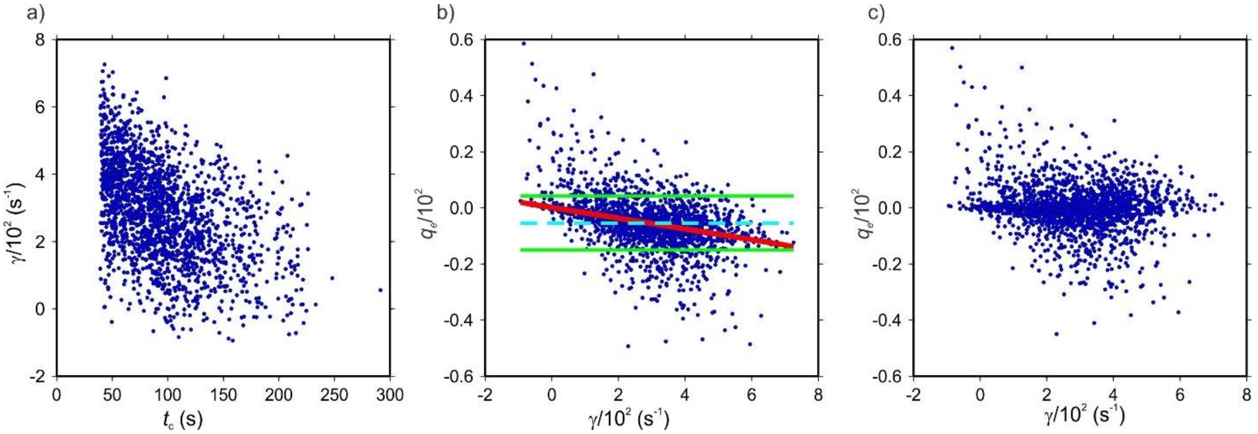

Figure 7.3. Measured attenuation coefficients in vertical-component Lg coda windows: a) values of γ versus coda times; b) cross-plot of q_e and γ, c) the same for corrected q_e. Lines in b) indicate the mean level of q_e (cyan dashed), its range of one standard deviation (green lines), and mean $q_e(\gamma)$ trend (thick red line).

The high and likely unmeasurable values of Q in this study are not surprising, and they can be seen directly from coda observations (Figure 7.3). Similar weak attenuation with $Q \approx 4000$ or higher was found for body S-waves for an adjacent area (chapter 5), from other body-wave attenuation studies (e.g., Palmer and Atkinson, 2020), and inferred by re-interpreting frequency-dependent Q from many other areas (Morozov, 2008b, 2010a, 2010b, 2011b). High crustal Q values can also be recognized from steep positive frequency dependencies of $Q(f)$ reported for many areas around the world (Morozov et al., 2018).

7.4. Empirical Regionalization of Lg Coda

As described in section 7.1, empirical coda regionalization directly attributes the measured data attributes such as the inverse Q-factors to the (sub)surface by using certain mapping rules. In this section, I show that similarly to Q^{-1}, coefficients γ and q_e of the Taylor series for the attenuation coefficient (eq. (6.11)) can be used with any of these mapping methods. Because these frequency-independent coefficients are better constrained and only two of them replace all maps of $Q(f)$ at multiple frequency bands, mapping of γ and q_e appears to be preferable for interpretation. More arguments about this subject were given in chapter 6.

To perform mapping of any coda attribute p_k such as Q_k^{-1}, γ_k, or $(q_e)_k$ measured in kth coda record from ith source measured on jth receiver, let us denote by an overbar ($\bar{p}(\mathbf{x})$) the corresponding mapped attribute at point **x**. Analogously to eq. (7.1), $\bar{p}(\mathbf{x})$ can be obtained by inverting the following linear forward model:

$$p_k = \int d^2\mathbf{x} K_k(\mathbf{x})\,\bar{p}(\mathbf{x}), \tag{7.5}$$

where $K_k(\mathbf{x})$ is the weighing kernel for this record, and the integration is performed over the surface of the Earth. The kernel is normalized so that $\int d^2\mathbf{x} K_k(\mathbf{x}) = 1$ (e.g., Del Pezzo et al., 2016). After discretization on a spatial grid $\{x_n\}$ shown in Figure 7.1, function $K_k(\mathbf{x})$ becomes matrix kernel K_{kn}, eq. (7.5) becomes matrix product $p_k = \sum_n K_{kn}\bar{p}_n$, and the normalization relation becomes $\sum_n K_{kn} = 1$.

Mapping of the measured attribute p_k into its gridded counterpart $\bar{p}_n$ is found by some form of an inverse of eq. (7.5). Iterative row-action ("tomographic") inverses are convenient for such large and mixed-determined problems. In row-action methods, each data point is modeled independently, and model updates $\delta p(\mathbf{x}_k)$ are constructed from the resulting data misfit δp_k. In this chapter, I utilize the so-called filtered Simultaneous Iterative Reconstruction Technique (SIRT), which is often used in travel-time tomography (Aster et al., 2018). As a starting model $p^0(\mathbf{x}_n)$, I use the minimum-length inverse (Menke, 1984) of the same problem, in which all eqs. (7.5) are summed: $p_{sum} = \sum_n K_n^{sum}\bar{p}_n$, where $K_n^{sum} \overset{\text{def}}{=} \sum_k K_{kn}$ and $p_{sum} \overset{\text{def}}{=} \sum_k p_k$.

In the coda Q mapping approach by Xie and Mitchell (1990), kernel $K_k(\mathbf{x})$ is selected equal to one when $t_S + t_R \le t_k$ and zero otherwise: $K_k(\mathbf{x}) = \theta(t_k - t_S - t_R)$, where t_k is the coda recording time, t_S and t_R are the travel times within the source- and receiver parts of the scattered wave path, and $\theta(\ldots)$ is the Heaviside step function. Equation $t_S + t_R = t_k$ gives the scattering surface, which is an ellipsoid (ellipse in 2-D) in the case of a homogenous Earth (e.g., Xie and Mitchell, 1990).

On the discrete model grid, kernel $K_k(\mathbf{x})$ is also represented by a matrix, which I denote $K_{kn} = \theta_{kn}$. In Figure 7.4, this model is inverted from γ and q_e values measured for the vertical-component Lg coda in the Zagros dataset. For comparison with other Lg coda studies (e.g., Xie and Mitchell, 1990; chapter 6), values of γ are transformed into γ_G (eq. (7.3)) using the reference geometrical spreading function for surface waves in a homogeneous half-space $G(d,t) = \frac{1}{\sqrt{2\pi d}}\left(\frac{V^2t^2}{d^2} - 1\right)^{-1/4}$, where d is the source-receiver distance (for its derivation, see Appendix A in Xie and Nuttli, 1988).

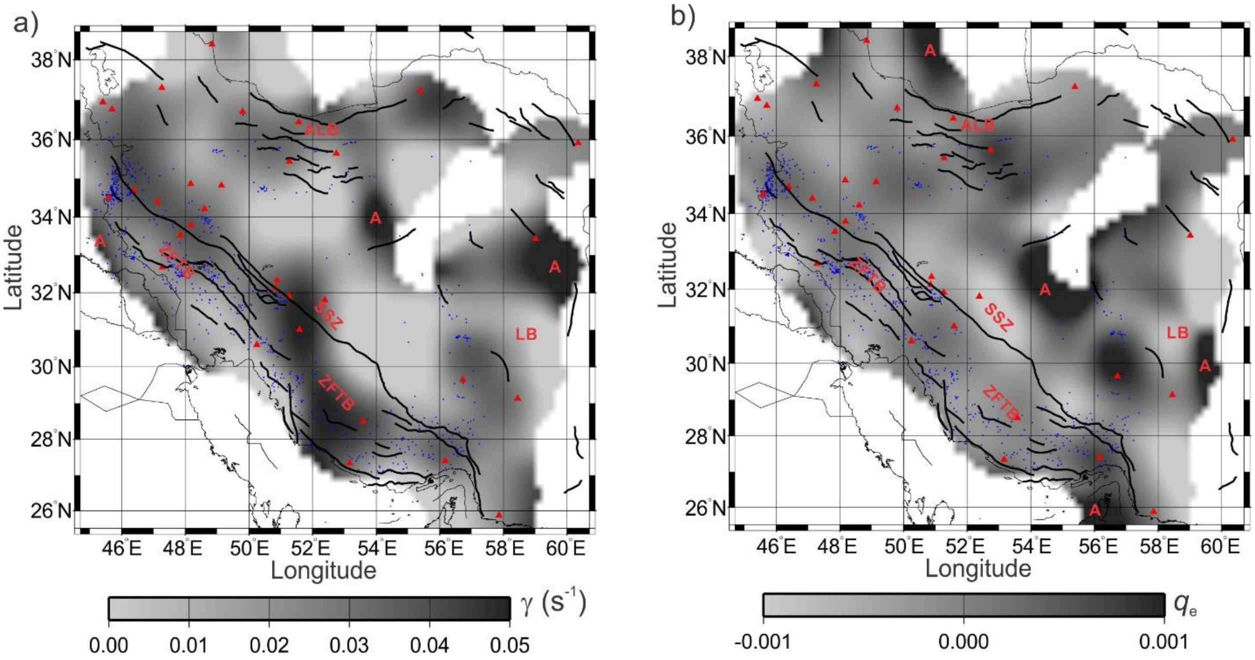

Figure 7.4. Mapped vertical-component Lg coda parameters using inversion of areal coda averaging as in the approach by Xie and Mitchell (1990): a) γ, and b) q_e. Lines show major faults. Labels indicate: LB –Lut block, ALB – Alborz, SSZ – Sannadaj-Sirjan zone, ZFTB – Zagros fold and thrust belt, and A – possible imaging artifacts. The model is only shown in areas covered by scattering ellipses (non-white).

The resulting map of $\gamma_G(\mathbf{x})$ shows a good correlation with geology and surface topography (Figure 7.4). Tectonically stable areas, such as the Lut block (e.g., Berberian et al., 2001) with low topography have a smaller value of $\gamma_G(\mathbf{x})$, but the active tectonic areas such as the Zagros fold and thrust belt (ZFTB) and Alborz have a larger value of $\gamma_G(\mathbf{x})$. q_e values are small, variable, and likely below the detection limit with anomalies scattered over parts of the map. High values of γ and q_e near the edges of the images likely represent imaging artifacts due to poorer coverage and data noise (labeled A in Figure 7.4).

As noted in section 7.3, the Lg coda is explained by a predominantly frequency-independent amplitude decrease with distance and travel time. As q_e values in the data, the mapped attenuation levels are weak and lie in the range of -0.001 to 0.001. In some areas like parts of the Sannadaj-Sirjan zone (SSZ), small negative values of q_e are obtained. Thus, comparison of these maps again shows that the coda is dominated by the spatial variations of $\gamma(\mathbf{x})$, which should be related to the elastic properties of the crust such as its thickness and layering (Morozov, 2008b).

The uniform areal averaging of Q_c^{-1} in Xie and Mitchell's (1990) mapping method is a heuristic choice not supported by any physical model of the coda. Integration over the constant-time surfaces $t_S + t_R = t_k$ is more viable if the coda is dominated by single scattering within the near surface (e.g., within sedimentary layers or on topographic variations or crustal faults), as suggested by Morozov (2011b) and in chapter 6 of this dissertation. Recently, Gabrielli et al. (2020) supported these inferences by direct observations of near-surface guided waves dominating the coda recorded at the Mount St Helen's volcano (state of Washington, U.S.A.). The single-scattering approximation is also successful in reflection seismology and seismic interferometry, in which the imaging environments are close to the observations of seismic coda. Note that function $G(d,t)$ above was also derived for single scattering of surface waves (Xie and Nuttli, 1988). The corresponding forward-model kernel for single scattering is $K_k(\mathbf{x}) = \delta(t_S + t_R - t_k)$, where $\delta(\ldots)$ here is the Dirac delta function. In practical calculations, the delta function was replaced with a "boxcar" function tapering the scattered-wave time $t_S + t_R$ to the duration of the observed coda window.

The resulting mapping of the vertical-component Lg coda is shown in Figure 7.5. As this figure shows, with sufficient data coverage, the results are close to those in Figure 7.4. This comparison shows that empirical coda mapping is relatively insensitive to the selection of the forward model. This is not surprising, because empirical mapping basically represents interpolation of the observed p_k values, and its spatial resolution is limited by the set of the available source and receiver points (see subsection 7.4.3).

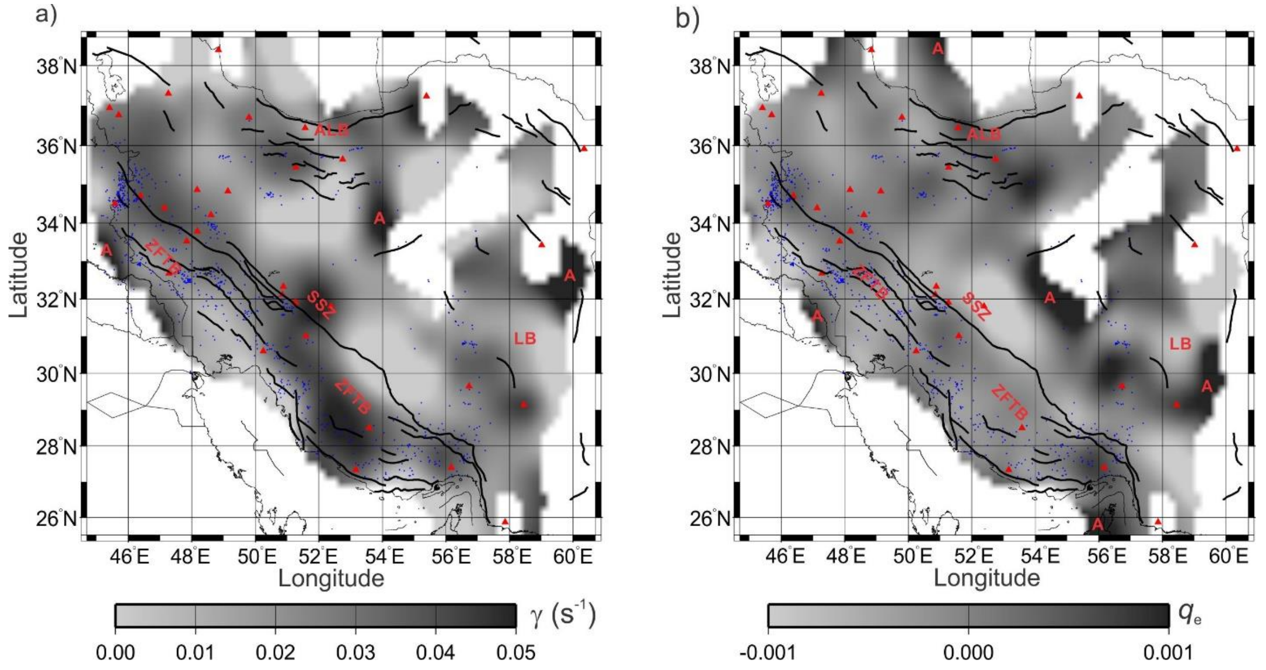

Figure 7.5. Mapped vertical-component Lg coda parameters using inversion of a single-scattering coda model: a) γ, and b) q_e. Plotting style and labels are as in Figure 7.4.

By using the mapped γ_G and q_e, the inverse frequency-dependent Lg coda Q can be obtained as $Q_c^{-1}(f) = q_e + \gamma_G / (\pi f)$ (eqs. (7.2) to (6.11)). This transformation of the maps in Figure 7.5 gives a mapping of the vertical-component $Q_c(f)$ (Figure 7.6), which can be directly compared to other regionalization studies (e.g., Singh et al., 2019). As in most studies (Morozov, 2008b, 2010a; chapter 6 in this dissertation), these maps are dominated by a trend of $Q_c(f)$ steeply increasing with frequency (Figure 7.6). This trend is principally caused by positive values of γ_G (Figure 7.5), which means that the geometrical spreading of coda waves occurs faster than expected in the reference $G(d,t)$ model. Overall, the two model- and frequency-independent maps $\gamma(\mathbf{x})$ and $q_e(\mathbf{x})$ contain the same information as the frequency-dependent Q_c at all frequencies. The two maps also seem to provide easier interpretations and more direct links to geological structure and physical properties (Figure 7.6).

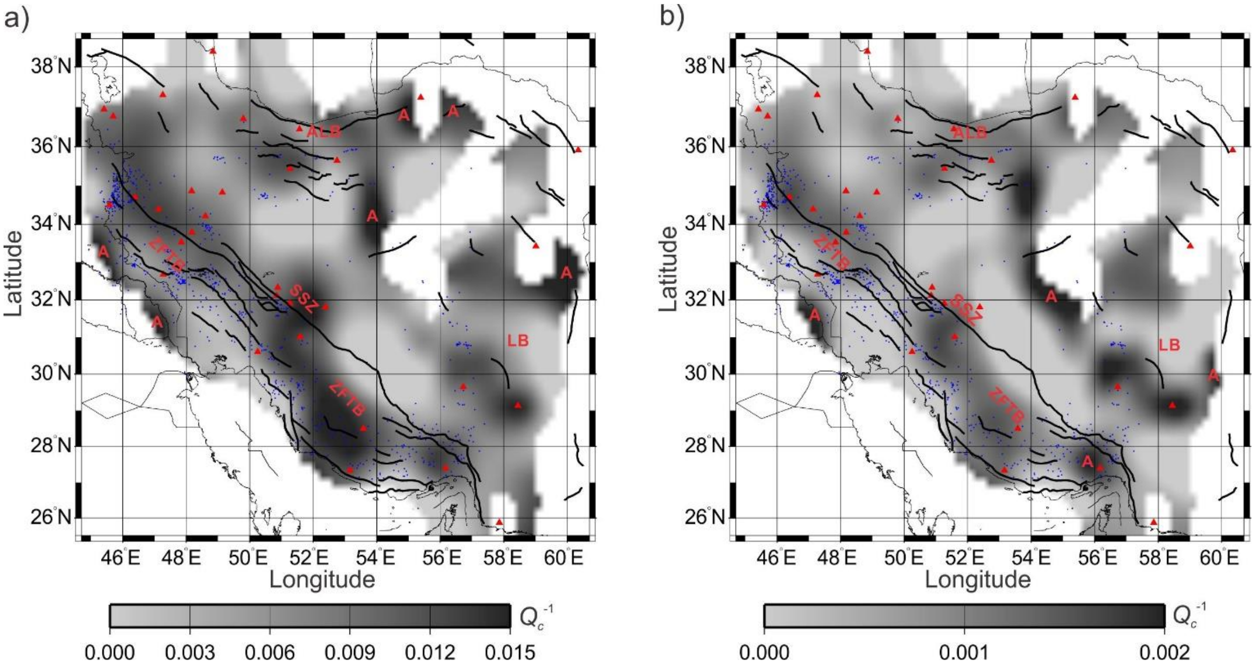

Figure 7.6. Coda Q^{-1} (Q^{-1}_{c}) inferred from the mapped γ and q_e: a) at frequency 1 Hz, b) at frequency 10 Hz. Plotting style and labels are as in Figure 7.4.

To characterize the scattering properties of the crust, it is useful to explore not only the vertical but also horizontal components of seismic records. For S waves scattered and traveling at various directions and to long distances within a heterogeneous crust, significant horizontal components of ground motion can be expected. Different wave modes (P, vertically and horizontally polarized S waves, surface and guided waves) exchange energy when interacting with dipping heterogeneities, and therefore multicomponent estimators of ground-motion amplitudes should provide better stability of the measurements. To evaluate such multicomponent Lg coda attributes, I repeated the above measurements and attribute mapping using the orientation-independent horizontal-component amplitudes (H2C; Figure 7.7) and the three-component amplitudes (3C; Figure 7.8).

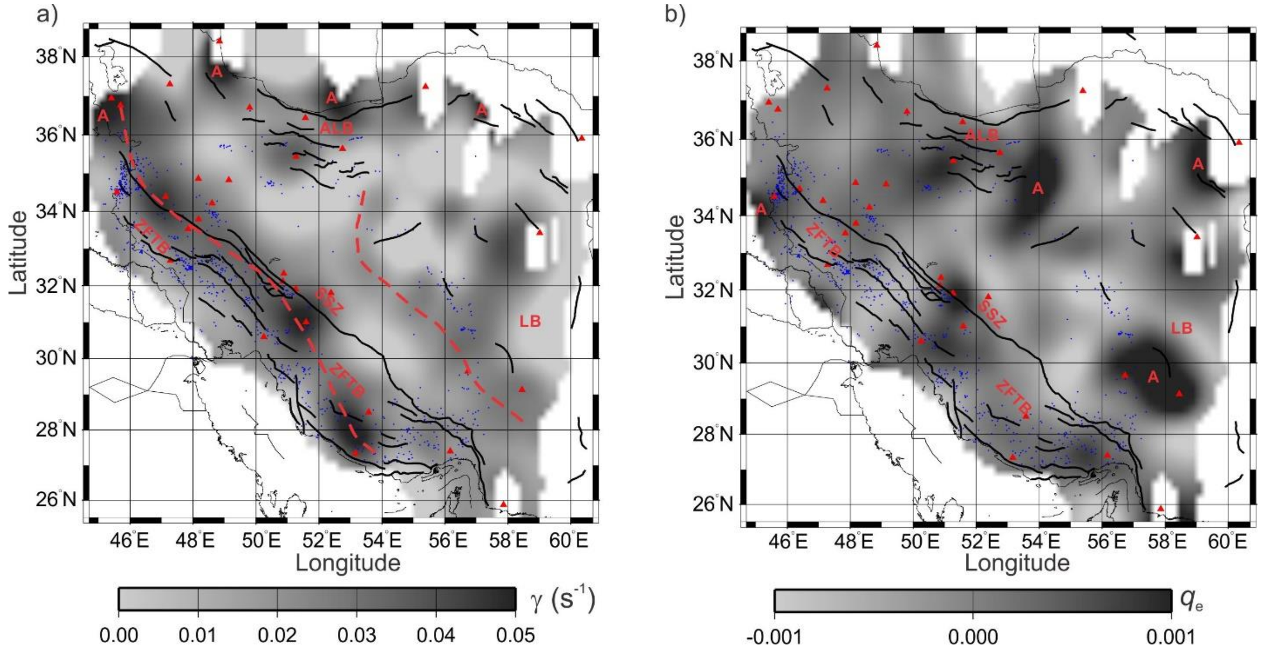

Figure 7.7. Maps of orientation-independent horizontal-component (H2C) Lg coda parameters using inversion of single-scattering coda model.: a) γ, and b) q_e. Dashed lines show NW- SE trends in γ. Plotting style and labels are as in Figure 7.4.

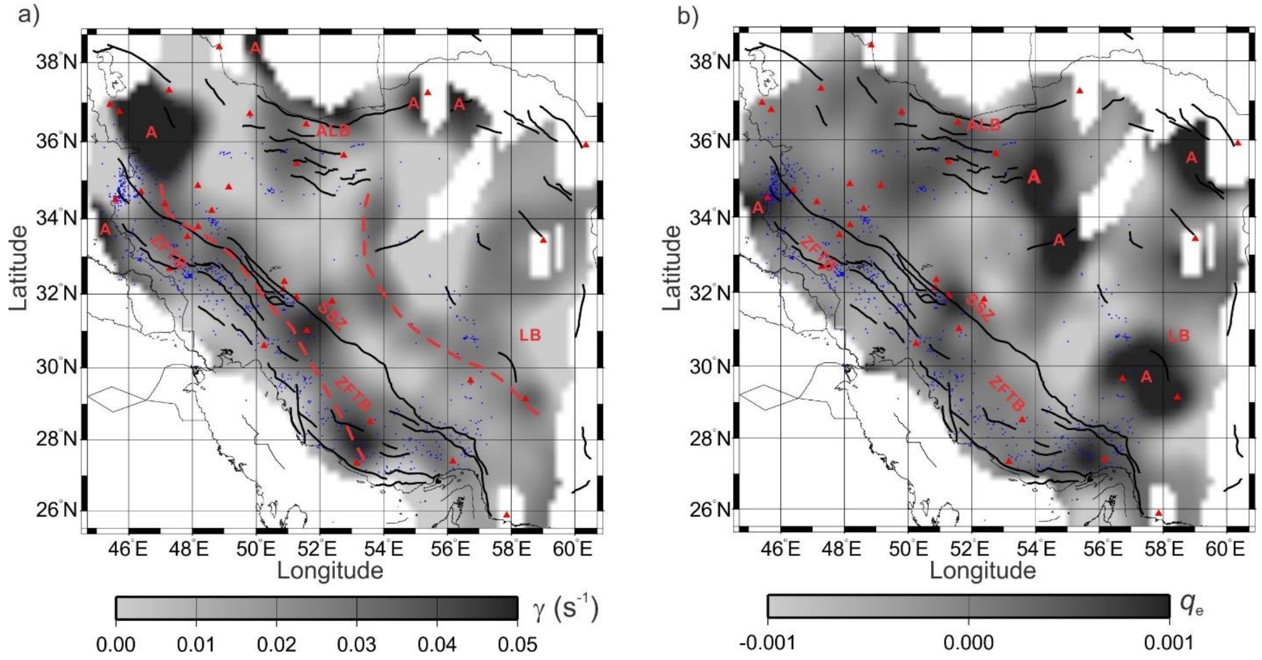

Figure 7.8. Maps of three-component (3C) Lg coda parameters using inversion of single-scattering coda model.: a) γ, and b) q_e. Dashed lines show NW-SE trends in γ. Plotting style and labels are as in Figure 7.4.

These multicomponent amplitudes were evaluated by relations used in chapter 5:

$$U_{\mathrm{H2C}} = \sqrt{|U_R|^2 + |U_T|^2}\text{ , and }\quad U_{\mathrm{3C}} = \sqrt{|U_V|^2 + |U_{\mathrm{H2C}}|^2}\text{ ,} \tag{7.6}$$

where U_V, U_R, and U_T are the instantaneous amplitudes (envelopes) of the vertical, radial, and transverse components of recordings, respectively.

Because q_e values are small and likely dominated by noise, I will emphasize the comparison of γ values in Figures 7.5 to 7.8). Compared to Figures 7.5a, maps of multicomponent γ appear to reveal more consistent NW-SE trending structures following the topography and tectonic features in Zagros and the Central-east Iran areas (dashed lines in Figures 7.7a and 7.8a). As a tomographic inverse, the SIRT-based mapping allows performing various resolution and covariance tests. For example, Figure 7.9 shows a model grid cell coverage for the single-scattering model of the vertical-component Lg coda mapping.

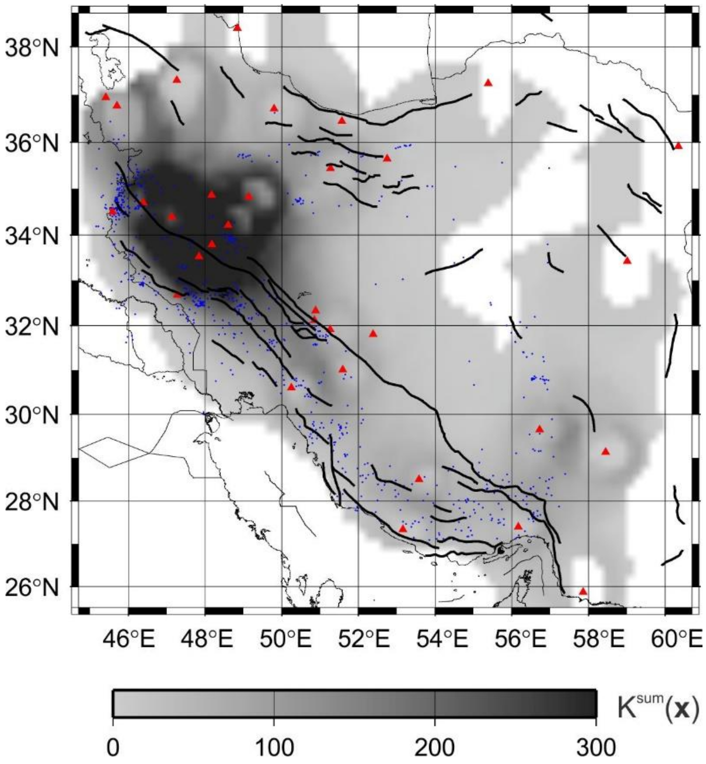

Figure 7.9. Model grid cell counts for the single-scattering model (Figure 7.5). The gray-scale bar shows the number of data points affected by each grid cell.

For each model grid cell, the gray scale level in this figure shows the numbers of data points affected by γ or q_e values in this cell. As this figure shows, the denser source and station distributions in the NW part of Zagros leads to significantly greater coverage of the model.

Figure 7.10 shows a standard checkerboard test for the spatial resolution of γ for vertical-component Lg coda mapping. Similar tests for Q_c were shown by Singh et al. (2019). The size of each of the input checkerboard blocks was 13 ×13 grid cells. As Figure 7.10 shows, such blocks are resolved by the inversion well in most of the study area, except two blocks in the eastern part of the image (at (34.5°N, 58°E) and (32°N, 56°E)). Trials of smaller checkerboard blocks (not shown here) showed degradation of resolution in the central part of the model. Therefore, this test shows that the available source and receiver distribution allows mapping variations of the “in-situ” γ or q_e on about 150 km spatial scale. Due to low coverage, the model is not well-resolvable for the block located near 34.5°N,58°E and also for the block at 32°N,56°E.

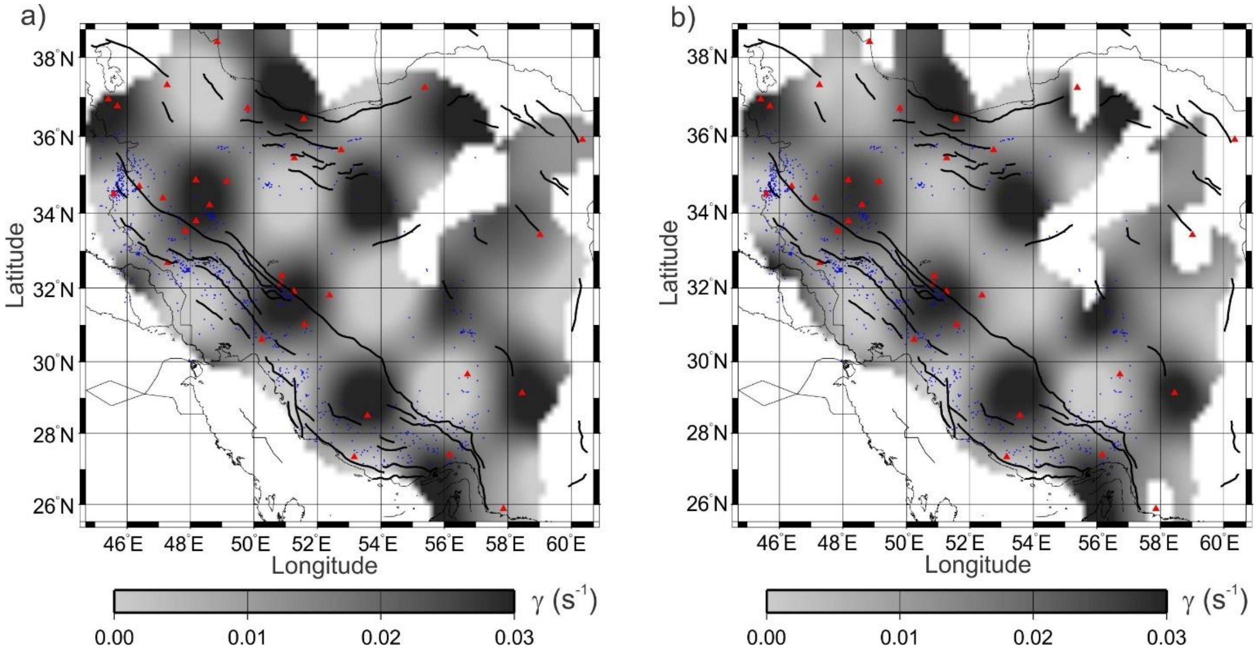

Figure 7.10. Checkerboard resolution tests for parameter γ: a) using the mapping method by Xie and Mitchell (1990) (Figure 7.4); b) using the single-scattering forward model for coda (Figure 7.5).

7.4.1. Interpretation of coda attribute maps

Although spatial variations of coda attributes can be mapped and show correlations with surface topography, crustal structure, and geology, these observations still do not answer the basic question about how the mapped properties can be understood physically. In the existing interpretations, maps of Q_c and similar coda attributes at spatial locations $\mathbf{x}$ are viewed as phenomenological "seismic attenuation" properties of the study areas (e.g., Xie and Mitchell, 1990; Calvet et al., 2013; Del Pezzo et al., 2016; Singh et al., 2019). However, the meanings of these maps are more complicated and not simply related to the subsurface. In this section, I briefly consider this meaning.

The usual interpretation of mapped $Q_c(\mathbf{x})$ as representing the "coda Q at point $\mathbf{x}$" is meaningful only when the spatial variation of Q_c across the scattering ellipse is insignificant, i. e. when the regionalization is actually unimportant. For example, this is the case of Aki and Chouet's (1975) model, in which the source and receiver are closely spaced, and a single Q_c value refers to the whole study area. However, this model is insufficient for regionalized Lg coda, for which the $Q_c(\mathbf{x})$ is expected to be different in the vicinities of the source, receiver, and near the scatterers (e.g., Xie and Mitchell, 1990).

The uncertainty in the physical meaning of coda maps arises from the lack of differentiation between the Q_c as a quantity measured from the data and the "in-situ" $Q_c(\mathbf{x})$ attributed to the subsurface. However, these namesake quantities are fundamentally different. The observed data consist of discrete readings $\left(Q_c^{-1}\right)_k$ taken within the k^{th} coda time window, which are characterized by two source and two receiver coordinates and the selected lapse time, but no specific spatial coordinates $\mathbf{x}$. Thus, coda data reside in a 2+2+1=5-dimensional data space, and they cannot be unambiguously mapped onto a 2-D surface or 3-D volume of the physical subsurface. Conversely, spatially mapped quantities such as $Q_c^{-1}\left(\mathbf{x}\right)$ are functions of a single 2-D or 3-D vector $\mathbf{x}$, and they cannot represent codas recorded from any given source-receiver combination and at different lapse times.

If Q_c cannot be associated with individual points in in the subsurface, then what is the meaning of the mapped $Q_c(\mathbf{x})$ field? For empirical regionalizations considered in this chapter and in the literature, this question can be answered as follows. To unambiguously interpret coda attributes mapped as functions of **x**, I need to transform them back into the data domain, i.e. to the shape of the observed coda envelope $A(t,f)$ for a given source, receiver, and recording time. This transformation consists in evaluating the same forward model as used for the back-projection inversion (eq. (7.5)). This forward modeling can be performed for new source and receiver positions and coda times that may not be present in the dataset. For example, Figure 7.11 shows such inferred values of γ for arbitrary source or receiver locations. To obtain these images, eq. (7.5) for the back-projection coda model was used, with a new data index 'k' corresponding to the source (for Figure 7.11a) or receiver (for Figure 7.11b) selected at the center of the model, and the other pair of coordinates varied across the coverage area. From this γ and a similarly mapped q_e, $Q_c(fb)$ at arbitrary pass-band frequency can also be estimated as in Figure 7.6 (not shown for brevity). As in the forward model, the scattering surfaces were constructed for times equal to the source-receiver distance in km divided by 2.6 km/s plus half of the coda window (45 s).

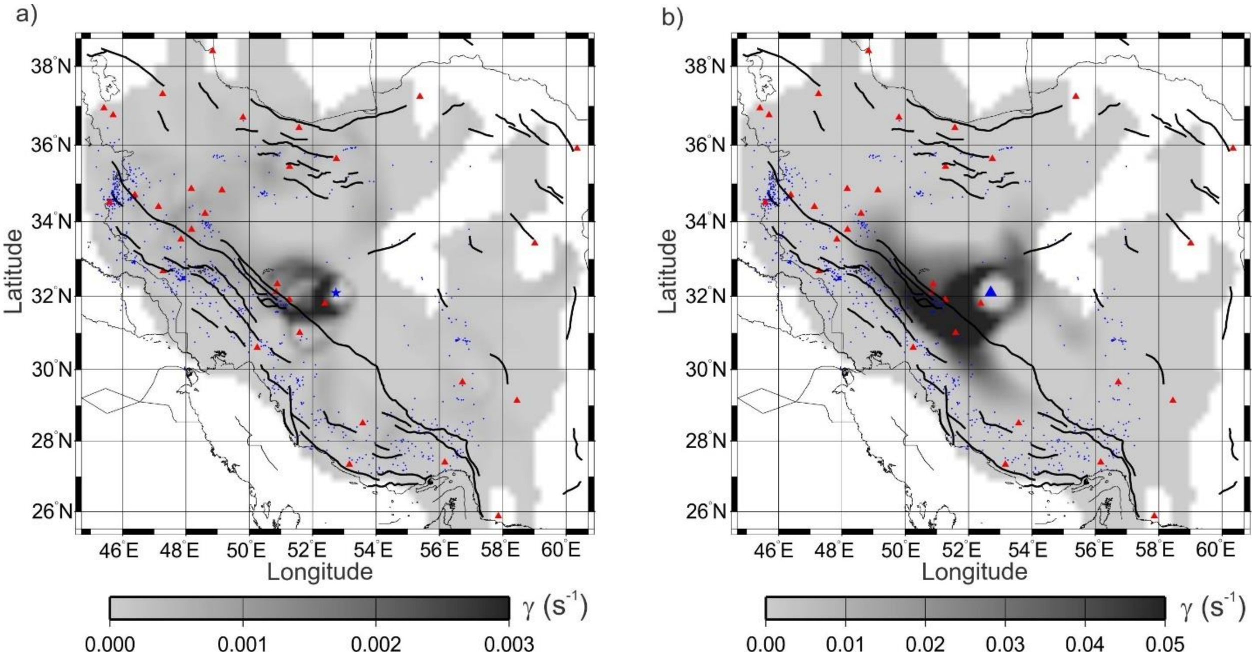

Figure 7.11. Lg coda γ predicted by the single-scattering model (Figure 7.5): a) for a new earthquake at the center of the study area (star), and arbitrary positions of receivers; b) for a new receiver at the center of the study area (blue triangle) and variable positions of the sources.

Maps of predicted measured parameters $\gamma(\mathbf{x})$, $q_e(\mathbf{x})$, or, $Q_c^{-1}(f,\mathbf{x})$ for a geographical area such as shown in Figure 7.11 can be used for interpreting coda measurements, assessing their spatial variability, or potentially for planning deployments of new seismic stations.

In summary of this subsection, the inverse-mapping and forward-modeling procedure represents *a form of spatial interpolation or extrapolation (resampling) of the Lg coda data*. The quantities produced by this procedure are coda parameters expected to be measured for source-receiver pairs $\left(Q_c^{-1}\right)_{k'}$ different from those in the actual data (Figure 7.11). The maps of $\gamma(\mathbf{x})$, $q_e(\mathbf{x})$, or $Q_c^{-1}(f,\mathbf{x})$ (e.g., Figures 7.5 to 7.8) are mainly auxiliary quantities used for this data prediction. Care should be exercised when attributing these quantities to the subsurface, and particularly when considering their spatial patterns.

7.4.2. Mapping by spatial interpolation

Once we realize that spatial mapping coda attributes represent a form of data interpolation, then it is important to note that such interpolation can be performed by many other algorithms. Some of these algorithms may provide better insights into the meanings of the mapped quantities or better accuracy in reproducing the measured data. For example, Figure 7.12 illustrate two forms of direct spatial filtering of coda data within the source and receiver planes.

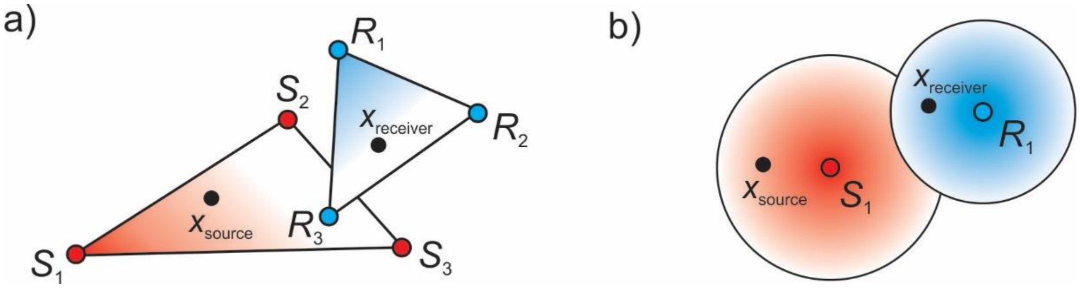

Figure 7.12. Schematic illustration of 4-D interpolation by source and receiver locations. For arbitrary source position $\mathbf{x}_{\text{source}}$ and receiver $\mathbf{x}_{\text{receiver}}$ (black dots), the nearest sources (labeled $S_{\text{j}=1,2,3}$) and receivers (labeled $R_{i=1,2,3}$) can be obtained in several ways: a) by Delaunay triangulations of the available locations (triangles); b) by conical spatial filters (circles)). Shading within the triangles indicates the values of functions $F_{j=S_1}^{S}(\mathbf{x})$ and $F_{i=R_1}^{R}(\mathbf{x})$, with dark colors corresponding to the value of one, and white corresponding to zero.

In this Figure, coda parameters at a continuum of receiver locations $\mathbf{x}_R$ and source locations $\mathbf{x}_S$ are derived from their discrete readings by: 1) using Delaunay triangulations within the source and receiver planes (Figure 7.12a), and 2) using convolution with a conical spatial filter (Figure 7.12b). Within the planes of source and receiver positions, these operations are described by the corresponding interpolation kernels $F_j^S(\mathbf{x})$ and $F_i^R(\mathbf{x})$,which are known as "shape functions" in finite-element modeling. For example, for Delaunay triangulation, a linear shape function $F_j^S(\mathbf{x})$ equals one at point $\mathbf{x} = \mathbf{x}_j$ and linearly decreases to zero at all adjacent source locations (shaded by red and blue in Figure 7.12a). With these kernels, any quantity p_j measured at the source (such as some coda attribute) can be simulated at $\mathbf{x}_S$ as $p(\mathbf{x}_S) = \sum_j F_j^S(\mathbf{x}_S)\, p_j$, and similarly for receivers: $p(\mathbf{x}_R) = \sum_i F_i^R(\mathbf{x}_R)\, p_i$. By interpolating within both of these planes, any coda attribute p_k can be transformed into one recorded at the source-receiver pair ($\mathbf{x}_S$, $\mathbf{x}_R$):

$$p(\mathbf{x}_S, \mathbf{x}_R) = \sum_{\substack{\text{all } k \\ (i,j \text{ pairs})}} F_j^S(\mathbf{x}_S)\, F_i^R(\mathbf{x}_R)\, p_k \ , \tag{7.7}$$

Note that this mapping is based only on the geometrical proximity of sources and receivers and does not require hypothesizing subsurface model attributes (eq. (7.5)) with all the epistemic complexities discussed in the preceding sections.

Figure 7.13 shows γ in the study area interpolated by using eq. (7.7) using the two types of spatial filters in Figure 7.12. The result represents another way of Lg coda Q mapping. In contrast to the "in situ" $Q_c(\mathbf{x})$ on a 2-D plane of $\mathbf{x}$, this quantity has a clear meaning of a measured coda attribute, which can be verified by conducting a seismic experiment at the new receiver location. However, because coda attributes exist not in a 2-D but in the 4-D space of ($\mathbf{x}_S$, $\mathbf{x}_R$) coordinates, this mapping is only successful in the vicinity of the actual source-receiver pairs. To predict coda attributes at other receiver positions, different source locations or much broader filters would need to be tried in Figure 7.12.

Note that unlike mappings based on inversions (eqs. (7.1) and (7.5)) or broad spatial filtering (Figure 7.12b), the interpolation using Delaunay triangulations (Figure 7.12a) accurately predicts each of the discrete data coda readings p_k (γ_k in Figure 7.13, but this is valid for any other coda attribute as well). Thus, this type of interpolation mapping is mathematically most accurate.

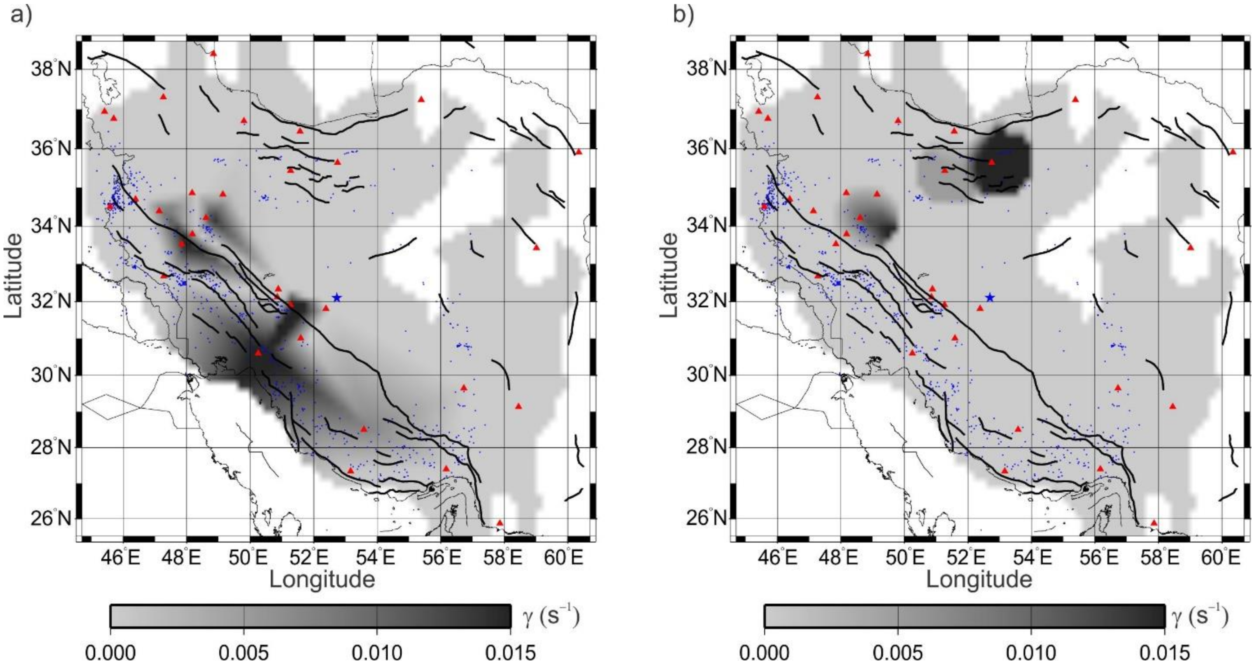

Figure 7.13. Lg coda γ predicted by 2-D filtering within the source- and receiver coordinate planes for a new earthquake at the center of the study area (star), and arbitrary positions of receivers: a) using Delaunay triangulation of the locations of receivers (Figure 7.12a); b) using conical filters centered on receivers (Figure 7.12b).

7.4.3. Spatial resolution

Although this may appear contrary to the traditional goals of regionalization (revealing spatial variations of scattering properties), it is important to note that because the mapped coda attributes are not subsurface properties but only *measured data* properties, their mapped patterns are algorithm-dependent on spatial scales smaller than the characteristic scales of the selected algorithms. These patterns and scales vary broadly for different inversion-based (e.g., Figures 7.4a and 7.5a) and interpolation-based approaches (Figures 7.13a and 7.13b). Generally, an increase of smoothness of a map reduces the accuracy of its predicting the observed coda data.

Because of the algorithm dependence, at smaller scales for which the images (e.g., Figures 7.4a, 7.5a, 7.11a, 7.11b, 7.13a, or 7.13b) differ, the mapped spatial variations of γ (and similarly q_e or $Q_c^{-1}(f)$) are likely unreliable for geological and physical interpretations. However, on larger spatial scales (i.e., disregarding the dependence on **x**), these attributes can be interpreted in a 1-D sense (a single parameter for the whole region), as in the original approach by Aki and Chouet (1975). In this limited sense, coda attributes represent "apparent" properties, analogously to the apparent resistivity in electrical imaging (Morozov and Baharvand Ahmadi, 2015). In a 1-D (layered) medium, these attributes would be near constant spatially (independent of **x)** and represent the pattern of layering. Because of their independence of filtering frequencies and reference models, attributes γ and q_e appear to be preferable for characterization of geological structures. These attributes also show good correlation with crustal types and tectonic ages of the crust (Morozov, 2008b, 2010a, 2011b), and they can be modeled numerically (Morozov et al., 2008). However, similar to the apparent resistivity, spatial variations of these quantities are hardly reliable on scales much shorter than the characteristic scales of the algorithms used for their inference.

7.5. Mapping of Scatterers

To step beyond empirical mapping schemes for measured coda attributes and obtain an objective characterization of the subsurface, models of true in-situ properties of the crust or mantle are needed. These models should utilize not only $\chi(t,f)$ but the complete coda envelopes $A(t,f)$. Ways for producing such a model will be outlined in chapter 8. In this section, I derive a simple initial approximation for this model by mapping the spatial distribution of scatterers within the study area.

The spatial pattern of crustal heterogeneity contributing to the observed coda can be constrained by mapping the intensity of scatterers (Nishigami, 1997). This mapping is analogous to migration broadly used in reflection data processing and in imaging teleseismic receiver functions. This mapping is based on the single-scattering approximation, in which the fluctuations of coda power at time t are caused by the variations of scattering intensity at points located on the scattering surface $t_S + t_R = t_k$ (eq. (7.5)). Similar to Nishigami (1997), for each coda window, I evaluated the average least-squares trend of the total (frequency-independent) coda power and measured the deviations from it within 2-s time intervals spanning the entire coda windows

(Figure 7.2). Let us denote $\delta P_k(t)$ the variations of coda power above and below the average envelope in coda record k. Similar to seismic reflection migration, the forward model for coda power fluctuations is

$$C_j \delta P_k\left(t\right) = \sum_n G_S\left(d_S\right) G_R\left(d_R\right) \theta_{kn} \delta\phi_n \,, \tag{7.8}$$

where n is a point in the gridded map, $\delta\phi_n$ is the scattering intensity at this point, $G_R(d)$ and $G_S(d)$ are the geometrical spreading functions for power, d_S and d_R are the distances from point n to the source and receiver, respectively, and weight matrix θ_{kn} combined with summation over n implement integration over the scattering surface (section 7.4). The source scaling factor C_j is needed for correcting the recorded power $\delta P_k(t)$ for the magnitude and spectra of the jth source.

Selection of the geometrical spreading functions $G_S(d)$ and $G_R(d)$ requires additional research. However, this selection does not significantly affect the qualitative results, and I can use simple approximations for these functions. For local coda, Nishigami (1997) used spherical-wave relations $G\left(d\right) = d^{-2}$, and here, I use the results of detailed S-wave amplitude inversion in chapter 5. From that chapter, this amplitude dependence for $G_S(d)$ can be parameterized as

$$G_S\left(d\right) = \left(\frac{d}{d_1}\right)^{-2\nu_{\text{near}}\psi_{\text{near}}\left(d\right)} \left(\frac{d}{d_2}\right)^{-2\nu_{\text{far}}\psi_{\text{far}}\left(d\right)} e^{2r\psi_r\left(d\right)}, \tag{7.9}$$

where d_1 = 90 km, d_2 = 115 km, $\nu_{\text{near}} = 1.21$, $\nu_{\text{far}} = 1.99$, and r = 0.89. For the receiver-side branch of the scattered wavefield, I use a surface-wave approximation, which is also normalized at distance d_1:

$$G_R\left(d\right) = \left(\frac{d}{d_1}\right)^{-1}. \tag{7.10}$$

Determination of the scaling factors C_j also requires detailed inversion, but here, I again use a simple approximation based on coda normalization (Aki, 1969). For each source j, let us select C_j

so that for constant scattering intensity $\delta\phi_n = 1$, the logarithm of the of coda power fluctuations falls on the same average dependence with distances: $\ln C_j + \ln \delta P_k = \ln \sum_n G_S\left(d_S\right) G_R\left(d_R\right)\theta_{kn}$, where *k* are the record numbers from source *j* (eq. (7.8)). Denoting the number of these records *N* and averaging this equation over all $k = 1 \ldots N$, factor C_j is obtained:

$$C_j = \exp\left\{\frac{1}{N}\sum_k\left[\ln\sum_n G_S\left(d_S\right)G_R\left(d_R\right)\theta_{kn} - \ln\delta P_k\right]\right\}. \tag{7.11}$$

The resulting spatial distribution of scatterers $\delta\phi(\mathbf{x})$ by inverting eq. (7.8) using the SIRT method is shown in Figure 7.14. Note that the distributions of scatterers form bands correlated with the coastline, topography, and tectonic structure of the region. Such correlations support the above argument that the scattering occurs near the surface and/or within the upper crust.

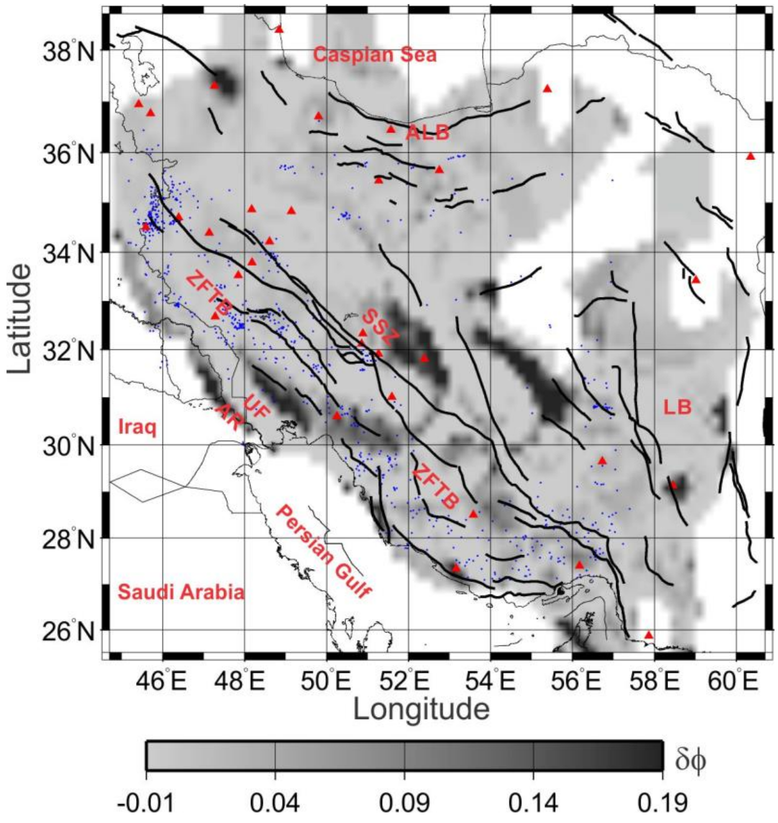

Figure 7.14. Scattering intensities contributing to Lg coda in the study area. The gray-scale bar shows scattering intensities. Lines and labels are as in Figure 7.1.

The high intensity of scattering (darker areas in Figure 7.14) appear to be associated with the north-east coastline of the Persian Gulf, the north-east margin of unfolded zone (labeled UF in Figure 7.14), the middle part of Sannadaj-Sirjan zone (SSZ), and in Arvand Rud river (labeled AR in Figure 7.14). The distribution of scattering intensities in Figure 7.14 could also serve as a more realistic and accurate alternative for the *ad hoc* averaging kernels used in section 7.3 (eq. (7.5); Figures 7.4 and 7.5).

7.6. Discussion and Conclusions

As shown by general arguments and examples in this chapter, the conventional regionalization of Lg coda parameters represents not rigorous characterization of the subsurface but a specific form of interpolation of the observed data. The measured coda attributes such as the inverse coda Q (Q_c^{-1}) or γ are interpolated with respect to source and receiver coordinates. Maps of Q_c and similar attributes represent intermediate products of this interpolation. Therefore, care should be exercised when using these maps in geological or geophysical interpretation. The mapped attributes can be viewed as apparent properties analogous, for example, to the apparent resistivity in electrical imaging. Such apparent properties are useful for interpretation, but their spatial variations are algorithm- and experiment- dependent and may be unreliable.

The variability of empirical mappings of Lg coda attributes is illustrated on coda windows extracted from the Zagros dataset, by using four types of mapping algorithms and three types of coda amplitudes: vertical-component, orientation-independent horizontal (H2C), and three-component (3C) envelopes. Instead of the conventional frequency-dependent Q_c, two parameters of the attenuation coefficient were used: the geometrical attenuation γ and the effective attenuation $q_e = 1/Q_e$. The (γ, q_e) parameterization is simpler and more robust (frequency and theoretical-model independent), and it allows clear correlations with crustal types. Four types of mapping algorithms were considered:

1) Coda averaging over scattering ellipses (the single scattering method);
2) Averaging over their interiors (currently popular back-projection method);
3) Four-dimensional spatial interpolation with respect to the source and receiver coordinates;

4) Migration of power fluctuations within the recorded codas.

All methods produced similar mapping results, although with significant differences in spatial patterns of mapped attributes.

All types of coda-attribute mapping show that Lg coda envelopes in the study area are dominated by the elastic structure of the crust, including its thickness, layering, and the surface- and near-surface topography. The geometrical (elastic) attenuation γ for vertical component shows values from about $\gamma \approx 0.005$ to $0.05\ \mathrm{s}^{-1}$, which are characteristic for areas of active tectonics similar to the value found for the eastern Indian Shield (chapter 6). Anelastic (Q-type) attenuation is weak ($Q \sim 6000$ or higher) and appears undetectable with the noise level in the data. When using the attenuation-coefficient analysis, similar observations have been made for other areas of the world. From the mapped γ and q_e, frequency dependent $Q_c(f)$ similar to those in many other areas are obtained.

As a next step, I need to characterize the Earth's crust not by apparent coda attributes but by true physical parameters. Rigorous forward models and inversion of complete coda envelopes is needed for this purpose. The model should be based on true physical properties such as velocity gradients, major reflectors, parameters of surface and subsurface topography, thicknesses and patterns of layering, and amounts of scatterers within various parts of the crustal and lithospheric structure. Such a model and inversion will be presented in a continuation of this study (chapter 8).

CHAPTER 8

CONCLUSIONS AND RECOMMENDATIONS FOR FUTURE RESEARCH

Because of the limited time span and length of this dissertation, I aimed not at comprehensive analysis of a single dataset but at addressing several interesting and key problems in regional-distance earthquake seismology:

1) Versatile analysis of large and complex datasets;
2) Models for body-wave amplitudes at a broad range of source-receiver distances;
3) Analysis of seismic coda;
4) Physical meaning and values of seismic attenuation, and its methodological role in other seismological studies.

In addition to these fundamental topics, I performed a more routine study of earthquake relocation and proposed an advanced approach to inverse problems encountered in seismology. In the following section 8.1, I present key conclusions on these topics in more detail. In section 8.2, I outline several unsolved problems and directions of further research inspired by this study.

8.1. Conclusions from this Study

Management and processing of a large earthquake datasets is a significant task in modern seismology. In this dissertation, I gave the first large-scale application of a new paradigm in this processing. I used the seismic processing package developed for many years in our group and named IGeoS (Morozov, 2008a), which utilizes the organization of data flows and many tools used in reflection and wide-angle controlled-source seismology. Combination of this high-throughput processing framework with multiple tools written in Octave allowed performing efficient processing of arbitrarily large or small datasets. Generic Mapping Tools (GMT) programs represented another important complement of this processing model, which allowed generation of numerous plots. Importantly, the combined IGeoS+Octave+GMT processing procedure described in this dissertation is completely self-documented and can be reproduced automatically at any time.

With regard to topic 2) above, a new frequency-time dependence standard model of spectral amplitude was developed for Rigan area in southeastern Iran. By selecting a more accurate parameterization of the geometrical spreading, source-receiver coupling, high frequency spectral decay, and Q-factors, significant physical properties of the Earth's crust were revealed for this area. The geometrical spreading selected in the form $t^{-\nu}$ was found to be significantly stronger than assumed in existing models, with power-law exponents $\nu_{\text{near}} \approx 1.7$ at distances closer than 90 km and $\nu_{\text{far}} \approx 2.45$ beyond 115 km for orientation-independent horizontal component (H2C). In the transition between these distances, amplitude increases by a factor of about three. This amplitude increase is not shown in existing models, but it appears to be expected and caused by the onsets of deep crustal waveguide modes and near-critical Moho reflections. The seismic attenuation (Q) factor exceeds about 2000, which means that the crustal attenuation is low. The above characteristic values of ν, critical-distance amplification, and characteristic Q values should also be applicable to many other areas around the world.

Another important group of conclusions for the standard model 2) relates to inversion methodology and measurement of uncertainties. For the standard model developed in chapter 5, two types of model uncertainties were measured. The first type of model uncertainty is caused by subjective selection of mathematical parameterization, such as the under-parameterized geometrical-spreading function combined with an over-parameterized frequency-dependent $Q(f)$. It was also shown that strong biases in the existing models are caused by conventional disregard of certain groups of model parameters such as receiver coupling, and by allowing data residuals to correlate with source-receiver distances. To control these uncertainties, I proposed using additional constraints in the inverse method. With the use of these constraints, the model became much more accurate across the whole distance range. Simultaneously, the model became more physically consistent and much simpler than the existing ones because of the use of a frequency-independent Q.

Even with sufficient parameterizations, the second type of model uncertainty needs to be studied, which is the uncertainty produced by random measurements errors in the data. This statistical analysis was conducted in chapter 5 and showed that all model parameters were correctly resolved. In addition, a new, "optimal" parameterization of the time- and frequency-dependent spectral amplitude was inverted by the principal-component analysis.

From coda studies in chapters 6 and 7 (topic 3 above), the key conclusion consists in proposing an alternate parameterization using the geometrical-spreading parameter γ and effective Q-factor denoted Q_e. I showed that this parameterization allows an insightful re-interpretation of conventional coda $Q(f)$ results (chapter 6) as well as analysis of new coda data (chapter 7). Parameters γ and Q_e are frequency-independent, which makes them much better constrained and simpler to compare for different geographic regions. The inverted levels of γ are 0.010 to 0.013 s^{-1} for the eastern part of Indian Shield and $\gamma \approx 0.005$ to 0.05 s^{-1} for Zagros area of Iran. The values of γ for H2C and 3C coda amplitudes are somewhat smaller than the vertical component ones. However, I found that the body-wave spectral multicomponent amplitudes decrease much faster than the vertical component (chapter 5). In contrast to many existing studies, this dissertation shows that the Q-type attenuation is actually weak, with values of Q_e above 2000–6000, which appear to be within measurement errors. These large Q_e values are likely dominated by noise in the recordings.

From the above large values of Q_e, a most spectacular and important conclusion from coda analysis in this dissertation is that in both datasets, the observed codas are *near-elastic*. Therefore, I conclude that coda shapes are principally determined by the structure of crust, and particularly in the near-receiver area. This interpretation differs from many conventional models, in which the coda is explained by a Q-factor of an effective homogeneous medium.

In addition to revealing the high values of Q_e and elastic character of codas, in chapter 6, I obtained frequency-dependent spatial patterns of coda amplification and deamplification (i.e., coda attenuation). This observation was validated by observations of raw coda spectral amplitudes and supported by further results of Lg coda in Zagros region (chapter 7).

Another group of conclusions for coda relates to the methodology of coda mapping (chapter 7). To my knowledge, this is the first study in which four mapping methods and three types of coda amplitudes (i.e., vertical component, H2C, and 3C) were compared, including a new method of direct interpolation with respect to the source and receiver coordinates. Instead of the conventional frequency-dependent Q, two frequency-independent parameters of attenuation coefficient (i.e., γ and $q_e = 1/Q_e$) were assessed.

All the mentioned mapping approaches yielded similar values of γ and q_e but with considerably different spatial patterns of mapped attributes. This difference was an important observation corroborating the general argument of this dissertation that coda mapping *cannot* be rigorously carried out in terms of coda attributes dependent on only surface or subsurface locations. However, parameter γ can be interpreted in a 1-D sense, as an indicator of crustal layering.

The results of coda studies in this dissertation (chapters 6 and 7) suggest that Lg coda envelopes are dominated by the elastic structure of crust (i.e., $Q^{-1} = 0$), which includes crustal layering, surface topography, and major structural features such as the Moho depth and the coastline. New mapping by coda power fluctuations (chapter 7) also indicated good correlation with topographic features and tectonic structures in Zagros area.

Finally, the event relocation analysis in this dissertation (chapter 4) was only an initial approximation using a crude 1-D travel-time model, and its results were preliminary. Most sources were relocated by 10 to 25 km, which was within location uncertainty. After their improvements during further research (next section), accurate earthquake source locations should be useful for many other applications, such as travel-time tomography and polarization measurements.

8.2. Directions of Future Research

The Zagros dataset and ideas of the dissertation suggest numerous other studies which could not be pursued here because of time limitations. In the following, I outline several promising research directions that can be followed with these data in the future. Some of these studies are already being cast into papers in preparation, some are in preliminary trials, and others still need to be explored:

1) Estimation of the velocity structure and Moho depths for Zagros area using *Pn* travel-time tomography. For large datasets like Zagros (chapter 2), travel-time tomography represents a standard part of seismic imaging, yielding information about the wave velocities and depths to the major velocity discontinuities such as the crust-mantle boundary. Identification of these features is critical for determining the tectonic structure of the region and answering the questions posed in chapter 2.
2) Concurrently with the *Pn* travel-time tomography, the more accurate velocity model would allow accurate modeling of the travel times predicted for various source and receiver combinations. Based on these predictions, travel times for P- and S-wave arrivals can be picked more accurately. This procedure would require an extensive amount of interactive data analysis, but it should further improve the accuracy of the tomographic model. Potentially, more accurate phase identification would allow constraining the depths of seismic sources and improve their locations.
3) With more accurate travel-time models produced by tomographic inversion, the relocation study of chapter 4 can be expanded to more earthquakes. Relocations would also become more accurate. If surface reflections (*Pp* phases) can be identified in the local-distance records, depths of the sources can also be estimated more accurately.
4) Applying joint spectral decomposition of chapter 5 to the large Zagros dataset and constraining parameters kappa for sources and receivers in Zagros area. Preliminary tests show that this task may be challenging because of the trade-off between the numerous source parameters and path attenuation effects. Therefore, further enhancements of the inversion methodology will likely be required. Most importantly, this study could yield unique constraints on the source spectra (like κ_{source}), differentiate them from receiver effects (κ_{receiver}), and estimate the true

geometrical spreading, and path attenuation (Q_e). None of these estimates are currently available for other areas.

5) Finding a standard model for complete coda envelopes. This would be a most important but also challenging task, because no such models have been developed before. This model would replace the empirical mapping schemes for measured coda attributes (chapters 6 and 7) with a model using true in-situ properties of the crust or mantle, such as proposed in chapter 5. Instead of utilizing only decay rates of the normalized coda envelopes ($\chi(t,f)$), the complete coda envelopes $A(t,f)$ would be used. With its large number of records, the Zagros-area dataset appears to be suitable for this major effort.
6) An interesting new hypothesis arises from the observations of low attenuation and elastic characters of coda envelopes (chapters 5, 6 and 7): it appears likely that codas and high-frequency receiver-site parameters kappa are mutually related, and both of them can be explained by elastic scattering. This scattering likely occurs near the receiver and with a strong contribution from surface waves. Currently, both codas and kappas are explained by body-wave Q-factors of the crust, and an alternative explanation by mostly elastic scattering could make an important shift in the paradigm.
7) Mapping of frequency-dependent and spatially variant coda amplification and deamplification for Zagros area. This mapping would provide additional information about the source and receiver site conditions, and it could complement the complete-coda amplitude model proposed above.
8) Analysis of wave polarizations and seismometer orientations. Regularly, P-wave arrivals are expected to occur with ground motions oriented within the plane of the back-azimuth direction to the source. However, deviations from this plane can occur due to two reasons: a) misorientations of the horizontal sensors (for example, because of using the magnetic compass in concrete buildings or near local magnetic anomalies), and b) physical effects of the earth's topography, sideway refractions, and scattering. With either of these explanations, the results of P-wave polarization

measurements should contribute to accurate characterization of the stations and study area. Variations of P-wave polarizations are often measured by methods similar to the principal-component analysis. Most of this analysis for Zagros records was already done when working on the present dissertation, and its interpretation can be completed during future research.

9) Analysis of the horizontal- to vertical-component ratios of spectral amplitudes (HVSR) for the different receiver sites in Zagros area. Resonance peaks in the HVSR spectra can be used for constraining layering of the near surface and constraining the seismic hazard near the stations. This knowledge can be used in further modeling and help understanding the effects of topography, buildings, and layered structures on ground motions. Numerous arrivals recorded in Zagros area would allow investigation of the dependence of HVSR on arrival types, angles of incidence, and on recording within body-wave or coda time windows.

REFERENCES

Agard, P., Omrani, J., Jolivet, L., and Mouthereau, F. (2005). Convergence history across Zagros (Iran): Constraints from collisional and earlier deformation. International Journal of Earth Sciences, **94**(3), 401–419. https://doi.org/10.1007/s00531-005-0481-4

Agard, P., Omrani, J., Jolivet, L., Whitechurch, H., Vrielynck, B., Spakman, W., Monié, P., Meyer, B., and Wortel, R. (2011). Zagros orogeny: A subduction-dominated process. Geological Magazine, **148**(5–6), 692–725. https://doi.org/10.1017/S001675681100046X

Aki, K. (1969). Analysis of the seismic coda of local earthquakes as scattered waves. Journal of Geophysical Research, **74**(2), 615–631. https://doi.org/10.1029/JB074i002p00615

Aki, K. (1980). Attenuation of shear waves in the lithosphere for frequencies from 0.05 to 25 Hz. Physics of the Earth and Planetary Interiors, **21**, 50–60.

Aki, K., and Chouet, B. (1975). Origin of coda waves: Source, attenuation, and scattering effects. Journal of Geophysical Research, **80**, 3322–3342.

Aki, K., and Richards, P. G. (2002). Quantitative seismology (2nd Ed.). University Science Books, ISBN 0-935702-96-2.

Alavi, M. (1991). Sedimentary and structural characteristics of the Paleo-Tethys remnants in northeastern Iran. Geological Society of America Bulletin, **103**, 983-992.

Alavi, M. (1994). Tectonics of the zagros orogenic belt of Iran: New data and interpretations. Tectonophysics, **229**(3–4), 211–238. https://doi.org/10.1016/0040-1951(94)90030-2

Anderson, D. L. (1989). Theory of the Earth. Blackwell Scientific Publications. ISBN 0865423350.

Anderson, J. G. (1991). A preliminary descriptive model for the distance dependence of the spectral decay parameter in southern California. Bulletin of the Seismological Society of America, **81**, 2186–2193.

Anderson, J. G., and Hough, S. E. (1984). A model for the shape of the Fourier amplitude spectrum of acceleration at high frequencies. Bulletin of the Seismological Society of America, **74**, 1969–1993.

Anderson, R. G., and McMechan, G. A. (1988). Noise-adaptive filtering of seismic shot records. Geophysics, **53**, 535–638.

Aster, R. C., Borchers, B., and Thurber, C. H. (2018). Parameter estimation and inverse problems (3rd Ed.). Elsevier, ISBN: 9780128046517.

Atkinson, G. M. (2004). Empirical attenuation of ground-motion spectral amplitudes in southeastern Canada and the northeastern United States. Bulletin of the Seismological Society of America, **94**, 1079–1095.

Atkinson, G. M. (2012). Evaluation of attenuation models for the northeastern United States and southeastern Canada. Seismological Research Letters, **83**, 166–178. https://doi.org/10.1785/gssrl.83.1.166

Atkinson, G. M., and Boore, D. M. (2006). Earthquake ground-motion prediction equations for eastern North America. Bulletin of the Seismological Society of America, **96**, 2181–2205.

Bagheri, S., and Stampfli, G. M. (2008). The Anarak, Jandaq and Posht-e-Badam metamorphic complexes in central Iran: New geological data, relationships and tectonic implications. Tectonophysics, **451**(1–4), 123–155. https://doi.org/10.1016/j.tecto.2007.11.047

Berberian, F., and Berberian, M. (1981). Tectono-plutonic episodes in Iran. In Zagros-Hindu Kush-Himalaya Geodynamic Evolution, 5-32, eds. Gupta, H. K., and Delany, F. M., Geodynamics Series, American Geophysical Union. https://doi.org/10.1029/GD003p0005

Berberian, M. (1976). Contribution to the seismotectonics of Iran. Part II. Geological Survey of Iran, **39**, 516.

Berberian, M. (1979). Evaluation of the instrumental and relocated epicentres of Iranian earthquakes. Geophysical Journal International, **58**(3), 625–630. https://doi.org/10.1111/j.1365-246X.1979.tb04798.x

Berberian, M. (1995). Master “blind” thrust faults hidden under the Zagros folds: Active basement tectonics and surface morphotectonics. Tectonophysics, **241**(3–4), 193–224. https://doi.org/10.1016/0040-1951(94)00185-C

Berberian, M., Jackson, J. A., Fielding, E., Parsons, B. E., Priestley, K., Qorashi, M., Talebian, M., Walker, R., Wright, T. J., and Baker, C. (2001). The 1998 March 14 Fandoqa earthquake (M_w 6.6) in Kerman province, southeast Iran: Re-rupture of the 1981 Sirch earthquake fault, triggering of slip on adjacent thrusts and the active tectonics of the Gowk fault zone. Geophysical Journal International, **146**(2), 371–398. https://doi.org/10.1046/j.1365-246x.2001.01459.x

Berberian, M., and King, G. C. P. (1981). Towards a paleogeography and tectonic evolution of Iran. Canadian Journal of Earth Sciences, **18**(2), 210–265. https://doi.org/10.1139/e81-019

Beresnev, I. A. (2019a). Interpretation of kappa and fmax filters as source effect. Bulletin of the Seismological Society of America, **109**, 822–826.

Beresnev, I. A. (2019b). Reply to “Comment on ‘Interpretation of Kappa and fmax filters as source effect’ by Igor A. Beresnev”. Bulletin of the Seismological Society of America, **109**, 2764–2766.

Besse, J., Torcq, F., Gallet, Y., Ricou, L. E., Krystyn, L., and Saidi, A. (1998). Late Permian to Late Triassic palaeomagnetic data from Iran: Constraints on the migration of the Iranian block through the Tethyan Ocean and initial destruction of Pangaea. Geophysical Journal International, **135**(1), 77–92. https://doi.org/10.1046/j.1365-246X.1998.00603.x

Bina, M. M., Bucur, I., Prevot, M., Meyerfeld, Y., Daly, L., Cantagrel, J. M., and Mergoil, J. (1986). Palaeomagnetism, petrology and geochronology of tertiary magmatic and sedimentary units from Iran. Tectonophysics, **121**(2–4), 303–329. https://doi.org/10.1016/0040-1951(86)90050-8

Blanckenburg, F. V., and Davies, J. H. (1995). Slab breakoff: A model for syncollisional magmatism and tectonics in the Alps. Tectonics, **14**(1), 120–131. https://doi.org/10.1029/94TC02051

Blanke, A., Kwiatek, G., Martínez-Garzón, P., and Bohnhoff, M. (2019). Sensitivity and stability analysis of coda quality factors at the Geysers geothermal field, California. Bulletin of the Seismological Society of America, **109**, 959-975,. https://doi.org/10.1785/0120180219

Bora, S. S., Cotton, F., Scherbaum, F., Edwards, B., and Traversa, P. (2017). Stochastic source, path and site attenuation parameters and associated variabilities for shallow crustal European earthquakes. Bulletin of Earthquake Engineering, **15**, 4531–4561.

Bouchon, M. (1982). The complete synthesis of seismic crustal phases at regional distances. Journal of Geophysical Research, **87**, 1735–1741.

Bowman, J., and Kennett, B. (1991). Propagation of Lg waves in the North Australian craton: Influence of crustal velocity gradients. Bulletin of the Seismological Society of America, **81**, 592–610.

Brune, J. N. (1970). Tectonic stress and spectra of seismic shear waves from earthquakes. Journal of Geophysical Research, **75**, 4997–5009.

Calvet, M., and Margerin, L. (2013). Lapse-time dependence of coda *Q*: Anisotropic multiple-scattering models and application to the Pyrenees. Bulletin of the Seismological Society of America, **105**, 1993–2010.

Calvet, M., Sylvander, M., Margerin, L., and Villaseñor, A. (2013). Spatial variations of seismic attenuation and heterogeneity in the Pyrenees: Coda *Q* and peak delay time analysis. Tectonophysics, **608**, 428–439.

Campbell, K. (2009). Estimates of shear-wave *Q* and κ_0 for unconsolidated and semi consolidated sediments in eastern North America. Bulletin of the Seismological Society of America, **99**, 2365–2392.

Campillo, M. (1987). Lg wave propagation in a laterally varying crust and the distribution of the apparent quality factor in central France. Journal of Geophysical Research, **92**, 12604–12614.

Castro, R. R., Anderson, J. G., and Singh, S. K. (1990). Site response, attenuation and source spectra of S waves along the Guerrero, Mexico, subduction zone. Bulletin of the Seismological Society of America, **80**(6), 1481–1503.

Dainty, A. M. (1981). A scattering model to explain seismic *Q* observations in the lithosphere between 1 and 30 Hz. Geophysical Research Letters, **8**, 1126–1128.

Dehghani, G. A., and Makris, J. (1984). The gravity field and crustal structure of Iran. Neues Jahrbuch Für Geologie Und Paläontologie - Abhandlungen, **168**(2–3), 215–229. https://doi.org/10.1127/njgpa/168/1984/215

Deichmann, N., and Garcia-Fernandez, M. (1992). Rupture geometry from high-precision relative hypocentre locations of microearthquake clusters. Geophysical Journal International, **110**(3), 501–517. https://doi.org/10.1111/j.1365-246X.1992.tb02088.x

Del Pezzo, E., Ibañez, J., Prudencio, J., Bianco, F., and De Siena, L. (2016). Absorption and scattering 2-D volcano images from numerically calculated space-weighting functions. Geophysical. Journal International, **206**, 742–756. https://doi.org/10.1093/gji/ggw171

Drouet, S., Chevrot, S., Cotton, F., and Souriau, A. (2008). Simultaneous inversion of source spectra, attenuation parameters, and site responses: Application to the data of the French accelerometric network. Bulletin of the Seismological Society of America, **98**, 198–219.

Edwards, B., Rietbrock, A., Bommer, J. J., and Baptie, B. (2008). The acquisition of source, path, and site effects from microearthquake recordings using *Q* tomography: Application to the United Kingdom. Bulletin of the Seismological Society of America, **98**, 1915–1935.

Engdahl, E. R., Jackson, J. A., Myers, S. C., Bergman, E. A., and Priestley, K. (2006). Relocation and assessment of seismicity in the Iran region. Geophysical Journal International, **167**(2), 761–778. https://doi.org/10.1111/j.1365-246X.2006.03127.x

Escudero, C. R., García-Millán, N., and Escalona-Alcázar, F. J. (2016). Attenuation of coda waves in western Mexico using local seismicity. Bulletin of the Seismological Society of America, **106**, 2545-2557. https://doi.org/10.1785/0120160027

Fang, Y., Zhou, Y., and Yao, Z. (2019). Model misfit minimization, Bulletin of the Seismological Society of America, **109**, 1729–1737.

Farrokhi, M., Hamzehloo, H., Rahimi, H., and Allamehzadeh, M. (2015). Estimation of coda-wave attenuation in the central and eastern Alborz, Iran. Bulletin of the Seismological Society of America, **105**, 1756–1767.

Fehler, M., and Sato, H. (2003). Coda. Pure and Applied Geophysics, **160**, 541–554.

Fehr, M., Kremers, S., and Fritsche, R. (2019). Characterization of seismic site effects influenced by near-surface structures using 3D waveform modelling. Journal of Seismology, **23**, 373–392.

Fisk, M. D., and Phillips, W. S. (2013a). Constraining regional phase amplitude models for Eurasia, Part 1: Accurate source parameters and geometrical spreading. Bulletin of the Seismological Society of America, **103**, 3248–3264.

Fisk, M. D., and Phillips, W. S. (2013b). Constraining regional phase amplitude models for Eurasia, Part 2: Frequency-dependent attenuation and site results. Bulletin of the Seismological Society of America, **103**, 3265–3288.

Frankel, A. (2019). Comment on "Interpretation of Kappa and fmax filters as source effect" by Igor A. Beresnev. Bulletin of the Seismological Society of America, **109**, 2762–2763.

Frankel, A., and Wennerberg, L. (1987). Energy-flux model of seismic coda: Separation of scattering and intrinsic attenuation. Bulletin of the Seismological Society of America, **77**, 1223–1251.

Gabrielli, S., Siena, L. D., Napolitano, F., and Del Pezzo, E. (2020). Understanding seismic path biases and magmatic activity at Mount St Helens volcano before its 2004 eruption. Geophysical Journal International, **222**, 169–188.

Giampiccolo, E., and Tuvè, T. (2018). Regionalization and dependence of coda *Q* on frequency and lapse time in the seismically active Peloritani region (northeastern Sicily, Italy. Journal of Seismology, **22**, 1059-1074. https://doi.org/10.1007/s10950-018-9750-0

Giese, P., Makris, J., Akashe, B., Röwer, P., Letz, H., and Mostaanpour, M. (1984). The crustal structure in southern Iran derived from seismic explosion data. Neues Jahrbuch Für Geologie Und Paläontologie - Abhandlungen, **168**(2–3), 230–243. https://doi.org/10.1127/njgpa/168/1984/230

Glennie, K. W., Boeuf, M. G. A., Clarke, M. W. H., Moody-Stuart, M., Pilaar, W. F. H. and Reinhardt, B. M. (1973). Late Cretaceous nappes in Oman mountains and their geologic evolution. American Association of Petroleum Geologists Bulletin, **57**, 5–27.

Graizer, V. (2017). Alternative (G-16v2) ground-motion prediction equations for central and eastern North America. Bulletin of the Seismological Society of America, **107**, 869–886.

Haendel, A., Anderson, J. G., Pilz, M., and Cotton, F. (2020). A frequency-dependent model for the shape of the Fourier amplitude spectrum of acceleration at high frequencies. Bulletin of the Seismological Society of America, **110**(6), 2743-2754. https://doi.org/10.1785/0120200118

Hassanzadeh, J., and Wernicke, B. P. (2016). The Neotethyan Sanandaj-Sirjan zone of Iran as an archetype for passive margin-arc transitions: Sanandaj-Sirjan Mesozoic arc. Tectonics, **35**(3), 586–621. https://doi.org/10.1002/2015TC003926

Hatzfeld, D., Tatar, M., Priestley, K., and Ghafory-Ashtiany, M. (2003). Seismological constraints on the crustal structure beneath the Zagros Mountain belt (Iran). Geophysical Journal International, **155**(2), 403–410. https://doi.org/10.1046/j.1365-246X.2003.02045.x

Havskov, J., Sørensen, M. B., Vales, D., Özyazıcıoğlu, M., Sánchez, G., and Li, B. (2016). Coda *Q* in different tectonic areas, influence of processing parameters. Bulletin of the Seismological Society of America, **106**, 956-970. https://doi.org/10.1785/0120150359

Hugh Wilson, H., and Glennie, D. K. W. (2001). The age of the Hawasina and other problems of Oman mountains geology. Journal of Petroleum Geology, **24**(4), 477–484. https://doi.org/10.1111/j.1747-5457.2001.tb00687.x

James, G. A., and Wynd J. G. (1965). Stratigraphic nomenclature of Iranian oil consortium agreement area. AAPG Bulletin, **49**, 2182–2245. https://doi.org/10.1306/A663388A-16C0-11D7-8645000102C1865D

Jhajhria, A., Morozov, I. B., and Teotia, S. S. (2017). Frequency-dependent coda amplitude decays in the region of Himalaya, India. Bulletin of the Seismological Society of America, **107**, 1817-1827. https://doi.org/10.1785/0120170032

Kadinsky-Cade, K., and Barazangi, M. (1982). Seismotectonics of southern Iran: The Oman line. Tectonics, **1**(5), 389–412. https://doi.org/10.1029/TC001i005p00389

Kinoshita, S. (1994). Frequency-dependent attenuation of shear waves in the crust of the southern Kanto area. Japan. Bulletin of the Seismological Society of America, **84**, 1387–1396.

Kiuchi, R., Mooney, W. D., and Zahran, H. M. (2019). Ground-motion prediction equations for western Saudi Arabia. Bulletin of the Seismological Society of America, **109**, 2722–2737.

Klimasewski, A., Sahakian, V., Baltay, A., Boatwright, J., Fletcher, J. B., and Baker, L. M. (2019). κ_0 and broadband site spectra in southern California from source model-constrained inversion. Bulletin of the Seismological Society of America, **109**, 1878–1889.

Komak Panah, A., Moghaddas, N. H., Ghayamghamian, M. R., Motosaka, M., Jafari, M. K., and Uromieh, A. (2002). Site effect classification in East-Central of Iran. Journal of Seismology and Earthquake Engineering, **4**, 37–46.

Krischer, L., Megies, T., Barsch, R., Beyreuther, M., Lecocq, T., Caudron, C., and Wassermann, J. (2015). ObsPy: A bridge for seismology into the scientific Python ecosystem. Computational Science and Discovery, **8**(1), 014003. https://doi.org/10.1088/1749-4699/8/1/014003

Ktenidou, O. J., Cotton, F., Abrahamson, N. A., and Anderson, J. G. (2014). Taxonomy of κ: A review of definitions and estimation approaches targeted to applications. Seismological Research Letters, **85**(1), 135–146. https://doi.org/10.1785/0220130027

Lacombe, C., Campillo, M., Paul, A., and Margerin, L. (2003). Separation of intrinsic absorption and scattering attenuation from Lg coda decay in central France using acoustic radiative transfer theory. Geophysical Journal International, **154**(2), 417–425. https://doi.org/10.1046/j.1365-246X.2003.01976.x

Lomax, A., Virieux, J., Volant, P., and Berge, C. (2000). Probabilistic earthquake location in 3D and layered models: introduction of a Metropolis-Gibbs method and comparison with linear locations. In Advances in Seismic Event Location, 101–134, eds. Thurber, C.H. and Rabinowitz, N.

Lomax, A., Zollo, A., Capuano, P., and Virieux, J. (2001). Precise, absolute earthquake location under Somma-Vesuvius volcano using a new three-dimensional velocity model. Geophysical Journal International, **146**(2), 313–331. https://doi.org/10.1046/j.0956-540x.2001.01444.x

Maggi, A., Jackson, J. A., Priestley, K., and Baker, C. (2000). A re-assessment of focal depth distributions in southern Iran, the Tien Shan and northern India: Do earthquakes really occur in the continental mantle? Geophysical Journal International, **143**(3), 629–661. https://doi.org/10.1046/j.1365-246X.2000.00254.x

Mayeda, K. (1993). mb (LgCoda): A stable single station estimator of magnitude. Bulletin of the Seismological Society of America, **83**, 851–861.

Mayor, J., Bora, S. S., and Cotton, F. (2018). Capturing regional variations of hard-rock κ_0 from coda analysis. Bulletin of the Seismological Society of America, **108**, 399–408.

Menke, W. (1984). Geophysical data analysis: Discrete inverse theory. Academic Press. https://doi.org/10.1016/B978-0-12-490920-5.X5001-7

Michelini, A., and Lomax, A. (2004). The effect of velocity structure errors on double-difference earthquake location. Geophysical Research Letters, **31**(9), 1-4. https://doi.org/10.1029/2004GL019682

Michell, B., Cong, L., and Jemberie, A. L. (2015). Continent-wide maps of Lg coda *Q* for North America and their relationship to crustal structure and evolution. Bulletin of the Seismological Society of America, **105**, 409-419. https://doi.org/10.1785/0120130235

Mirzaei, N., Gao, M., and Chen, Y. (1998). Seismic source regionalization for seismic zoning of Iran: Major seismotectonic provinces, Journal of Earthquake Prediction Research, **7**, 465–495.

Mirzaei, N., Gao, M.-T., Chen, Y.-T., and Wang, J. (1997). A uniform catalog of earthquakes for seismic hazard assessment in Iran. Acta Seismologica Sinica, **10**(6), 713–726. https://doi.org/10.1007/s11589-997-0003-5

Mitchell, B. (2010). Prologue and invitation to participate in a forum on the frequency dependence of seismic *Q*. Pure and Applied Geophysics, **167,** 1129-1129. https://doi.org/10.1007/s00024-010-0180-3.

Mitchell, B. J., and Cong, L. (1998). Lg coda *Q* and its relation to the structure and evolution of continents: A global perspective. Pure and Applied Geophysics, **153**, 655–663.

Moghadam, H. S., Stern, R. J., and Rahgoshay, M. (2010). The Dehshir ophiolite (central Iran): Geochemical constraints on the origin and evolution of the Inner Zagros ophiolite belt. Geological Society of America Bulletin, **122**(9–10), 1516–1547. https://doi.org/10.1130/B30066.1

Morozov, I. (2008a). Open-source software framework integrates data analysis. Eos, Transactions American Geophysical Union, **89**(29), 261. https://doi.org/10.1029/2008EO290002

Morozov, I. B. (2008b). Geometrical attenuation, frequency dependence of *Q*, and the absorption band problem. Geophysical Journal International, **175**(1), 239–252. https://doi.org/10.1111/j.1365-246X.2008.03888.x

Morozov, I. B. (2010a). On the causes of frequency-dependent apparent seismological *Q*. Pure and Applied Geophysics, **167**, 1131-1146. https://doi.org/10.1007/s00024-010-0100-6

Morozov, I. B. (2010b). Attenuation coefficients of Rayleigh and Lg waves. Journal of Seismology, **14**, 803-822. https://doi.org/10.1007/s10950-010-9196-5

Morozov, I. B. (2011a). Mechanisms of geometrical seismic attenuation. Annals of Geophysics, **54**(3), 235-248. https://doi.org/10.4401/ag-4780

Morozov, I. B. (2011b). Temporal variations of coda *Q*: An attenuation-coefficient view. Physics of the Earth and Planetary Interiors, **187**(1–2), 47–55. https://doi.org/10.1016/j.pepi.2011.04.012

Morozov, I. B. (2013). Frequency dependence of long-period *t**. Journal of Seismology, **17**, 265-280. https://doi.org/10.1007/s10950-012-9315-6

Morozov, I. B., and Baharvand Ahmadi, A. (2015). Taxonomy of *Q*. Geophysics, **80**(1), 41–49. https://doi.org/10.1190/geo2013-0446.1

Morozov, I. B., Jhajhria, A., A., and Deng, W. (2018). On strong positive frequency dependencies of quality factors in local-earthquake seismic Studies. Pure and Applied Geophysics, **175**, 2595-2607. https://doi.org/10.1007/s00024-018-1826-9

Morozov, I. B., and Pavlis, G. L. (2011a). Management of large seismic datasets: I. Automated building and updating using BREQ_FAST and NetDC. Seismological Research Letters, **82**(2), 211–221. https://doi.org/10.1785/gssrl.82.2.211

Morozov, I. B., and Pavlis, G. L. (2011b). Management of large seismic datasets: II. Data center-type operation. Seismological Research Letters, **82**(2), 222–226. https://doi.org/10.1785/gssrl.82.2.222

Morozov, I. B, and Safarshahi, M. (2020). Elastic character of seismic coda envelopes within east Indian shield. Pure and Applied Geophysics, **177**, 5799–5818. https://doi.org/10.1007/s00024-020-02600-2

Morozov, I. B., Zhang, C., Duenow, J. N., Morozova, E. A., and Smithson, S. B. (2008). Frequency dependence of coda *Q*, Part I: Numerical modeling and examples from Peaceful Nuclear Explosions. Bulletin of the Seismological Society of America, **98**, 2615-2628. https://doi.org/10.1785/0120080037

Motaghi, K., Shabanian, E., and Kalvandi, F. (2017). Underplating along the northern portion of the Zagros suture zone, Iran. Geophysical Journal International, **210**(1), 375–389. https://doi.org/10.1093/gji/ggx168

Motazedian, D., and Atkinson, G. M. (2005). Stochastic finite-fault modeling based on a dynamic corner frequency. Bulletin of the Seismological Society of America, **95**, 995–1010.

Nishigami, K. (1997). Spatial distribution of coda scatterers in the crust around two active volcanoes and one active fault system in central Japan: Inversion analysis of coda envelope. Physics of the Earth and Planetary Interiors, **104**, 75–89. https://doi.org/10.1016/S0031-9201(97)00058-7

Nishigami, K. (2006). Crustal heterogeneity in the source region of the 2004 Mid Niigata Prefecture earthquake: Inversion analysis of coda envelopes. Pure and Applied Geophysics, **163**, 601-616. https://doi.org/10.1007/s00024-005-0024-8

Novelo-Casanova, D. A., Polanco-Rivera, E., Suárez, G., Martinez, F., and Moreta, A. M. (2020). Seismic S-wave coda attenuation in the Dominican Republic as a tool for seismic hazard mitigation. Natural Hazards, **103**(3), 2849–2863. https://doi.org/10.1007/s11069-020-04105-6

Nowroozi, A. A. (1971). Seismo-tectonics of the Persian plateau, eastern Turkey, Caucasus, and Hindu-Kush regions. Bulletin of the Seismological Society of America, **61**(2), 317-341.

Oth, A., Bindi, D., Parolai, S., and Giacomo, D. D. (2011). Spectral analysis of K-NET and KiK-net data in Japan, part II: on attenuation characteristics, source spectra, and site response of borehole and surface stations. Bulletin of the Seismological Society of America, **101**, 667–687.

Oth, A., Bindi, D., Parolai, S., and Wenzel, F. (2008). S-wave attenuation characteristics beneath the Vrancea region in Romania: New insights from the inversion of ground-motion spectra. Bulletin of the Seismological Society of America, **98**, 2482–2497.

Palmer, S., and Atkinson, G. M. (2020). The high-frequency decay slope of spectra (kappa) for $M \geq 3.5$ Earthquakes on rock sites in eastern and western Canada. Bulletin of the Seismological Society of America, **110**(2), 471-488. https://doi.org/10.1785/0120190206

Parolai, S. (2018). κ_0: Origin and usability. Bulletin of the Seismological Society of America, **108**, 3446–3456.

Parvez, I. A., Sutar, A. K., Mridula, M., Mishra, S. K., and Rai, S. S. (2008). Coda *Q* estimates in the Andaman Islands using local earthquakes. Pure and Applied Geophysics, **165**, 1861–1878. https://doi.org/10.1007/s00024-008-0399-4

Paul, A., Hatzfeld, D., Kaviani, A., Tatar, M., and Péquegnat, C. (2010). Seismic imaging of the lithospheric structure of the Zagros mountain belt (Iran). Geological Society, London, Special Publications, **330**(1), 5–18. https://doi.org/10.1144/SP330.2

Paul, A., Kaviani, A., Hatzfeld, D., Vergne, J., and Mokhtari, M. (2006). Seismological evidence for crustal-scale thrusting in the Zagros mountain belt (Iran). Geophysical Journal International, **166**(1), 227–237. https://doi.org/10.1111/j.1365-246X.2006.02920.x

Pavlis, G. L. (1986). Appraising earthquake hypocenter location errors: a complete, practical approach for single-event locations. Bulletin of the Seismological Society of America. **76**(6), 1699-1717.

Pilz, M., Cotton, F., Zaccarelli, R., and Bindi, D. (2019). Capturing regional variations of hard-rock attenuation in Europe. Bulletin of the Seismological Society of America, **109**, 1401–1418.

Poupinet, G., Ellsworth, W. L., and Frechet, J. (1984). Monitoring velocity variations in the crust using earthquake doublets: An application to the Calaveras Fault, California. Journal of Geophysical Research: Solid Earth, **89**(B7), 5719–5731. https://doi.org/10.1029/JB089iB07p05719

Rayhani, M. H. T., El Naggar, M. H., and Tabatabaei, S. H. (2008). Nonlinear analysis of local site effects on seismic ground response in the Bam earthquake. Geotechnical and Geological Engineering, **26**(1), 91–100. https://doi.org/10.1007/s10706-007-9149-0

Safarshahi, M. (2011). Identification of the source parameters of the Rigan Earthquake, based on stochastic finite fault model [Master’s thesis, University of Tehran, Institute of Geophysics].

Safarshahi, M., and Morozov, I. B. (2019) Processing of large earthquake datasets from Zagros region (Iran). 27th IUGG General Assembly, Montreal, Canada, July 2019.

Safarshahi, M., and Morozov, I. B. (2021a). Robust empirical time-frequency relations for seismic spectral amplitudes, part 1: Application to regional S waves in southeastern Iran. Bulletin of the Seismological Society of America, **111**, 173-192. https://doi.org/10.1785/0120200172

Safarshahi, M., and Morozov, I. B. (2021b). Robust empirical time-frequency relations for seismic spectral amplitudes, part 2: Model uncertainty and optimal parameterization. Bulletin of the Seismological Society of America, **111**, 193-205. https://doi.org/10.1785/0120200180

Safarshahi, M., Rezapour, M., and Hamzehloo, H. (2013). Stochastic finite-fault modeling of ground motion for the 2010 Rigan earthquake, southeastern Iran. Bulletin of the Seismological Society of America, **103**(1), 223–235. https://doi.org/10.1785/0120120027

Safarshahi, M., and Morozov, I. B., Quantitative interpretation of Lg coda envelopes: Several types of mapping and spatial interpolation in Zagros area of Iran. Manuscript submitted to Geophysical Journal International.

Sato, H. (1977). Energy propagation including scattering effects single isotropic scattering approximation. Journal of Physics of the Earth, **25**(1), 27–41.

Sato, H. (1978). Mean free path of S waves under the Kanto district of Japan. Journal of Physics of the Earth, **26**, 185–198.

Sato, H. (1990). Unified approach to amplitude attenuation and coda excitation in the randomly inhomogeneous lithosphere. Pure and Applied Geophysics, **132**(1–2), 93–121. https://doi.org/10.1007/BF00874359

Sedaghati, F., and Pezeshk, S. (2016). Estimation of the coda-wave attenuation and geometrical spreading in the New Madrid Seismic Zone. Bulletin of the Seismological Society of America, **106**, 1482–1498.

Şengör, A. M. C. (1990). A new model for the late Palaeozoic—Mesozoic tectonic evolution of Iran and implications for Oman. Geological Society, London, Special Publications, **49**(1), 797–831. https://doi.org/10.1144/GSL.SP.1992.049.01.49

Şengör, A. M. C, and Hsu, K. J. (1984). The Cimmerides of Eastern Asia: history of the eastern end of Paleo-Tethys. Mémoires de la Société géologique de France, **147**, 139-167.

Shafaii Moghadam, H., and Stern, R. J. (2011). Geodynamic evolution of Upper Cretaceous Zagros ophiolites: Formation of oceanic lithosphere above a nascent subduction zone. Geological Magazine, **148**(5–6), 762–801. https://doi.org/10.1017/S0016756811000410

Shapiro, S. A., and Treitel, S. (1997). Multiple scattering of seismic waves in multilayered structures. Physics of the Earth and Planetary Interiors, **104**(1–3), 147–159. https://doi.org/10.1016/S0031-9201(97)00043-5

Shomali, Z. H., Keshvari, F., Hassanzadeh, J., and Mirzaei, N. (2011). Lithospheric structure beneath the Zagros collision zone resolved by non-linear teleseismic tomography. Geophysical Journal International, **187**(1), 394–406. https://doi.org/10.1111/j.1365-246X.2011.05150.x

Singh, R., Sharma, S., Mitra, S., and Khan, P. K. (2019). Mapping of coda-wave attenuation and its frequency dependency over eastern Indian Shield. Pure and Applied Geophysics, **176**, 5291-5313. https://doi.org/10.1007/s00024-019-02284-3

Singh, S., and Herrmann, R. B. (1983). Regionalization of crustal coda *Q* in the continental United States. Journal of Geophysical Research, **88**(B1), 527–538.

Snyder, D. B., and Barazangi, M. (1986). Deep crustal structure and flexure of the Arabian Plate Beneath the Zagros collisional mountain belt as inferred from gravity observations. Tectonics, **5**(3), 361–373. https://doi.org/10.1029/TC005i003p00361

Stampfli, G.M., and Borel, G.D. (2004). The TRANSMED transects in space and time: constraints on the paleotectonic evolution of the Mediterranean domain. In The TRANSMED Atlas: The Mediterranean Region from Crust to Mantle, 53–80, eds. Cavazza,W., Roure, F., Spakman, W., Stampfli G.M. and Ziegler, P., Springer-Verlag, Berlin.

Stocklin, J. (1968). Structural history and tectonics of Iran: A review. AAPG Bulletin, **52**,1229-1258. https://doi.org/10.1306/5D25C4A5-16C1-11D7-8645000102C1865D

Stoneley, R. (1981). The geology of the Kuh-e Dalneshin area of southern Iran, and its bearing on the evolution of southern Tethys. Journal of the Geological Society, **138**(5), 509–526. https://doi.org/10.1144/gsjgs.138.5.0509

Tatar, M., Hatzfeld, D., and Ghafory-Ashtiany, M. (2004). Tectonics of the Central Zagros (Iran) deduced from microearthquake seismicity. Geophysical Journal International, **156**(2), 255–266. https://doi.org/10.1111/j.1365-246X.2003.02145.x

Tchalenko, J.S., and Braud, J. (1974). Seismicity and structure of the Zagros: the main recent fault between 33° and 35°N. Philosophical Transactions of the Royal Society of London, **277**, 1–25.

Trugman, D., and Shearer, P. (2018). Strong correlation between stress drop and peak ground acceleration for recent M 1–4 earthquakes in the San Francisco Bay area. Bulletin of the Seismological Society of America,**108**, 929–945. https://doi.org/10.1785/0120170245

Tsujiura, M. (1978). Spectral analysis of the coda waves from local earthquakes. Bulletin of the Earthquake Research Institute, University of Tokyo, **53**, 1–48.

Verdel, C., Wernicke, B. P., Hassanzadeh, J., and Guest, B. (2011). A Paleogene extensional arc flare-up in Iran. Tectonics, **30**(3), 1–20. https://doi.org/10.1029/2010TC002809

Vernant, Ph., Nilforoushan, F., Hatzfeld, D., Abbassi, M. R., Vigny, C., Masson, F., Nankali, H., Martinod, J., Ashtiani, A., Bayer, R., Tavakoli, F., and Chéry, J. (2004). Present-day crustal deformation and plate kinematics in the Middle East constrained by GPS measurements in Iran and northern Oman. Geophysical Journal International, **157**(1), 381–398. https://doi.org/10.1111/j.1365-246X.2004.02222.x

Waldhauser, F., Ellsworth, W. L. (2000). A double-difference earthquake location algorithm: method and application to the northern Hayward fault, California. Bulletin of the Seismological Society of America, **90**(6), 1353–1368. https://doi.org/10.1785/0120000006

Walker, R., Jackson, J., and Baker, C. (2003). Surface expression of thrust faulting in eastern Iran: source parameters and surface deformation of the 1978 Tabas and 1968 Ferdows earthquake sequences. Geophysical Journal International, **152**, 749–765.

Wessel, P., and Smith, W. H. F. (1998). New, improved version of the generic mapping tools released. EOS Transactions American Geophysical Union, **79**(47), 579. http://dx.doi.org/10.1029/98EO00426

Xie, J., Gok, R., Ni., J., and Aoki, Y. (2004). Lateral variations of crustal seismic attenuation along the INDEPTH profiles in Tibet from Lg *Q* inversion. Journal of Geophysical Research, **109**, B10308. https://doi.org/10.1029/2004JB002988

Xie, J., and Mitchell, B. (1990). A back-projection method for imaging large-scale lateral variation of Lg coda Q with application to continental Africa. Geophysical Journal International, **100**, 161–181.

Xie, J., and Nuttli, O. W. (1988). Interpretation of high-frequency coda at large distances: Stochastic modeling and method of inversion. Geophysical Journal International, **95**, 579–595.

Yang, X., Lay, T., Xie, X. -B., and Thorne, M. S. (2007). Geometrical spreading of Pn and Sn in a spherical Earth model. Bulletin of the Seismological Society of America, **97**, 2053–2065. https://doi.org/10.1785/0120070031

Zeng, Y., Su, F., and Aki, K. (1991). Scattering wave energy propagation in a random isotropic scattering medium: 1. Theory. Journal of Geophysical Research, **96**, 607–619.

APPENDIX A

INVERSION WITH EXACT MODEL CONSTRAINTS

To derive the solution for variables **m** satisfying eqs. (5.10) and (5.11) in chapter 5 exactly and simultaneously, I use the Lagrange multiplier method. In this method, it is first noted that the least-squares solution of eq. (5.10) minimizes the following penalty function (squared data error):

$$\Phi_d\left(\mathbf{m}\right) = \frac{1}{2}\left(\mathbf{d} - \mathbf{Lm}\right)^T\left(\mathbf{d} - \mathbf{Lm}\right). \tag{A-1}$$

To additionally constrain the solution by eq. (5.11), this penalty function is modified as

$$\Phi\left(\mathbf{m}, \boldsymbol{\lambda}\right) = \Phi_d + \boldsymbol{\lambda}^T\left(\mathbf{Bm} - \mathbf{c}\right), \tag{A-2}$$

where $\boldsymbol{\lambda}$ is a vector of N_λ Lagrange multipliers, with one multiplier corresponding to each row (constraint equation) in matrix **B**. Quantities $\boldsymbol{\lambda}$ represent additional model unknowns, and the minimization equations $\partial\Phi/\partial\mathbf{m} = \mathbf{0}$ and $\partial\Phi/\partial\boldsymbol{\lambda} = \mathbf{0}$ become

$$\mathbf{K}\begin{pmatrix}\mathbf{m}\\ \boldsymbol{\lambda}\end{pmatrix} = \begin{pmatrix}\mathbf{L}^T\mathbf{d}\\ \mathbf{c}\end{pmatrix}, \tag{A-3}$$

where

$$\mathbf{K} \equiv \begin{bmatrix}\mathbf{L}^T\mathbf{L} & \mathbf{B}^T\\ \mathbf{B} & \mathbf{0}^{N_\lambda \times N_\lambda}\end{bmatrix}, \tag{A-4}$$

and notation $\mathbf{0}^{N\times M}$ means a zero matrix with N rows and M columns. By inverting matrix **K**, the model and Lagrange multipliers are obtained:

$$\begin{pmatrix} \mathbf{m} \\ \boldsymbol{\lambda} \end{pmatrix} = \mathbf{K}^{-1} \begin{pmatrix} \mathbf{L}^T \mathbf{d} \\ \mathbf{c} \end{pmatrix}. \tag{A-5}$$

Since $\Phi(\mathbf{m}, \boldsymbol{\lambda}) = \Phi_d(\mathbf{m})$ for any **m** satisfying $\mathbf{Bm} = \mathbf{c}$, solution (A-5) is unbiased and exactly minimizes the LS norm $\Phi_d(\mathbf{m})$ within the set of models satisfying the constraints.

Note that in many applications of geophysical inversion (such as of smoothing of nonparametric models by Castro et al. (1990) or use of "prior" model by Drouet et al. (2008); subsection 5.7.1 in chapter 5), model constraining is performed in a different way, which is called "regularization." The squared data error is modified as (Tikhonov regularization; e.g., Menke, 1984):

$$\Phi(\mathbf{m}, \boldsymbol{\lambda}) = \Phi_d + \alpha(\mathbf{Bm} - \mathbf{c})^T (\mathbf{Bm} - \mathbf{c}), \tag{A-6}$$

where the single parameter α is fixed. For example, by selecting **B** equal the identity matrix and $\mathbf{c} = \mathbf{m}_0$, the solution can be attracted toward some "prior", or preferred model $\mathbf{m}_0$.

For the modified objective function in eq. (A-6), vector $\boldsymbol{\lambda}$ in eq. (A-2) is fixed and related to **m** by $\boldsymbol{\lambda} = \alpha(\mathbf{Bm} - \mathbf{c})$. Because this value of $\boldsymbol{\lambda}$ is not optimal, the original data error (A-1) is not minimized, and this solution is biased toward the constraint. The amount of this bias and the stability of model **m** depends on selecting α, which may be not easy to do (Fang et al., 2019). By contrast, when using the solutions obtained by eqs. (A-2) to (A-5), there is no need for the subjective parameter α, and solution **m** exactly minimizes the data error (A-1) within the subspace of models exactly satisfying the required constraints.